

**DESIGN AND TESTING OF THERMOACOUSTIC
ELECTRICITY GENERATORS FOR RURAL AREAS OF
DEVELOPING COUNTRIES**

Kalid Oumer Ali Abdoulla

Submitted in accordance with the requirements of the degree of
Doctor of Philosophy

The University of Leeds
School of Chemical and Process Engineering

May, 2016

The candidate confirms that the work submitted is his own, except where work which has formed part of jointly-authored publications has been included. The contribution of the candidate and other authors to this work has been explicitly indicated below. The candidate confirms that appropriate credit has been given within the thesis where reference has been made to the work of others.

The work of jointly-authored publications are presented in Chapter 3 and Chapter 4 of the thesis.

The first paper was presented in the 19th International Congress on Sound and Vibration, Vilnius, Lithuania, in July 2012. The title is “design of a low-cost two-stage thermoacoustic electricity generator for rural communities in developing countries”. Authors are Kalid Abdoulla, Zhibin Yu and Artur J Jaworski. This paper describes the numerical design of a two-stage looped-tube thermoacoustic electricity generator to provide electrical power for households in remote and rural areas of developing countries. The work was done by the candidate under supervision of professor Jaworski and technical support from Dr Yu (PDRA, who left Leicester in 2012).

The second paper was presented in the Proceeding of the World Congress on Engineering, London, in July 2013. The title is “travelling wave thermoacoustic electricity generator for rural areas using a side-branch alternator arrangement”. Authors are Kalid Abdoulla, Huifang Kang and Artur J Jaworski. This paper illustrates the design, construction and testing of a looped-tube travelling wave thermoacoustic electricity generator that provides low-cost electrical power for remote and rural areas of developing countries. The experimental and numerical work, analysing the results and preparing the paper was done by the candidate under supervision of professor Jaworski (some fragments of numerical coding in Delta EC was helped by Dr Kang, who was then a short term visitor academic at Leicester in 2012/13).

This copy has been supplied on the understanding that it is copyrighted material and that no quotation from the thesis may be published without proper acknowledgement.

ACKNOWLEDGEMENTS

First and foremost, I would like to express my sincere gratitude to my supervisor, Professor Artur J. Jaworski, for his guidance, support and mentorship throughout my study. With his patience, understanding and encouragement, I have achieved many hard tasks and overcome difficulties. His observations, comments, instructions and advice have been constantly showing me the right path and direction in how to become an independent thinker and a team player in the thermoacoustic research group led by him.

I would like to express my appreciation to my co-supervisor, Dr. Xiaoan Mao for his support, valuable advice and many research discussions that helped me to develop my research skills. I would like also to express my thanks to Dr. Zhibin Yu, for the great experience of working with him during my stay at the University of Leicester. His patience, guidance, advice and research ideas have helped me a great deal to improve the design of my experimental work. Also, a lot of useful advice I received from Dr Huifang Kang, when developing the early DeltaEC codes, is gratefully acknowledged.

I would also like to thank all technicians at the University of Leeds and the University of Leicester for the massive help they supplied (specifically Mr Gurdev Bhogal), during the time of setting up and troubleshooting the experimental rigs.

The financial support from the Libyan Government to carry out my PhD studies in UK is gratefully acknowledged.

Last, but by no means least, I would like to express my extreme appreciations and thanks to the spirit of my beloved father who passed away last year, my beloved mother, and my wife for their support, sacrifice and prayers throughout the time of my study. Thank you very much indeed.

ABSTRACT

This thesis outlines a detailed study comprising the simulation, design, construction, and experimental validation of two prototypes of looped-tube travelling wave thermoacoustic electricity generators. The prototypes used air at atmospheric pressure as working gas, an audio loudspeaker as linear alternator, while most of acoustic resonator parts were made of PVC components. The hot heat exchangers were externally heated. The first prototype was a small size, single-stage generator powered by combustion from a propane gas burner. The feedback pipe includes a branched alternator and an acoustic impedance matching stub. The effect of the heat input on the generator performance has been investigated. 13W of electrical power, extracted by 12Ω electric load, was achieved at flue gas temperature of 627.4°C and regenerator temperature difference of 430K. The second prototype was a larger sized (resonator inner diameter is 128 mm) two-stage generator. Here, the heat source was an electric air heat “gun” than provides air stream at 650°C . Firstly, the single-stage engine was examined at frequencies of 48.82, 64.45 and 70.31Hz. The experiments show that the streaming can reduce acoustic power from 110.63 to 63.4W at 70.31Hz. Furthermore, the acoustic power increases from 111.45 to 153 W when the frequency is increased from 48.82 to 64.45 Hz. Subsequently, a linear alternator was attached to the engine to convert the produced acoustic power into electricity. At a load of 9Ω the single-stage generator achieved 8.52W of electricity and 1.47% efficiency. The generator was further improved by incorporating an identical second stage. The effects of matching stub length, variable load and heat input were investigated. The two-stage prototype generated 14.18W of electrical power to a load of 9Ω with a thermal-to-electrical efficiency of 2.1%. The result indicated that the generators can supply enough electricity to power LED bulbs, and charge mobile phones and batteries.

Table of Contents

CHAPTER 1	1
INTRODUCTION	1
1.1 Overview of Thermoacoustics	1
1.2 Motivation of the Study	3
1.3 Aim and Objectives of the Study	4
1.4 Outline of the Thesis	7
CHAPTER 2	9
LITERATURE REVIEW.....	9
2.1 Fundamentals of Thermoacoustics.....	9
2.1.1 History of thermoacoustics	9
2.1.2 Important parameters	12
2.1.3 Standing wave devices	16
2.1.4 Travelling wave devices.....	19
2.2 The Linear Theory and Modelling	22
2.2.1 The governing equations of stacks and regenerators.	24
2.2.2 DeltaEC program	30
2.3 Measurement of Acoustic Power	31
2.3.1 The two-microphone method	31
2.3.2 The piston or loudspeaker method	33
2.4 Electro-acoustic Power Transducers	34
2.5 Acoustic Streaming	37
2.5.1 Gedeon streaming.....	38
2.5.2 Rayleigh streaming.....	41
2.5.3 Jet-driven streaming	42
2.5.4 Streaming within a regenerator or stack.....	42
2.6 Developments in Thermoacoustic Devices	43
2.6.1 Thermoacoustic refrigerators	43
2.6.2 Thermoacoustic standing wave engines	44
2.6.3 Thermoacoustic cascade engines	48
2.6.4 Thermoacoustic travelling wave engines and electricity-generators	51
2.7 Summary	68
CHAPTER 3	71
DESIGN, OPTIMISATION AND EXPERIMENTAL SET-UP OF THE PROTOTYPES INVESTIGATED	71

3.1 Design Strategy of Prototypes.....	71
3.2 The 54-mm Diameter One-stage Looped-tube Travelling Wave Electricity Generator.....	73
3.2.1 DeltaEC simulation.....	74
3.2.2 Experimental apparatus.....	74
3.2.3 Instrumentation and experimental procedure.....	79
3.3 Experimental Setup and Models for 128-mm diameter Travelling-wave Prototype Devices.....	81
3.3.1 One-stage Looped-tube Thermoacoustic Engine.....	81
3.3.2 One-stage Looped-tube Electricity Generator.....	84
3.3.3 Two-stage Looped-tube Electricity Generator.....	86
3.4 Summary.....	108
CHAPTER 4.....	109
RESULTS AND DISCUSSIONS.....	109
4.1 The 54-mm Diameter Single-stage Looped-tube Travelling Wave Thermoacoustic Electricity Generator.....	109
4.1.1 Simulation results.....	109
4.1.2 Experimental and calculated results.....	113
4.2 The 128-mm diameter Diameter One-stage Travelling Wave Engine.....	119
4.2.1 Simulation results.....	120
4.2.2 Effect of the acoustic streaming on the performance of the engine at different stub lengths.....	123
4.2.3 Effects of different working frequencies.....	128
4.3 The 128-mm diameter Diameter One-stage Electricity Generator.....	133
4.3.1 Simulation results.....	133
4.3.2 Effects of load resistance on performance of one-stage generator.....	137
4.3.3 Effects of heating power on one-stage electricity generator.....	141
4.4 The 128-mm diameter Two-stage Looped-tube Electricity Generator.....	149
4.4.1 Simulation results.....	149
4.4.2 Effect of the length of the matching stub.....	153
4.4.3 Effect of load resistance.....	169
4.4.4 Effect of heating power input.....	179
4.5 Summary.....	189
CHAPTER 5.....	191
CONCLUSION AND FUTURE WORK.....	191
5.1 Conclusion.....	191
5.2 Future Work.....	195

BIBLIOGRAPHY	197
APPENDICES	207
Appendix A: List of publications.....	207
Appendix B: List of DeltaEC models.	207
Appendix C: Detail of thermoacoustic core design for 128-mm diameter systems	238

List of Tables

Table 2. 1 The thermoviscous function h and its spatial average f of some stack geometries.....	27
Table 3. 1 Nominal and measured parameters of the loudspeaker (B&C speakers)	78
Table 3. 2 The configuration of the main parts of each stage in two-stage generator	89
Table 3. 3 Optimal values of the optimised parameters	97
Table 3. 4 Dimensions of parts in the experimental set-up.....	102
Table 4. 1 The results of measured and simulated pressure amplitudes along the loop of the engine.....	121
Table 4. 2 The results of measured and simulated pressure amplitudes along the loop of the single-stage generator	137
Table 4. 3 The effect of load resistance on the heat input, heat rejected at the first stage.....	171
Table 4. 4 The effect of load resistance on the heat input, heat rejected at the second stage.....	172
Table 4. 5 The increase of the heat input and rejected in Stage 1	183
Table 4. 6 The increase of the heat input and rejected at Stage 2	184

List of Figures

Figure 1. 1 Phase difference between acoustic pressure and velocity for two types of devices (Ceperley, 1979): (a) Phase difference between pressure and velocity of 90° for standing wave device; (b) Phase difference of 0° for travelling wave device.....	2
Figure 1. 2 Road map of the research activities of all looped-tube configurations....	8
Figure 2. 1 (a) Sondhauss tube, (b) Rijke tube.....	10
Figure 2. 2 Back and forth optimum displacement of a gas parcel between a stack and its adjacent heat exchanger.....	14
Figure 2. 3 Schematics of thermoacoustic effects in a standing wave engine. (a) Standing wave thermoacoustic engine, (b) The enlarged view of the thermoacoustic oscillation in the stack and (c) pressure and volumetric velocity in the resonator ...	17
Figure 2. 4 Schematics of thermoacoustic effects in standing wave refrigerator. (a) Standing wave thermoacoustic refrigerator, (b) The enlarged view of the thermoacoustic oscillation in the stack and (c) pressure and volumetric velocity in the resonator.	18
Figure 2. 5 Schematics of thermoacoustic effects in travelling wave engine. (a) Travelling wave engine, (b) The enlarged view of gas-solid interaction during the oscillation in the regenerator, (c) The thermodynamic cycle in the regenerator (Yu and Jaworski, 2010a).....	20
Figure 2. 6 Schematics of thermoacoustic effects in travelling wave refrigerator. (a) The core of the refrigerator, (b) the enlarging view of the oscillation in the stack...	22
Figure 2. 7 The spatial average function f for different geometries (Swift, 2002). .	25
Figure 2. 8 Schematic drawing of the two sensors method.....	32
Figure 2. 9 Schematics of a linear alternator (Yu et al, 2010a). (a) Schematic of physical model of alternator. (b) Equivalent impedance circuit of the alternator.....	35
Figure 2. 10 General types of acoustic streaming in thermoacoustic devices (the time-average velocity represented by arrows), (Swift, 2002). (a) Gedeon streaming, (b) Rayleigh streaming, (c) Jet-driven streaming and (d) streaming within a regenerator or stack	38
Figure 2. 11 The Gedeon streaming in the thermoacoustic Stirling engine is stopped a jet pump (Backhaus and Swift, 2000).	39
Figure 2. 12 The cooler performance before and after inserting the membrane (Huan et al., 2015). (a) the effect of the heating power on the pressure ratio, and (b) the effect of the heating power on the temperature of the heating block.....	40

Figure 2. 13 Schematics of Rayleigh streaming in a tube (Swift, 2002). (a) the net drift of the gas parcel near the wall and (b) the net drift near the wall by the tube taper.....	41
Figure 2. 14 Picture of Rayleigh streaming in a standing wave resonator (Yazaki and Tominaga, 1998).	42
Figure 2. 15 The dimensionless critical temperature gradient Θ_{crit} versus $r_{h\delta_k}$ for different positions in the stack.....	47
Figure 2. 16 The cascade thermoacoustic engine (Gardner and Swift, (2003). (a) A schematic drawing of the engine. (b) A detailed schematic diagram of the three stages of the engine. The first stage is a standing-wave engine, the second and third stages are travelling.....	50
Figure 2. 17 Schematic drawing of the thermoacoustic Stirling engine (Backhaus and Swift, 2000): (a) drawing of the complete engine. (b) drawing of the bypass part of the engine. (c) lumped-element diagram of the engine.	58
Figure 2. 18 The looped-tube travelling wave thermoacoustic engine (Yazaki et al., 1998).	59
Figure 2. 19 A schematic diagram of the travelling wave engine (Abduljalil et al. 2011).	60
Figure 2. 20 The effects of the mean pressure. (a) Mean pressure versus pressure amplitude, and (b) mean pressure versus acoustic power.	62
Figure 2. 21 The performance outputs of the engine (Yu et al. 2010b). (a) The power outputs as functions the heating power and temperature difference in the regenerator. (b) The electricity output versus the load resistance.....	64
Figure 2. 22 A photograph of the thermoacoustic-electricity generator. (Yu et al. 2012).	65
Figure 2. 23 Schematic drawing of the two-stage electricity generator	67
Figure 3. 1 The block diagram of the segments in the DeltaEC model: (1) ambient heat exchanger (AHX), (2) regenerator (REG), (3) hot heat exchanger (HHX), (4) thermal buffer tube (TBT), (5) the first stub where the speaker is located at the end (Stub1), (6) the tub	74
Figure 3. 2 Schematic drawing of the experimental thermoacoustic generator	75
Figure 3. 3 Photograph of the thermoacoustic generator tested.....	75
Figure 3. 4 The photograph of the ambient heat exchanger (AHX)	76
Figure 3. 5 Photograph of the hot heat exchanger (HHX), the thermal buffer tube (TBT) and the holder of the regenerator (REG).....	77

Figure 3. 6 A block diagram of the single stage 128-mm diameter thermoacoustic engine.....	82
Figure 3. 7 A schematic diagram of the single stage 128-mm diameter thermoacoustic engine.....	83
Figure 3. 8 Photograph of the experimental apparatus of the single stage 128-mm diameter thermoacoustic engine.....	83
Figure 3. 9 A block diagram of the single stage 128-mm diameter electricity generator.....	84
Figure 3. 10 A schematic diagram of the single stage 128-mm diameter electricity generator.....	85
Figure 3. 11 Photograph of the experimental apparatus of the single stage 128-mm diameter electricity generator.....	86
Figure 3. 12 The block diagram of the two-stage thermoacoustic electricity generator.....	88
Figure 3. 13 Impact of the porosity of both regenerators on the electrical output..	91
Figure 3. 14 Effect of the hydraulic radius of the regenerator on the electrical output.	92
Figure 3. 15 Impact of the length of the regenerator on the electrical output.	93
Figure 3. 16 Effect of porosity of the hot heat exchanger on the electrical output. .	94
Figure 3. 17 Effect of the hydraulic radius of the hot heat exchanger on the electrical output.....	95
Figure 3. 18 Effect of the length of the hot heat exchanger on the electrical output.	95
Figure 3. 19 Effect of the diameter of the feedback pipe on the electrical output..	96
Figure 3. 20 The photograph of rectangular cuts of the stainless steel screen of the regenerator.....	98
Figure 3. 21 Photograph of the configuration of the ambient heat exchanger (AHX). (a) The car heater matrix as a heat exchanger. (b) Push-in ports for cooling water access to the AHX.....	99
Figure 3. 22 The shape change of a pipe after the flattening process	100

Figure 3. 23 Photographs of the hot heat exchanger configuration (a) the flattening tool; (b) the flattened tube; (c) the hot heat exchanger; (d) the thermoacoustic core	100
Figure 3. 24 (a) Photograph of the combined two-stage thermoacoustic cores; (b) Photograph of the elastic membrane.....	101
Figure 3. 25 A schematic drawing of the two-stage thermoacoustic electricity generator.....	103
Figure 3. 26 Photograph of the experimental apparatus of the two-stage electricity generator.....	104
Figure 3. 27 Photograph of the water cooling system of the generator.	106
Figure 4. 1 The calculation results of the distributions of the acoustic power flow and the acoustic field in the 54-mm diameter electricity generator. (a) Pressure amplitude, (b) Volumetric velocity, (c) Acoustic impedance (d) Phase angle and (e) Acoustic power.....	112
Figure 4. 2 The relationship between the temperature difference of two ends of the regenerator and the electricity output.....	114
Figure 4. 3 Effects of the temperature difference at two ends of the regenerator on the coil displacement of the alternator	115
Figure 4. 4 Effects of the temperature difference of two ends of the regenerator on the acoustic power extraction of the alternator	116
Figure 4. 5 Effect of the temperature difference at two ends of the regenerator on the acoustic-to-electric efficiency of the alternator.....	117
Figure 4. 6 Effects of the temperature difference of the two ends of the regenerator on the acoustic power flow in the feedback pipe.	117
Figure 4. 7 The effect of the temperature difference at two ends of the regenerator on pressure amplitudes.....	118
Figure 4. 8 The effect of the temperature difference at two ends of the regenerator on the temperature distribution in the HHX.....	119
Figure 4. 9 The simulation results of the acoustic field in the 128-mm diameter thermoacoustic engine. (a) Pressure amplitude, (b) Volumetric velocity, (c) Acoustic impedance, (d) Phase difference and (e) Acoustic power flow.....	122
Figure 4. 10 Effect of the stub length on temperature along the regenerator without membrane in the loop. (a) Temperature versus position of thermocouple. (b) Temperature versus stub length.	124

Figure 4. 11 Effect of the stub length on temperature along the regenerator with a membrane inserted into the loop. (a) Temperature versus position of thermocouple. (b) Temperature versus stub length.....	124
Figure 4. 12 Effect of the stub length on the temperature difference in the regenerator.....	125
Figure 4. 13 Effect of the stub length on the ratio of temperature slopes.	126
Figure 4. 14 Effect of the stub length on acoustic pressure distribution along the loop without a membrane in the loop. (a) Pressure amplitude versus loop length, and (b) Pressure amplitude versus stub length.....	126
Figure 4. 15 Effects of the stub length on pressure amplitudes along the loop with a membrane in the loop. (a) Pressure amplitude versus loop length and (b) Pressure amplitude versus stub length.	127
Figure 4. 16 Effect of the stub length on the acoustic power flow along the loop. (a) Without membrane and (b) With a membrane installed in the loop.	127
Figure 4. 17 Effect of the stub length on the acoustic power delivered to the loop.	128
Figure 4. 18 Effect of the stub length on the temperature profile in the regenerator and working frequency of 48.82Hz. (a) Temperature versus length of the regenerator and (b) Temperature versus stub length	129
Figure 4. 19 Effects of the stub length on the temperature profile in the regenerator and working frequency of 64.45Hz. (a) Temperature versus length of the regenerator and (b) Temperature versus stub length.	130
Figure 4. 20 Effect of the stub length on the temperature difference in the regenerator for the frequencies 48.82 and 64.45 Hz.	130
Figure 4. 21 Effect of the stub length on the ratio of the thermal penetration depth to the hydraulic radius in the regenerator for the frequencies 48.82 and 64.45 Hz. ...	131
Figure 4. 22 Effects of the stub length on the pressure ratio for the frequencies 48.82 and 64.45 Hz.	132
Figure 4. 23 Effects of the stub length on the acoustic power in the loop for the frequencies 48.82 and 64.45 Hz.	133
Figure 4. 24 The calculation results of the acoustic field in the large diameter, one stage electricity generator. (a) pressure amplitude (b) volumetric velocity (c) acoustic impedance (d) phase angle and (e) acoustic power flow.	135
Figure 4. 25 Effect of the load resistance on the coil displacement of the alternator.	138

Figure 4. 26 Effect of the load resistance on the acoustic power extracted by the alternator.	139
Figure 4. 27 Effect of the load resistance on the thermoacoustic engine efficiency.	139
Figure 4. 28 Effect of the load resistance on the electricity produced by the alternator	140
Figure 4. 29 Effect of the load resistance on the total efficiency of the generator	140
Figure 4. 30 Effect of the load resistance on the alternator efficiency.....	141
Figure 4. 31 Effect of the heat input on the temperature profile of the regenerator.	142
Figure 4. 32 Relationship between the pressure ratio and the heat input and heat rejected.	143
Figure 4. 33 Effect of the increasing the heating power on the temperature difference in the regenerator.	144
Figure 4. 34 Effect of increasing the heat input on the acoustic pressure amplitudes along the loop.	144
Figure 4. 35 Effect of the heating power on the acoustic power flow in the loop.	145
Figure 4. 36 Influence of the heat input on the relationship between the pressure ratio and the coil displacement of the alternator.	145
Figure 4. 37 Effect of the heat input on the relationship between the pressure ratio and acoustic power extracted by the alternator	146
Figure 4. 38 Effect of the heat input on the relationship between the pressure ratio and the engine efficiency.	147
Figure 4. 39 Effect of the heat input on the relationship between the pressure ratio and the electricity.	147
Figure 4. 40 Effect of the heating power on the relationship between the pressure ratio and the thermal-to-electric efficiency.	148
Figure 4. 41 Effect of the heat input on the relationship between the pressure ratio and the acoustic-to-electric efficiency.	149
Figure 4. 42 The numerical simulations of the acoustic field in the 128-mm diameter, two-stage electricity generator. (a) Pressure amplitude (b) Volumetric velocity (c) Acoustic impedance (d) Phase angle and (e) Acoustic power flow.....	150

Figure 4. 43 Effect of stub length on temperature distribution along the regenerator, including the effects of acoustic streaming. (a) The first stage and (b) the second stage.....	155
Figure 4. 44 Effect of stub length on temperature distribution along the regenerator after installing the membrane and the suppression of the acoustic streaming in the loop. (a) The first stage and (b) the second stage.....	155
Figure 4. 45 Effect of stub length on the temperature difference in the regenerator. (a) Without the membrane and (b) with the membrane.	157
Figure 4. 46 Effect of changing stub length on the heating power. (a) Without the membrane and (b) with the membrane.....	158
Figure 4. 47 Effect of stub length on the heat rejected from ambient heat exchangers. (a) Without the membrane and (b) with the membrane.	158
Figure 4. 48 The slope ratio of the temperature distribution in a regenerator.....	159
Figure 4. 49 Relationship between stub length and temperature slope ratio in the regenerator (without a membrane in the loop).....	161
Figure 4. 50 Relationship between stub length and temperature slope ratio in the regenerator (with the membrane in the loop).....	162
Figure 4. 51 The pressure amplitude distribution along the loop at different stub lengths. (a) Pressure amplitude versus the loop length and (b) Pressure amplitude versus the stub length.	162
Figure 4. 52 Effect of the stub length on the pressure amplitude at different locations in the loop.	163
Figure 4. 53 Effect of stub length on the coil displacement of the alternator.	164
Figure 4. 54 Effect of stub length on the acoustic power extracted by the alternator.	165
Figure 4. 55 Effect of stub length on the thermal-to-acoustical efficiency.....	166
Figure 4. 56 Effect of the stub length on the electricity produced.	167
Figure 4. 57 Effect of stub length on the total efficiency of the generator.	167
Figure 4. 58 Effect of stub length on the alternator efficiency.	168
Figure 4. 59 Effect of the load resistance on temperature profiles in the thermoacoustic core. (a) the first stage and (b) the second stage.....	170
Figure 4. 60 Heat rejected at ambient heat exchanger versus load resistance.	170
Figure 4. 61 Effect of load resistance on the pressure amplitude distribution.	173

Figure 4. 62 Effect of load resistance on the coil displacement of the alternator. .	173
Figure 4. 63 Effect of load resistance on the acoustic power extracted by the alternator.	175
Figure 4. 64 Effect of load resistance on the efficiency of the thermoacoustic engine.	176
Figure 4. 65 Effect of load resistance on the electrical output.....	177
Figure 4. 66 Effect of load resistance on the thermal-to-electrical efficiency of the generator.....	178
Figure 4. 67 Effect of load resistance on the efficiency of the alternator.	178
Figure 4. 68 The effect of the heating temperature of the heat gun on the hot air flow.	179
Figure 4. 69 Effect of heating power on the change in temperature along the stage. (a) the first stage, and (b) the second stage.	180
Figure 4. 70 Effect of heating power on the profile of temperatures in the regenerator. (a) the first stage and (b) the second stage.	181
Figure 4. 71 Effect of heating power on temperature difference in the two regenerators.	182
Figure 4. 72 Effect of heating power on the pressure amplitude distribution along the loop. (a) pressure amplitude versus loop length and (b) pressure amplitude versus heat input.....	184
Figure 4. 73 Effect of heating power on the relationship between the pressure drive ratio and the coil displacement of the alternator.	185
Figure 4. 74 Effect of heating power on the relationship between the pressure ratio and the acoustic power extraction of the alternator.	186
Figure 4. 75 Effect of heating power input on the relationship between the pressure drive ratio and the thermoacoustic efficiency.	186
Figure 4. 76 Effect of the heat input on the relationship between the pressure ratio and the electrical output	187
Figure 4. 77 Effect of heating power on the relationship between the pressure ratio and the entire efficiency of the generator.....	188
Figure 4. 78 Effect of heating power input on the relationship between the pressure ratio and the alternator efficiency.	189

NOMENCLATURE

A	Cross sectional area (m^2)
Bl	Force factor (N/A)
a	Speed of sound (m/s)
c	Compliance per unit length (m^3/Pa)
c_p	Specific heat capacity ($\text{J}/\text{kg} \cdot \text{K}$)
d	Diameter (m)
E	Acoustic power (W)
e	2.71828
f	Frequency (Hz)
f	Spatially averaged thermoviscous function
g	Gain factor
H	Total power flux (W)
h	Thermoviscous function
I	Current (A)
i	$\sqrt{-1}$
K_m	Coil stiffness (N/m)
k	Thermal conductivity ($\text{W}/\text{m} \cdot \text{K}$)
L	Inductance (mH)
l	Inertance per unit length (kg/m^3)
M_2	Second order time averaged mass flux ($\text{kg}/\text{s} \cdot \text{m}^2$)
M_m	Moving mass of the alternator diaphragm (kg)

n	Screen mesh number (inch^{-1})
P	Power (W)
p	Pressure (Pa)
Q	Heat transfer rate (W)
R	Resistance (Ω)
\mathfrak{R}	Gas constant ($\text{J/kg} \cdot \text{K}$)
r_h	Hydraulic radius (m)
s	Entropy per unit mass ($\text{J/kg} \cdot \text{K}$)
T	Temperature ($^{\circ}\text{C}$)
t	Time (s)
U	Volumetric flow rate (m^3/s)
u	Velocity in x direction (m/s)
V	Volume (m^3)
V	Voltage (V)
v	Velocity vector (m/s)
W	Acoustic power (W)
X	Alternator displacement (mm)
Z	Acoustic impedance ($\text{Pa} \cdot \text{s}/\text{m}^3$)

Greek letters

β	Thermal expansion coefficient (K^{-1})
γ	Ratio of isobaric to isochoric specific heats

Δ	Difference
δ	Penetration depth (m)
ε_s	Ratio of gas to solid heat capacities
η	Efficiency
λ	Wavelength (m)
μ	Dynamic viscosity (kg/m · s)
ν	Kinematic viscosity (m ² /s)
ξ	Gas displacement (m)
Π	Perimeter (m)
Θ	Normalised temperature gradient
π	3.14159
ρ	Density (kg/m ³)
σ	Prandtl number
ϕ	Volumetric porosity
ϕ	Phase angle
ω	Angular frequency (s ⁻¹)

Subscripts

a	Ambient
a	Acoustic
a	Air
alt	Alternator

c	Cold
e	Electric
h	Hot
m	Mean value
w	Water
k	Thermal
v	Viscous
<i>crit</i>	Critical
<i>gas</i>	Gas
<i>in</i>	Inlet
<i>Onset</i>	Onset temperature
<i>out</i>	Outlet
<i>wetted</i>	Gas-solid contact area
1	First order acoustic variable
2	Second order acoustic variable

Special symbols

Im []	Imaginary part of
Re []	Real part of
$\langle \rangle$	Spatial average perpendicular to x
$ $	Magnitude of complex number
Overdot	Time derivative
Overbar	Time average

Tilde Complex conjugate

Abbreviations

ALT Alternator

AHX Ambient heat exchanger

DeltaEC Design Environment for Low-amplitude
Thermoacoustic Energy Conversion

FBP Feedback pipe

HHX Hot heat exchanger

REG Regenerator

TAE Thermoacoustic engine

TAEG Thermoacoustic electricity generator

TASHE Thermoacoustic Stirling Heat Engine

TBT Thermal buffer tube

STUB Side branch tube

CHAPTER 1

INTRODUCTION

1.1 Overview of Thermoacoustics

Broadly speaking, thermoacoustics can be defined as an area of science and technology that employs concepts from heat transfer, thermodynamics, and acoustics to design thermodynamic machines (e.g. engines or coolers) with no moving parts. Glass blowers have known for centuries that the cooling down vessels would emit sound. In 1777, Byron Higgins recorded the first observation of heat-to-acoustic conversion that was referred to as “singing flame” when he heated up a vertical open-ended tube using a hydrogen flame (Putnam and Dennis, 1956). It was noted that the energy of the sound wave produced was affected by the location of the flame.

The thermoacoustic technology can be generally divided into thermoacoustic refrigerators and thermoacoustic engines based on the mechanism of the thermoacoustic effect that is controlled by the interactions between sound waves (pressure and displacement oscillations) and heat transfer (temperature oscillations). In a thermoacoustic refrigerator/cooler/heat pump, a compressible fluid is excited by a generated sound wave that travels through a porous medium. The wave creates pressure and displacement (velocity) oscillations in the working gas. It also establishes a temperature gradient in the porous medium along the direction of the sound wave. If the porous medium is sandwiched between an ambient heat exchanger and cold heat exchanger (forming so called thermoacoustic core), and the phasing between the acoustic pressure and displacement of the oscillating particles of the working gas is appropriate, the temperature gradient will be steeper and cooling effects will be produced where heat exchange takes place from the cold to the ambient side of the porous medium.

In the thermoacoustic engine/prime mover, the porous material is located between a hot and ambient heat exchanger. As the temperature difference between the two sides of the solid material increases, a temperature gradient increases leading to spontaneous generation of sound waves. The generated sound waves oscillate the gas particles which start exchanging heat with the solid boundaries at

different locations. The appropriate phasing between the oscillating pressure and velocity of the gas particles, in the vicinity of the solid material, enhances the energy conversion from thermal to acoustic power.

Thermoacoustic engines and refrigerators are categorized into standing-wave and travelling-wave devices. In the standing wave device, the solid materials are porous media and are called “stack” while in the travelling wave device, the porous media is called the “regenerator” (Abduljalil et al., 2011a). In the standing wave engines, the heat exchange between the stack and the gas particles is imperfect due to the phase difference between the acoustic pressure and velocity of the working fluid being close to 90° (Yazaki et al., 1998). This causes an inefficient system where a low percentage of the heat power input is converted into acoustic power and the rest is conducted and lost into the stack. In the travelling wave engines, the phase difference between the oscillating pressure and velocity is close to 0° (Yu et al., 2012). Therefore, travelling wave engines are considerably more efficient due to the perfect thermal contact between the gas particles and the regenerator (Ceperley, 1979). The difference between velocity and pressure phasing in the two types of thermoacoustic devices is shown schematically in Figure 1.1.

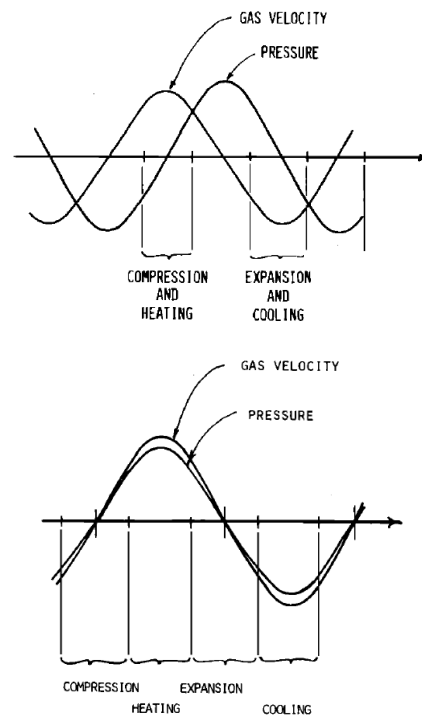


Figure 1. 1 Phase difference between acoustic pressure and velocity for two types of devices (Ceperley, 1979): (a) Phase difference between pressure and velocity of 90° for standing wave device; (b) Phase difference of 0° for travelling wave device.

Thermoacoustic technology has a very promising future compared to conventional technologies. The thermoacoustic devices use environmentally friendly working fluids: usually noble gases which are non-toxic, and non-flammable (Swift, 2002). In addition, they have the ability to utilize low temperature heat sources such as solar energy, recover waste heat from industrial processes or flue gases from combustion (De Blok, 2010). Apart from alternators (acoustic-to-electricity transducers) which are the only moving parts, thermoacoustic electricity generators are very simple in construction. This results in potentially low capital and maintenance costs of devices which convert heat into electric power without using mechanically moving parts (Wu et al., 2011). Although alternators are the most expensive parts in thermoacoustic generators (the rest is just a network of pipes), their fatigue-resistance is well established while there is no need for lubrication in their life-time (Backhaus et al., 2004).

Because of the above advantages, many researchers have extensively studied travelling wave electricity generators and major developments were achieved in the past decade. For instance, Backhaus et al. (2004) built and tested a thermoacoustic electricity generator that delivers 58 W of electricity with a thermal-to-electrical efficiency of 15%. Luo et al. (2008) built and tested a travelling wave electricity generator, which produced 100 W and achieved a total efficiency of 3.6%. Wu et al. (2011) and Wu et al. (2012) could extract 481 W of electric power from a solar powered thermoacoustic electricity generator at an efficiency of 15%. A travelling wave thermoacoustic generator producing 1043 W of electricity at a thermal-to-electrical efficiency of 19.8% and was designed and tested by Wu et al. (2014a).

1.2 Motivation of the Study

The substantial improvements in thermoacoustic devices over the past decades, as discussed in section 1.1, suggest that they have potentially wide-ranging applications in electricity generation, in particular from waste heat recovery and renewable energy sources. They have also a potential of low cost if mass produced due to the lack of moving parts. However, at this stage, the prototypes and laboratory demonstrators do not yet fulfil this long-term potential – the devices which use pressurised gasses (e.g. helium at 5 MPa) are difficult to make as one-off units. Therefore, a question arises if they can be made economically feasible if using

inexpensive gases (air) at low or atmospheric pressure. Here, an unavoidable downside would be a drop in thermodynamic performance (low efficiencies) as well as low power levels. However, use of atmospheric air as working fluid opens the opportunities of applying truly inexpensive materials – for example plastic parts as opposed to certified steel piping.

Indeed, such way of thinking about the application of thermoacoustic generators has been the background of EPSRC funded project SCORE (2007-2012). It has showed that the technology could be used for providing small-scale electricity generation capability to many people who live in remote and rural areas in developing countries. More than 2 billion people have no access to the national electricity grids and no supplies at all of the conventional power sources such as natural gas and fuel (Douglas et al. 1997). A large population of these people use biomass materials (e.g. wood) as fuel to cook their food on stone-stoves, as well as for heating and lighting. However, the smoke released from biomass burning has very serious effects on peoples' health and often poses fire hazard. The thermoacoustic electricity generator can solve some of these problems. While cooking, the heat released from combustion of the burning wood in the cooking stove can be used to power a thermoacoustic electricity generator if the flue gases can be appropriately channelled through its hot heat exchanger. This generated electric power would be enough to power LED lamps, laptops, and charge mobile phones and batteries and thus improve the quality of life. These ideas will be further explored in section 1.3.

1.3 Aim and Objectives of the Study

Based on a number of complex engineering and technical principles in designing a thermoacoustic generator, the electric power produced can be scaled up from a few watts to several kilowatts. Firstly, the electricity extracted from the generator is mainly proportional to the mean pressure of the working gas inside the generator (Swift, 1988). However, increasing the mean pressure also increases the cost of materials used to build the generator. Noble gases (such as helium) are environmentally friendly and very appropriate to use as working gases in thermoacoustic generators due to their low viscosity (Belcher, 1999). However, their poor availability in rural communities and high prices affect the total cost of the

thermoacoustic generator. Furthermore, linear alternators also play a major role in thermoacoustic generation in terms of the acoustic-to-electric efficiency conversion (typically 90%) (Kang et al. 2015). However, their high prices affect the advantages of simplicity and cost-effectiveness of thermoacoustic generators (Abdoulla et al., 2013). Therefore, with their low transduction efficiencies (around 45%), loudspeakers can replace linear alternators because they are cheaper and commercially available (Yu et al., 2012). From another aspect, thermoacoustic generators also have the ability to utilise the low grade heat source to convert it to electricity. Comparing with a one stage generator, the two-stage configuration is more powerful for lower temperature difference across the regenerator of each stage (Blok, 2010).

The aim of this study was to build upon the developments of the previous project, SCORE, to build and test a simple, cost-effective and environmentally friendly thermoacoustic electricity generator to deliver low-scale electricity (approximately in the range of 15 W) for people in remote and rural areas in developing countries.

To achieve the main target of the study, the project is divided into several subsequent objectives outlined below. It should be noted that while objective “a” is mainly focused on extending a previous project (SCORE) through modelling and validation based on comprehensive experimentation on a new configuration variant, the remaining objectives (“b” to “g”) focus on a new challenge of designing a two-stage generator. However, due to the anticipated complexity of such two-stage system, this overall aim is to involve “simpler” steps as outlined below in individual objectives – the procedure aiming at a subsequent better system integration under objectives “f” and “g”.

- a) To evaluate the performance of a 54-mm resonator diameter looped-tube travelling wave thermoacoustic electricity generator powered by flue gases developed during SCORE project. In particular, this is to consist of an experimental campaign aiming to investigate the influence of selected variables on performance and using the simulation program DeltaEC (Design Environment for Low-amplitude Thermoacoustic Energy Conversion) to develop modelling capabilities. The work would include testing and modelling of a new network (branched loud-speaker connected to the loop as

an alternator) for an existing thermoacoustic core that was previously designed and developed for a different arrangement of a combustion-driven electricity generator by Yu and Jaworski (2012) and which was also used for a combustion-driven thermoacoustic cooler by Saechan et al., (2013). As a target of designing a simple and inexpensive generator, air at atmospheric pressure and a cheap and commercially available loudspeaker were considered as the working gas and alternator, respectively.

- b) Based on the lessons learnt from objective a) above, to design a relatively larger size prototype of a looped-tube travelling wave thermoacoustic engine using a car heater matrix as an ambient heat exchanger and a hot heat exchanger that can be manufactured by simple "black-smith" methods in rural communities. The design is to be based on DeltaEC simulations with the working gas as atmospheric air.
- c) Using DeltaEC simulation results from objective b), to construct and test the designed prototype of the engine. For safety reasons and convenience, the heat power source of the generator is to be an electric air "heat-gun". For simplicity and cost-effectiveness reasons, use PVC piping and fittings to loop the engine.
- d) Based on the results from objective c) above, to simulate a prototype of a larger size, single-stage, looped-tube travelling wave thermoacoustic electricity generator. The design is to be based on DeltaEC simulations with a linear alternator in the form of an ordinary audio loudspeaker.
- e) To construct and test the prototype of a single-stage generator with the linear alternator attached to the loop of the engine. The experimental data obtained for different operating conditions are to be used to validate the DeltaEC model under different working conditions.
- f) Based on lessons from b) through to e), to model a prototype of a two-stage looped-tube travelling wave thermoacoustic electricity generator using two identical stages of the engine. Subsequently, to construct the prototype of the two-stage generator by incorporating an identical stage to that in the single stage loop.

- g) To test the two-stage prototype to find out the effects of different parameters on the performance of the generator and to validate the numerical model using the experimental results.

1.4 Outline of the Thesis

Following this introductory chapter (Chapter 1) the rest of the thesis is structured into the following chapters.

Chapter 2 reviews the background and the fundamentals of thermoacoustic devices including a short history of thermoacoustic technology over the last two centuries. Also, illustrations of the acoustic linear theory and DeltaEC program as a tool to design and simulate the thermoacoustic devices are included. Then, the measurement techniques that were applied to measure acoustic power flow are presented. Moreover, the chapter illustrates the types of the harmful acoustic streaming that exist in thermoacoustic devices. Additionally, an extensive survey of standing wave and travelling wave thermoacoustic engines in terms of simplicity, performance, and efficiency is addressed in this chapter. Furthermore, the chapter also focuses on the relevant literature on travelling wave electricity generators and their improvements in terms of electricity production and conversion efficiency.

Chapter 3 describes the design concepts, DeltaEC model, optimisations and modifications of the 54-mm diameter single-stage travelling-wave electricity generator. This is followed by outlining the subsystems of the two-stage electricity generator and their subsequent integration. The modelling procedure and experimental set up for the 54-mm diameter electricity generator are shown. Firstly, the design, DeltaEC modelling and experimental apparatus of the larger size looped-tube thermoacoustic engine are discussed and presented. Secondly, the simulation and experimental set up of the larger size, single-stage electricity generator is presented. Finally, the modelling and experimental apparatus of the two-stage generator are shown.

Chapter 4 presents the experimental and numerical results for all configurations studied as part of this PhD programme. Comparisons between experimental and numerical results obtained from DeltaEC models are discussed in detail. The effects of different parameters on acoustic power, electricity output and

efficiency generators are investigated. The road map shown in Figure 1.2 indicates the work done in Chapter 3 and Chapter 4.

Chapter 5 presents the concluding remarks of this study and recommendations for future work

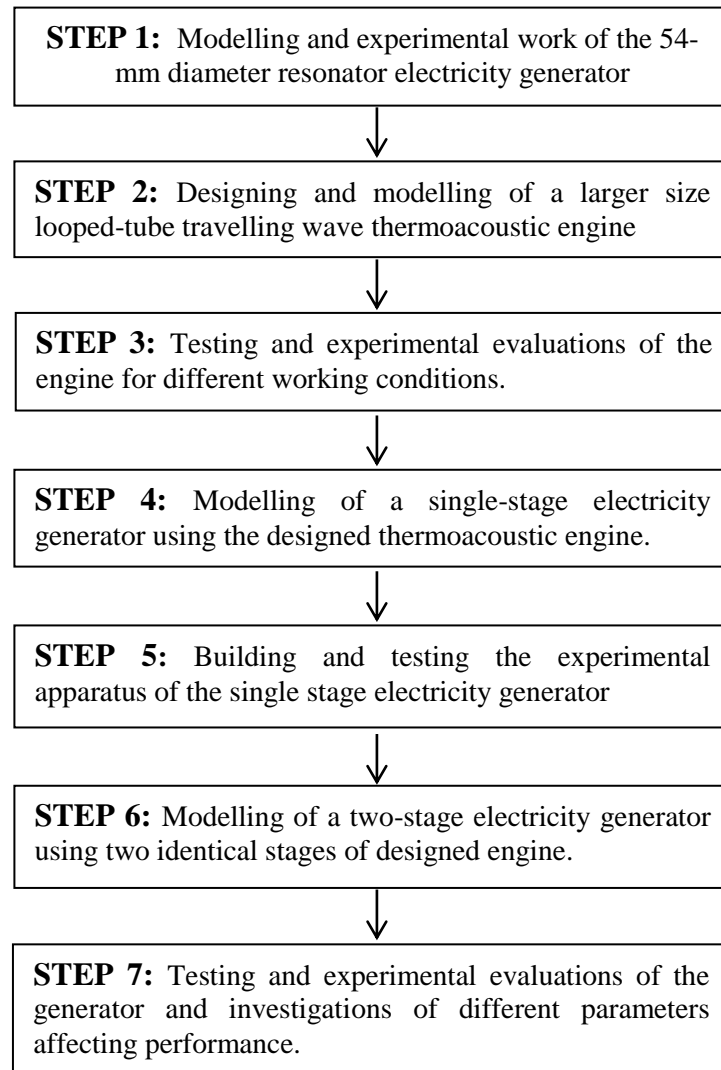


Figure 1. 2 Road map of the research activities of all looped-tube configurations.

CHAPTER 2

LITERATURE REVIEW

Due to the importance of connecting the current study to the field of research, this chapter presents some links to the previous relevant work in thermoacoustics. Firstly, in section 2.1, the historical justifications and explanations of earlier studies on thermoacoustics are briefly reviewed. The key parameters related to the performance of thermoacoustic devices are also shown. Then, the basic concepts of the standing wave and travelling wave engines are described. In section 2.2, the linear thermoacoustic theory is described and represented by the governing equations. Aspects related to modelling thermoacoustic devices using DeltaEC simulation package are also discussed. The measurement techniques of estimating the acoustic power are presented in section 2.3. Brief overview of acoustic-electric power conversion is introduced in section 2.4. In section 2.5, different types of acoustic streaming in the travelling wave engines and their effects are highlighted. The penultimate section 2.6 presents the survey of the developments in thermoacoustic engines, coolers and electricity generators. Finally, an overview and comments on the chapter are given in section 2.7.

2.1 Fundamentals of Thermoacoustics

2.1.1 History of thermoacoustics

Historically, the fundamental concepts of thermoacoustics were established over past two centuries. Early work dates back to 1850 when Sondhauss discovered that the frequency of oscillating media is proportional to the length and volume of the container enclosing the gas medium (Feldman, 1968a). He realized that heating the closed end of a tube opened to the air disturbs the gas inside the tube by producing sound waves in it as seen in Figure 2.1a. A few years later, Rijke carried out further investigations on sound waves in 1859 (Feldman, 1968b). Instead of the horizontal tube used by Sondhauss, Rijke focused on the effects of the natural convection on the acoustic oscillations by heating a wire mesh located in an open-sided vertical tube as seen in Figure 2.1b. In 1894, Rayleigh stated that, “*if heat be*

given to the air at the moment of greatest condensation, or be taken from it at the moment of greatest rarefaction, the vibration is encouraged” (Rayleigh, 1896).

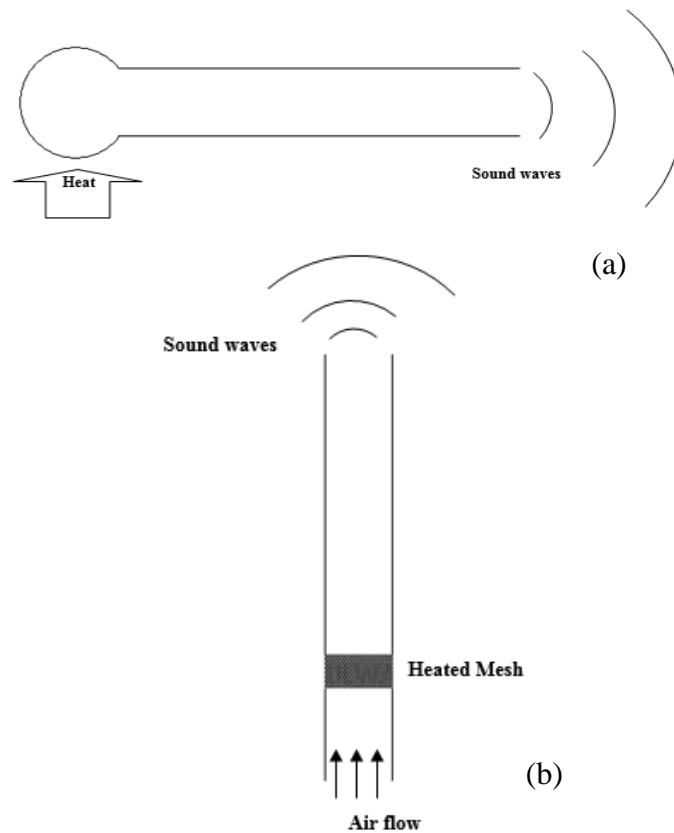


Figure 2. 1 (a) Sondhauss tube, (b) Rijke tube.

Taconis et al. (1949) investigated the Sondhauss vibration using a different technique. Their oscillation was enforced by immersing the open end of a glass tube into cold liquid helium while the closed end of the tube was exposed to room temperature. As a temperature gradient established in the tube, “Taconis oscillations” started to propagate in the tube. More studies on these phenomena were performed later (Yazaki et al., 1979).

The first thermoacoustic refrigerator based on pulse tube cycle was built by Gifford and Longworth (1964). At low frequency oscillation in an open-closed tube, they were able to produce cooling effects at a low temperature of (140 K). In comparison to other thermoacoustic refrigerators, pulse tube coolers are simple to construct and reliable but not effective and cannot manage high cooling loads. Mikulin et al. (1984) were able to improve the performance of these coolers by

adding an orifice to the pulse tube. It was proved that with no cooling load and regenerator this system could provide cooling temperatures down to - 40 °C.

Observations of thermoacoustic oscillations in a tube filled with gas were performed by Merkli and Thomann (1975). First, they calculated the heat transferred within the oscillations. Then they performed a range of experiments to verify the theoretical results and good agreement was obtained. They also reported that the cold side of oscillation occurs at the wave velocity anti-node while the hot side occurs at the velocity node.

Carter et al. (1962) studied the thermoacoustic effects occurring in a stack. Using the principle of the Sondhauss tube, they implemented a “stack” made out of a bundle of glass tubes to study the potential of converting heat power to acoustic power. They utilised different groups of small tubes that had different lengths and diameters in order to find similar connections with the Sonhauss oscillation in terms of frequency. They used different parameters such as resonator length, stack position and length and heat input to investigate the strength of the thermoacoustic effects. They pointed out that the feasibility of obtaining good thermal contact between the gas and the stack is one of the key points in improving the acoustic oscillations. Finally, after several trials they were able to convert 600W of heat into 27W of acoustic power.

A breakthrough in the development of thermoacoustic engines came when Ceperley (1979; 1982) proposed the thermoacoustic Stirling engine. The major contribution of this engine was to use the principle of the 150 year old conventional Stirling engine in developing a reversible cycle of thermoacoustic effects that leads to higher efficiency. Basically, this would replace the inefficient and irreversible cycle of standing wave engines to phasing of (°0) between the oscillating pressure and velocity. Thus, higher heat transfer is obtained between the oscillating gas and the adjacent solids (Ceperley, 1985).

The major breakthrough in thermoacoustics came with Rott’s theoretical investigations. Through a number of papers, Rott (1969; 1973; 1975) added a sound mathematical description of “Taconis oscillations” and significant contributions to the field. To date, his fruitful “thermoacoustic linear theory” has been the solid foundation and reference for many studies in thermoacoustics. The theory enhanced the depth for understanding the links between the acoustic oscillations of working

gas and the temperature gradient in stacks and regenerators in thermoacoustic engines and refrigerators.

Yazaki et al. (1980) confirmed Rott's theory by a set of experimental results when studying "Taconis vibrations". They inspected the generation of oscillations between a closed warm side and an open cold side of a resonator filled with helium. Performance stability and frequency effects of the oscillations were investigated by changing the length of the cold side and the warm side.

Wheatley et al. (1983a; 1983b; 1985) designed and built an experimental rig of a standing wave thermoacoustic cooler to understand the thermoacoustic effects and heat transfer in the thermoacoustic core. The target of a number of experiments was to conduct "thermoacoustic coupling" between the stack and the two heat exchangers. For simplicity, they employed a single stack without surrounding heat exchangers and an arranged group of thermocouples positioned at both sides of the stack. After exciting a standing wave in several positions of the stack in the resonator, thermoacoustic cooling effects were observed within the stack and a temperature difference was established between the two ends of the stack. It was pointed out that the level of the temperature difference which occurred at the two ends reflects the strength of the cooling effects. Besides the experiments, theoretical modelling was developed to calculate the temperature difference and results linked to the thermoacoustic theory of Rott (1969; 1975).

2.1.2 Important parameters

Generally, the working frequency f of sound wave travels in medium with sound speed a can be represented as follows:

$$f = \frac{a}{\lambda} \quad (2.1)$$

where λ is the wavelength. In addition, the speed of sound in an ideal gas is independent of frequency and can be expressed as follows:

$$a = \sqrt{\gamma RT} = \sqrt{\frac{\gamma p_m}{\rho}} \quad (2.2)$$

where γ is ratio of isobaric to isochoric specific heats, \mathfrak{R} is gas constant, T is gas temperature, p_m is mean pressure and ρ is density. From Equation (2.2) it is obvious that the speed of sound is proportional to the mean pressure of the gas.

In thermoacoustics, there are two main key parameters that control the heat transfer and viscous effects between the solid boundaries and the oscillating gas. The first one is called the thermal penetration depth δ_k which is a dimensional parameter in the direction perpendicular to the direction of the oscillation. It is mainly involved in and controls the thermal boundary layer between the oscillating gas parcel and the solid material (Swift, 2002). The thermal penetration depth is expressed as follows:

$$\delta_k = \sqrt{\frac{2k}{\omega \rho_m c_p}} = \sqrt{\frac{2K}{\omega}} \quad (2.3)$$

where k is thermal conductivity, K is diffusivity, ω is angular frequency, ρ_m is gas density and c_p is isobaric specific heat of the working gas.

Similarly, the second important parameter is the viscous penetration depth (in direction perpendicular to the gas motion). It represents the layer of the viscous effects that are responsible for acoustic power losses. Correspondingly, the viscous penetration depth can be written as follows:

$$\delta_v = \sqrt{\frac{2\mu}{\omega \rho_m}} = \sqrt{\frac{2\nu}{\omega}} \quad (2.4)$$

here μ is dynamic viscosity and ν is kinematic viscosity.

Generally, these characteristic depths reflect how strong the heat and viscosity diffuse latterly into the gas in an oscillation time interval ($T = 1/f$). Therefore, high thermal penetration depths and low viscous penetration depths are favourable (Wheatley et al., 1985).

It is also preferred to increase the mean pressure in the cavity to the level that is affordable by the construction due to the power density of the acoustic oscillation being proportional to p_m of the working gas (Tijani et al., 2002a). Furthermore, it is also desirable to increase the resonance working frequency of the thermoacoustic device due to the linear relationship with the power density in the device (Swift, 1988). However from Equations (2.3) and (2.4), mean pressure p_m and working frequency ω are inversely proportional to the square root of the thermal and viscous penetration depths. This indicates that it is difficult and costly to make a stack of very small spacing size at high frequency or mean pressure.

Another significant parameter in the direction of oscillating motion is the gas peak-to-peak displacement amplitude, $2|\xi_1|$, that denotes the maximum distance

covered by the gas parcel within one acoustic cycle. Figure 2.2 shows the gas parcel displacement between a heat exchanger and a stack. The gas displacement, $|\xi_1|$, is half of the complete displacement and much shorter than wavelength and can be defined as:

$$|\xi_1| = \frac{|u_1|}{\omega} \quad (2.5)$$

here ω is the angular frequency of the oscillation and,

$$\omega = 2\pi f \quad (2.6)$$

As the gas parcel oscillates back and forth by $|2\xi_1|$, it is preferred to limit a heat exchanger by the same length in order to achieve effective heat transfer (Backhaus and Swift, 2000).

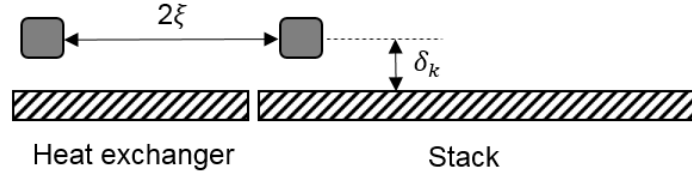


Figure 2. 2 Back and forth optimum displacement of a gas parcel between a stack and its adjacent heat exchanger

The performance of a thermoacoustic device is also determined by the size and dimension of the stack or regenerator of the device. These parameters are recognised as the volumetric porosity ϕ and the hydraulic radius r_h . The cross-sectional porosity of a regular configuration porous medium (stack or regenerator) can be defined as the cross sectional area filled with gas to the total cross sectional area of the medium, while for the irregular geometries of stacks and regenerators (e.g. compacted wire mesh screens) the porosity needs to be defined as the ratio of the volume of gas in the regenerator to the total volume of the regenerator. Equation (2.7) represents the cross sectional porosity, while equation (2.8) gives the formula for the volumetric porosity with a particular approximation valid for wire mesh screen stacks/regenerators.

$$\phi = \frac{A_{gas}}{A} \quad (2.7)$$

$$\phi = \frac{V_{gas}}{V} \approx 1 - \frac{\pi n d_{wire}}{4} \quad (2.8)$$

here A_{gas} is the cross section of the gas and A is the total cross section of the whole stack or regenerator including the solid and the gas.

In Equation (2.8), V_{gas} , is the volume of the gas within the porous material, V is the total volume of the material including the gas and the solid, n is the number of wires per unit length and d_{wire} is the wire diameter of the material.

The hydraulic radius of the mesh screen can be defined as the ratio of the gas volume to the gas-solid contact area.

$$r_h = \frac{V_{gas}}{A_{wetted}} \approx d_{wire} \frac{\phi}{4(1-\phi)} \quad (2.9)$$

where A_{wetted} represents the contact area between the solid and the gas.

For a regular stack or regenerator it is the ratio of the cross sectional area of the gas to the perimeter Π of the same area.

$$r_h = \frac{A_{gas}}{\Pi} \quad (2.10)$$

Eliminating the viscous effects of low viscosity gases, generally in thermoacoustics, the level of the thermal interaction between the gas parcel and the solid is measured by the ratio of the thermal penetration depth to the hydraulic radius (δ_k/r_h).

If the thermal penetration depth is much smaller than the hydraulic radius $\delta_k/r_h \ll 1$, then there is no, or very poor, thermal contact between the gas and the solid and no heat transfer is enforced.

If the thermal penetration depth is about the hydraulic radius $\delta_k/r_h \approx 1$, then there is an imperfect thermal contact between the gas and the solid such as standing wave devices (explained in section 2.1.3).

If the thermal penetration depth is much greater than the hydraulic radius $\delta_k/r_h \gg 1$, then there is a perfect thermal contact between the gas and the solid such as travelling wave devices (explained in section 2.1.4).

For better performance and efficiency of thermoacoustic devices, characteristics of working gases that provide high heat transfer and low viscous losses between gases and solids are preferred. Features of this type of working gas are restrained by how great the thermal penetration depth δ_k is and how small the viscous penetration depth δ_v is that can be obtained inside porous media. The square ratio of the viscous penetration depth to the thermal penetration depth is defined as ‘‘Prandtl number’’ (Swift, 2001).

$$\sigma = \left(\frac{\delta_v}{\delta_k}\right)^2 = \frac{\mu c_p}{k} \leq 1 \quad (2.11)$$

Gases with low Prandtl number are preferred due to their large thermal penetration depth or small viscous penetration depth (Tijani et al., 2002b). Noble gases, such as helium, are desirable as working media in thermoacoustic devices due to the following:

- Environmental friendliness,
- High thermal conductivity,
- High speed of sound,
- Low Prandtl number.

2.1.3 Standing wave devices

The two main types of standing wave devices are defined on the basis of whether the acoustic power is produced (engine/prime mover) or consumed (refrigerator/cooler) by the device. Although standing wave devices can be utilised in a quarter wave length and half wave length, quarter wave length devices are cheaper in terms of material cost and more efficient in terms of the amount of acoustic power dissipated within the resonator. For example, a quarter wave length standing wave engine is an ideal demonstrator to represents the thermoacoustic effects in these devices. Figure 2.3 shows a schematic of thermoacoustic effects in a standing wave engine.

The standing wave engine can be represented by a pipe (resonator) that has a length of $(\lambda/4)$ with one flexible end and one closed end as seen in Figure 2.3a. The resonator contains a stack sandwiched between a hot heat exchanger (HHX) and an ambient heat exchanger (AHX). The thermoacoustic core (the pair of heat exchangers and the stack) is located at the closed end of the pipe while the open end is used to locate a linear alternator (in the case of electricity generator). When (HHX) is heated up by applying heat to it to raise its temperature and when (AHX) is cooled down to keep the ambient temperature low, a temperature gradient is established along the stack. When the temperature gradient is very steep and reaches its critical value, the acoustic wave is propagated and heat power is taken through the stack from (HHX) to (AHX) (Swift, 1988). As a result, the excitation of the standing wave will occur between both ends of the pipe causing pressure anti-node

(high pressure amplitude) and velocity node (zero velocity) at the closed end while velocity anti-node (high velocity amplitude) and pressure node (very low acoustic pressure) are formed at the open end as shown in Figure 2.3c

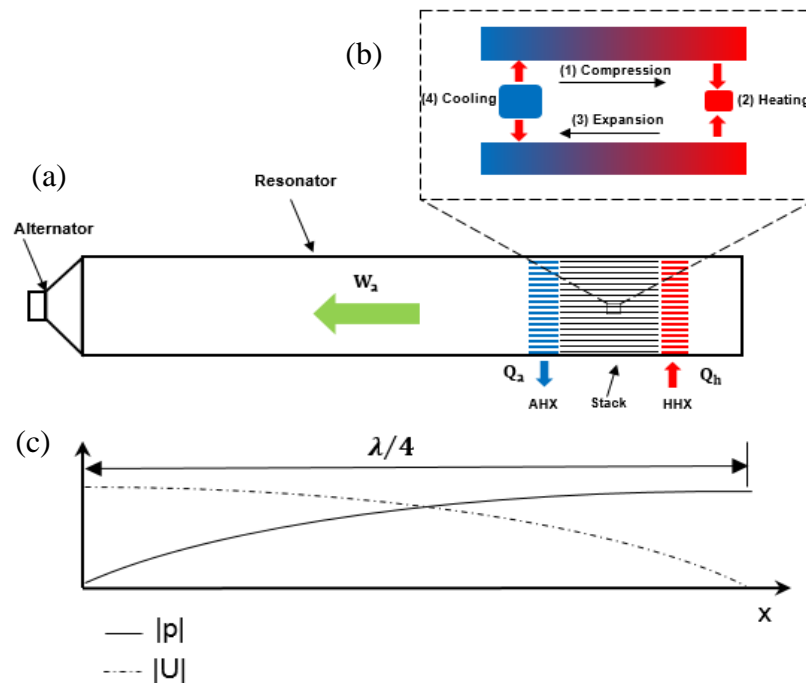


Figure 2. 3 Schematics of thermoacoustic effects in a standing wave engine. (a) Standing wave thermoacoustic engine, (b) The enlarged view of the thermoacoustic oscillation in the stack and (c) pressure and volumetric velocity in the resonator

A deeper insight into the thermoacoustic effects in a single pore of the stack is shown in Figure 2.3b. Firstly, the gas parcel in the pore experiences adiabatic compression and moves to the hot side. At the hot side, the gas parcel is colder than the adjacent solid boundaries. Thus, heat is transferred from the solid to the gas parcel and experiences thermal expansion. Thereafter, the parcel is adiabatically expanded while it is moved to the cold side of the stack. At this position, the temperature of the gas parcel is much hotter than the adjacent solid. Therefore, the absorbed heat is rejected to the solid boundaries decreasing the parcel temperature and causing thermal contraction to the parcel. This mechanism is utilised to convert

part of the transferred heat power (from HHX to AHX) into acoustic power that is converted into electricity in a generator or into cooling effects in a refrigerator.

The thermoacoustic effects in the standing wave refrigerator follow a similar principle with differences in heat transfer direction, acoustic power direction and steepness of the temperature gradient. These principles can be understood from the schematic drawings of a standing wave refrigerator shown in Figure 2.4. The acoustic driver located at the left side of the resonator provides acoustic power in the working gas as displayed in Figure 2.4a. When the standing wave is excited by the driver, quarter wave length conditions are established, presenting pressure anti-node and velocity node at the closed end and pressure node and velocity anti-node at the driver location.

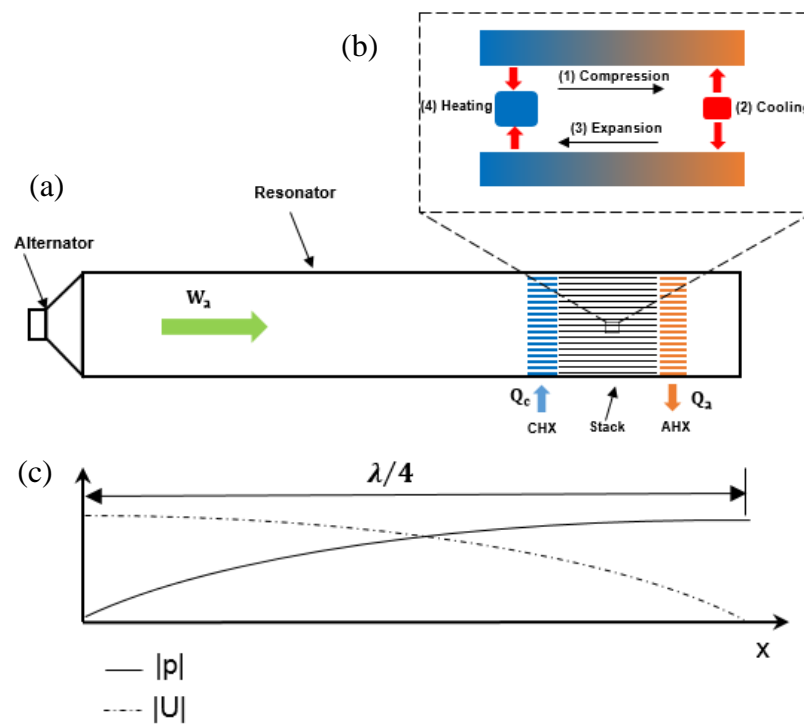


Figure 2. 4 Schematics of thermoacoustic effects in standing wave refrigerator. (a) Standing wave thermoacoustic refrigerator, (b) The enlarged view of the thermoacoustic oscillation in the stack and (c) pressure and volumetric velocity in the resonator.

Taking a closer look at the stack pore as seen in Figure 2.4b, at the beginning, the gas parcel is compressed and moved to the ambient side. The gas parcel at the ambient side is warmer than the adjacent solid because of the increase in temperature during the compression. Thus thermal contraction occurs due to heat

transfer from the gas parcel to the solid. Thereafter, the parcel moves to the cold side of the stack and is expanded during the movement. At the cold side, the gas parcel is colder than the adjacent solid and gas experiences thermal expansion due to transferring heat from the solid to the gas. This heat pumping from the cold side to the ambient side results in cooling effects and a temperature gradient much lower in steepness than the temperature gradient of the engine. The acoustic oscillations in standing wave devices need to have a time delay of $(\pi/2)$ between the acoustic pressure and velocity (Wheatley et al., 1985). This time delay is achieved by designing stack pores spaced in the order of thermal penetration depth (δ_k) in order to obtain imperfect heat contact between the gas parcels and the solid boundaries (Tijani et al., 2002).

2.1.4 Travelling wave devices

In the travelling wave devices the favourable phase difference between the acoustic pressure and velocity is close to zero (Ceperley, 1979). This condition should be achieved by enforcing perfect thermal contact between the pressure and velocity in the core of a travelling wave device. Instead of the largely spaced layers of a stack, a regenerative porous medium (“regenerator”) is capable of providing very low phase difference between the oscillating pressure and velocity by obtaining an ideal thermal contact between the solid material and the gas parcels. The perfect heat exchange is performed by implementing much smaller hydraulic radius of the regenerator compared to the thermal penetration depth within the regenerator $\delta_k/r_h \gg 1$ (Swift, 2002).

As with standing wave devices, travelling wave devices are also divided into travelling wave engines and refrigerators. The thermoacoustic mechanism and effects in travelling wave engines are briefly described in Figure 2.5. It can be seen from Figure 2.5a that the travelling wave engine contains the thermoacoustic core in a looped tube. The core consists of a porous medium (the regenerator) that is located and sandwiched between the ambient heat exchanger (AHX) and the hot heat exchanger (HHX). The hot heat exchanger provides heat to the system while the ambient heat exchanger rejects the heat from the system. By this process, a temperature gradient occurs along the regenerator and the thermoacoustic core works as an amplifier of the acoustic power (mechanical work). This is clearly

realised when the acoustic power flowing from the feedback pipe through the ambient heat exchanger is amplified in the regenerator by the conversion of heat to acoustic power that leaves the hot heat exchanger to the feedback pipe again. This useful acoustic power can be extracted and converted into electricity by connecting (in series or branched) an acoustic/electrical transducer (an alternator) to the loop.

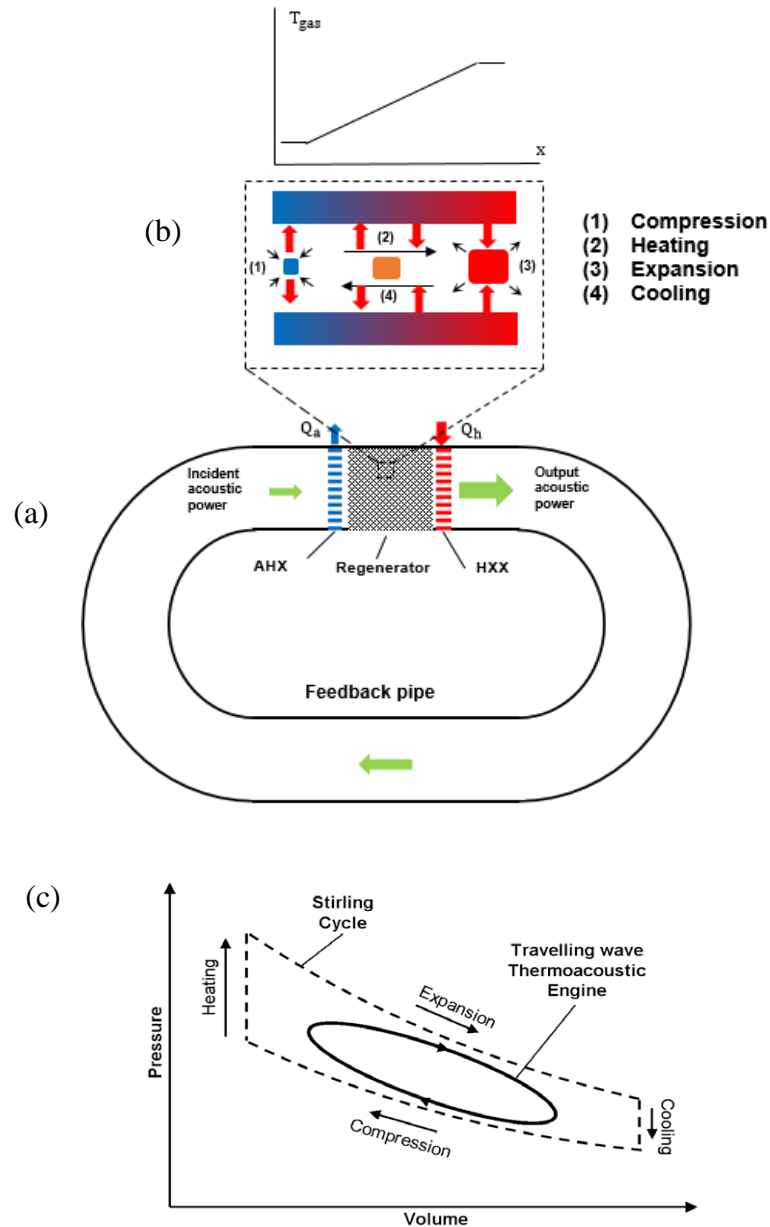


Figure 2. 5 Schematics of thermoacoustic effects in travelling wave engine. (a) Travelling wave engine, (b) The enlarged view of gas-solid interaction during the oscillation in the regenerator, (c) The thermodynamic cycle in the regenerator (Yu and Jaworski, 2010a)

Figure 2.5b shows a clearer picture of the interactions between the regenerator and the gas parcels. As the sound wave starts to propagate in the regenerator, the

heat transfer interactions start between the solid boundaries of the regenerator and the working fluid parcels. With the correct phasing between the parcel displacement and acoustic pressure, the parcel begins to compress adjacent to the cold side of the regenerator. When the gas parcel moves towards the hot side of the regenerator, the parcel temperature is lower than the adjacent solid temperature and heat transfers from the solid to the gas parcel to increase its temperature and pressure and experiences thermal expansion, while heat transfer from the gas to the solid occurs and the gas parcels experience thermal contraction if the parcel is moving back to the cold side of the regenerator (Ceperley, 1979; Ceperley, 1985). As seen in Figure 2.5c, during this oscillating process, the gas parcel undergoes a thermodynamic cycle that is very similar to the conventional Stirling cycle of Stirling engines (Ceperley, 1985).

When the temperature gradient in the regenerator is enough to overcome the viscous losses in the loop, acoustic power is amplified proportionally to the amplification ratio of (T_h/T_c) from the cold side to the hot side of the regenerator (Swift, 2007). Although the hydraulic radius of the regenerator should be small to ensure being able to obtain a very small temperature difference between the gas parcels and the regenerator solid material. However, a very small hydraulic radius considerably affects the oscillatory flow in the regenerator by increasing viscous effects (Swift, 2001).

Likewise, the principle of travelling wave refrigerators can be briefly discussed with minor differences from engines as seen in Figure 2.6. Figure 2.6a shows the schematic drawing of a core of a travelling wave thermoacoustic refrigerator. It is seen that as the acoustic power (produced by an acoustic driver or an engine) flows through the regenerator, it is consumed and converted into cooling power. The cooling effects can be displayed in the enlarged pore of the regenerator in Figure 2.6b. After the gas parcel is compressed at the ambient side of the regenerator, the parcel temperature is higher than the adjacent solid and heat transfer occurs from the gas to the solid material. Then, the gas parcel is pushed to the cold side of the regenerator undergoing thermal contraction as it rejects heat to the closed solid. At the cold side, the gas temperature is lower than the solid temperature because of the expansion and heat transfer occurs from the solid to the gas. Finally,

the gas parcel is returned back to the warmer side taking heat from the solid while it experiences thermal expansion.

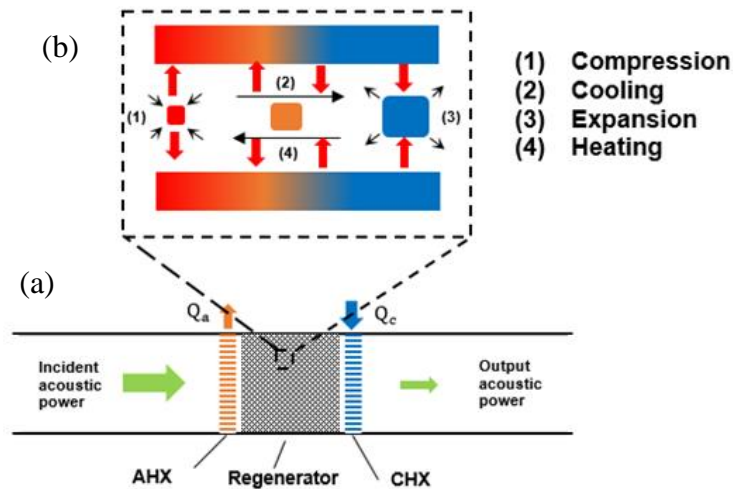


Figure 2. 6 Schematics of thermoacoustic effects in travelling wave refrigerator. (a) The core of the refrigerator, (b) the enlarging view of the oscillation in the stack.

2.2 The Linear Theory and Modelling

Thermoacoustics as a science has been studied for about two centuries. These studies included observations and experimental investigations. However, the theoretical side of predicting the thermoacoustic oscillations has only been revealed during the last century. The first formal theoretical work to predict and model the thermoacoustic vibrations in a tube was done by Kramers (1949). He realised “Taconis oscillations” at high amplitudes were due to the temperature gradient within the tube. By limiting the oscillations to small amplitudes, he tried to simplify the linearity of the calculations. Due to mismatching between his results and previous experimental results, the first successful calculation of the linear thermoacoustic theory was developed by Rott (1969). The continuity, momentum and energy equations that govern the heat and fluid flow were linearized within the low amplitude acoustic oscillations. The linear thermoacoustic theory was established on the following assumptions:

- The acoustic wave gradient in the radial direction is neglected,
- The axial heat conducted within the oscillation is ignored,
- The radial gradient of the average temperature and viscosity are neglected.

Further simplifications of the linear thermoacoustic theory equations were added to the literature (Wheatley et al., 1983a; 1983b and 1985). In addition, the calculation of the behaviour of low amplitude acoustic pressure thermoacoustic devices can be achieved by applying the following assumptions (Swift, 2002):

- The solid boundaries of the stack or regenerator are fixed and stationary,
- The length of the stack or regenerator is short,
- The oscillation is in its steady state,
- Turbulence and acoustic steaming are neglected,
- The temperature changes over the stack are smaller than the absolute temperatures,
- The viscosity is completely independent of the temperature.

The steady state sinusoidal acoustic wave propagates in the x direction. The subscript “ m ” represents the mean values of the variables while “1” represents the first order part of the variable.

$$\rho = \rho_m(x) + \text{Re} [\rho_1(x, y, z)e^{i\omega t}] \quad (2.12)$$

$$T = T_m(x) + \text{Re} [T_1(x, y, z)e^{i\omega t}] \quad (2.13)$$

$$p = p_m(x) + \text{Re} [p_1(x)e^{i\omega t}] \quad (2.14)$$

$$v = \text{Re} [v_1(x, y, z)e^{i\omega t}] \quad (2.15)$$

$$s = s_m(x) + \text{Re} [s_1(x, y, z)e^{i\omega t}] \quad (2.16)$$

$$\mu = \mu(x) \quad (2.17)$$

$$a = a(x) \quad (2.18)$$

$$k = k(x) \quad (2.19)$$

here ρ, T, p, v, s, μ, a and k are the gas density, temperature, pressure, velocity, entropy, dynamic viscosity, speed of sound, and thermal conductivity respectively.

Also, the complex notation is $i = \sqrt{-1}$, and $e^{i\omega t} = \cos(\omega t) + i\sin(\omega t)$.

2.2.1 The governing equations of stacks and regenerators.

Generally the governing equations of fluid motion are defined by the continuity, momentum and energy equations. Similarly, in thermoacoustics the same equations control and describe the behaviour of the oscillating motion of the working gas. However, the time dependent variables in these equations are replaced by the sinusoidal form that is represented in the complex quantity (Swift, 2002). The well-known continuity equation that designates the conservation of fluid flow through a controlled volume is shown as follows:

$$\frac{\partial \rho}{\partial t} + \nabla \cdot (\rho v) = 0 \quad (2.20)$$

The steady flow continuity of Equation (2.20) can be converted into an oscillating flow continuity equation by applying Equations (2.15) and (2.19) in Equation (2.20), and ignoring any second order products. The result of that is:

$$\frac{\partial}{\partial t} \text{Re}[\rho_m(x, y, z)e^{i\omega t}] + \nabla \cdot \{\rho_m(x) \text{Re}[v_1(x, y, z)e^{i\omega t}]\} = 0 \quad (2.21)$$

The sinusoidal steady state oscillation change $\frac{\partial}{\partial t}$ to $i\omega$. This results in the first order continuity equation of oscillating flow as follows:

$$i\omega \rho_1 + \nabla \cdot (\rho_m v_1) = 0 \quad (2.22)$$

The momentum equation of the oscillatory flow in the x direction is defined as:

$$dp_1 = -\frac{i\omega \rho_m dx/A}{1-f_v} U_1 \quad (2.23)$$

where A is the cross sectional area of the channel, U_1 is the volumetric velocity flow in the channel. The approximation of Equation (2.23) can measure the effects of the volumetric velocity flow U_1 and the dimensions of the channel on the pressure gradient.

The oscillating temperature equations for arbitrary channel geometry are based on the thermoviscous function h and the spatial averaged thermoviscous function f as shown in Equation (2.24) and Equation (2.25):

$$T_1 = \frac{1}{\rho_m c_p} (1 - h_k) p_1 - \frac{1}{i\omega A} \frac{dT_m}{dx} \frac{(1-h_k) - \sigma(1-h_v)}{(1-f_v)(1-\sigma)} U_1 \quad (2.24)$$

$$\langle T_1 \rangle = \frac{1}{\rho_m c_p} (1 - f_k) p_1 - \frac{1}{i\omega A} \frac{dT_m}{dx} \frac{(1-f_k) - \sigma(1-f_v)}{(1-f_v)(1-\sigma)} U_1 \quad (2.25)$$

where the brackets $\langle \ \rangle$ imply the spatial average or the cross sectional average , σ , is Prandtl number.

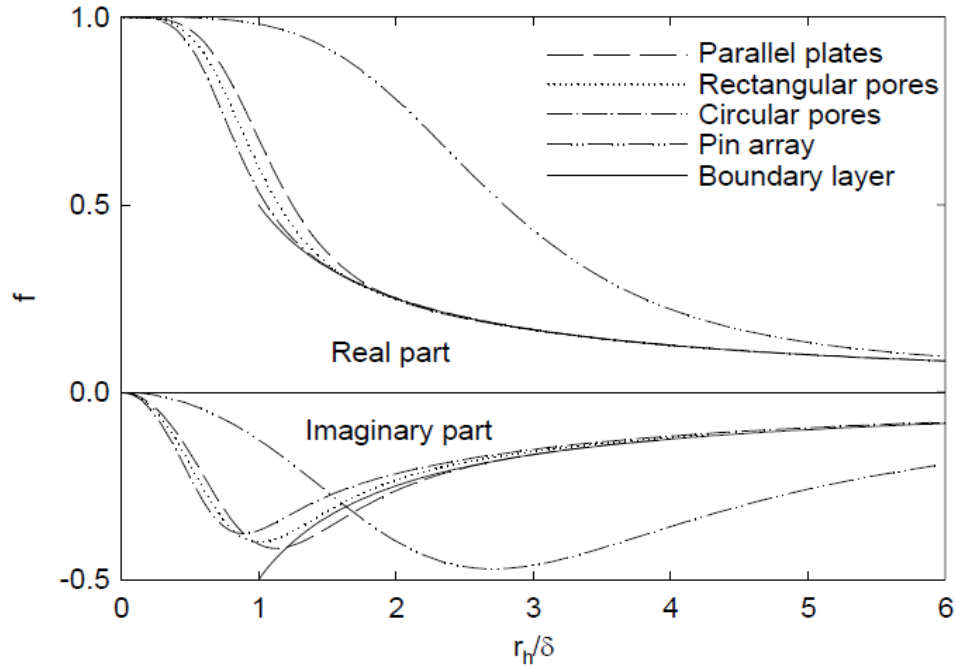


Figure 2. 7 The spatial average function f for different geometries (Swift, 2002).

The functions f_k and f_v are the spatial average thermoviscous functions. The function f_k is proportional to the ratio of the hydraulic radius to the thermal penetration depth r_h/δ_k . Basically, f_k is the bridge between the adiabatic state of the oscillation when there is no gas-solid thermal contact with $f_k = 0$ and between the isothermal state when there is a perfect thermal contact with $f_k = 1$. The function f_v is proportional to the ratio of the hydraulic radius to the thermal penetration depth r_h/δ_v . It measures the level of viscosity of the flow from inviscid flow with $f_v = 0$ to viscous flow with $f_v = 1$. Essentially, when the size of the channel is relatively large, the spatial average functions f_v and f_k are small and sometimes close to zero, while if $f_v = 1$ and $f_k = 1$ the channel size is small. The relationship between the thermoviscous functions and the ratio r_h/δ for some stack geometries are shown in Figure 2.7 where r_h/δ_k was used to obtain f_k and r_h/δ_v was used to

find f_v from the graph. Additionally, h_v and h_k functions and their spatial averages f_v and f_k are presented for some channel geometries in Table 2.1.

Taking the ideal gas equation of state and substituting Equations (2.12), (2.13), and (2.14) into it yields:

$$p_m(x) + \text{Re} [p_1(x)e^{i\omega t}] = \{\rho_m(x) + \text{Re} [\rho_1(x, y, z)e^{i\omega t}]\} \Re \{T_m(x) + \text{Re} [T_1(x, y, z)e^{i\omega t}]\} \quad (2.26)$$

where \Re is the ideal gas constant. Keeping first order terms in the resulting equation and dividing it by the simple zero-order equation of state, $p_m = \rho_m \Re T_m$ yields:

$$\frac{p_1}{p_m} = \frac{T_1}{T_m} + \frac{\rho_1}{\rho_m} \quad (2.27)$$

Taking the spatial average of density yields:

$$\langle \rho_1 \rangle = \frac{\rho_m}{T_m} \langle T_1 \rangle + \frac{\rho_m}{p_m} p_1 \quad (2.28)$$

Adding the x dependence of ρ_m to the continuity equation yields:

$$i\omega \langle \rho_1 \rangle + \frac{d}{dx} (\rho_m \langle u_1 \rangle) = 0 \quad (2.29)$$

Substituting Equations (2.25) and (2.28) in (2.29) gives:

$$dU_1 = -\frac{i\omega A dx}{\gamma p_m} [1 + (\gamma - 1)f_k] p_1 + \frac{(f_k - f_v)}{(1 - f_v)(1 - \sigma)} \frac{dT_m}{T_m} U_1 \quad (2.30)$$

Equations (2.28) and (2.37) can be combined together to produce Rott's wave equation:

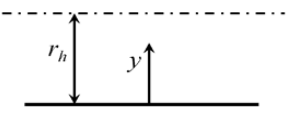
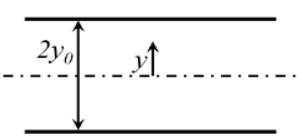
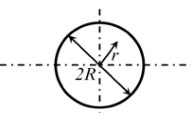
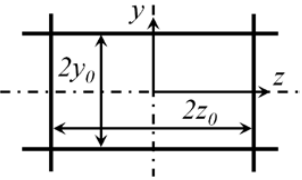
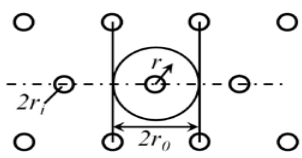
$$[1 + (\gamma - 1)f_k] p_1 + \frac{\gamma p_m}{\omega^2} \frac{d}{dx} \left(\frac{1 - f_v}{\rho_m} \frac{dp_1}{dx} \right) - \frac{\alpha^2}{\omega^2} \frac{f_k - f_v}{1 - \sigma} \frac{1}{T_m} \frac{dT_m}{dx} \frac{dp_1}{dx} = 0 \quad (2.31)$$

Within the momentum and continuity equations, the thermoviscous function f describes the effects of inertance and compliance, viscous and thermal-relaxation resistance and volumetric flow prompted by temperature gradient.

From the momentum Equation (2.23), it can be rewritten in the form:

$$dp_1 = -(i\omega l dx + r_v dx)U_1 \quad (2.32)$$

Table 2. 1 The thermoviscous function h and its spatial average f of some stack geometries.

Geometry	Functions (h and f)
Wide-open channels (Swift, 2002) 	$h = e^{-(1+i)y/\delta}$ $f = \frac{(1-i)\delta}{2r_h}$
Parallel plates (Swift, 2002) 	$h = \frac{\cosh[(1+i)y/\delta]}{\cosh[(1+i)y_0/\delta]}$ $f = \frac{\tanh[(1+i)y_0/\delta]}{(1+i)y_0/\delta}$
Circular pores (Swift, 2002) 	$h = \frac{J_0[(i-1)r/\delta]}{J_0[(i-1)R/\delta]}$ $f = \frac{2J_1[(i-1)R/\delta]}{J_0[(i-1)R/\delta](i-1)R/\delta}$
Rectangular channels (Arnott et al., 1991) 	$h = 1 - \frac{16}{\pi^2} \sum_{m,n \text{ odd}} \frac{\sin(m\pi y/2y_0)\sin(m\pi z/2z_0)}{mnC_{mn}}$ where $C_{mn} = 1 - i \frac{\pi^2 \delta^2}{8y_0^2 z_0^2} (m^2 z_0^2 + n^2 y_0^2)$ $f = 1 - \frac{64}{\pi^4} \sum_{m,n \text{ odd}} \frac{1}{m^2 n^2 C_{mn}}$
Pin array (Swift and Keolian, 1993) 	$h \cong \frac{Y_1(\alpha_0)J_0(\alpha) - J_1(\alpha_0)Y_0(\alpha)}{Y_1(\alpha_0)J_0(\alpha_i) - J_1(\alpha_0)Y_0(\alpha_i)}$ where $\alpha = (i-1)r/\delta$ $f \cong \frac{2\alpha_i}{\alpha_0^2 - \alpha_i^2} \frac{Y_1(\alpha_0)J_1(\alpha_i) - J_1(\alpha_0)Y_1(\alpha_i)}{Y_1(\alpha_0)J_0(\alpha_i) - J_1(\alpha_0)Y_0(\alpha_i)}$

where:

$$l = \frac{\rho_m}{A} \frac{1 - \text{Re}[f_v]}{|1 - f_v|} \quad (2.33)$$

and

$$r_v = \frac{\omega \rho_m \text{Im}[-f_v]}{A |1-f_v|^2} \quad (2.34)$$

where l is the channel inertance and r_v is the viscous resistance in the channel. For large channel sizes, it is obvious that $l \rightarrow \rho_m/A$ and $r_v \rightarrow 0$. However, when the channel hydraulic radius is small, $l \rightarrow 0$ and $r_v \rightarrow \infty$. Equation (2.30) can be rewritten in the form:

$$dU_1 = - \left(i\omega c dx + \frac{1}{r_k} dx \right) p_1 + g dx U_1 \quad (2.35)$$

where:

$$c = \frac{A}{\gamma p_m} (1 + [\gamma - 1] \text{Re}[f_k]) \quad (2.36)$$

and

$$\frac{1}{r_k} = \frac{\gamma - 1}{\gamma} \frac{\omega A \text{Im}[-f_k]}{p_m} \quad (2.37)$$

The symbol c indicates the compliance of the channel and r_k is the thermal-relaxation resistance. The volume flow rate induced source shows the gain factor increases within the temperature gradient as:

$$g = \frac{(f_k - f_v)}{(1 - f_v)(1 - \sigma)} \frac{1}{T_m} \frac{dT_m}{dx} \quad (2.38)$$

The second order time average acoustic power intensity flowing in the x direction is:

$$\dot{E}_2(x) = \frac{1}{2} \text{Re}[p_1 \tilde{U}_1] = \frac{1}{2} \text{Re}[\tilde{p}_1 U_1] \quad (2.39)$$

$$\dot{E}_2(x) = \frac{1}{2} |p_1| |U_1| \cos \phi_{pU} \quad (2.40)$$

where ϕ_{pU} is the phase angle between p_1 and U_1 and the subscript “2” represents the second order. Applying the derivative of Equation (2.39) within length of Δx yields:

$$\frac{d\dot{E}_2}{dx} = \frac{1}{2} \text{Re} \left[\tilde{U}_1 \frac{dp_1}{dx} + \tilde{p}_1 \frac{dU_1}{dx} \right] \quad (2.41)$$

Substituting the gradients $\frac{dp_1}{dx}$ and $\frac{dU_1}{dx}$ from the momentum equations of (2.23) and continuity equation of (2.30) into (2.41) yields:

$$\frac{d\dot{E}_2}{dx} = -\frac{r_v}{2} |U_1|^2 - \frac{1}{2r_k} |p_1|^2 + \frac{1}{2} \text{Re}[g \tilde{p}_1 U_1] \quad (2.42)$$

The negative sign in the first and second terms on the RHS show that the viscous and thermal-relaxation resistances always dissipate acoustic power while in the third term the production or consumption of the acoustic power depends on the complex gain or loss factor “ g ” that includes the temperature gradient dT_m/dx as seen in Equation (2.38). The third term in the case of engines characterises the acoustic power production when T_m rises in the progressive direction of the acoustic power

flow, whereas in the situation of refrigerators it represents the acoustic power consumption when T_m falls in the positive direction of the acoustic power (Yu and Jaworski, 2010).

In the thermoacoustic oscillations, the total power is a second order in the oscillating variables and it is generally presented as:

$$\dot{H}_2 = \frac{1}{2} \text{Re} \left[p_1 \tilde{U}_1 \left(1 - \frac{f_k - \tilde{f}_v}{(1+\sigma)(1-\tilde{f}_v)} \right) \right] + \frac{\rho_m c_p |U_1|^2}{2A\omega(1-\sigma)|1-\tilde{f}_v|^2} \text{Im}(f_k + \sigma \tilde{f}_v) \frac{dT_m}{dx} - (Ak + A_{soild}k_{solid}) \frac{dT_m}{dx} \quad (2.43)$$

The first term on the RHS of Equation (2.43) is the acoustic power and the second term is the kinetic energy affected by the change of T_m and the third term is the heat conduction.

Equation (2.43) can be simplified using an approximation method. Besides the assumption that the stack or the regenerator are short, and the change of temperature is eliminated that all T_m dependents are considered constants. In this context, from Equation (2.23) the change in pressure within the short length Δx of the stack or regenerator is approximated as:

$$\Delta p_1 \simeq - \frac{i\omega\rho_m\Delta x U_1}{A(1-f_v)} \quad (2.44)$$

Furthermore, from Figure 2.6, and for a parallel plate regenerator having a small hydraulic radius r_h , the real part of the spatially averaged thermoviscous function is $\text{Re}[f] \simeq 1$ whereas $\text{Im}[f]$ is close to zero. This simplifies Equation (2.43) to the approximate expression of:

$$\dot{H}_2 \simeq - \frac{17}{35} \frac{\rho_m c_p}{A\omega} \frac{r_h^2}{\delta_k^2} |U_1|^2 \frac{dT_m}{dx} - (Ak + A_{soild}k_{solid}) \frac{dT_m}{dx} \quad (2.45)$$

The acoustic power flow in a regenerator presented in Equation (2.42) can also be simplified in the same way as:

$$\Delta \dot{E}_2 \simeq \dot{E}_{2,0} \left(\frac{T_{(h \text{ or } c)}}{T_0} - 1 \right) - \frac{3\mu \Delta x}{2Ar_h^2} |U_1|^2 - \frac{\omega^2 Ar_h^2 \Delta x}{6kT_m} |p_1|^2 \quad (2.46)$$

where $\Delta \dot{E}_2$ is the produced or consumed acoustic power, $\dot{E}_{2,0}$ is the acoustic power at the ambient side of the regenerator with an ambient temperature T_a , and $T_{(h \text{ or } c)}$ represents the temperature at the hot side of the regenerator in the case of the engine as T_h or it denotes the temperature of the cold side of the regenerator in the case of the refrigerator as T_c .

2.2.2 DeltaEC program

DeltaEC (Design Environment for Low-Amplitude Thermoacoustic Energy Conversion) is a widely accepted computer tool that is capable of simulating and designing a range of different acoustic and thermoacoustic applications from simple resonators to complicated thermoacoustic engines and refrigerators. It is a powerful computational tool to predict thermoacoustic devices experimental performance with errors less than 10% (Ward et al., 2008). The program utilises the linear theory to integrate the one dimensional wave equation over a geometrical segment or a number of segments that are included in one thermoacoustic device such as ducts, cones, heat exchangers thermal buffer tubes, stacks and regenerators. In DeltaEC programming the general parameters such as frequency, mean pressure and local geometric parameters such as length and diameter of ducts are taking place during the solving process of the governing equations along the device (Ward et al., 1994). This integration solves the coupling equations of the acoustic pressure, volumetric velocity, acoustic energy and the oscillatory temperature over the connected segments. The governing equations of each segment depend upon whether the change of mean temperature along working axis $dT_m/dx = 0$ as in isothermal segments such as ducts and cones or $dT_m/dx \neq 0$ as in stacks and regenerators. For instance, the governing equations of a stack in a standing wave device can be displayed.

The general wave equation or Rott's equation as:

$$\left(1 + \frac{(\gamma-1)f_k}{1+\varepsilon_s}\right) p_1 + \frac{\rho_m a^2}{\omega^2} \frac{d}{dx} \left(\frac{(1-f_v)}{\rho_m} \frac{dp_1}{dx} \right) - \beta \frac{a^2}{\omega^2} \frac{(f_k-f_v)}{(1-\sigma)(1+\varepsilon_s)} \frac{1}{T_m} \frac{dT_m}{dx} \frac{dp_1}{dx} = 0 \quad (2.47)$$

The momentum equation as:

$$\frac{dp_1}{dx} = - \frac{i\omega\rho_m}{A(1-f_v)} U_1 \quad (2.48)$$

The continuity equation as:

$$\frac{dU_1}{dx} = - \frac{i\omega A}{\rho_m a^2} \left[1 + \frac{(\gamma-1)f_k}{1+\varepsilon_s} \right] p_1 + \frac{\beta(f_k-f_v)}{(1-f_v)(1-\sigma)(1+\varepsilon_s)} \frac{dT_m}{dx} U_1 \quad (2.49)$$

The energy equation as:

$$\begin{aligned} \dot{H}_2 = & \frac{\rho_m c_p |U_1|^2}{2A\omega(1-\sigma)|1-f_v|^2} \frac{dT_m}{dx} \operatorname{Im} \left(\tilde{f}_v + \frac{(f_k-\tilde{f}_v)(1+\frac{\varepsilon_s f_v}{f_k})}{(1+\varepsilon_s)(1+\sigma)} \right) - (Ak + A_{solid}k_{solid}) \frac{dT_m}{dx} + \\ & \frac{1}{2} \operatorname{Re} \left[p_1 \tilde{U}_1 \left(1 - \frac{(f_k-\tilde{f}_v)}{(1+\varepsilon_s)(1+\sigma)(1-\tilde{f}_v)} \right) \right] \end{aligned} \quad (2.50)$$

Among the geometrical segments mentioned earlier, DeltaEC can simulate acoustic-electric transducers such as linear alternators and loud-speakers. In addition, the software supplies a variety of working fluids such as air, hydrogen, helium and a group of mixtures, e.g. helium-argon. DeltaEC is also capable of providing a selection of different geometries solid materials such as stainless steel and copper. Furthermore, user-defined pure gases, user-defined gas mixtures and user-defined solids are available in DeltaEC to help the designer to build the required specific working gas and solid material.

The numerical solving process of all equations along the x axis is done by employing a Fourth-order Runge-Kutta integration method. The calculation of the boundary conditions in DeltaEC uses the shooting method algorithm to solve the integration by initialising a number of “guesses” and meeting the same number of “targets”. By setting the “targets” boundary conditions somewhere in the model, the “guesses” start to find out their appropriate values that achieve the “targets” and accomplish the convergence of the calculations.

2.3 Measurement of Acoustic Power

According to Equation (2.39), that represents an estimation of the acoustic energy flows within a duct, the required variables in the equation are the amplitude of the acoustic pressure $|p_1|$ and the amplitude of the volumetric velocity $|U_1|$ and the phase angle between them ϕ_{pU} . In this regard, the most easy, effective and reliable measurement methods are the two microphone method and piston or loudspeaker method.

2.3.1 The two-microphone method

The two pressure sensors method is fully presented and described by Fusco et al. (1992). The advantages of this method are the simplicity to accurately measure the pressure amplitudes and their phase angles at different locations within the experimental cavity. Besides the pressure measurements the volumetric velocity can be found in the midway between two pressure amplitudes. The basic concept of the method is to locate two pressure sensors away from each other by a distance Δx to measure the dynamic pressure amplitude at these two locations $|P_A|$ and $|P_B|$ and the phase angle difference between P_A and P_B . Figure 2.8 shows a schematic drawing of

the two pressure sensors placed on an acoustic duct of radius r_0 and the distance between them is Δx .

By assuming that $\Delta x \ll \lambda$ and neglecting the attenuation, the velocity is proportional to the pressure gradient. This yields:

$$i\omega\rho_m u_1 = -dp_1/dx \quad (2.51)$$

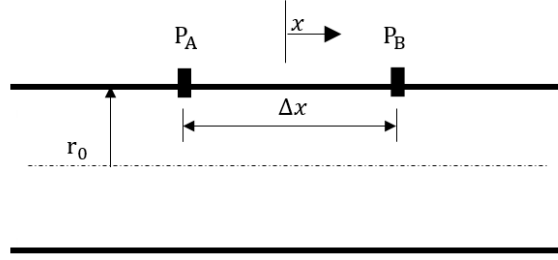


Figure 2. 8 Schematic drawing of the two sensors method

By integrating the equation for the cross sectional area, A , the volumetric velocity at the mid-way between the pressure sensors can be presented as:

$$U_1 \simeq \frac{iA}{\omega\rho_m} \frac{p_{1B} - p_{1A}}{\Delta x} \quad (2.52)$$

The pressure amplitude at the mid-way between the pressure sensors is calculated from the average of the two pressure amplitudes obtained from the sensors as follows:

$$p \simeq \frac{p_A + p_B}{2} \quad (2.53)$$

By calling the acoustic power equation:

$$\dot{E} = \frac{1}{2} \text{Re}[p_1 \tilde{U}_1] \simeq \frac{A}{2\omega\rho_m\Delta x} \text{Im}[p_{1A} \tilde{p}_{1B}] = \frac{A}{2\omega\rho_m\Delta x} |p_{1A}| |p_{1B}| \sin\theta \quad (2.54)$$

where θ is the phase angle difference between the two sensors. For more accurate measurement of the acoustic power, the attenuation is taken into account in the calculation.

$$\begin{aligned} \dot{E} = & \frac{A}{2a\rho_m \sin(\omega\Delta x/a)} \left(\text{Im}(p_A \tilde{p}_B) \left\{ -\frac{\delta_v}{2r_0} \left[1 - \frac{\gamma-1}{\sqrt{\sigma}} + \left(1 + \frac{\gamma-1}{\sqrt{\sigma}} \right) \frac{\omega\Delta x}{a} \cot\left(\frac{\omega\Delta x}{a}\right) \right] \right\} + \right. \\ & \left. \frac{\delta_v}{4r_0} (|p_A|^2 - |p_B|^2) \left[1 - \frac{\gamma-1}{\sqrt{\sigma}} + \left(1 + \frac{\gamma-1}{\sqrt{\sigma}} \right) \frac{\omega\Delta x}{a} \csc\left(\frac{\omega\Delta x}{a}\right) \right] \right) \end{aligned} \quad (2.55)$$

It is difficult in the experiments to measure the accurate phase angle between the pressure sensors. Therefore, it is preferred to locate a velocity anti-node half-way between the sensors to increase the phase angle close to 90° and reduce the measurement errors of the acoustic power (Swift, 2002).

2.3.2 The piston or loudspeaker method

In the piston, alternator or loudspeaker method, the principle of measuring the pressure amplitude and the velocity amplitude and their phases is relatively different from the previous method. For measuring the velocity amplitude, it is based on measuring the displacement amplitude and its phase angle of the moving loudspeaker or the piston by using a contact type displacement sensor such as a linear variable differential transformer (LVDT) or a non-contact type such as a laser displacement sensor. This measured displacement amplitude can be converted into velocity amplitude using the following equation (Swift, 2002):

$$|U_1| = \omega A_{alt} |\xi_1| \quad (2.56)$$

where ω is the angular speed of the loudspeaker or the alternator, A_{alt} is the effective moving area of the alternator and $|\xi_1|$ is the amplitude of the displacement of the alternator. The phase angle of the velocity is obtained from the following relationship as:

$$\phi_U = \phi_\xi + 90^\circ \quad (2.57)$$

where ϕ_ξ is the phase angle of the piston displacement delivered by the displacement sensor.

The measurement of the pressure amplitude $|p_1|$ and its phasing ϕ_p are obtained directly from the pressure sensor that is located on the front of the alternator or loudspeaker. The acoustic power in front of the piston can be measured using the amplitude of the piston displacement (Swift, 2002) as:

$$\dot{E}_2 = -\frac{\omega A_{alt}}{2} \text{Im}[p_1 \tilde{\xi}_1] = -\frac{\omega A_{alt}}{2} |p_1| |\xi_1| \sin\phi_{p-\xi} \quad (2.58)$$

where $\phi_{p-\xi}$ is the phase difference between the pressure and displacement.

The acoustic power can also be measured using the pressure amplitude in front of the piston and the velocity amplitude of the piston (Swift, 2002). After converting the measured displacement into velocity, the acoustic power is:

$$\dot{E}_2 = \frac{A_{alt}}{2} \text{Re}[p_1 \tilde{u}_1] = \frac{A_{alt}}{2} |p_1| |u_1| \cos \phi_{p-u} \quad (2.59)$$

where ϕ_{p-u} is the phase difference between the pressure and the velocity. It is also possible to use an accelerometer to measure the acceleration of the moving piston or loudspeaker and calculate the acoustic power (Swift, 2002). This can be done from the following equation:

$$\dot{E}_2 = \frac{A_{alt}}{2\omega} \text{Im}[p_1 \tilde{a}_1] = \frac{A_{alt}}{2\omega} |p_1| |a_1| \sin \phi_{p-a} \quad (2.60)$$

where $|a_1|$ is the piston acceleration amplitude and ϕ_{p-a} is the phase difference between the pressure and the acceleration of the piston.

Due to the flexibility of the moving cone of a loud speaker, it is quite difficult to determine the exact moving area of the cone, however, in the case of a rigid piston of a linear alternator this problem is solved (Swift, 2002). In comparison, the two-sensor method is simpler in terms of installation and preparation. Otherwise, the piston method needs specific design to position the linear alternator or loudspeaker. Furthermore, the piston and loudspeaker causes acoustic dissipation in the system unless the piston is positioned on purpose such as converting acoustic power to electric power as presented in this study.

2.4 Electro-acoustic Power Transducers

The acoustic power produced in thermoacoustic engines can be converted into electricity by the application of electro-acoustic power transducers. These can also work as drivers in thermoacoustic refrigerators to convert the electric power applied to the system into useful acoustic power required for the thermoacoustic cooling effects to take place. There are a number of power transduction mechanisms, including the electro-dynamic linear alternators and loudspeakers, as well as piezoelectric generators, that can be utilized in thermoacoustic devices (Yu et al, 2010b). Due to the poor efficiency of the piezoelectric generator, the transducers of the electro-dynamic type are considered the most appropriate devices to employ. Based on their simple construction, where the electromagnetic field is excited by electrical coils and permanent magnets, they satisfy the principle of (dynamic to

electric energy conversion) (Swift, 2002). Two examples of applications based on the electro-dynamic mechanism are the linear alternator and the ordinary loudspeaker. In comparison to loudspeakers, linear alternators have larger mass and more accurate mechanical resonance frequency (Swift, 2002). Moreover, linear alternators are considered more advanced in terms of reliability and efficiency especially those which are supported with flexure-bearings (Backhaus et al, 2004). Ordinary loudspeakers have comparatively low transduction efficiency (typically at most 50%) and usually have small stroke displacement, while their paper cones are brittle and fragile. This makes them inappropriate for high power thermoacoustic generators where high pressure difference between the two sides of the cone would be applied. Basically, from the cost effectiveness point of view, the possibility of using widely available audio loudspeakers is the key advantage in the design of low cost thermoacoustic-electricity generators to deliver cheap electricity to rural areas in developing countries. Here, the commercially available ordinary loudspeakers can replace the expensive linear alternators required for high pressure systems.

An example of an ordinary loudspeaker is presented in Figure 2.9 which shows a schematic diagram of a loudspeaker located in the duct of a thermoacoustic engine. Figure 2.9a shows the loudspeaker subject to acoustic pressure difference Δp while Figure 2.9b displays the representative impedance circuit of the loudspeaker.

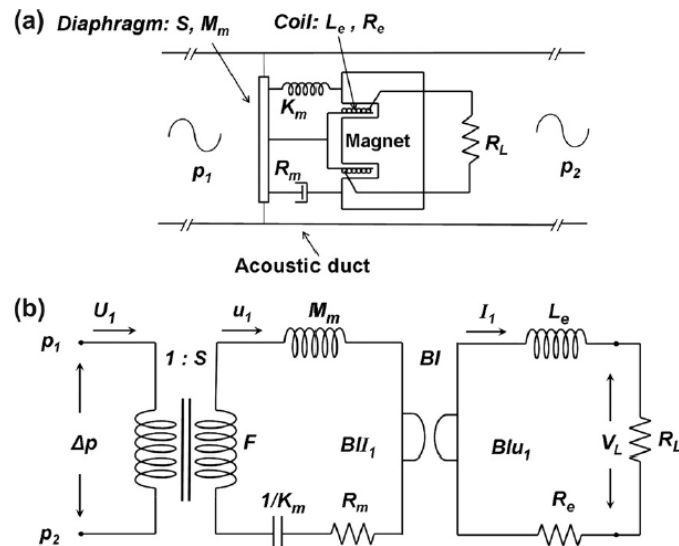


Figure 2. 9 Schematics of a linear alternator (Yu et al, 2010a). (a) Schematic of physical model of alternator. (b) Equivalent impedance circuit of the alternator.

The model of the loudspeaker describes briefly how the acoustic power P_a is converted into electric power P_e within a number of equations (Yu et al., 2010a):

The acoustic power extracted by the loudspeaker is:

$$P_a = \frac{1}{2} \text{Re}[\Delta p \widetilde{U}_1] = \frac{1}{2} |\Delta p| |U_1| \cos \phi_{\Delta p-U} \quad (2.61)$$

where:

$$\Delta p = \frac{Bl}{S} I_1 + \frac{R_m + j(\omega M_m - \frac{K_m}{\omega})}{S^2} U_1 \quad (2.62)$$

and U_1 is the volumetric velocity due to the speaker's diaphragm displacement, $\phi_{\Delta p-U}$ is the phase angle between U_1 and Δp , Bl is the magnetic force factor, I_1 is the electric current, S is the effective area of the diaphragm, M_m is moving mass and K_m is the mechanical stiffness.

The acoustic power extracted by the alternator in Equation (2.61) can be represented by the dissipation at the mechanical resistance R_m , the resistance of the coil R_e and the load resistance R_L :

$$P_a = \frac{1}{2} \frac{|U_1|^2}{S^2} \times \left[R_m + \frac{(Bl)^2 R_e}{(R_e + R_L)^2 + \omega^2 L_e^2} + \frac{(Bl)^2 R_L}{(R_e + R_L)^2 + \omega^2 L_e^2} \right] \quad (2.63)$$

while the extracted electricity by the load is:

$$P_e = \frac{1}{2} R_L |I_1|^2 = \frac{1}{2} \frac{|V_L|^2}{R_L} \quad (2.64)$$

where L_e is the coil inductance and V_L is the voltage on the load resistance.

From Equation (2.63) it is seen that the acoustic power extracted by the loudspeaker is dissipated by the mechanical resistance, the coil resistance and the load resistance. By neglecting the coil inductance, the extracted electric power output can be written as;

$$P_e = \frac{1}{2} \frac{|U_1|^2}{S^2} \frac{(Bl)^2 R_L}{(R_e + R_L)^2} \quad (2.65)$$

The maximum extracted power is obtained where $R_L = R_e$

$$P_{e,max} = \frac{1}{8} \frac{|U_1|^2 (Bl)^2}{S^2 R_e} \quad (2.66)$$

The acoustic-electric efficiency can be defined as:

$$\eta_{a-e} = \frac{P_e}{P_a} \quad (2.67)$$

$$\eta_{a-e} = \frac{(Bl)^2 R_L}{R_m (R_e + R_L)^2 + (Bl)^2 (R_e + R_L)} \quad (2.68)$$

The maximum efficiency can be obtained when $R_L = R_e \sqrt{1 + \frac{(Bl)^2}{R_m R_e}}$ as:

$$\eta_{a-e,max} = \frac{(Bl)^2 \sqrt{1 + (Bl)^2 / R_m R_e}}{R_m R_e \left(1 + \sqrt{1 + (Bl)^2 / R_m R_e}\right)^2 + (Bl)^2 \left(1 + \sqrt{1 + (Bl)^2 / R_m R_e}\right)} \quad (2.69)$$

The alternator efficiency is significantly influenced by the total acoustic impedance of the alternator and it can be presented as:

$$Z_{total} = \frac{\Delta p}{U_1} = \frac{1}{S^2} \left[\frac{(Bl)^2}{(R_e + R_L + j\omega L_e)} + R_m + j \left(\omega M_m - \frac{K_m}{\omega} \right) \right] \quad (2.70)$$

The inductance of the coil can be neglected, because ωL_e is much smaller than R_e or R_L . When the alternator is at resonance $\omega^2 = K_m / M_m$ the phase angle $\phi_{\Delta p-U}$ between Δp and U_1 is $\phi_{\Delta p-U} = \mp n\pi$, $n = (0, 1, 2, 3 \dots)$.

Finally, the equations listed above represent the ideal performance of the linear alternator according to the linear theory. However, the actual performance of the loudspeaker in real practical conditions is quite different. Due to the fact that the air flow resistance and spring losses depend on the frequency while the coil vibrates, the total mechanical resistance of the loudspeaker is significantly affected by that frequency.

2.5 Acoustic Streaming

The acoustic streaming is an unwanted acoustic phenomenon usually occurring in thermoacoustic engines and refrigerators. In these devices, the first-order oscillating acoustic mass-flux density or velocity drives a smaller steady second-order mass-flux density or velocity that is superimposed on the first order oscillations (Swift, 2002). In other words, within the oscillating gas flow, the acoustic streaming occurs as a steady flow causing harmful convective heat transfer to the device such as taking heat away from a hot heat exchanger in an engine which results in heat losses or adding unwanted load to the cooling load in a refrigerator. Consequently, it is obvious that the acoustic streaming has to be suppressed due to its significant negative effects on the performance and efficiency of thermoacoustic devices. According to the literature, there are four types of acoustic streaming that affect thermoacoustic device performance. These are known as Gedeon streaming, Raleigh streaming, Jet-driven streaming and Internal streaming within a regenerator or stack. Figure 2.10 shows the four types of acoustic streaming.

2.5.1 Gedeon streaming

Gedeon or DC streaming occurs in travelling wave engines and coolers. The streaming of steady flux flows within the acoustic oscillations along the loop of these devices degrades their performance and efficiency. Gedeon streaming can be easily defined as a net second-order time-averaged mass flux associated with the acoustic wave and observed in the loop of travelling wave thermoacoustic devices (Backhaus and Swift, 2000). This streaming or the steady-state time-averaged flow can be expressed mathematically as:

$$\dot{M}_2 = \frac{Re[\rho_1 \tilde{U}_1]}{2} + \rho_m U_{2,0} \quad (2.71)$$

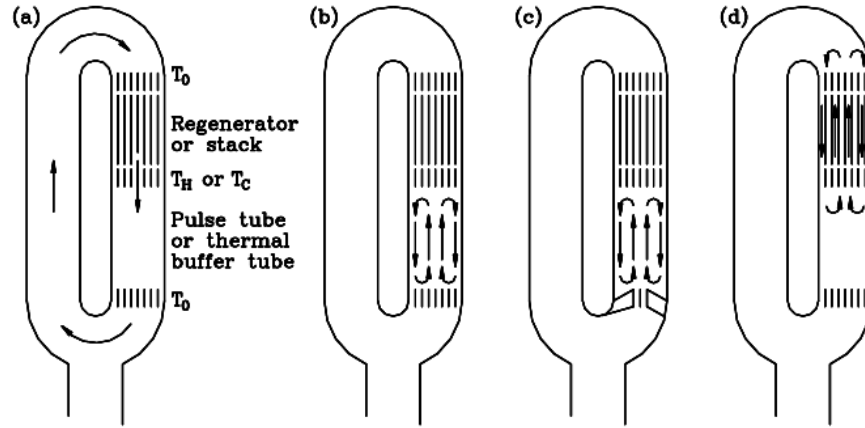


Figure 2. 10 General types of acoustic streaming in thermoacoustic devices (the time-average velocity represented by arrows), (Swift, 2002). (a) Gedeon streaming, (b) Rayleigh streaming, (c) Jet-driven streaming and (d) streaming within a regenerator or stack

where ρ_1 is the first-order complex density oscillation amplitude, \tilde{U}_1 is the time-averaged volumetric velocity, ρ_m is the mean density and $U_{2,0}$ is the second-order steady volumetric flow. Obviously when Gedeon streaming is taking place in a torus of a Stirling thermoacoustic engine, an amount of the heat input applied to the hot heat exchanger (the HHX) is taken to the thermal buffer tube (the TBT) and the second ambient heat exchanger by the streaming and reduces the efficiency (Backhaus and Swift, 2003). These effects should be eliminated by suppressing the streaming to increase the performance of thermoacoustic devices. A jet pump, alternator in series and elastic membrane are techniques usually utilised to stop the Gedeon streaming. The idea behind the jet pump, as seen in Figure 2.11, is to establish a pressure gradient that is opposite to the pressure gradient developing the

streaming. This can be done when a jet pump is installed just before the ambient heat exchanger (AHX) to provide a pressure drop in the regenerator by controlling the flow through the asymmetric passages of the pump. As a result, the streaming is stopped.

Although jet pumps are effective and successful in eliminating the Gedeon streaming, they also dissipate a considerable amount of acoustic power. They are also difficult to manufacturing and challenging in their "tuning" to actually stop the streaming under different working conditions (Hu et al., 2010; Backhaus and Swift, 1999). Besides their function to convert the acoustic power to electricity when they are installed in a loop facing the acoustic wave, linear alternators and loudspeakers can also be beneficial to eliminate the streaming in the loop. However, they also degrade the acoustic impedance in the loop by introducing a pressure drop (Kang et al., 2015; Yu and Jaworski, 2012). Introducing an elastic membrane to the loop is an effective method to completely suppress the Gedeon streaming (Kang et al., 2010a).

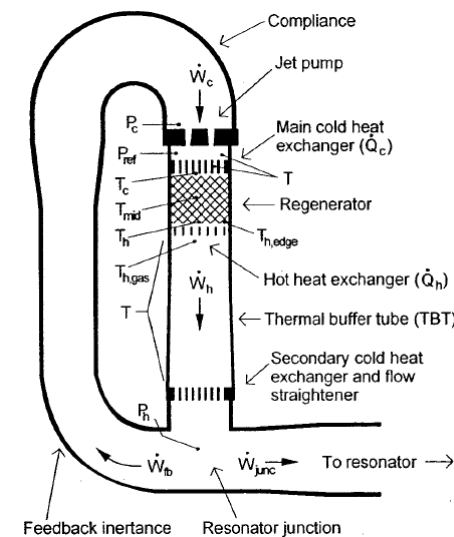


Figure 2. 11 The Gedeon streaming in the thermoacoustic Stirling engine is stopped a jet pump (Backhaus and Swift, 2000).

Huan et al. (2015) built a pulse tube refrigerator driven by a three stage travelling wave thermoacoustic engine. The system was tested, first at 4 MPa (40 bar) of air as a mean pressure and without cooling load being applied to the cooler. The first run of the rig showed the harmful impact of the total performance was caused by the Gedeon streaming. Therefore, a flexible membrane was added and

fitted into the loop in order to eliminate these harmful effects without any negative impact on the oscillations by allowing the acoustic wave to travel through the acoustically-transparent elastic membrane. Consequently, a remarkably increased performance of the system was noticed compared to the previous version (the loop with no membrane). Figure 2.12 shows the performance of the first stage before and after installing the membrane. It can be seen from Figure 2.12a that the pressure ratio at a position just before the ambient heat exchanger of the first stage of the engine is dramatically influenced by the streaming, specifically when the heating power is increased. In Figure 2.12b it is also noticed that when the elastic membrane was added, the heating temperature significantly increased compared to the same system when the streaming effects were present. Finally, the cooler was tested at 3.5 MPa (35 bar) of pressurised air as a working gas and 923 K of heating temperature at the hot side of the regenerator of the engine in each stage. It was reported that under these conditions, the cooler could achieve a minimum cooling temperature of 76 K and could also accomplish liquefaction of natural gas at a cooling load of 100 W and cooling temperature of 130 K. In addition, the overall relative Carnot efficiency of 3.5% was achieved.

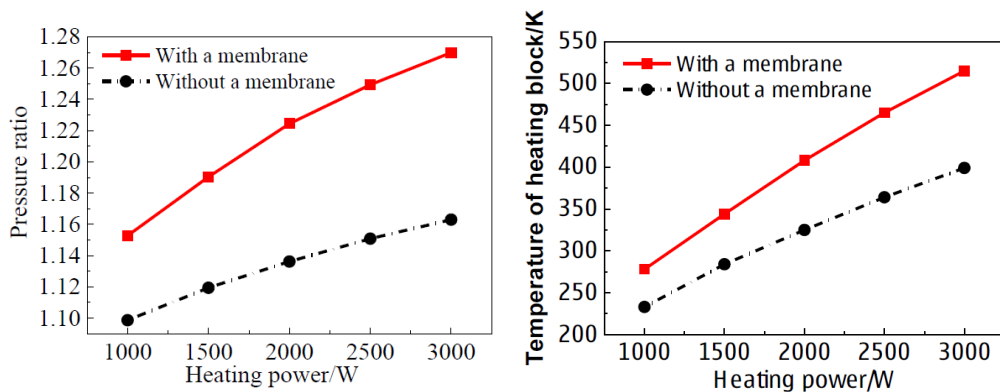


Figure 2. 12 The cooler performance before and after inserting the membrane (Huan et al., 2015). (a) the effect of the heating power on the pressure ratio, and (b) the effect of the heating power on the temperature of the heating block.

Qui et al., (2006) also investigated the effect of the streaming and compared the results of stopping the Gedeon streaming by using a jet pump and a flexible membrane. In comparison, the experiments showed that the elastic membrane was more effective than the jet pump which can cause some acoustic power losses.

Eventually achieving zero mass flux by installing the elastic membrane in the loop, doubled the acoustic power in the loop.

2.5.2 Rayleigh streaming

Compared to Gedeon streaming, Rayleigh streaming can exist in all thermoacoustic devices and particularly in thermal buffer tubes and pulse tubes. Taking a closer look at the wall of a thermal buffer tube or a pulse tube that has a temperature gradient along the wall is seen in Figure 2.13a (Swift, 2002). The oscillating gas moves back and forth along the wall – and within the viscous boundary layer is affected by the change in temperature along its displacement. Therefore, the viscosity of the gas is also changed depending on the temperature. Due to the change in gas viscosity at different locations within the gas displacement, the different viscous drag impacts the gas displacement and causes a shift in the original position of the gas parcel within the oscillating cycle. Therefore the net drift that is caused in each cycle develops mass flux in the tube. In addition, the high degree of taper of the tube contributes to the streaming by the flow separation as seen in Figure 2.13b.

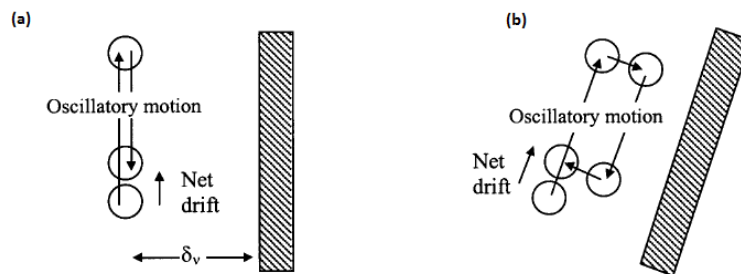


Figure 2. 13 Schematics of Rayleigh streaming in a tube (Swift, 2002). (a) the net drift of the gas parcel near the wall and (b) the net drift near the wall by the tube taper.

Yazaki and Tominaga (1998) observed Rayleigh streaming in the resonator of a standing wave engine and visualised the phenomenon using Doppler velocimetry system as seen in Figure 2.14.

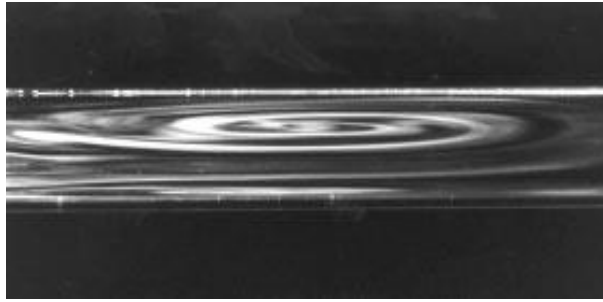


Figure 2. 14 Picture of Rayleigh streaming in a standing wave resonator (Yazaki and Tominaga, 1998).

2.5.3 Jet-driven streaming

Besides Rayleigh streaming, jet-driven streaming also exists in thermal buffer tubes and pulse tubes where there is a change in the cross sectional area. When the oscillating gas flow is inserted into a tube of larger cross sectional area, a jet is blown into the tube from all the smaller area causing a time-averaged convection driven by the jet streaming within the tube (Swift, 2002). This jet-streaming can be eliminated by using some techniques to break up the jet that occurs. Flow straighteners can be used to stop the streaming by introducing resistance to the flow inside the straightener channels and causing pressure drop (Swift, 2002). Although, flow straighteners are effective in suppressing the jet streaming, they also produce unavoidable acoustic power dissipation (Swift, 2002).

2.5.4 Streaming within a regenerator or stack

The reasons for generating the streaming in a regenerator could be the same reasons that cause Rayleigh streaming, especially when the abrupt change in the cross sectional area from the a smaller area of the resonator to the larger area of the ambient heat exchanger and the regenerator is present (Swift, 2002). In addition, the chance of producing an acoustic streaming instability in the regenerator arises because of poor thermal and hydrodynamic connections transverse to the acoustic power direction (So et al., 2004). This streaming instability is controlled by the non-linear viscous flow in the regenerator which eventually reduces the efficiency of the system by losing heat down the temperature gradient in the regenerator (So et al. 2006).

2.6 Developments in Thermoacoustic Devices

2.6.1 Thermoacoustic refrigerators

With the advantage of no mechanically moving parts and possibility of using waste heat or freely available renewable heat sources, thermoacoustic refrigerators have attracted the attention of several researchers during past decades.

Huang et al. (2005) designed and constructed a travelling wave thermoacoustic refrigerator driven by a standing wave thermoacoustic engine. The linear thermoacoustic theory was applied to the design, which resulted in a considerable experimental disagreement with the calculated 80 W, -20 °C, 2.86% of the cooling power, cold temperature and COP, respectively. A membrane solved the problem of instability of the cold temperature that was caused by the Gedeon streaming, which led to a good agreement with the cooling power at 265 K. The best results obtained were 108 W of cooling power at 0 °C, which suggested pointed to the ability of home refrigeration.

Another study carried out by Miwa et al. (2006) investigated the acoustic power produced by a travelling wave thermoacoustic engine. The acoustic power obtained from the engine was converted to cooling effects at a travelling wave thermoacoustic cooler connected in series with the same engine. The two loops and the resonator were made of stainless steel tubes with an inner diameter of 48 mm and were filled with pressurized helium at 0.5 MPa. Furthermore, the regenerator of the engine loop was made of stacked stainless steel screen meshes of length 42 mm and a mesh number of 60, whereas, the cooler regenerator was 50 mm in length and used the mesh number of 24. By adding heat power of 416 W to the hot heat exchanger, the system started oscillation with a net increase of the acoustic power of 14 W, as it was amplified through the regenerator of the engine. As a consequence, the acoustic power generated from the engine loop was estimated to be 12 W delivered to the resonator, while the rest of the power (2 W) dissipated in the loop. Moreover, the acoustic power flowing from the engine decreases to 6 W at the entrance of the cooler loop which was at a cooling temperature of 0 °C. In conclusion, it was reported that the most efficient point was only 6% of the Carnot efficiency, and it was concluded that a steady mass flow in the loop caused significant heat losses (30% of the input heat) and thereby decreased the efficiency.

Recently, some studies have used DeltaEC to design and develop thermoacoustic refrigerators. Dai et al. (2006) designed and built a travelling wave thermoacoustic refrigerator driven by a travelling wave thermoacoustic engine using the thermoacoustic linear theory. The design was optimized by the DeltaEC program in order to finalize the experimental parameters in terms of a high refrigeration performance. Very good experimental agreement was achieved with the calculations regarding the working frequency and 250 W of cooling power was obtained at -22.1°C. It was concluded that the Rayleigh streaming was observed inside the thermal buffer tube of the cooler. Kang et al. (2010a) used DeltaEC to design and build a thermoacoustic refrigerator driven by a thermoacoustic engine. A very good agreement was achieved: typically 93%, between the calculated and measured working pressure and 99.5% in the working frequency. However, the experimental overall performance represents 42% of the computed performance at cooling temperature of 0°C. In conclusion, cooling power of 40 W at 300 W of heating power was accomplished which indicated a high efficiency of the system.

2.6.2 Thermoacoustic standing wave engines

Due to their thermodynamic irreversibility which leads to low thermal efficiency compared to travelling wave engines, standing wave engines have received less attention from researchers. However, due to the absence of the travelling wave mode, standing wave engines are free of the most harmful acoustic streaming such as Gedeon streaming (Yu and Jaworski, 2010c). Furthermore, the simplicity in construction of these engines has allowed this configuration to be considered in some applications (Yu et al., 2010).

Swift (1992) built a large standing wave thermoacoustic engine to be applicable for a number of different loads. The linear acoustic theory was applied to design the engine with high pressure of helium gas. As mentioned, the large diameter of the engine means that the heat exchangers and stack could be constructed easily, which resulted in a thermal penetration depth of $\frac{1}{2}$ mm. Similarly, the resonator losses did not absorb a large fraction of the acoustic power so that the efficiency was reasonably high. Firstly, the measurements were done at low pressure drive ratio (less than 3%) at the same temperature and frequency and an excellent agreement with Rott's theory was observed. However, measurements of

the square of the pressure amplitude versus heater power differed systematically from the predicted results by 20%. Briefly, the measurements were made under several conditions, with a spanning factor of 4 in mean pressure, a factor of 6 in frequency, a factor of 3 in gas sound speed, and including various acoustic loads comparable to the dissipation in the resonator and heat exchangers. Rott's theory was confirmed by overall agreement between measurements and calculations. Yet, significant discrepancies were found in pressure amplitude at higher levels of heater power. Because the engine was designed to be capable of working at higher pressure ratios of the order of 10%, deviation from Rott's linear acoustic approximation theory was observed as the peak pressure amplitude was as high as 16% of the mean pressure resulting in high Reynolds and high Mach numbers. Consequently, Swift altered the working frequency by modifying the geometry of the resonator to suppress the harmonics. Furthermore, it was seen that the gas displacement amplitudes larger than the length of the heat exchangers can reduce the thermal contact between the working gas and the heat exchanger metal. As a result, high amplitude measurements of heating power versus pressure amplitude agreed with the calculations of linear theory as they do at low pressure amplitudes. Finally, the engine of 1.38 MPa helium gas delivered 630 W of acoustic power to the acoustic load, and the engine which is supplied with 7 kW of heating power at a temperature of 700 °C can achieve an efficiency of 9% and 13% of Carnot efficiency and 6% pressure drive ratio. It can be concluded that good agreement between the experimental and the calculated results was obtained, noting that temperature difference, load power, and efficiency were within 15% of the predicted values and the operating frequency within 2% using Rott's theory.

The maximum energy density of linear sound waves is low, and this leads to ineffective energy convection when the working pressure is atmospheric. However, alternative working media can be investigated. For example liquid alkali metals have high thermal expansion coefficients (liquid sodium has around 33% of thermal expansion coefficient of ideal gas). Swift and Migliori (1988) built a thermoacoustic standing wave engine using liquid sodium as a working medium. As a result, the acoustic oscillation began when the heating power input reached a value of 630 W. The maximum outcome of the running engine achieved 18 W of acoustic power with 990 W of heating power and efficiency of 1.8%. This was delivered at the

highest pressure amplitude that could be accomplished with temperature difference of 360 K between the cold end and the hot end of the stack. Comparing to the numerical calculation, the measured performance of the engine disagrees significantly and there was no explanation for this discrepancy. Finally, it was concluded that further predictions of having a magneto-hydrodynamic transducer in the engine would increase the efficiency of the engine and to be a major fraction of Carnot efficiency, while its power density would be comparable to that of the conventional heat engines. The final calculations show that although half of the acoustic power that would be generated is dissipated by the resonator, the engine can achieve at least 18% efficiency at the operational condition of the temperature difference in the stack of 600 K, heat input of 3 kW, and mean pressure of 20 MPa.

In a recent study, Yu and Jaworski (2009) investigated the influences of the stack geometry, the characteristic channel dimension, and the local acoustic impedance on the critical temperature gradient of the stack in a thermoacoustic standing wave engine. The theoretical and numerical work was done according to the assumption of a short stack in a standing wave acoustic field and an ideal gas in order to optimize the transverse channel dimensions to obtain the minimum onset temperature of a self-oscillating system. The critical temperature gradient investigated was normalized in order to reduce the number of unknown parameters and simplify the calculations. The normalized critical temperature gradient is:

$$\Theta_{crit} = \frac{(dT_m/dx)_{crit}}{T_m/\lambda} \quad (2.72)$$

It was shown for the parallel plate stack that dimensionless critical temperature Θ_{crit} was significantly influenced by changing r_h/δ_k and the location of the stack in the acoustic field. It indicates that as $r_h/\delta_k < 1$ the viscous dissipation dominates in the stack compared to the thermal relaxation dissipation and vice versa if $r_h/\delta_k > 1$. This can be seen in Figure 2.15.

In addition, a comparison between the parallel plate, pin-array and circular pore stacks was done in terms of the lowest temperature gradient in these stacks and all proved that the optimum location of the stack is to be between the node and the anti-node of the velocity. Also, the pin-array stack showed a better performance regarding the lowest Θ_{crit} and parallel plate being the medium and circular pore being the worst of the group. Finally, it was concluded that the critical temperature

gradient is strongly affected by the local acoustic impedance and the geometry dimensions of the channel.

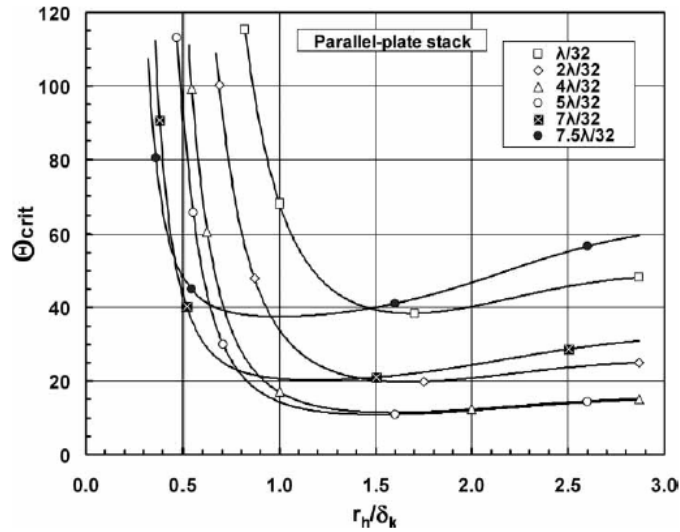


Figure 2.15 The dimensionless critical temperature gradient Θ_{crit} versus r_h/δ_k for different positions in the stack.

Yu G, et al. (2010) investigated the non-linear phenomena in a thermoacoustic standing wave engine using the commercial CFD code FLUENT 6.1. As the motivation of the study was to improve the standing wave engine for the space applications, the high frequency operation at 300 Hz was needed to compact the size of the engine. A successful simulation was obtained for a fluid-solid coupled model that represents the finite heat exchange between the working gas and solid boundary inside the stack. A good agreement in the comparison between the computational and experimental results was found. The predictions of the onset temperature agreed with the experimental onset temperature indicating that the largest discrepancy was within 30 °C. The predicted frequency was in good agreement with the experiments. However, the calculated pressure amplitude has a maximum difference up to 10% compared with the experiments, particularly when the pressure approached the value of 282 kPa. It was shown that the CFD simulation can qualitatively and quantitatively represent the mechanism and performance of the high frequency standing wave engine however, it is a time-consuming simulation. It was concluded that there is no Gedeon DC streaming existing in the standing wave engine.

Nouh, et al. (2009) designed and optimized a model of non-conventional resonator shape of a thermoacoustic standing wave engine using the DeltaEC

computer code. The investigation was to determine the influence of the resonator geometry on the acoustic pressure regarding the resistance of the flow in the resonator. The new resonator of half wavelength was shaped by increasing the cross sectional area in four steps. The final shape has five different diameters along the length of the resonator. By using a parallel plate stack, the new resonator was compared to the conventional one in terms of performance and efficiency. It was seen that resonant frequency f decreases and the quality factor Q increases as the cross sectional area is increased gradually. In addition, the acoustic pressure amplitude was increased for the fundamental mode with a reduction in amplitude of the higher harmonics. As the engine was assumed to contain air as the working gas at 2000 W heat input, working frequency of 152 Hz and 1 MPa (10 bar) mean pressure, the engine maximum efficiency achieved was 8.5%. At this mean pressure, the frequency increased to 394 Hz accomplishing an efficiency of 14.54% and producing approximately 291 W of acoustic power. The engine theoretically worked at an efficiency of 27.6% of that of the Carnot cycle.

Because of phase delay between pressure and velocity and the thermodynamic irreversibility in the stack, standing wave engines are inefficient (Ceperley, 1979). This is very clear where even high efficiency standing wave engines dissipate more than half of the acoustic power produced in the resonator (De Blok 2012). In addition, the high acoustic impedance impacts cheap ordinary loudspeakers making them inappropriate for converting power in standing wave engines. This is represented by the large pressure difference across the diaphragm (Yu and Jaworski, 2010c).

2.6.3 Thermoacoustic cascade engines

Recently, a combination of standing wave and travelling wave engines have been developed to benefit from the advantage of the high acoustic impedance of the standing wave mode and the low phase difference between the pressure and velocity in the regenerator in the travelling wave engine.

This hybrid engine has been recognized as being more efficient than the standing wave engine. Gardner and Swift (2003) designed and embodied a cascade thermoacoustic engine combined with a standing wave stage and several travelling wave stages in series. Figure 2.16 shows a schematic drawing of the cascade thermoacoustic engine. This engine was designed and modelled using DeltaEC

software. The design was begun by considering the number of stages and the resonator type. By considering the ratio of hot and ambient temperatures $\tau = T_h/T_a$ (the hot side and the ambient side temperatures of the regenerator) the number of travelling wave stages N was calculated by using the efficiency equation $\eta = (\tau^N/2 + 3\tau^N)$ in order to obtain the highest efficiency of the multi-stage engine.

As the number of travelling wave stages affects the efficiency of the engine in terms of achieving zero phase difference between the acoustic pressure and velocity near the regenerator (sweet spot), it is difficult for more than two travelling wave stages to effectively share one sweet spot where $|Z| \gg \rho_m a$ and the velocity is very low.

Due to the relatively high velocity that occurs in a pure travelling wave, it can reduce the amount of acoustic power by the presence of the viscous dissipation of the power in the regenerator. Thus, the best performance requires $|Z| \approx 10 \rho_m a$ and assuming that this condition in travelling wave stages can be done by changing area from stage to stage to increase the performance of the engine.

It was shown that the perfect heat insulation distance between the ambient end of one stage and the hot end of the next stage that is represented by the TBT length must be of the order of 10 times the gas displacement amplitude $|u_1|/\omega$. Results obtained from this engine show that at pressure drive ratio of 10%, disagreement between measured and calculated complex pressures is typically 2% and at most 6% in amplitude and between 1° and 3° in phase. Also, the calculated and measured frequency difference was about 0.5% to 1.6%. The engine delivers up to 2 kW of acoustic power with efficiency (the ratio of acoustic power to heater power) of up to 20%. As there was reasonable agreement between the calculated and measured powers and temperatures, some of the measured thermal power which could not be calculated can be referred to Rayleigh streaming in the two thermal buffer tubes with the largest aspect ratios.

Ultimately, it was finalized that straightforward steps in this work can be taken to improve the efficiency. This includes minimizing passages in the heat exchangers by a factor of two to increase heat transfer. In addition, redesigning the resonator to put the second and third stage thermal buffer tubes far from zero Rayleigh streaming in the engine can be considered. This can increase the efficiency to reach 40% of Carnot efficiency.

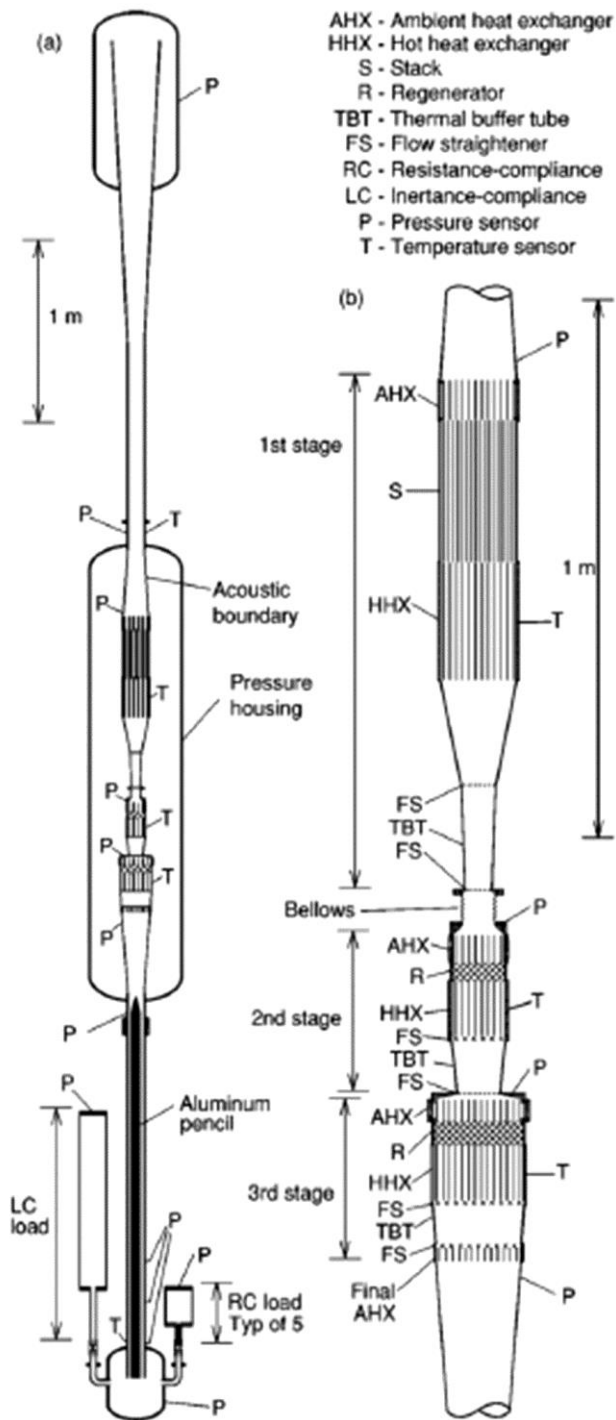


Figure 2.16 The cascade thermoacoustic engine (Gardner and Swift, (2003). (a) A schematic drawing of the engine. (b) A detailed schematic diagram of the three stages of the engine. The first stage is a standing-wave engine, the second and third stages are travelling.

The high performance and efficiency of the cascade thermoacoustic engines was demonstrated numerically and experimentally to be 20% of standing wave engine unit and 33% of travelling wave unit of four miniature cascade thermoacoustic engines designed and constructed by Hu et al. (2006a) and Hu et al. (2006b). By using the DeltaEC program, the designed configuration presents a very good example of an effective method of converting heat power of 300 W to acoustic power of 68 W by increasing the length of the travelling wave stage and extending the diameter ratio of the stages to be 1.69 which eventually was capable of achieving a thermal efficiency of 22.74%. A good agreement between the calculations and the experiments was found among the temperature distributions and the working frequency, whereas the calculated pressure amplitudes partially disagree with the experimental values because of the inadequate arrangement between the hot heat exchanger and the stack.

Due to the irreversibility in the standing wave section, the efficiency would be limited to a small fraction of the efficiency of the travelling wave part which indicates that travelling wave engines are a better choice to consider (Ceperley, 1979; Ceperley, 1982).

2.6.4 Thermoacoustic travelling wave engines and electricity-generators

Ceperley (1979) introduced the first concept of a thermoacoustic heat engine with no moving parts based on travelling wave propagation. These travelling wave heat engines use the reversible Sterling thermodynamic cycle. The theory states that an applied temperature gradient along the length of a regenerator by external reservoirs, which heat one end and cool the other end of the regenerator, can produce the propagation of a travelling wave through the regenerator.

For the engine it was demonstrated that a wave travelling in the regenerator would cause a compression of the gas parcels, followed by the movement of the parcels towards the hot end combined with transferring heat from the regenerator to the gas, subsequently followed by expansion while moving to the cold end releasing the heat to the cold reservoir. In the heat pumps, it was pointed out that the waves pump heat in a direction opposite to their propagation direction. Ceperley (1979) derived the theoretical gain of a travelling wave heat engine of a short regenerator. The power gain was modelled by $g = T_h/T_a$, where T_h is the hot absolute

temperature and T_a is the cold absolute temperature of the regenerator. As a consequence, it was realised that the travelling wave heat engine is an acoustical amplifier which can be significantly utilized in a variety of energy conversion applications.

To show the importance and the effect of regenerators on the Sterling cycle in terms of transforming energy between thermal and acoustic power, Ceperley (1979; 1982; 1985) derived and deduced gain and efficiency equations of a thermoacoustic travelling wave heat engine. The derivation assumed non-turbulent flow conditions, a linear drag coefficient, a constant heat exchange coefficient and neglected the regenerator end effects. The complex characteristic impedance, gain, and efficiency were calculated for a regenerator in terms of dimensionless variables. The assumption of non-zero drag, finite thermal conduction between the regenerator and the gas, linear temperature profile in the regenerator, and wave propagation in one direction were only considered. As a result, it was showed that for all frequencies, the normalized gain becomes negative at very low values of normalized temperature gradient of the regenerator because of viscous losses. Instead, for a range of normalized frequencies between 0.001 and 0.032, the gain exceeds 85% of the ideal gain at values of the normalized temperature above unity. Also, the results explained the decrease of the gain and the efficiency after increase at higher values of the normalized temperature gradient. It was attributed to the wasteful flux of heat caused at large temperature gradients. Similarly, Ceperley (1985) showed that for a Prandtl number of 0.7 and acoustical impedances of travelling waves, the efficiency is limited by 10% of Carnot efficiency due to viscous losses in the regenerator. Furthermore, higher efficiencies of Carnot efficiency can be obtained with higher impedances of the order of 10 times a free travelling wave impedance. In conclusion, it was reported that a high gain and high efficiency regenerator is very much shorter than an acoustic wavelength with higher temperature gradient across the regenerator.

Zhou et al. (2008) built a miniature thermoacoustic Stirling engine (TASHE) - 0.65 m in length and 0.22 tall. According to linear thermoacoustic theory the engine was designed and optimized to improve the performance and the efficiency of the system. It was mentioned that the increase in the diameter of the resonator can cause the pressure amplitude to rise, however at some values of the diameter, the pressure

amplitude starts to fall as the diameter is being enlarged at different heat power inputs. This indicates that increasing the resonance tube diameter will need to increase the input heating power in order to obtain maximum pressure amplitude. The increase in the onset temperature was referred to as the increase of the working frequency if the resonator diameter increased. Good agreement was found between the calculations and experiments.

However, in the experiments the heating power is 3-4 times the amount of the computed one to reach the same pressure amplitude and pressure ratio. It was thought that there were many reasons behind this discrepancy. Heat leakage to the surroundings is unavoidable as well as the Gedeon streaming where this time averaged mass flow is associated with acoustic work flow which can transport heated gas from the hot heat exchanger to the ambient heat exchanger and these can be the main factors that cause this disagreement. The most effective operating point of the engine was obtained at a helium mean pressure of 2 MPa, 111 kPa of the pressure amplitude, 5.5% of pressure ratio and heating power of 638 W which can produce a heating temperature of 310 °C and different applications can be driven by this engine as a refrigerator and linear electrical generator. Eventually, it was pointed out that the engine can self-oscillate steadily without higher harmonics, and the onset temperature is also low, which means that the basic performance of the constructed engine is rather good and is a steady system.

Ling et al. (2006) presented a numerical model and an experimental rig of a thermoacoustic Stirling engine. The numerical model was built by using the transcendental equation of complex frequency to match the temperature distribution of the whole thermoacoustic system with given heating power. The engine simulated contained a regenerator of a stainless steel screen of 60 mesh, working gas of helium, mean pressure of 2.15 MPa, and 1188 W of heating power. As a result of the simulations, a comparison of the pressure amplitudes between the calculations and experiments under three different mean pressures of 2, 2.6, and 3 MPa was shown. It was found that the system can achieve higher pressure ratios as the mean pressure decreased and as heating power increased. In conclusion, the experimental readings presented accuracy of about 70% of the calculated results, in spite of the difference in working frequency being only about 0.5 Hz.

Many studies have investigated the effects of the major characteristic components in the performance of travelling wave engines. Yu and Jaworski (2010) numerically investigated and analysed the relationship between the acoustic impedance, flow resistance, viscous losses, heat relaxation loss, and channel transverse dimensions inside a travelling wave engine regenerator. This study was carried out according to the linear thermoacoustic theory to generate and develop theoretical and numerical concepts to compare between regenerators in different geometrical configurations. As the calculations were performed according to the travelling wave engine of Backhaus and Swift, 2000, the hot and cold temperatures were 725 °C and 40 °C, with a regenerator length of 7.3 cm, working frequency of 84 Hz, and mean pressure of 3.1 MPa. It was found that the power decreases rapidly as z_n (the dimensionless local acoustic impedance factor) increases if δ_k/r_h is constant and this indicates that the local acoustic impedance and channel dimension significantly affect the acoustic power output of the regenerator in travelling wave engines.

Further work was carried out on this study to represent the calculated results of the DeltaEC model based on Backhaus and Swift's (2000) experimental results. It was shown that $|p_1|$ decreases from the cold end to the hot end of the regenerator while $|U_1|$ increases along the length of the regenerator which was indicated by the influence of the temperature gradient. Similarly, z_n decreases along the length of the regenerator from the cold to the hot end, whereas the mean value z_n of the stacked screen regenerator is about 1.7 times of that in the parallel plate regenerator. Consequently, it was indicated that the possible maximum capacity of acoustic power output for the parallel plate regenerator is about twice of that of the stacked screen regenerator. Accordingly, it was concluded as follows:

- 1- At a given pressure amplitude $|p_1|$, a higher impedance z_n leads to lower acoustic power input at the ambient end of the regenerator.
- 2- For a particular pressure amplitude $|p_1|$, increasing z_n will decrease the volumetric velocity $|U_1|$ and therefore will decrease the acoustic power output of the engine.
- 3- At a specific $|p_1|$, the higher resistance will decrease $|U_1|$ through the regenerator which, in turn, will cause the high impedance of the regenerator.

In another analysis of the characteristics of regenerators, Yu et al. (2004) experimentally investigated the effects of the mean pressure and the regenerator hydraulic radius on the onset temperature difference ΔT_{onset} in the thermoacoustic travelling wave engine of a looped tube and resonator. The length of the loop was 0.708 m and for the resonator was 1.138 m. They investigated the effect of increasing the mean pressure from 0.1 to 2.6 MPa by steps of 0.1 MPa in regenerator with mesh number of 120. Working gases of nitrogen and helium were used, with working frequencies of 76 Hz, and 211 Hz, respectively. The optimal mean pressures leading to the lowest onset temperature difference ΔT_{onset} were 0.4 MPa and 1.1 MPa for the two cases respectively. Consequently, the measured optimal values of the ratios of the regenerator hydraulic radius to the thermal penetration depth r_h/δ_k were 0.24 and 0.2 for nitrogen and helium, respectively. It was proved that the hydraulic radius of the regenerator r_h has a significant influence of the performance of the engine. As the nitrogen mean pressure was fixed at 0.6 MPa, r_h was altered from 20 to 100 μm and the lowest onset temperature difference was captured at $r_h/\delta_k = 0.2$. It can be concluded that the experimental optimal ratio of the hydraulic radius to the thermal penetration depth in the regenerator r_h/δ_k was in the range of (0.17 to 0.25).

To reveal the importance and the influence of the hydraulic diameter r_h resonator length, and the mean pressure on the characteristics of a thermoacoustic engine having a looped tube and resonator. Yu et al. (2005) experimentally studied the effects of these parameters on the excitation and performance of two different oscillating modes in the engine. These two acoustic modes were a high frequency mode (with a frequency independent of the resonator length) and a low frequency mode (with a frequency depending on the resonator length). It was mentioned that decreasing the mean pressure and the hydraulic radius will increase the relative penetration depth which leads to reducing the possibility of high frequency mode.

Also, the low onset temperature difference in the engine was represented by the measured optimal mean pressure which increases as hydraulic radius decreases. In addition, it was observed that the pressure amplitude increases as the mean pressure increases. Ultimately, the experimental results indicate that the regenerator can be optimised in a thermoacoustic travelling wave engine by choosing an

appropriate value of relative penetration depth when the working gas, mean pressure, and operating frequency are given.

The dimensions of a regenerator have a substantial influence on the engine performance. Resonator shape also has a significant effect on improving the performance of the engine. Yu et al. (2007) designed and tested a tapered resonator of EF-TASHE (energy focused thermoacoustic Stirling heat engine) in order to reach the highest possible pressure ratio in the miniature engine. The engine was designed using a computational fluid dynamics (CFD) code. The resonator consisted of two sections: one was tapered and was used to suppress high harmonic oscillation modes, and the other one was a cylindrical section with large volume, which forms a quarter wavelength acoustical system. Several measurements were made in the engine with nitrogen and helium as working gases and different values of mean pressures. As a result, the engine achieved a high pressure ratio of 1.4 with 1.5 MPa nitrogen gas, heating power input of 3 kW and a heating temperature of 671°C. In conclusion, a relatively low onset temperature of 73 °C was observed which indicated the possibility of its application in the field of using a low-grade heat source.

Furthermore, Luo et al. (2006) investigated the effects of the shape and size of the resonator on the acoustic field in the thermoacoustic Stirling heat engine. The experimental research involved the comparison of the performance between an iso-diameter resonator and a tapered resonator. For the same looped tube size of engine and the same frequency and working gas such as helium and a heating temperature of 600 °C, the engine with the tapered resonator can achieve a pressure ratio of 1.17, and acoustic power of 200 W, whereas the iso-diameter only achieved a pressure ratio of 1.15 and acoustic power of 160 W. The highest pressure ratio that the engine could achieve was above 1.3 at a mean pressure of 1.54 MPa helium gas and net acoustical power produced by the engine of more than 450 W under heating power input of 1.5 kW.

With the support of the easily controlled optimization advantage of DeltaEC, Tijani et al. (2008) designed and built a travelling wave thermoacoustic engine. The engine used a thermal power input of 1 kW produced by electric cartridge heaters to generate acoustic power. The working gas was helium at a mean pressure of 4 MPa and operating frequency of 110 and 150 Hz. These two operating frequencies were

established in two different resonators of about a quarter wave length. To eliminate any type of acoustic streaming, an elastic membrane was installed next to the ambient heat exchanger to stop Gedeon streaming and two flow straighteners were placed on both sides of the thermal buffer tube. The first resonator was a straight tube which ended in a cylindrical volume, and this resonator introduced high acoustic power dissipation and resulted in high onset temperature of the engine. The other resonator was designed to be a combination of four sections to eliminate this problem and reduce acoustic losses. As a result of changing the resonator, the resonance frequency of the engine increased from 110 Hz to 150 Hz. Ultimately, the engine generated 190 W of acoustic power at a pressure ratio of 7.1% and with an efficiency of 22.5% corresponding to 36% of Carnot efficiency.

In very useful investigation (Backhaus and Swift, 1999; Backhaus and Swift, 2000) introduced a detailed study of a thermoacoustic Stirling engine delivering a deep insight into how to improve the performance and efficiency of a heat-acoustic power converter without moving parts. Figure 2.17 shows a schematic diagram of the thermoacoustic Stirling engine (torus configuration). According to a pure travelling wave where $|p_1|/|U_1| = \rho_m c_p / A$ and for realistic gases, U_1 would be considerably large and cause viscous losses which, in turn, would reduce the efficiency. However, increasing the left side of the previous equation $|p_1|/|U_1| \gg \rho_m c_p / A$ will enlarge the efficiency and minimize the viscous losses. Nevertheless, this design of the thermoacoustic Stirling engine would provide the conditions to achieve high performance and efficiency. This engine includes a quarter wavelength resonator filled with helium at a mean pressure of 3 MPa to work at a low frequency of 80 Hz and coupled to a looped tube that contained hot heat exchangers, a regenerator and a thermal buffer. Also, introducing the inertance and the compliance to the loop is to adjust the phase difference between the acoustic pressure and velocity to be close to 0° (the travelling wave mode) and to obtain a pressure antinode and velocity node which helps to reduce the viscous losses and increase the acoustic impedance within the regenerator.

As a result of adjusting the dimensions of the inertance, compliance and the hydraulic radius, porosity and length of the regenerator, the local acoustic impedance $|p_1|/|U_1| \approx 30 \rho_m c_p / A$ reached high levels which reduced the viscous dissipation in the regenerator. The jet pump was used to eliminate the Gedeon

streaming in the looped tube. It contains two tapered rectangular channels above the cold heat exchanger which were used by adjusting the jet area to eliminate the second order mass flux \dot{M}_2 and leaking of heat. The thermal buffer tube (TBT) was designed to be flared with a 1.35° half angle taper to eliminate Rayleigh streaming which is responsible for creating a time average mass flux density that drags the gas within the thermal penetration depth inside (TBT). Therefore, it was concluded that the maximum thermal efficiency obtained is $\eta = 30\%$ (42% of Carnot efficiency) at an approximate pressure ratio of $|p_1/P_m| = 0.06$ at a hot gas temperature of $T_h = 725^\circ\text{C}$ and acoustic power of 710 W delivered to the resonator. In contrast, the engine delivered 890 W to the resonator at $|p_1/P_m| = 0.1$ with a lower efficiency of $\eta = 22\%$ and this point represents the most powerful operating point of the engine.

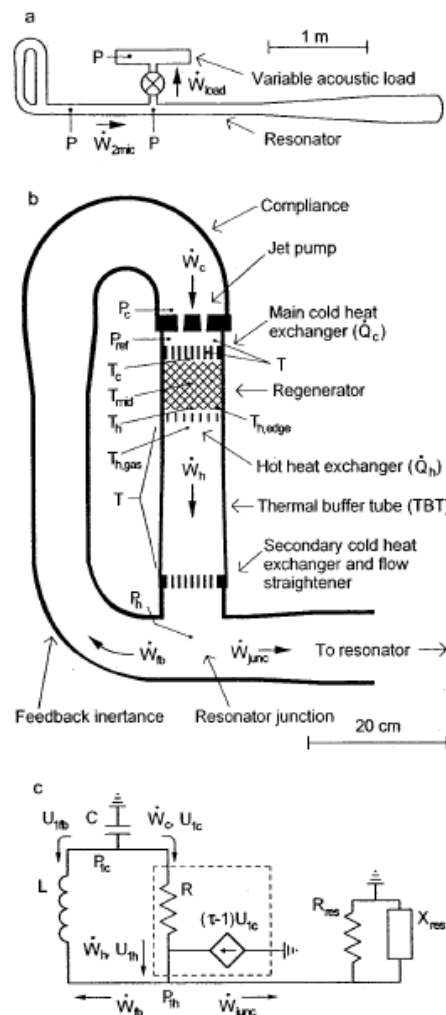


Figure 2. 17 Schematic drawing of the thermoacoustic Stirling engine (Backhaus and Swift, 2000): (a) drawing of the complete engine. (b) drawing of the bypass part of the engine. (c) lumped-element diagram of the engine.

Although the thermal efficiency achieved by this type of engine is high in comparison to conventional engines, the design and construction of this engine was relatively complicated due to the difficulty that the acoustic resonance was provided by the alternator (Yu et al. 2010a).

Additionally, in the standing wave resonator of a bypass configuration travelling wave engine, the high acoustic impedances in the resonator cause high acoustic losses and the reflection factor is close to one resulting in very low acoustic power being consumed by the load that is the net product of interference between the forward and reverse wave (De Blok 2010). Moreover, studies show that torus configuration travelling wave engines producing an amount of acoustic power are significantly larger in size than the looped-tube travelling wave engine producing the same acoustic power (De Blok 2012).

Yazaki et al. (1998) designed and tested the first thermoacoustic looped-tube engine that used the travelling wave mode to transfer sound energy. The resonator was designed to contain one wave length sound wave which was used to convert heat power to acoustic power. The thermoacoustic core shown in Figure 2.18 consists of a stack sandwiched between a hot heat exchanger and a cold heat exchanger.

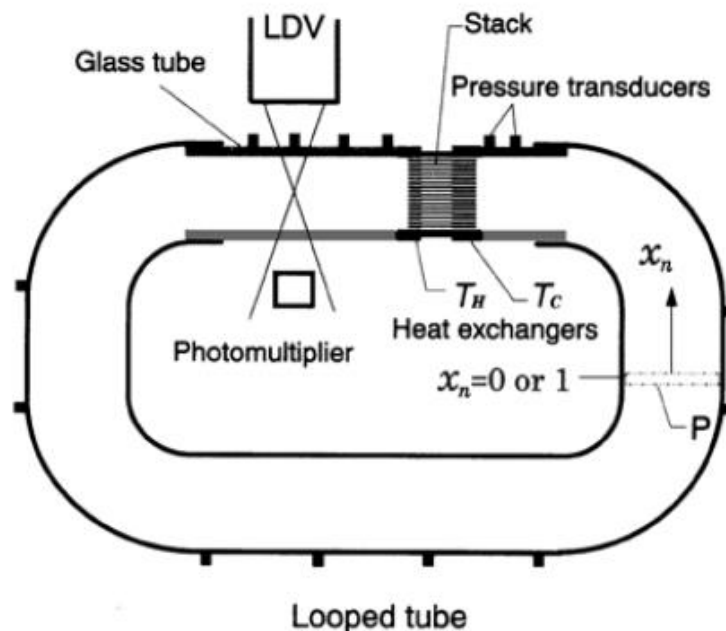


Figure 2. 18 The looped-tube travelling wave thermoacoustic engine (Yazaki et al., 1998).

The study involved the investigation of the stability boundary between oscillatory and non-oscillatory regions of the travelling wave mode. One aim of the study was to make a comparison between the travelling wave and standing wave modes. To present the standing wave in the engine, the looped tube was blocked by a partition which was thin, flat and rigid so that it did not change the length of the loop. By adjusting the partition position keeping the same operating frequency, the optimum position of the partition to obtain the maximum thermoacoustic effects and minimum onset temperature ratio T_h/T_a was at $x_n = 0.19$ which is at the midpoint between the pressure node and the velocity node where x_n is the position normalized by the length of the tube. As a result, it was shown from the stability curves that the travelling wave thermoacoustic engine has a smaller onset temperature ratio T_h/T_a compared to the standing wave engine, at all different mean values of mean pressure. Although, the very low acoustic impedance viscous losses were due to high velocities in the travelling wave engine which can significantly influence the performance and efficiency of the engine, it was shown that the perfect thermal contact between the gas and the stack walls was preferred to the looped tube engine, whereas imperfect thermal contact was favourable to the resonance tube engine. In conclusion, it was shown that the dependence of the reversibility of the heat-acoustic conversion can be a feature of reducing the onset temperature of the self-oscillations which plays a major role in the travelling wave engines.

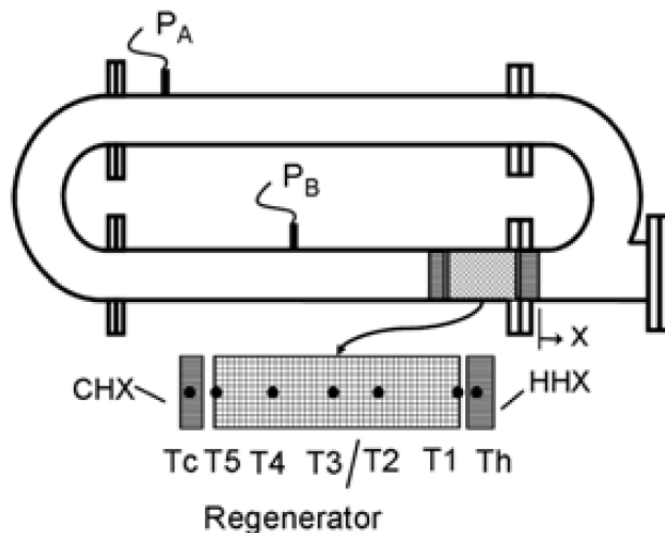


Figure 2. 19 A schematic diagram of the travelling wave engine (Abduljalil et al. 2011).

Obviously, looped tube thermoacoustic engines are the most appropriate option for producing electric power. This is because of the simplicity in construction, and high performance compared to standing wave engines (Yazaki et al., 1998).

Moreover, the travelling wave mode can decrease the pressure difference across the alternator diaphragm allowing the insertion of a cheap loudspeaker in the loop (Yu et al., 2010c).

As a part of the project of utilizing the solar energy to power a solar driven thermoacoustic engine, Abduljalil et al. (2009a) and Abduljalil et al. (2011) designed, built and tested a looped tube travelling wave thermoacoustic engine equipped with a ceramic regenerator. Figure 2.19 shows a schematic drawing of the looped tube travelling wave engine.

DeltaEC was the fundamental and major method used to design the engine (Ward et al. 2008). The engine was designed to operate at a working frequency of 110 Hz and was constructed of stainless steel pipe with a total length of 3 m and was filled with pressurized air at 1 MPa as working gas. For indoor experiments, the solar power was demonstrated by testing the engine with an electrical cartridge heater to supply of 600 W of heating power. Under these operating conditions, the engine was tested in a horizontal position, vertical position and an inclined position with an angle of 15° from the horizontal direction. As a result, it was observed that the horizontal orientation of the engine could achieve the most linear temperature gradient in the regenerator and the highest heating temperature of 750 °C at the hot end of the regenerator, as well as the highest acoustic power produced by the engine. The reason was reported that the influence of natural convection effects were extremely strong in the engine when it was oriented in the other two positions which also decreased the time needed to start the acoustic oscillations compared with the other cases. The acoustic power flow in the loop was measured by the two-microphone measurement method (Swift, 2002). In comparison with DeltaEC calculations, obviously there was good agreement at high mean pressures (around 10% difference at more than 303 kPa) while a discrepancy of 30% difference was seen at low mean pressure as seen in Figure 2.20a. It was also reported that there is good agreement between the measurements and the calculations of the acoustic

power at high average pressure in the engine (above 0.6 MPa) as seen in Figure 2.20b:

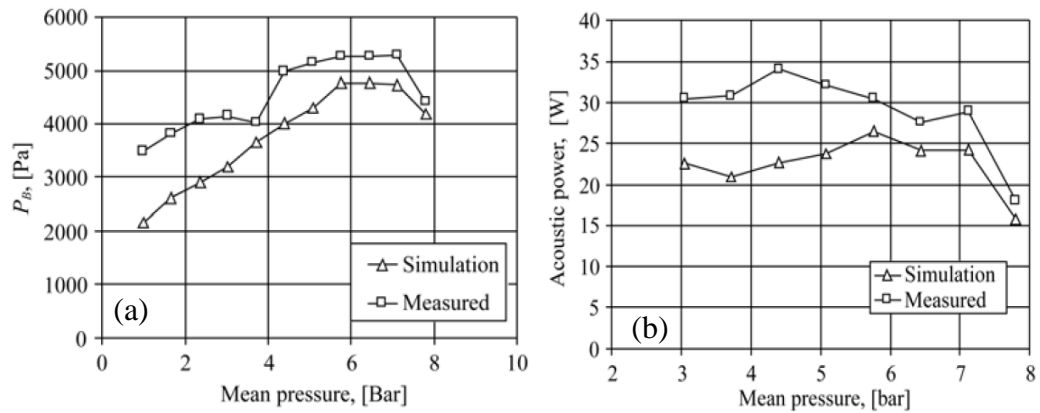


Figure 2. 20 The effects of the mean pressure. (a) Mean pressure versus pressure amplitude, and (b) mean pressure versus acoustic power.

Performance studies on this engine were further enhanced by Abduljalil et al. (2009b) and Abduljalil et al. (2011b) which involved studies on the effect of three regenerators made of three different types of material. Having almost the same hydraulic diameter (about 200 μm) and the same length (100 mm) of the regenerator, these materials were chosen to be: the mesh wire screens, stainless steel scourers (steel wool) and ceramic substrate. According to the results, the lowest ΔT_{onset} was achieved by using the mesh screens regenerator and the minimum ΔT_{onset} corresponded to the optimum mean pressure being different for each regenerator. Also it was noticed that changing the volume available to the gas in the regenerator, which is limited to different porosities of regenerators, influences the pressure amplitude where the porosity of mesh screens, ceramic, and steel wool regenerators were 72%, 88%, and 94% respectively. Measurements of the hot temperature of each regenerator were performed in terms of increasing the mean pressure. As a consequence, increasing the mean pressure decreases the hot temperature. So, the mesh screen regenerator accomplished the lowest hot temperature while the ceramic regenerator recorded the medium hot temperature, whereas the hottest regenerator temperature was achieved by the stainless steel regenerator. It was also outlined that the influence of high pressure amplitude can affect the heat exchanged between the gas and the regenerator. In addition, the

decrease of the porosity increases the viscous losses in the regenerator which reduces the volume velocity as in the mesh screen regenerator. Despite the impact of the different hydraulic radius of these regenerators it was declared that the porosity, as well as the flow resistance can significantly influence the regenerator performance. Ultimately, it was found that the tested wire mesh screen regenerator had the best performance in terms of both the onset temperature difference and the pressure amplitude.

As part of SCORE project, Yu et al. (2010a) designed and built a low cost travelling wave thermoacoustic engine for remote rural areas. To match the criteria of the remote rural area conditions, several parameters were taken into account. Among a variety of working gases, the air at atmospheric mean pressure is the most convenient medium to reflect the simplicity of the engine construction, the low cost of manufacture and materials. Furthermore, the approach of converting the acoustic power to electricity represented in a transduction device was utilized by inserting an ordinary audio loudspeaker in series in the loop. Because of the resonant frequency dependence of the driving forces of the alternator, and due to the fragility of the cone of the alternator, the working frequency was chosen to be close to the alternator's resonant frequency which was indicated as 70 Hz. Using DeltaEC programme, the engine was successfully simulated at solid temperature of the hot and cold heat exchangers of 870 K and 300 K respectively as well as the drive ratio of $D_r = 4.8\%$ and input heating power of 543 W. As a result, this indicates the calculated engine efficiency (heat-acoustic efficiency) $\eta_{h-a} = 3.7\%$, and alternator efficiency (acoustic-electric efficiency) $\eta_{a-e} = 52.5\%$, and generator efficiency (heat-electric efficiency) $\eta_{h-e} = 1.93\%$. Experimentally, the influence of increasing the working frequency and the input heating power were investigated and compared to the calculations. In addition, both the calculated and experimental results show linearity of increase in the electric power output as the heating power increased. Briefly, the experiments showed that the engine can produce 11.58 W of electricity at a heat input of 703 W. At this operating point, the engine measures an engine efficiency of $\eta_{h-a} = 3.5\%$, while the alternator efficiency is $\eta_{a-e} = 46\%$, and finally the generator efficiency is $\eta_{h-e} = 1.65\%$. In conclusion, the good agreement

between the calculations and the measurements demonstrates the reliability of the DeltaEC.

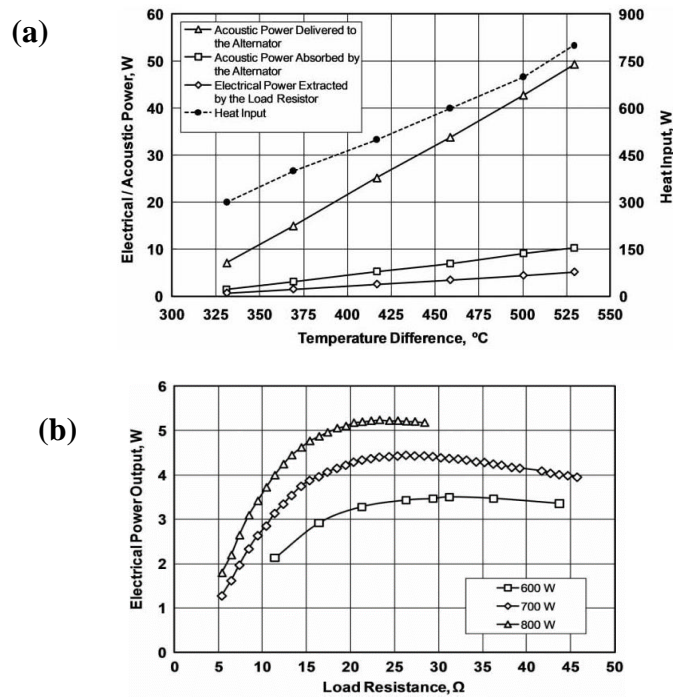


Figure 2. 21 The performance outputs of the engine (Yu et al. 2010b). (a) The power outputs as functions the heating power and temperature difference in the regenerator. (b) The electricity output versus the load resistance.

Yu et al. (2010b) also achieved more studies of the looped-tube low cost travelling wave thermoacoustic engine. In the experiment, the characteristics of the alternator were measured as a function of the input heat power and the temperature difference across the regenerator. As a result, it was shown that the acoustic power extracted by the alternator increases as the heat input and the temperature difference of the regenerator increases. Figure 2.21a shows the effects of the heating input on the electric and the acoustic power outputs in the alternator.

Besides the influence of the heat power input, the impact of the load resistance R_L on the performance of the alternator was investigated in terms of the electricity production and the acoustic to electric conversion efficiency. It was pointed out that the high output of the electricity can be achieved if the heating power input is increased at a fixed load resistance. However, it was theoretically demonstrated that if the load resistance decreases to values lower than the coil resistance value at fixed heat input, the acoustic impedance of the alternator increases and leads to a decrease

in the volumetric velocity of the acoustic oscillation. Consequently, the feedback acoustic power decreases and less net acoustic power can be produced in the regenerator. Figure 2.21b presents the impact of the load resistance on the electricity outputs.

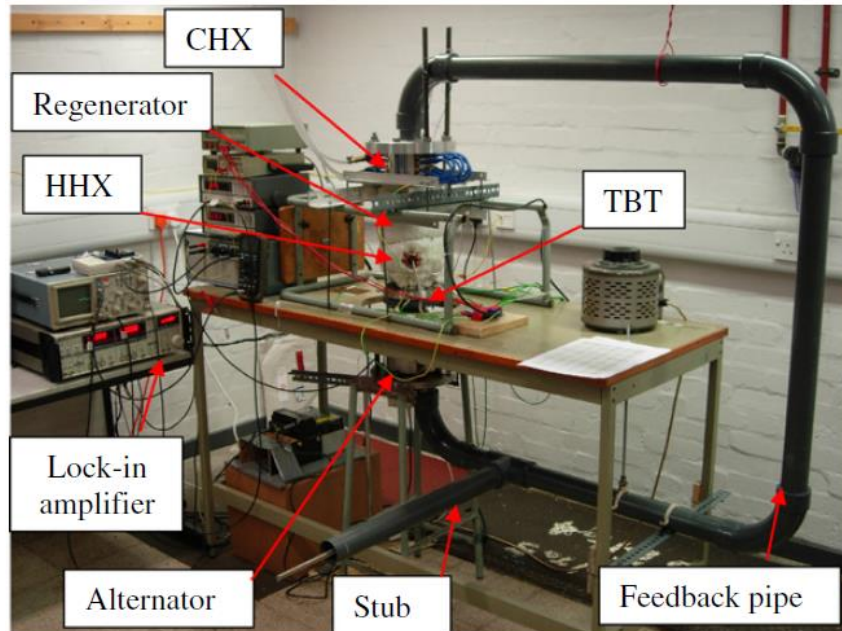


Figure 2. 22 A photograph of the thermoacoustic-electricity generator. (Yu et al. 2012).

Similarly, the impact of altering the load resistance on the alternator efficiency was investigated. As a consequence, it was experimentally and computationally found that increasing the load resistance increases the displacement of the diaphragm of the alternator and consequently increases the efficiency. However, due to the limitation of the cone's displacement of the alternator, the efficiency decreases as the stroke reaches its maximum value. This was attributed to the loss due to non-linear effects at maximum displacement.

In the preliminary results of the engine with a heat input of 800 W, and comparing to DeltaEC results, the engine performance was very low. The acoustic power which arrived at the alternator was about 49.3 W, while the acoustic power absorbed by the alternator is 10.3 W. Ultimately, as the alternator has an efficiency

of around $\eta_{a-e} = 50\%$, the load resistor extracts 5.17 W, indicating the low engine efficiency $\eta_{h-a} = 1.29\%$, and generator efficiency $\eta_{h-e} = 0.65\%$.

Improvements in the performance of the engine have been achieved by Yu et al. (2012). Figure 2.22 shows the travelling wave thermoacoustic-electricity generator designed by (Yu et al. 2012). Firstly, an ultra-compliant alternator was installed in the region of low impedance to avoid high pressure drop across the alternator which causes streaming in the clearance seal. Secondly, the low impedance caused by the low impedance alternator needs to be increased to overcome the viscous losses in the feedback pipe (the FBP). This impedance matching is adjusted by introducing a side-branch tube (STUB). This function of the STUB is tuned by being the compliance resistance larger than the inertia resistance of the STUB ($1/\omega C_s \gg \omega L_s$), where C_s, L_s are the compliance and inertance of the STUB. This leads to a constant acoustic pressure amplitude $|p_1|$ at the coupling point between the stub and the FBP and part of the volumetric velocity flows into the stub so that ΔU_1 lags p_1 by almost 90° in the FBP. Thirdly, the 90 mm long CHX with a porosity of 10% was designed to provide a low phase difference angle at the cold side of the regenerator. Consequently, the engine was optimized using DeltaEC by applying heating power of 434 W and heating temperature of $T_h=733$ K at the hot side of the regenerator to produce 27 W of net acoustic power by amplification in the regenerator. Electric power of 10.3 W was extracted from the loudspeaker where applied load resistance was $R_L = 15.6 \Omega$ and peak to peak stroke of the alternator was $|\xi| = 6.25$ mm.

By comparing the results with the measured results at a heating power of 500 W, It was shown that the increase of the stub length can significantly influence the engine performance and the calculated and measured results agree that the optimum length of the stub ranges between 600 mm to 680 mm. Finally, the most efficient operating point was reported at measured electricity of 7.1 W, with a thermal-to-electric efficiency of 1.4%, acoustic-electric efficiency of 46.5%, and thermal-to-acoustic efficiency of 3%. However, increasing the alternator displacement to be $|\xi| = 8.5$ mm by the highest input power tested of 900 W can increase the electric power to 11.6 W as well as the decrease in the thermal-electric efficiency 1.3%. This was attributed to the strong distorted waveform that occurs in the voltage across the

load resistance because of exceeding the maximum excursion of the alternator (Yu et al. 2012).

Among the developments of travelling wave thermoacoustic engines is the utilisation of the advantages of the travelling wave mode by locating a number of regenerators along the loop to increase the acoustic power by the regenerators and reduce the acoustic losses by shortening the FBPs length between the regenerators. In addition, the acoustic impedance should be high enough to overcome viscous dissipation by increasing the cross sectional area of the regenerators compared to the FBPs (De Blok, 2012). For the purpose of enhancing higher acoustic power in each stage unit, the phase difference between the acoustic pressure and velocity in the regenerator should be close to zero. As an advantage, the low acoustic losses in multi-stage engines establish the low onset temperature in stages (Abdoulla et al., 2012). In order to achieve a feedback phasing of 2π in each stage, the length of the loop should be equal to one wave length and the backward waves or reflection in each stage is reduced or suppressed by adjusting the acoustic impedance to the local impedance of its FBP (De Blok, 2010).

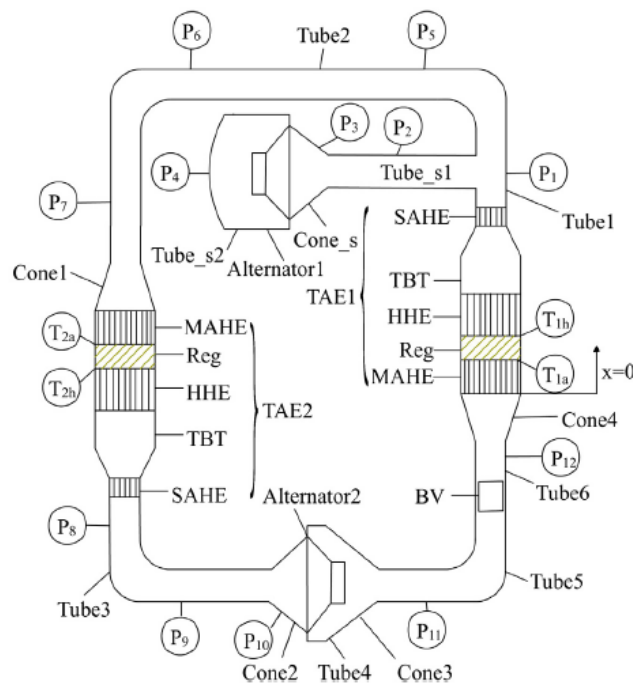


Figure 2. 23 Schematic drawing of the two-stage electricity generator

One of the multi-stage thermoacoustic electric generators that have been developed recently is the one that was designed, built and tested by Kang et al. (2015). Figure 2.23 shows a schematic drawing of the two-stage travelling wave electricity generator. This generator was designed using DeltaEC to be a combination of two thermoacoustic stages that are arranged in one loop of a travelling wave length. The novel design also includes a combination of two loudspeakers (represented as alternators) to convert the acoustic power produced into electricity.

One of these loudspeakers is located in the loop facing the acoustic power to suppress the Gedeon streaming that flows with the travelling wave. The other one is located at the end of a branched tube that has a length of about a quarter of the wave length and branched off the loop at a point close to a pressure anti-node. Besides that, the engine was also provided with a ball valve to tune the acoustic field in the loop. The engine was designed to be filled with helium as the working gas at 1.8 MPa mean pressure and to work at a working frequency of 171 Hz.

In the experiments the engine was firstly tested by supplying 1.5 kW of heat input (by electrical heater at the HHX) at each stage and by applying a load resistance of 10Ω at each loudspeaker. As a result and by adjusting the ball valve to reach the optimal opening at 10° , the generator produced 95 W of electricity in total from both alternators. Secondly after changing the heating power input of each stage to be varied from 1.5 kW to 3 kW, the maximum achieved heat-to-electrical efficiency was 3.43% with electricity output of 190 W whereas the maximum electricity output accomplished was 204 W with a thermal-to-electrical efficiency of 3.41%. It was concluded that an ordinary commercial loudspeaker can be used in a cost-effective electricity generator to produce electric power in the order of hundreds of watts.

2.7 Summary

In this chapter, a review of the theoretical, experimental and technical work and studies that are related to this study has been reported. The chapter began with a brief review of the history of thermoacoustics over the last two centuries. Next, the

significant dimensional and dimensionless scales in thermoacoustics were presented, as well as their impact on the performance of thermoacoustic devices. A short description of the classifications of thermoacoustic devices was introduced and the physics of each device was briefly illustrated. The linear thermoacoustic theory was shown as well as the main equations that control the thermoacoustic effects in stacks and regenerators and how DeltaEC computer software uses these equations to model and simulate a thermoacoustic device. Later, the chapter showed a concise description of the most relevant methods and tools of measurements that are utilized in thermoacoustics to measure acoustic power and acoustic pressure. Afterwards, a review of the electro-acoustic power transducers for converting acoustic power to electricity (or vice versa) was carried out. The chapter also showed the most commonly known types of acoustic streaming that usually arise in thermoacoustic devices causing harmful effects to the performance of these devices and how they can be suppressed or eliminated. Finally, there was a short review of the development of the some thermoacoustic devices revealing the reliability, simplicity and considerable performance of these devices.

In comparison, it can be seen clearly from the literature that most of the research's attention has been paid to developments of the travelling wave engines due to their simplicity and high efficiency. Therefore, they can be a very good choice in using thermoacoustics to produce electricity in remote and rural areas where there is no access to electrical grid. So far a number of researchers have achieved the design and building and study of multi-stage travelling wave generators (Chen et al., 2013; Wu et al., 2014; Bi et al., 2015). Most of these efforts have concentrated on improving the performance and to increase the thermal-to-electric efficiency using electro-dynamic high efficiency (but also very expensive) linear alternators. Furthermore, the essential point of designing these effective and efficient generators is to use the expensive noble gases and to pressurize the system to several of megapascals. This requires the use of thick and strong materials that can withstand high pressure, which adds costs to the budget of building the generators. Moreover, most of these studies used electric heaters as a hot heat exchanger to demonstrate and investigate the effect of the heating power which cannot be applicable in real applications. Therefore, there are several engineering and scientific points that should be addressed and investigated in this study. First of all,

the ability to use DeltaEC to design one-stage and two-stage travelling wave thermoacoustic electricity generators using an ordinary loudspeaker as a linear alternator. The second issue is the feasibility of designing and applying the components and parts that are used to build the generator in developing countries. Thirdly, the use of hot flue gases as the heating power source for the hot heat exchanger needs to be demonstrated to utilise cook stoves for electricity generation in rural areas. Fourthly, the measurements of heating input, heat rejected, pressure amplitudes and their phase angles, temperatures, acoustic power flow and electrical output. Finally, the debugging process to fix operational problems and improve performance of devices. As shown in the objectives of this study in Chapter one, there are three prototypes of travelling wave electricity generator and one prototype of looped tube thermoacoustic engine designed, developed and tested:

- 1- A 54-mm diameter resonator one stage looped-tube travelling wave thermoacoustic electricity generator (modified from previous project and tested/modelled as a competence building exercise).
- 2- A 128-mm diameter resonator diameter looped-tube travelling wave thermoacoustic engine.
- 3- A 128-mm diameter resonator diameter one stage looped-tube travelling wave thermoacoustic electricity generator.
- 4- A 128-mm diameter resonator diameter two-stage looped-tube travelling wave electricity generator.

Hopefully the prototypes presented in this study will contribute to the field of thermoacoustics and particularly in terms of delivering cheap electricity generators for remote and rural areas of developing countries.

CHAPTER 3

DESIGN, OPTIMISATION AND EXPERIMENTAL SET-UP OF THE PROTOTYPES INVESTIGATED

This chapter gives the details of designing, building and testing the prototypes of thermoacoustic devices studied in this work. The strategy of designing prototypes is discussed in section 3.1. Section 3.2 describes the DeltaEC model, the experimental set up and the instrumentation used in the measurements carried out for the prototype of the 54-mm diameter electricity generator. The conceptual design, the DeltaEC model and the experimental rigs developed in the pursuit of the large-size two-stage electricity generator are fully illustrated in section 3.3. In particular, section 3.3.1 deals with early work on the thermoacoustic engine with no electricity output; section 3.3.2 deals with issues of developing a large-scale single-stage device; finally, section 3.3.3 deals with the integration of the two-stage electricity generator. The chapter is summarised in section 3.4.

3.1 Design Strategy of Prototypes

As mentioned in Chapter one, the main goal of this study was to design a reliable, simple generator system that can be built using inexpensive materials available from the market. This generator is to use the widely available biomass fuel (e.g. wood) to produce cheap electricity for remote and rural areas of developing countries as a by-product of daily cooking activities. Based on this assumption, the looped-tube travelling wave thermoacoustic engine configuration was selected to demonstrate the technology.

According to the literature, this arrangement compared to the others is very efficient with the phase difference between the acoustic pressure and velocity being very low along the whole loop. However, the viscous losses that occur due to the long loop can cause acoustic dissipation. In order to overcome the viscous losses in the loop, the acoustic impedance of the thermoacoustic core must be much larger than the acoustic impedance in the feedback pipe (Yazaki et al., 1998). Therefore, the ratio of the cross sectional area of the thermoacoustic core (AHX, REG and HHX) to the cross sectional area of the feedback pipe must be much larger than 1.

The working frequency of the generators investigated here must be selected after consideration of several issues. Firstly, the working frequency should be near the resonance frequency of the alternator so the efficiency of the alternator is not significantly affected. Secondly, the increase in the frequency increases the power density in the loop, however and from Equation 2.3, the thermal penetration depth δ_k decreases as the frequency increases and accordingly there is less thermal contact between the gas the solid in the regenerator. Therefore, the working frequency after the optimisation was different for each particular prototype (but generally in the range 45 – 75 Hz).

Some of the acoustic power produced in the regenerator flows into the loop and is extracted into a branched-tube (the stub) to be converted into electric power by the alternator at the end of the branch. Although inserting the alternator in the loop to stop the acoustic streaming as a second function besides the main function of producing electricity would be beneficial, this arrangement may cause unnecessary disturbance of the acoustic field where there is high pressure drop caused by the alternator (Kang et al. 2015). Instead, the suppression of the acoustic streaming could be achieved by inserting an elastic membrane.

Although linear alternators have high efficiency, their prices are considerably high and they cannot be considered as part of a cost-effective electricity generator. In this case a low efficiency, but cheap and commercially available, ordinary loudspeaker is an appropriate candidate to replace the linear alternator. The working gas inside the generator is one of the critical issues to be taken into account regarding the low-cost generator; therefore the generator prototypes investigated here used air.

The mean pressure inside the loop is another critical point, where mean pressure is preferred to be as high as possible due to the fact that the power density is proportional to the mean pressure (Swift, 1988). However, any increase in the mean pressure (higher than 0.1 MPa) should be taken into account with consideration of the following two issues. Firstly, in Equation 2.3, any increase on the mean pressure leads to decreased δ_k/r_h in the regenerator and the HHX. This ratio can be increased in the regenerator by decreasing the hydraulic radius of the regenerator r_h since the regenerator is a number of stacked screens and they are

commercially available with very small r_h . In this case, care must be taken due to the very small hydraulic radius as they cause viscous losses and acoustic dissipation. However, it is quite challenging and expensive to fabricate the HHX with very small pores or channels. Secondly, increasing the mean pressure also requires a high pressure vessel which increases the cost of the generator. Therefore, and due to these reasons, the mean pressure inside the generator is kept at atmospheric pressure. Consequently, it is practical to use very cheap pipes and fittings made of PVC material in the acoustic connections of the loop of the generator. A side tube (the STUB) was branched off the loop to match the acoustic impedance between the engine core and the loop (Yu et al. 2012). It is a PVC pipe, around 1 m long, which has a piston that slides in the tube to change the volume inside the tube.

The heating power input into the HHXs of all prototypes is meant to be a demonstration of heat from a real cooking stove. In section 3.2, the heating power is absorbed from flue gas provided by a stove powered by propane gas as fuel. However, for safety reasons the heating power from flue gases is mimicked in the devices described in section 3.3 with a hot air "gun". More details will be presented in the following sections.

3.2 The 54-mm Diameter One-stage Looped-tube Travelling Wave Electricity Generator

The name given to this generator ("the 54-mm diameter") is due to the diameter of the feed-back pipe (FBP). This is the smaller version of the prototype, which was originally developed for the SCORE project. For this reason, the configuration of the heat exchangers, the regenerator hydraulic radius and porosity, the cross sectional area of the thermoacoustic core and the diameter of the FBP are to large extent fixed. However, previous work (Yu and Jaworski, 2012) focused on the so-called "in-line" configuration of the alternator, i.e. where it is installed in series within the engine. In the current approach some modifications were made to the acoustic network in order to place the alternator in the side branch of the main loop and develop new modelling capabilities related to this new configuration. These points will be discussed in detail in the next sections.

3.2.1 DeltaEC simulation

In the current work, DeltaEC is used to simulate the acoustic field and the acoustic power flow in the thermoacoustic generator under study. A block diagram of the system is shown in Figure 3.1. An x-co-ordinate is set up for the convenience of calculations and analysis of the system. Here, the right side of the ambient heat exchanger (AHX) of the thermoacoustic electricity generator (TAEG) is set as the origin of the co-ordinate ($x = 0$ m), while the positive direction is then pointing towards the regenerator (REG) as shown in Figures 3.1 and 3.2.

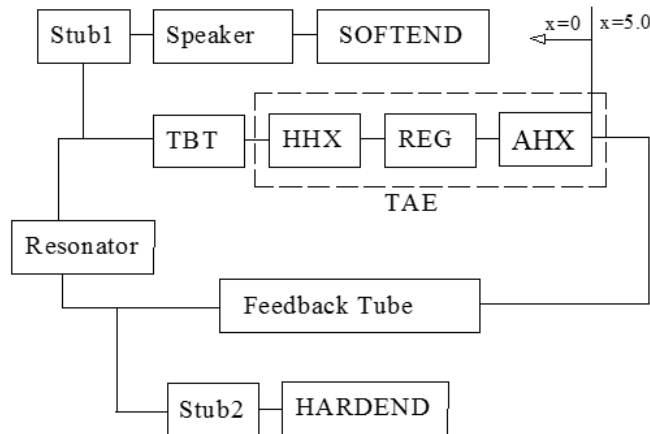


Figure 3. 1 The block diagram of the segments in the DeltaEC model: (1) ambient heat exchanger (AHX), (2) regenerator (REG), (3) hot heat exchanger (HHX), (4) thermal buffer tube (TBT), (5) the first stub where the speaker is located at the end (Stub1), (6) the tub

3.2.2 Experimental apparatus

According to the block diagram in Figure 3.1, the experimental set-up is shown schematically in Figure 3.2 whereas Figure 3.3 shows the embodiment of the generator in the experimental apparatus. Along the engine loop there are: ambient heat exchanger (AHX), stacked screen regenerator (REG), hot heat exchanger (HHX), thermal buffer tube (TBT), side branched alternator (ALT), side branched matching stub, and a feedback pipe. The total length of the loop is around 5.0 meters, the alternator side branch pipe is around 920 mm, and the side branch stub is around 450 mm, and the working frequency was around 64.5 Hz.

The regenerator was manufactured from stainless screen disks (110 mm in diameter), with the mesh number 34 and the wire diameter 0.16 mm. 72 discs were

piled up in a stainless steel can which has a wall thickness of 2 mm and the can is placed in the regenerator holder. The disks form a 23 mm long regenerator. Consequently, the calculated porosity and hydraulic radius are 83.3% and 198 μm , respectively. The porosity and the hydraulic radius of the regenerator were calculated using Equations 2.8 and 2.9 respectively.

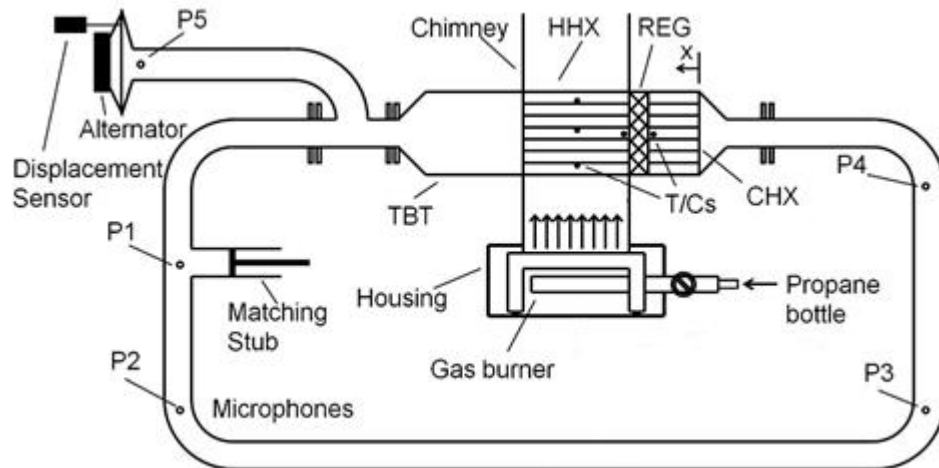


Figure 3. 2 Schematic drawing of the experimental thermoacoustic generator

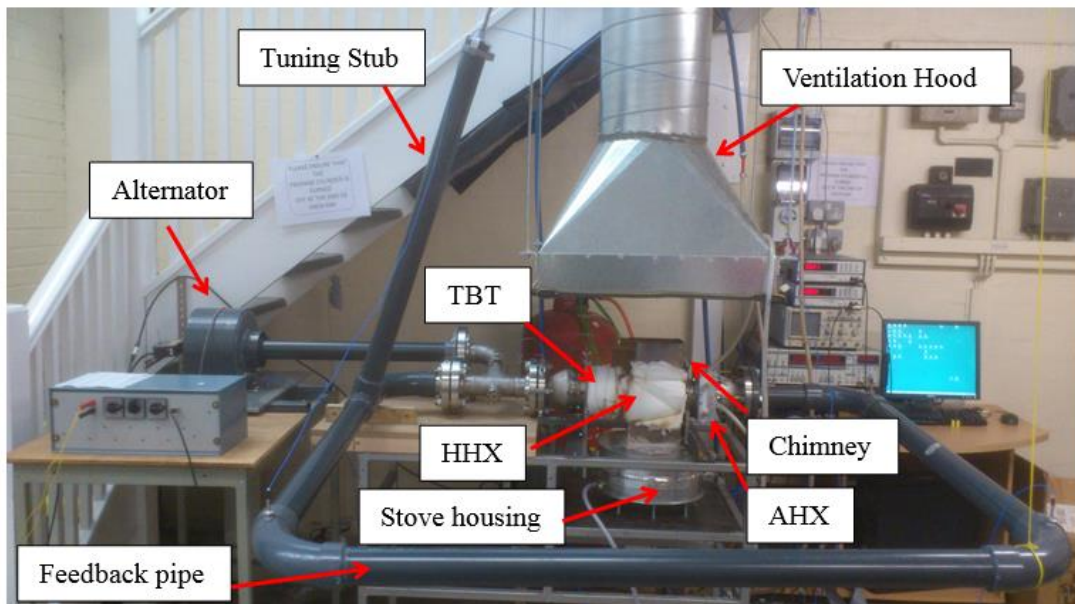


Figure 3. 3 Photograph of the thermoacoustic generator tested

The ambient heat exchanger (AHX) was made from an aluminum block, 60 mm long and has a 110 mm diameter. Gas passages are made in the form of 430 holes with a diameter of 3 mm, drilled parallel to the heat exchanger's centre-line.

20 holes with the diameter of 6 mm were drilled perpendicular to the heat exchanger axis to pass cooling water. The porosity of the cold heat exchanger was approximately 32%. Figure 3.4 shows a photograph of the ambient heat exchanger (AHX) of the generator.

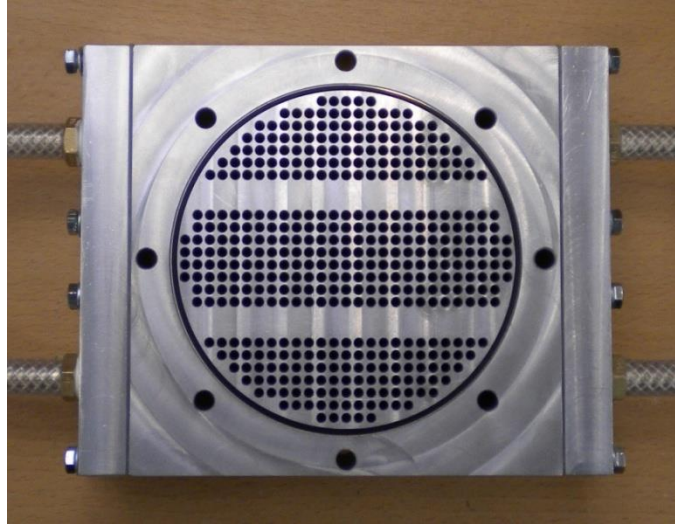


Figure 3. 4 The photograph of the ambient heat exchanger (AHX)

The hot heat exchanger (HHX) has a shell-and-tube configuration and is connected to the thermal buffer tube. It has a bundle of 37 stainless steel tubes. Each tube has an inside diameter of 8 mm, outside diameter of 10 mm, and a length of 160 mm. The centre-to-centre distance between two neighboring tubes is 15 mm on a triangular distribution. The porosity of the hot heat exchanger is about 19.6%. Using an adjustable valve the HHX is heated by a propane gas burner that had an adjustable heating power in the range of 0~5 kW. The flue gas from the gas burner flows around the outer surface of the bundle of tubes by natural convection and then out to the ventilation hood, while the working gas oscillates inside these tubes. Figure 3.5 shows a photograph of the hot heat exchanger connected to the thermal buffer tube on one side and to the regenerator holder on the other side. The configuration of the hot heat exchanger has been chosen as a compromise between the performance and ease of manufacture. Here it is hoped that welding 37 relatively large diameter tubes will be fairly easy to repeat in a “blacksmithing” workshop in remote rural areas.

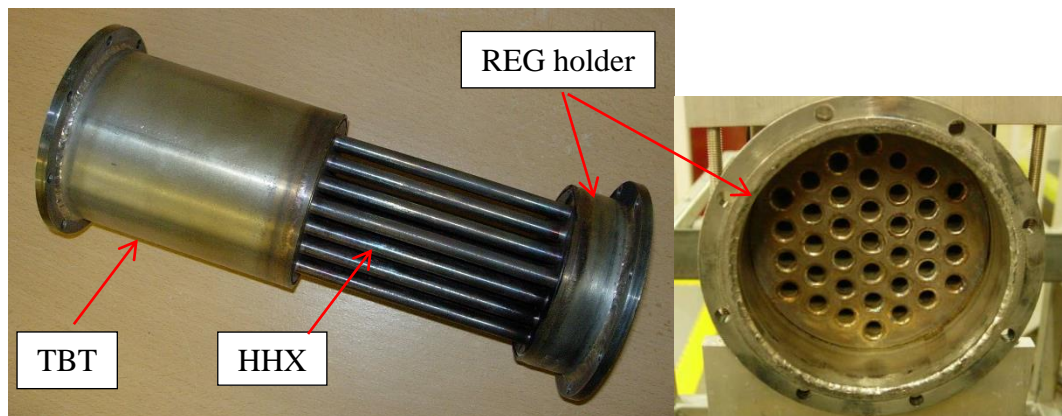


Figure 3. 5 Photograph of the hot heat exchanger (HHX), the thermal buffer tube (TBT) and the holder of the regenerator (REG).

As seen from Figures 3.2 , 3.3, and 3.5, after the hot heat exchanger, there is a thermal buffer tube, which is simply a section of stainless steel pipe (ID=110 mm) with a length of 178 mm, and a wall thickness of 2 mm. The 110 mm diameter buffer tube connects to a smaller thermal buffer tube via a short transition cone, which reduces the diameter from 110 mm to 54 mm over a distance of 54 mm. The small diameter buffer tube is around 160 mm long and has an internal diameter of 54 mm (a section of standard stainless steel 2-inch tube, with 2.77 mm wall thickness). To simplify the design, the thermal buffer tube is not thermally insulated, and therefore it can be cooled by the ambient air. A “T” section is connected to the thermal buffer tube as shown in Figures 3.2 and 3.3 using flanges. About 15 centimeters away from the end flange of TBT, a branch pipe is connected to the loop. The branch pipe is about 92 centimeters in length, and the alternator is installed at the end. A “stub” tube (450 mm in length) is connected to the resonator through another T-junction to improve the impedance matching between the branched alternator and the engine.

Part of the acoustic power produced is extracted by the branched alternator. Here, from the economic point of view, a standard audio loudspeaker, 8 inch B&C 8BG51 sub-woofer, was utilized as the alternator due to its relatively high transduction efficiency and low impedance according to the selection criteria summarized in (Kang et al., 2010). Table 3.1 shows the list of nominal and measured parameters of the loudspeaker.

Table 3. 1 Nominal and measured parameters of the loudspeaker (B&C speakers)

Parameter	Nominal	Measured	Standard Deviation
F (Hz)	52	39.77	± 1.1 %
Bl (N/A)	11.8	10.694	± 1.3 %
L_e (mH)	0.5	0.478	± 1.46 %
R_e (Ω)	5.1	5.3	± 0.14 %
M_m (g)	35	27.446	± 2.16 %
K_m (N/m)	3736	1725.544	± 2.2 %
R_m (kg/s)	0.93	1.364	± 3.19 %
X (mm)	+/- 6.5		
A_{alt} (cm ²)	220		

Here F is the loudspeaker resonance frequency, Bl is force factor, L_e is electric inductance, R_e is electric resistance, M_m is moving mass, K_m is stiffness, R_m is the mechanical resistance, X is diaphragm displacement, A_{alt} is the effective area of the loudspeaker. It should be noted that the measurements of the parameters of the loudspeaker were achieved after several hours' usage (Gomez-Meda, 1991). It can be found that the measured spring factor is much lower than the nominal one (Yu et al., 2011). This is due to the fact that the suspension has been softened after long time operation.

The remaining part of the rig is the feedback pipe, with a total length of 3.77 m. Because the engine is designed to operate with air at atmospheric pressure, the maximum pressure difference between the inside and the outside of the resonator corresponds to the acoustic pressure, which is usually less than 10 kPa. Therefore,

the feedback pipe is made of standard 54 mm inside diameter (2-inch) PVC pipe and 90° bends (Class E, OD: 60.3 mm, thickness 4.5 mm) instead of a metal pipe, to reduce costs.

3.2.3 Instrumentation and experimental procedure

As shown in Figure 3.2, five pressure transducers (microphones) have been installed and marked as P1 to P5. P1 to P4 were placed in the loop to measure the acoustic oscillations within the engine and the transducer P5 is placed near the end of (stub 1) to measure the amplitude and phase of the acoustic pressure in front of the loudspeaker. All of the pressure sensors are PCB PIEZOTRONICS model 112A2. They have a resolution of 7 Pa, and have been calibrated prior to the experiments. The sensors have been interchanged to double check their reliability. A laser displacement sensor (Keyence LK-G152) is installed at the back of the speaker to measure the displacement of the speaker diaphragm. It has a stand-off distance of 150 mm and a measuring range of ± 40 mm. The sampling frequency was 50 kHz and the resolution was 0.5 μm . Two Type-K thermocouples (TC-Direct model 408-119) are installed near the centre line of the thermoacoustic core at the two ends of the regenerator. They measure the temperature difference between the hot end and the ambient end of the regenerator as shown in Figure 3.2. Additionally, three Type-K thermocouples were placed vertically in three tubes of the HHX to monitor the solid temperature of the tube wall at the bottom, the centre and the top of the HHX and the approximate positions of these thermocouples are schematically shown in Figure 3.2. The output signals of the pressure transducers are passed through a three-channel, ICP(R) sensor signal conditioner (Model 480B21) with x1, x10, and x100 gain outputs, to amplify the RMS values of pressure signals. A data acquisition card (OMEGA OMB-Daq Temp Model 14) is used to record the amplified signals of the pressure traducers and signal outputs of all thermocouples with an accuracy of 0.01°. Using a designed LABVIEW programme, all data recorded by the acquisition card, including the phase difference between the pressure signals, are recorded.

Using the two-microphone method (Swift, 2002) presented in section 2.3, the measurements of pressure amplitudes and their phases from P1 and P2 can estimate the acoustic power flow to the feedback pipe, whereas the measurements from P3 and P4 can estimate the acoustic power flow back to the cold heat exchanger.

Furthermore, using the piston and loudspeaker method shown in section 2.3, the acoustic power extracted by the alternator can be estimated by the laser displacement sensor and microphone P5. A high power variable resistor is adopted as an electrical load for the alternator to extract electrical power. The voltage difference and the current flowing through the load resistor are measured using a standard voltmeter (with a resolution of 0.001 V) and ammeter (with a resolution of 0.01 A).

In the experiments with the burner located in a housing at the base of the HHX, there is no way to measure the hot flow rate of flue gases that is caused by the natural convection. Therefore for measuring the heat flux, a special design of an orifice flowmeter at the bottom of the housing may be considered. At this stage of experiments with a real cooking stove demonstration, this special design is not taken into account. The resistance of 12 Ω is connected to the speaker as a load to consume the electric power produced. If the control valve is slightly open and the burner is ignited, the temperatures inside the HHX and the hot end of the regenerator started to rise from ambient to higher values. When the temperature gradient in the regenerator reaches a certain value, enough to overcome the viscous resistance, the oscillation is initiated. When the acoustic oscillation starts the generator, the acoustic power produced flows into the FBP. Part of the acoustic power enters the branch where is the loudspeaker is located and the loudspeaker starts to vibrate. As a result, the electrical power extracted by the load resistor is deduced. The rest of the acoustic power flows in the loop back to the AHX. Once stable temperature values are reached, all measurements of pressure amplitudes and phases, temperatures, laser displacement readings and electrical output readings are recorded. This procedure was repeated at several high temperatures of the HHX with an interval of around (50-60 °C) each. The maximum temperature recorded at the bottom of the HHX was 627.4°C. The comparison between the calculated and measured results is shown in Chapter 4.

3.3 Experimental Setup and Models for The 128-mm Diameter Travelling-wave Prototype Devices

This section is intended as an overview of the experimental setups and DeltaEC models of devices in the second strand of the current research devoted to the large-scale two-stage generator. As already explained in the objectives of the work, due to the complexity of the problem, somewhat simpler devices were developed before reaching the final prototype. These include a single-stage engine (section 3.3.1) and a single-stage generator (section 3.3.2). However, to avoid the duplication in the description of some common components in all three configurations, they will be described only once – namely in the final section 3.3.3 to give the full flavour of the final experimental. This in particular concerns the hot heat exchanger, which was designed as a “twin” heat exchanger in a single unit due to the fabrication costs. The same hot heat exchanger was therefore used in the work described in all sections 3.3.1 through to 3.3.3 – however for single-stage devices only one heat exchanger in the “twin” configuration would be used. Similar comments can be made regarding the use of a car heat exchanger matrix for the ambient heat exchanger in all three configurations.

3.3.1 One-stage Looped-tube Thermoacoustic Engine

The initial and simplest configuration considered was the one-stage looped-tube engine. Here, the main idea is to generate the acoustic power in the loop, which would be dissipated by friction in the loop itself. The important tests would regard finding the best operating frequency, location and length of the matching stub, and any potential problems generated by Gedeon streaming if present. At this stage extraction of electrical power was not regarded important. Instead, the level of acoustic power circulating in the loop was used as an indicator of performance.

A. DeltaEC simulation

The block diagram of the system is shown in Figure 3.6. Here, the right side of the ambient heat exchanger (AHX) of the thermoacoustic electricity generator (TAEG) is set as the origin of the co-ordinate ($x = 0$ m), while the positive direction is then pointing towards the regenerator (REG), the hot heat exchanger (HHX) and the thermal buffer tube (TBT). At the branch, the matching stub is located whereas

the rest of the loop is the feedback pipe that is connected to the AHX at ($x = 6.4$ m) as shown in Figures 3.6 and 3.7.

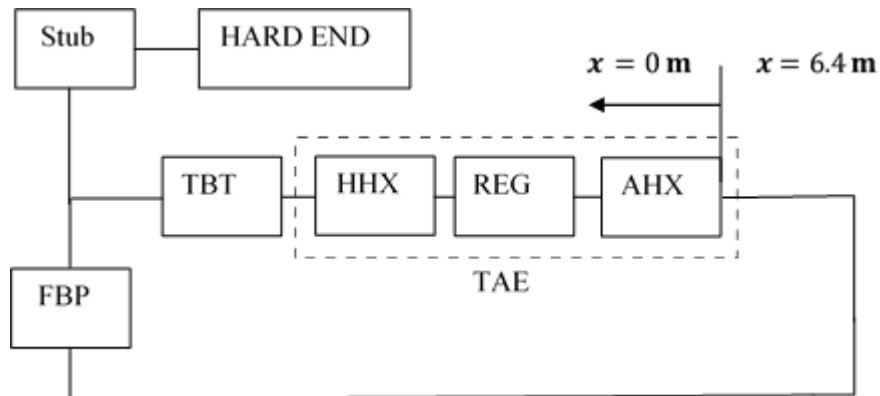


Figure 3. 6 A block diagram of the single stage 128-mm diameter thermoacoustic engine.

B. Experimental apparatus

The 128-mm diameter single stage engine shown in Figure 3.7 and the photograph in Figure 3.8 is a combination of the thermoacoustic core presented in detail later in section 3.3.3 and 128-mm diameter PVC piping forming a loop and a side branch matching stub.

The distribution of thermocouples follows the same outline as described in section 3.3.3. However, there are six pressure sensors (P1-P6) distributed along the loop to measure the acoustic power flow. The pressure sensor (P6) is placed close to the thermoacoustic core to estimate the pressure drive ratio of the engine. There is also a flexible membrane inserted to suppress the acoustic streaming (when it proved to be a problem at the debugging stage) and it is placed close to the velocity node of the loop. Using the experimental instrumentation described in detail in 3.3.3 experimental work was performed on this engine to include the effect of the stub length on the performance of the engine. Results of these experiments are presented in Chapter 4.

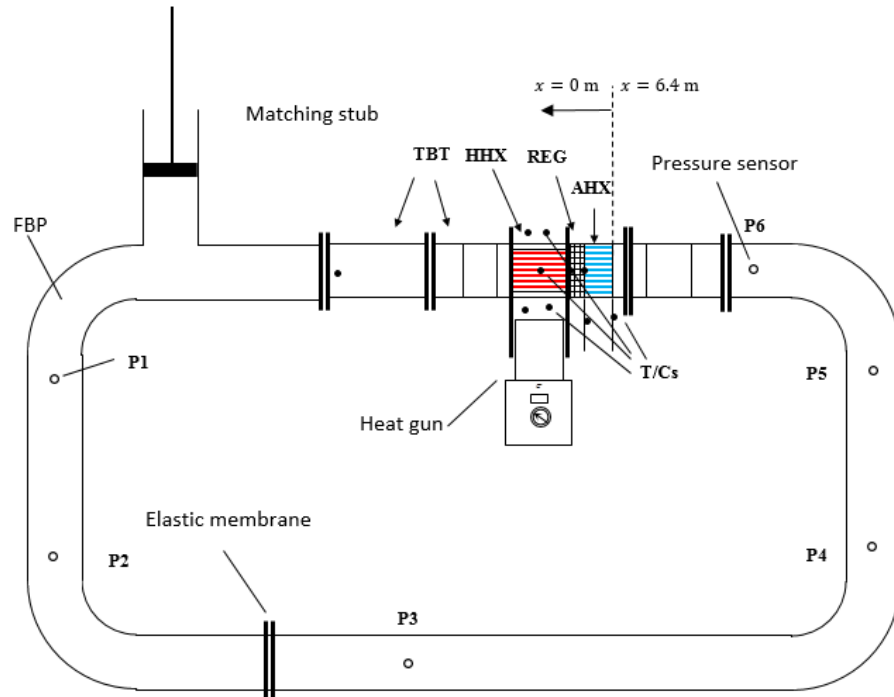


Figure 3. 7 A schematic diagram of the single stage 128-mm diameter thermoacoustic engine.

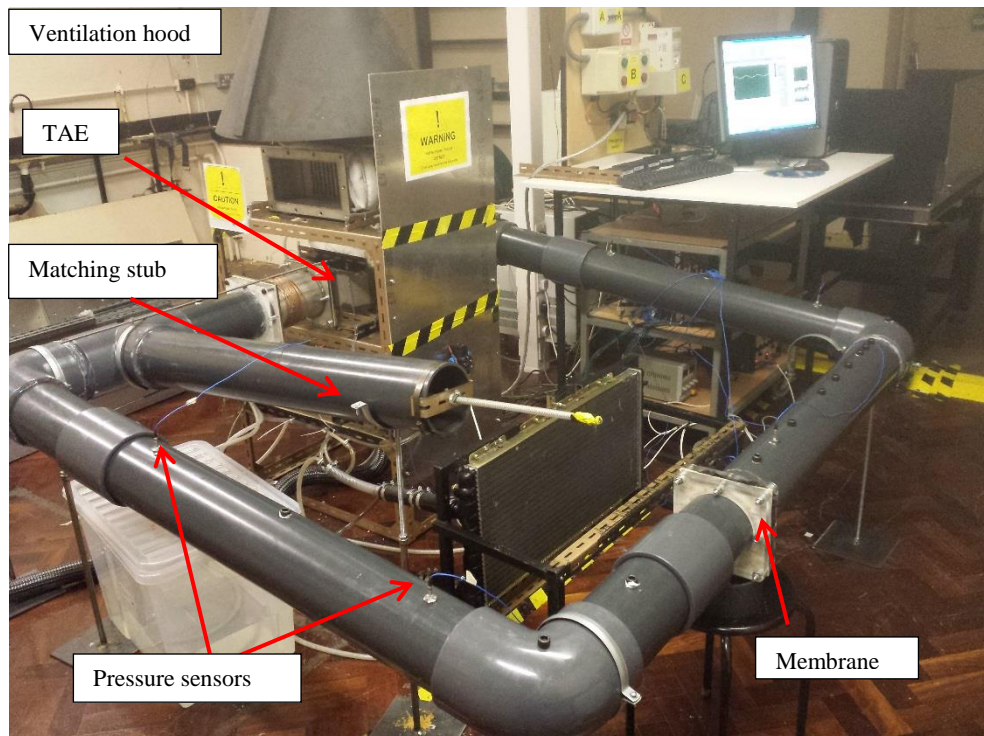


Figure 3. 8 Photograph of the experimental apparatus of the single stage 128-mm diameter thermoacoustic engine.

3.3.2 One-stage Looped-tube Electricity Generator

The one-stage electricity generator is based on using just one of the “twin” hot heat exchangers and a PVC loop with an alternator connected through a branch from the main loop. The main idea behind this investigation is to understand the best topology (of a single-stage type) for generating useful electricity, whilst also investigating the effects of resistive loading and heating power. Using the experience from the single-stage engine, the Gedeon streaming is tackled in an analogous way.

A. DeltaEC simulation

DeltaEC was used to simulate the acoustic field and the acoustic power flow in the 128-mm diameter single-stage thermoacoustic generator. A block diagram of the system is shown in Figure 3.9. An x-co-ordinate is set up for convenience of calculations and analysis of the system. As before, the right side of the ambient heat exchanger (AHX) of the thermoacoustic electricity generator (TAEG) is set as the origin of the co-ordinate ($x = 0$ m), while the positive direction is then pointing towards the regenerator (REG), the hot heat exchanger (HHX) and the thermal buffer tube (TBT). At the branch, there is a stub for the loudspeaker whereas the rest of the loop is the feedback pipe that is connected to the AHX at ($x = 5.9$ m) as shown in Figures 3.9 and 3.10.

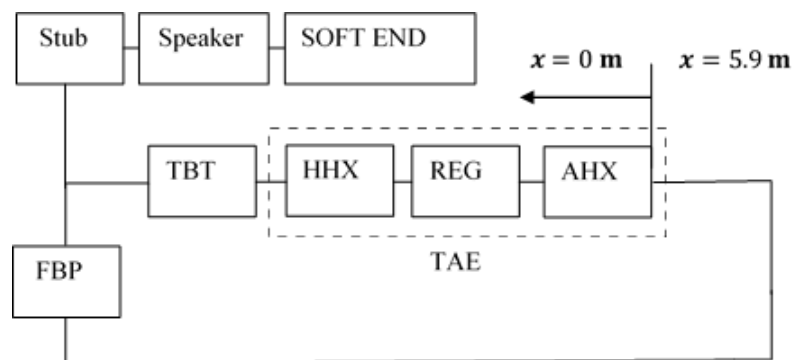


Figure 3. 9 A block diagram of the single stage 128-mm diameter electricity generator.

B. Experimental apparatus

The 128-mm diameter single-stage generator uses one of the “twin” hot heat exchangers in a similar way as in the single-stage engine. The ambient heat

exchanger, the regenerator, the hot heat exchanger, the thermal buffer tube and the 128-mm diameter PVC pipe as feedback pipe remain practically the same. However, there is no matching stub as such because the optimisation of this generator introduced a 54-mm diameter pipe connected between the speaker and the 128-mm diameter (stub) pipe to match the acoustic impedance, as can be seen in Figure 3.10 and the photograph in Figure 3.11. The distribution of thermocouples follows the same philosophy as for the single-stage engine. However, there are five pressure sensors (P1-P5) distributed along the loop to measure the acoustic power and one pressure sensor (P6) located at the front of the loudspeaker to measure the pressure amplitude and phasing at the loudspeaker. The displacement sensor is located at the back face of the loudspeaker to measure the displacement of the loudspeaker diaphragm. There is also a flexible membrane inserted to suppress the acoustic streaming and it is located close to the velocity node of the loop. Using the experimental instrumentation described later in detail in section 3.3.3, experiments were conducted to include the effect of the load resistance connected to the loudspeaker and the effect of changing heating power on the generator performance. Results of these experiments are presented in Chapter 4.

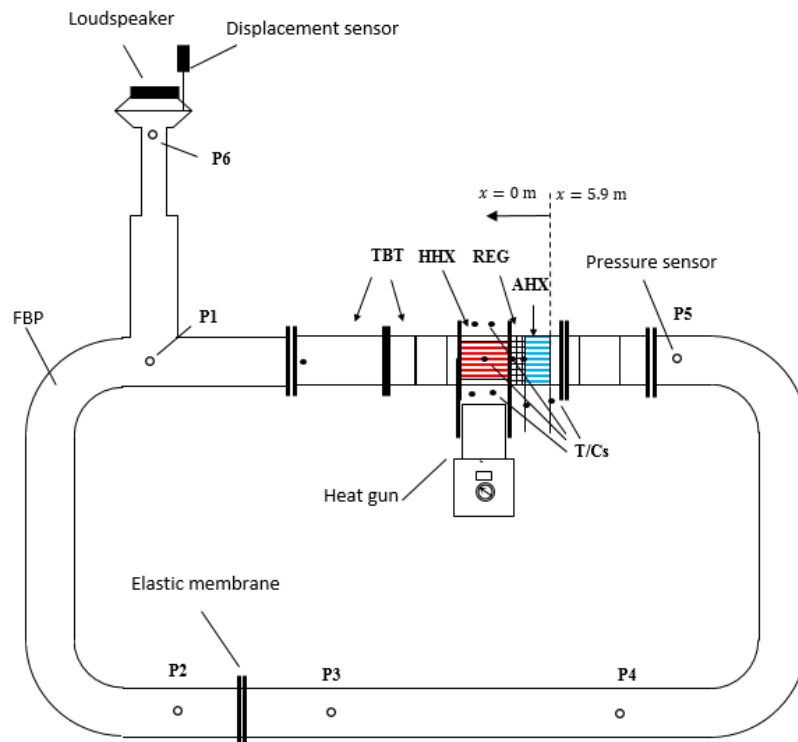


Figure 3. 10 A schematic diagram of the single stage 128-mm diameter electricity generator.

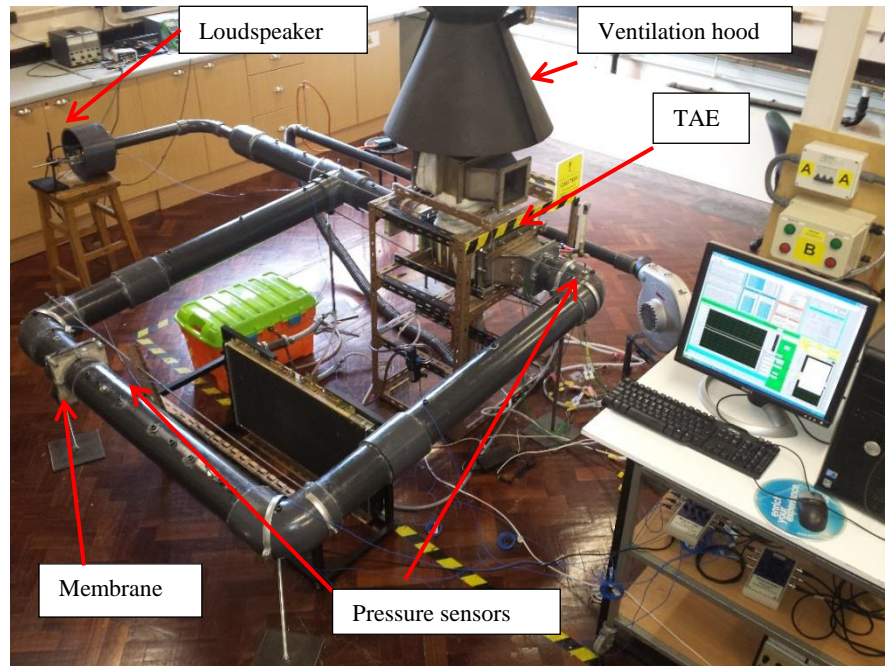


Figure 3. 11 Photograph of the experimental apparatus of the single stage 128-mm diameter electricity generator.

3.3.3 Two-stage Looped-tube Electricity Generator

The principle of the configuration of a two-stage generator is similar to the concept of the one stage generator described in section 3.3.1. They share the same concept of one wave length of travelling wave device. The difference here is the introduction of a second stage that shares the same resonator length. In order to introduce heat to the core of the second stage, the second hot heat exchanger of the “twin” unit is utilized. The goal of adding a second stage was to increase the acoustic power produced in the loop and subsequently the electrical output.

A. Design and optimisation procedure

Before using DeltaEC to design and simulate the generator, some points regarding the design were taken into account. In addition to the design strategy discussed in section 3.1, here issues are highlighted regarding the ambient and hot heat exchangers that reduce the total cost of the generator.

1. For the AHX, a car heater matrix can be a replacement for expensive purpose-made heat exchangers (such as that shown in Figure 3.4). These heat exchangers are low-cost and commercially available. Moreover, their fin-and-tube configuration allows high porosity and high surface area per unit volume to be obtained which increases the effectiveness of the heat exchanger. Eventually, the aluminium-made car heater matrix of the Land Rover Freelander (1997 model) was selected due to its low price, and high efficiency (high porosity and large heat transfer area).
2. The shell-and-tube configuration (such as shown in Figure 3.5) was conceptually modified to further decrease the manufacturing costs if the unit was to be made in large volumes. This was done by introducing the “flattened pipe” heat exchanger. This is based on flattening stainless steel pipe by simple “blacksmithing” methods to provide high aspect ratio channels thus decreasing their hydraulic radius and increase the heat transfer area between the flue gas and oscillating gases inside the thermoacoustic loop, as well as to increase the porosity of the HHX.

The two-stage electric generator includes two identical thermoacoustic cores that produce acoustic power delivered to one acoustic-to-electric transducer (loudspeaker). The loudspeaker is located in a branched tube (stub 1) just after the first stage. The block diagram of the two-stage generator is presented in Figure 3.12. As shown in the diagram, the loop also includes a second branch for the matching stub. In order to achieve the modelling of one wave length travelling wave system with two branches using DeltaEC, a number of boundary conditions must be defined.

The acoustic pressure amplitude $|p_1|$, the phase of the pressure (phase (p_1)), the volumetric velocity amplitude $|U_1|$, the phase of the volumetric velocity (phase (U_1)) and the total power \dot{H} at the starting point of the loop “BEGIN segment” ($x = 0$ m) must be respectively equal to the same parameters downstream at the end of the loop ($x = 6.3$ m):

$$|p_1|_{x=0 \text{ m}} = |p_1|_{x=6.3 \text{ m}} \quad (3.1)$$

$$(\text{Phase } (p_1))_{x=0 \text{ m}} = (\text{Phase } (p_1))_{x=6.3 \text{ m}} \quad (3.2)$$

$$|U_1|_{x=0 \text{ m}} = |U_1|_{x=6.3 \text{ m}} \quad (3.3)$$

$$(\text{Phase } (U_1))_{x=0 \text{ m}} = (\text{Phase } (U_1))_{x=6.3 \text{ m}} \quad (3.4)$$

$$\dot{H}_{x=0 \text{ m}} = \dot{H}_{x=6.3 \text{ m}} \quad (3.5)$$

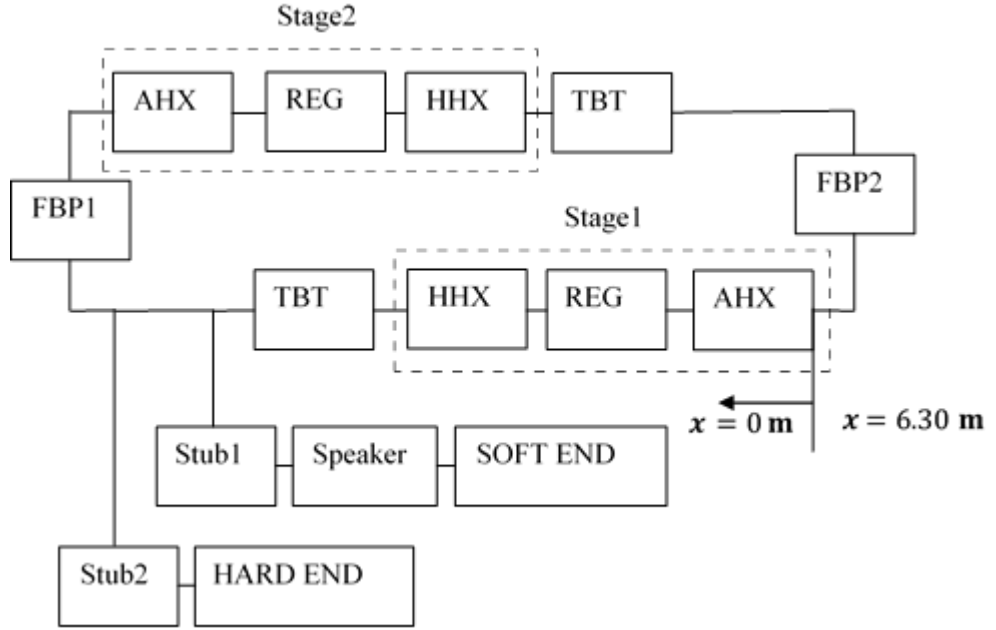


Figure 3. 12 The block diagram of the two-stage thermoacoustic electricity generator.

At the junction point of the oscillating flow of the first branch (stub1), the volumetric velocity of the trunk splits into two streams as:

$$|U_1|_{trunk} = |U_1|_{stub1} + |U_1|_{FBP1} \quad (3.6)$$

However, at the split-up point, the pressure amplitude and temperature are the same:

$$|p_1|_{Trunk} = |p_1|_{Stub1} = |p_1|_{FBP1} \quad (3.7)$$

$$T_{Trunk} = T_{Stub1} = T_{FBP1} \quad (3.8)$$

The soft end of the (stub 1) is represented by the acoustic impedance at the back of the loudspeaker being zero:

$$z = \frac{|p_1|}{|U_1|} = 0 \quad (3.9)$$

Similarly, the conditions for the (stub 2) are identical to (stub 1). However, the hard end is represented by the inverse of acoustic impedance being equal to zero:

$$\frac{1}{z} = \frac{|U_1|}{|p_1|} = 0 \quad (3.10)$$

The solid temperatures of the AHXs are assumed to be fixed at 300 K which matches the average of the cooling water temperature, whereas the flue gas temperature at the HHXs is assumed to be fixed at 800 K. The working frequency of the system is assumed to be variable and it is controlled by the dimensions of the loop and the other parts in the generator.

Because the dimensions of the AHX are fixed and cannot be changed, and because it is contained in the cavity where the regenerator is located, the size of the thermoacoustic core has to be within the boundaries of the AHX. The hydraulic radius of the stacked screen regenerator is assumed to be very small according to the condition ($\delta_k/r_h \gg 1$) whereas the porosity is assumed to be 0.7 which is an average of the mesh screen available on the market. The applicable porosity for the HHX is between 0.1 and .5 and .25 was chosen to be the initial porosity for the simulation. The working gas is air at atmospheric pressure. Table 3.2 shows the configuration of the main components for each stage in the system.

Table 3. 2 The configuration of the main parts of each stage in two-stage generator

Component	Configuration
Ambient heat exchanger (AHX)	Fin and tube heat exchanger (car heater matrix)
Regenerator (REG)	Stainless steel mesh screen
Hot heat exchanger (HHX)	Stainless steel Shell-and-tube
Feedback pipe (FFP)	PVC pipe

After setting the boundary conditions according to the above equations (cf. Figure 3.12), the process of solving the linear thermoacoustic equations for the whole system was initiated by guessing the solutions that meet the targets, as illustrated in section 2.2.3. The guesses that meet the targets are found by the use of the shooting method (Press et al., 1992). The convergence of calculations is achieved once all guesses are consistent with targets. At this point of the simulation, the level of the calculated electrical output is low due to the need of optimising the model.

Further optimisation of each dimension in all components increases the predicted output of electricity. This is performed by increasing and decreasing the dimension of each component individually in order to find the optimal value that increases the electrical output. The main parameters that were under optimisation are the hydraulic radius, porosity and the length of the regenerator and the HHX and the diameter of the FBP. However, the AHX and the cross sectional area of the thermoacoustic core including the regenerator and the HHX are excluded from the optimisation because they are subject to the AHX dimensions as well as pre-manufactured “twin” hot heat exchanger unit. When the extracted electric power is at maximum value, the optimisation is completed and the optimal dimensions are considered.

Although the optimisation process eventually obtains the optimal value of each parameter, the optimal values of some parameters cannot be utilised in the system due to technical and manufacturing issues and also due to the availability on the market. For example, the HHX have higher performance at larger porosity and smaller hydraulic radius, but it is challenging to manufacture a heat exchanger with these features. In addition, standard PVC pipes have specific sizes and it may be difficult to find a diameter that matches the optimal value obtained from the calculations. It is also challenging to find a stainless steel mesh screen that has the optimal porosity compatible with the optimal hydraulic radius. Therefore, matching between the optimal values of the parameters and the availability would be compromised. Finally, the heat exchangers, the regenerators and the thermal buffer tube are assumed to be well insulated where heat exchange between the system and

the environment only exists through the heat exchangers. Strictly this cannot be guaranteed.

B. Optimisation results

Before presenting the results of the optimisations that determine the final dimensions of the optimised parameters, it is interesting to look at the sensitivity of each parameter and its effect on the electric power produced. As the electrical output is proportional to the acoustic power generated in the two stages, the results shown below are related to the electric power output as a function of the optimised parameter.

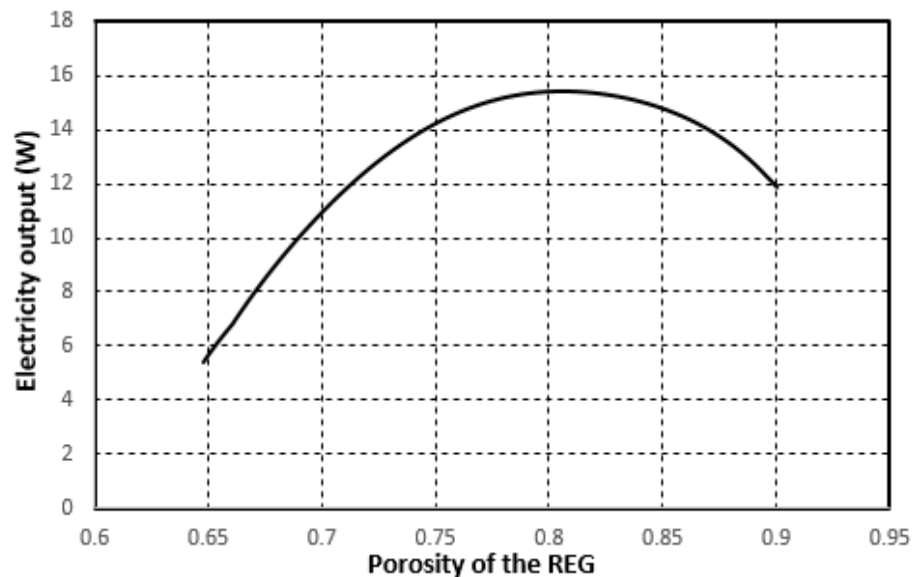


Figure 3. 13 Impact of the porosity of both regenerators on the electrical output.

According to the literature, the regenerator is considered the heart of the thermoacoustic device and thus it has the highest impact on the performance of travelling wave devices. The optimisation of the regenerator in this simulation included the porosity, the hydraulic radius and the length of both stages. The sensitivity and significant impact of optimising the porosity of the regenerator on the electrical output is shown in Figure 3.13. As the porosity increases from 65% to 80%, the electrical power output rises from 5 W to 15.5 W. However, any further increase in the porosity will decrease the electrical power to reach 12 W at a porosity of 90%. The increase in power is attributed to the increase in the volumetric

velocity when the porosity is increased as seen in Equation (2.40). However, further increases in porosity beyond the optimum point will increase the compliance in the regenerator which leads to a decline in the displacement of the gas parcels and, in turn, the power is reduced.

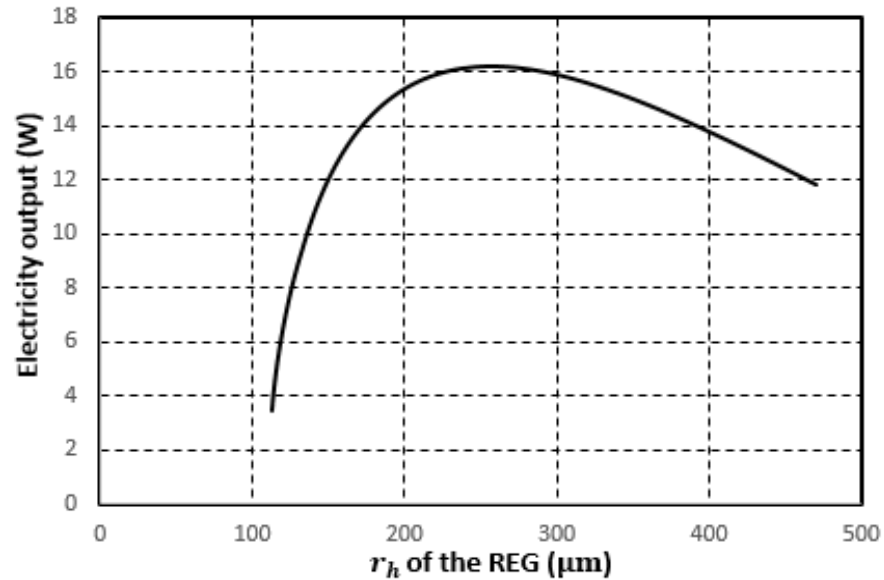


Figure 3. 14 Effect of the hydraulic radius of the regenerator on the electrical output.

The hydraulic radius of the regenerator is the most sensitive and critical parameter of the regenerator. Obviously, it is the measure of the strength of the thermal contact between the oscillating gas and the solid material of the regenerator. Therefore, any increase or decrease in the hydraulic radius impacts on the performance of generating acoustic power. Thus, optimisation of this parameter increases the performance significantly as seen in Figure 3.14. According to the literature, the hydraulic radius should be at a value where the thermal penetration depth is ($\delta_k/r_h \gg 1$) for travelling wave mode. This will increase the temperature difference across the regenerator which increases the acoustic power and, in turn, increases the electric power output. However, when the hydraulic radius is too small, there will be considerable viscous losses that dissipate the acoustic power in the regenerator. On the other hand, the large hydraulic radius reduces the thermal contact between the oscillating gas particles and the regenerator material. In Figure 3.14 the optimal hydraulic radius of the regenerator is 245 μm .

The length of the regenerator also has a major impact on the performance of the engine. Figure 3.15 presents the effect of increasing the length of the regenerator on the electrical output of the generator. It can be seen from the graph that the electric power increases from 6 W at a length of 5 mm to reach the optimum value of 15.5 W at a length of 30 mm. However, it drops to 12 W of electrical output where the length of the regenerator is 75 mm. The increase in the regenerator length will lead to an increase in the temperature difference between its two ends. As a result, the amplifying ratio of the hot temperature to the ambient temperature (T_h/T_a) will increase and result in the higher acoustic power production. However, a further increase in the regenerator length will decrease the temperature gradient due to the limitation of the heating temperature that results in weaker acoustic power amplification. Actually, there are many complicated different effects working together in this aspect. Additionally, further increasing of the regenerator length will cause acoustic dissipation because of the viscous loss.

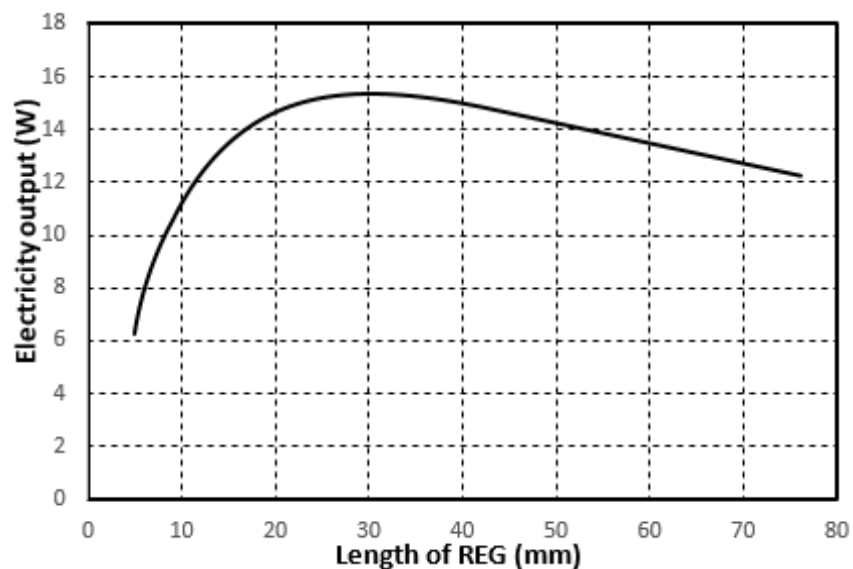


Figure 3. 15 Impact of the length of the regenerator on the electrical output.

The hot heat exchanger is a very important part of the system and is the component that delivers heating power to the thermoacoustic core of the engine. All parameters of the HHX need to be optimised because they have significant effects on the performance of the engine. The porosity of the hot heat exchanger is optimised as shown in Figure 3.16. From the graph it is seen that the increase of the porosity has a positive effect on the electricity extracted from the loudspeaker. The

increase in porosity raises the heat transfer area available to the oscillating gas inside the HHX by increasing the number of channels and eventually leads to increased generation of the acoustic power. In addition, this involves reduction of the oscillating velocity which reduces the viscous effects inside the channels of the heat exchanger. The optimal porosity of the hot heat exchanger is found to be at values higher than 70%.

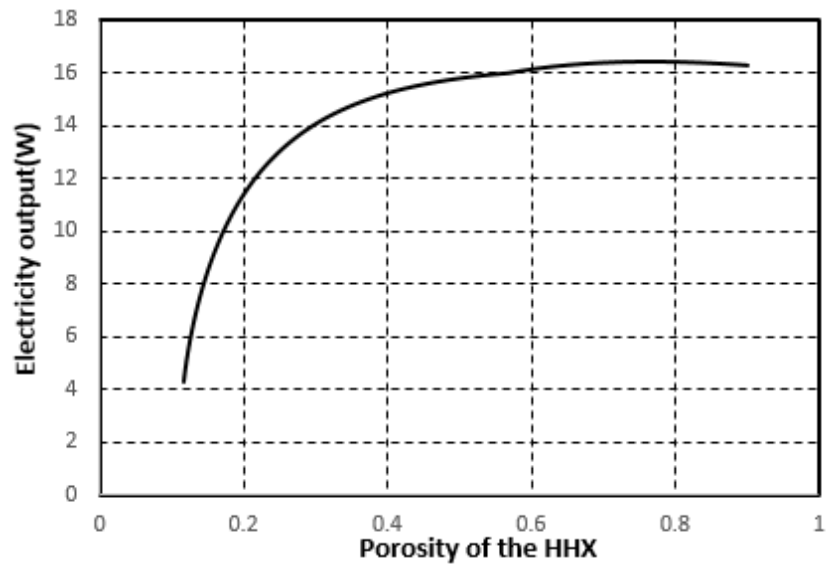


Figure 3. 16 Effect of porosity of the hot heat exchanger on the electrical output.

Among the parameters that were optimised, the hydraulic radius of the HHX was also included. The importance of the hydraulic radius is that it measures the thermal contact between the gas particles and the solid wall of the channel. Figure 3.17 presents the effects of changing the hydraulic radius of the HHX on the electrical output of the generator. As shown in the graph, the optimal value of the hydraulic radius is 3 mm. It is obvious from the graph that at lower hydraulic radius values, the generator produces less electric power. This is due to the viscous effects that increase at lower hydraulic radius. On the other hand, the electrical output also decreases when the hydraulic radius is increased at values higher than 3 mm. This is because the degree of thermal contact is reduced and consequently less heating power is transferred to the oscillating gas.

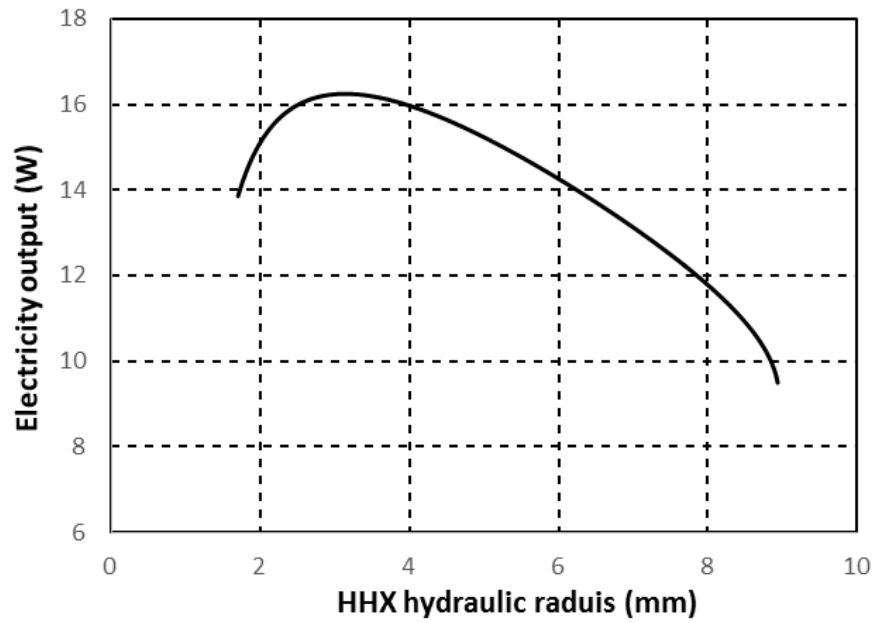


Figure 3. 17 Effect of the hydraulic radius of the hot heat exchanger on the electrical output.

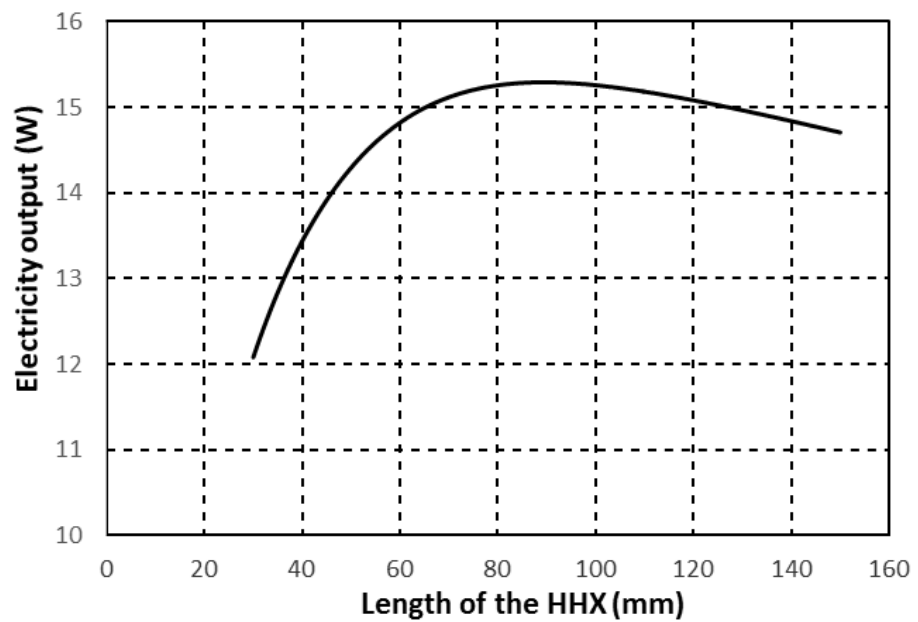


Figure 3. 18 Effect of the length of the hot heat exchanger on the electrical output.

The other parameter that influences the generation of the electric power is the length of the hot heat exchanger. In order to obtain optimal heat exchange between the oscillating gas parcels and the solid walls of the heat exchanger, the peak-to-peak displacement amplitude of the gas parcels should be equal to the total length of the heat exchanger (Swift, 2002). In this context, and as is seen in Figure 3.18, when

the length increases from 30 mm to 95 mm, the electrical output increases from 12 W to 15.5 W. However, increasing the length above 95 mm, reduces the electrical output due to viscous losses.

Figure 3.19 shows the effects of the cross sectional area of the feedback pipe on the electrical power production. It can be seen from this graph that as the cross sectional area of the feedback pipe increases, the electrical output reaches its maximum and then decreases. The maximum electrical power output is obtained at a diameter of 123 mm. The significant effect of the feedback pipe cross sectional area can be attributed to the fact that the change in its cross sectional area changes the acoustic impedance distribution along the loop. As discussed above, the cross sectional area ratio between the thermoacoustic core and feedback pipe is designed to be much bigger than 1, so that the local acoustic impedance in the regenerators can be higher to avoid the acoustic losses within the regenerator. On the other hand, the feedback pipe needs to have a cross sectional area large enough to transport the acoustic power through it. As a result, the trade-off between these two effects will lead to certain optimal value as shown in Figure 3.19.

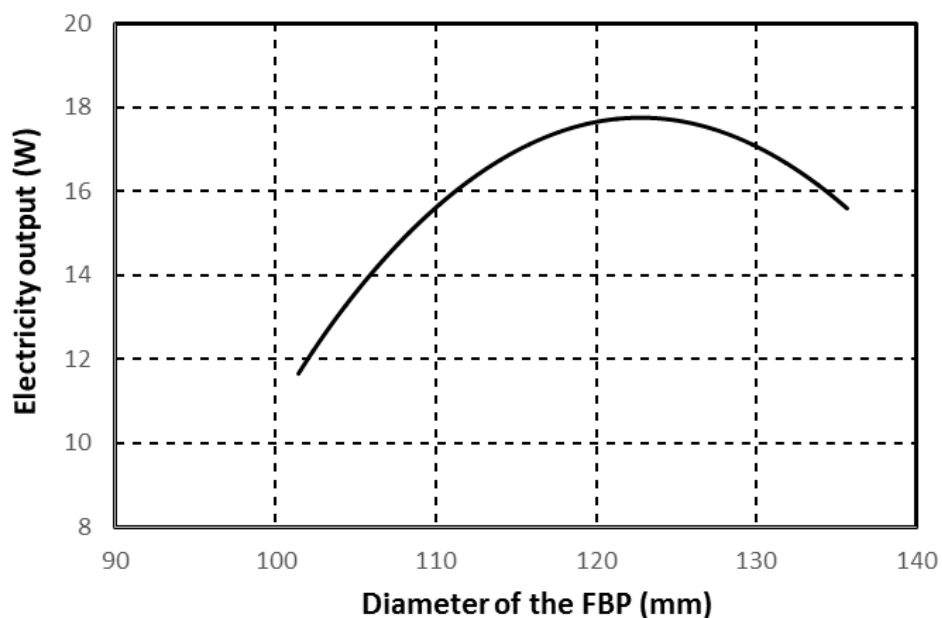


Figure 3. 19 Effect of the diameter of the feedback pipe on the electrical output

Table 3. 3 Optimal values of the optimised parameters

Component	Optimal value
Ambient heat exchanger	Not optimised
Regenerator <ul style="list-style-type: none">• Length• Porosity• Hydraulic radius	30 mm 80% 245 μm
Hot heat exchanger <ul style="list-style-type: none">• Length• Porosity• Hydraulic radius	84 mm 60% 3 mm
Feedback pipe diameter	123 mm

After finishing the DeltaEC modelling of the electricity generator and optimising the main parameters as presented in the above figures, the working frequency was 50.23 Hz and the optimal values are tabulated in Table 3.3. Consequently, the parameters of the actual components of the experimental apparatus need to be obtained based on these optimal values.

C. Experimental apparatus

When optimisation of the model was completed and the final optimal dimensions of all parameters were obtained, the final values were used to build the experimental set-up. For economical and practical reasons, some components were selected at standard sizes close to the optimal dimensions. These parts are stainless steel screens for the regenerator and the PVC pipe for the feedback pipe. The final

configuration of the hot heat exchanger could not follow the optimal size from the simulation. This was due to the difficulty in matching the optimal porosity and hydraulic radius. Therefore, a trade-off was set between the two parameters. The practical configurations of the components are illustrated in this section.

94 layers of the rectangular shape mesh screens forming the regenerator (Figure 3.20) were manufactured from stainless steel wire mesh with mesh number 34 and the wire diameter of 0.16 mm. Between the AHX and the HHX, the 30 mm long regenerator was piled up in the stainless steel channel which has a wall thickness of 2 mm. Consequently, the calculated porosity and hydraulic radius are 83.3% and 198 μm , respectively. The porosity and the hydraulic radius of the regenerator were calculated using Equations (2.8) and (2.9) respectively.



Figure 3. 20 The photograph of rectangular cuts of the stainless steel screen of the regenerator

For economical and practical reasons as mentioned earlier, a car heater matrix is used as an ambient heat exchanger. At this stage, the car heater matrix of a Land Rover Freelander (1997) was selected and prepared to be inserted inside the rectangular-shaped experimental channel next to the regenerator. The core dimensions of the heat exchanger are 235 mm wide, 120 mm high and 49 mm deep, parallel to the oscillating centre-line; whereas the outer dimensions 280 mm, 125 mm, and 60 mm are width, height and depth respectively. The aluminium-made heat exchanger contains 13 flat tubes with vertical spacing of 8 mm and fin spacing of 1 mm with a core porosity of 63.3%. The AHX was surrounded by a 2 mm thick aluminium plate that is folded to form a complete rectangular shape. Gaps between

the frame and the AHX were filled with high temperature silicone sealant to enforce the flow through the core of the heat exchanger as seen in Figure 3.21a. Two plastic tubes are connected between the heat exchanger and push-in fitting ports to transport the cooling water as seen in Figure 3.21b.

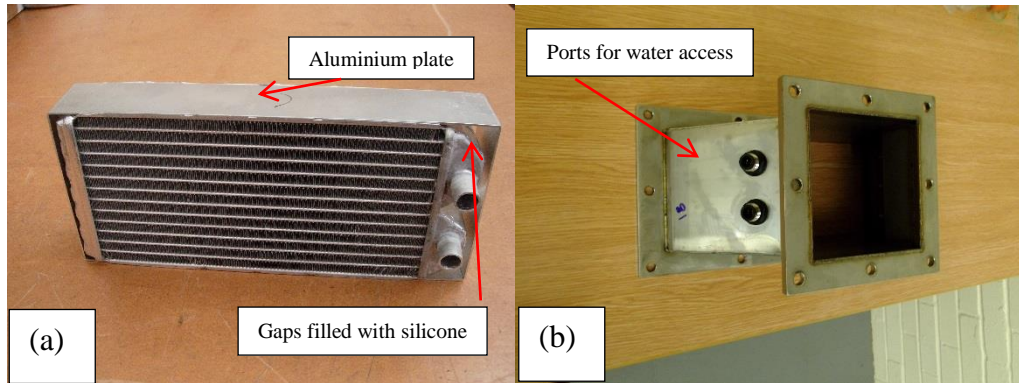


Figure 3. 21 Photograph of the configuration of the ambient heat exchanger (AHX). (a) The car heater matrix as a heat exchanger. (b) Push-in ports for cooling water access to the AHX.

The hot heat exchanger (HHX) has a shell-and-tube configuration and is connected to the thermal buffer tube on one side and on the other side it is connected to the rectangular channel that contains the regenerator and the AHX. It has a bundle of 13 stainless steel flattened tubes with a thickness of 1 mm, width of 10 mm, height of 120 mm, radius of both curved ends of 5 mm and total length of 120 mm. Figure 3.22 shows a schematic drawing of the flattened tube. These tubes were cut from an 80 mm outside diameter stainless steel pipe and squashed using the flattening tool seen in Figures 3.23a and 3.23b. For a supportive structure, the HHX tubes were terminated on both sides by two stainless steel plates of 8 mm thickness, leaving only 104 mm of the total length to be exposed to the hot air from the heat gun. The porosity of the hot heat exchanger is about 40% and the hydraulic radius is about 4.3 mm. The HHX is heated by hot air flow provided by an electric heat gun that has an adjustable heating power in the range of 0~16 kW and adjustable heating temperature up to 650°C.

The hot air from the heat gun flows around the outer surface of the bundle of tubes by forced-convection and then out to the ventilation hood, while the thermoacoustic gas oscillates inside these tubes. Figure 3.23c shows a photograph of

the hot heat exchanger and Figure 3.23d shows the HHX connected to the rectangular channel where the regenerator and the AHX are contained.

On the other side of the hot heat exchanger, there is a thermal buffer tube, which consists of four parts. The first part is a rectangular section of area of $3 \times 10^{-2} \text{m}^2$ and 2.8 mm long, the second part is a transition from a rectangular section with a cross sectional area of $3 \times 10^{-2} \text{m}^2$ to a squared cross sectional area

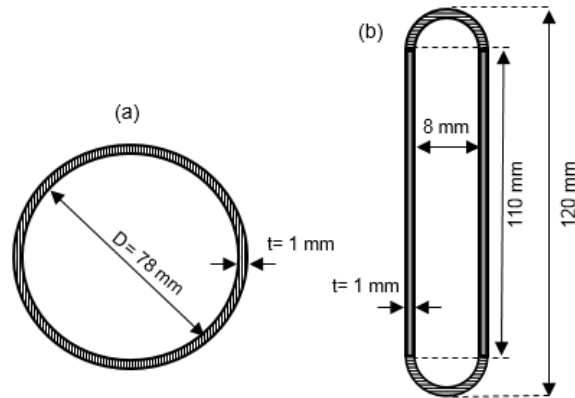


Figure 3.22 The shape change of a pipe after the flattening process.

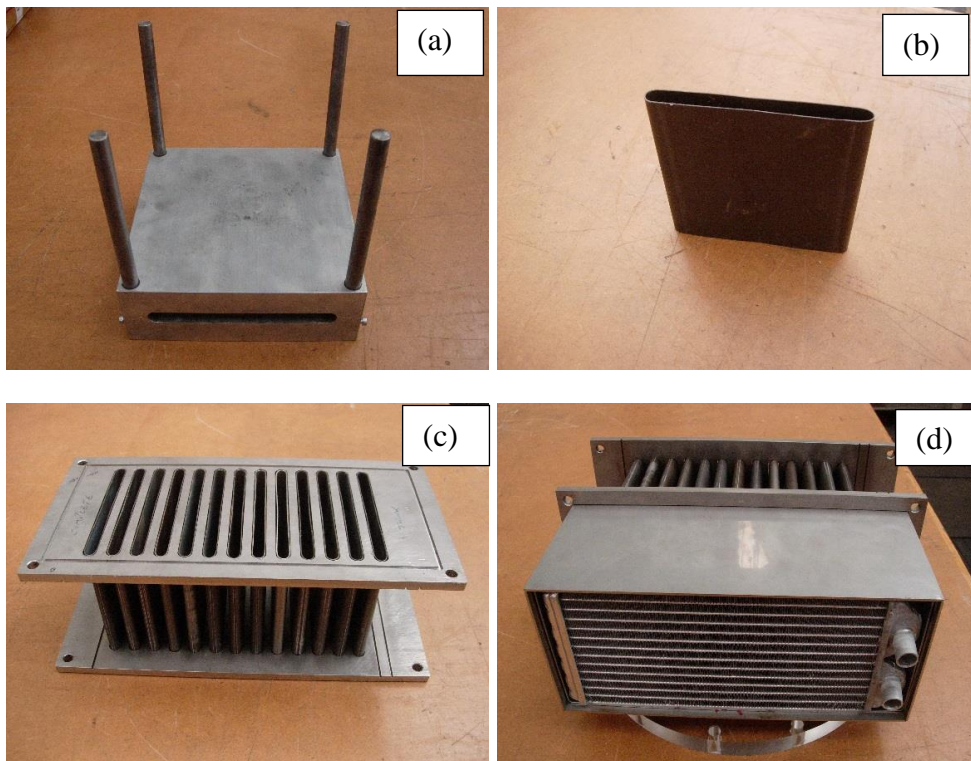


Figure 3.23 Photographs of the hot heat exchanger configuration (a) the flattening tool; (b) the flattened tube; (c) the hot heat exchanger; (d) the thermoacoustic core

of $1.69 \times 10^{-2} \text{m}^2$. The third part is a pipe of a squared cross sectional area of $1.69 \times 10^{-2} \text{m}^2$ and length of 8 mm. The fourth section is a stainless steel pipe (ID=129 mm) with a length of 200 mm, and a wall thickness of 2 mm. The first buffer tube, second and third are connected via welding, whereas the fourth tube is tightened by a flange to the other thermal buffer tubes. Drawings of the detailed construction of the engine including thermal buffer tubes sections are provided in Appendix C.

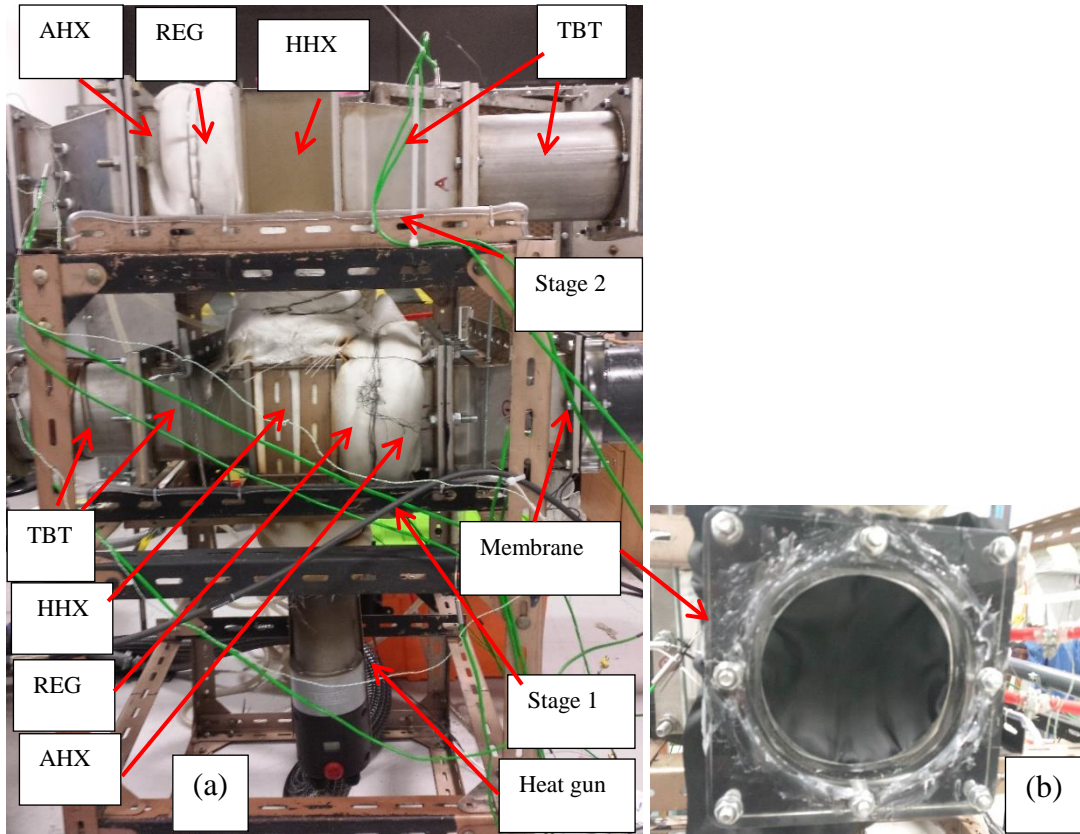


Figure 3. 24 (a) Photograph of the combined two-stage thermoacoustic cores; (b) Photograph of the elastic membrane..

In comparison, the thermal buffer tube is defined in the simulation as well-insulated, and any heat rejection is only through a dummy second ambient heat exchanger of 1 mm length. However, in the experimental apparatus, the thermal buffer tube is not thermally insulated and there is no second ambient heat exchanger, and therefore it can be cooled by the ambient air. This does not apply to the HHX, the AHX and the regenerator as they are insulated in the simulation and well-insulated in reality with a 50 mm thick ceramic fibre blanket as shown in the experimental set-up in Figure 3.24a.

Table 3. 4 Dimensions of parts in the experimental set-up.

Component	Actual configuration and dimensions
Ambient heat exchanger: <ul style="list-style-type: none"> • Length • Porosity • Plate spacing 	Fin-and tube (Land Rover heater matrix) <ul style="list-style-type: none"> 49 mm 62.5% 1 mm
Regenerator: <ul style="list-style-type: none"> • Length • Porosity • Hydraulic radius 	Stainless steel mesh screen <ul style="list-style-type: none"> 30 mm 83.3% 198 μm
Hot heat exchanger: <ul style="list-style-type: none"> • Length • Porosity • Hydraulic radius 	Stainless steel shell-and-tube configuration <ul style="list-style-type: none"> 120 mm 40% 4.3 mm
Thermal buffer tube: <ul style="list-style-type: none"> • Total length 	Stainless steel tube <ul style="list-style-type: none"> 308 mm
Feedback pipe : <ul style="list-style-type: none"> • Inner diameter • Length of FBP1 • Length of FBP2 	128-mm diameter PVC pipe <ul style="list-style-type: none"> 128 mm 2.375 m 2.36 m

Eventually, as shown in Figure 3.24a, all parts were combined together in the full two-stage configuration with thermocouples distributed to measure local temperature at certain points and the heat gun at the bottom to heat up the HHX of the first stage followed by the second stage. Figure 3.24b shows a picture of the

elastic membrane that is located just before the ambient heat exchanger of the first stage to suppress acoustic streaming. The actual dimensions of all parts used in the experimental apparatus are listed in Table 3.4

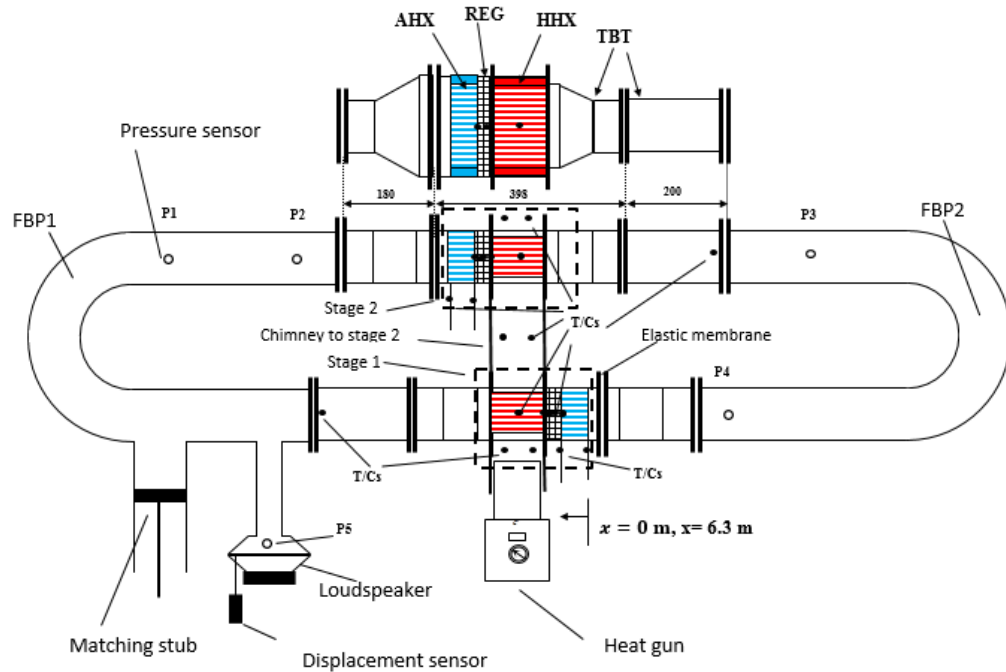


Figure 3. 25 A schematic drawing of the two-stage thermoacoustic electricity generator.

The complete configuration of the experimental set-up is shown schematically in Figure 3.25 whereas Figure 3.26 shows the practical experimental apparatus of the electricity generator. From the starting point at ($x = 0$ m) along the engine loop and back to the same point at ($x = 6.3$ m) there are: first stage components which are ambient heat exchanger (AHX1), stacked screen regenerator (REG1), hot heat exchanger (HHX1) and thermal buffer tube (TBT1) then a side branched alternator (ALT), side branched matching stub and feedback pipe (FBP1), then second stage components which are ambient heat exchanger (AHX2), stacked screen regenerator (REG2), hot heat exchanger (HHX2), thermal buffer tube (TBT2) and feedback pipe (FBP2) to connect back to the first stage. The alternator side branch pipe is around 240 mm, and the length of side branch stub is up to 1 m. The working frequency was around 49 Hz.

When the acoustic oscillations start, acoustic power is amplified in the regenerators of the first and second stages. The acoustic power produced in the first

stage is transferred through (TBT1) to the first branch. Because the two-stage generator is also designed to operate with air at atmospheric pressure, the feedback pipe is made of standard 128 mm inner diameter (5-inch) PVC pipe (128 mm), T-connections and 90° elbows as seen in Figure 3.26.

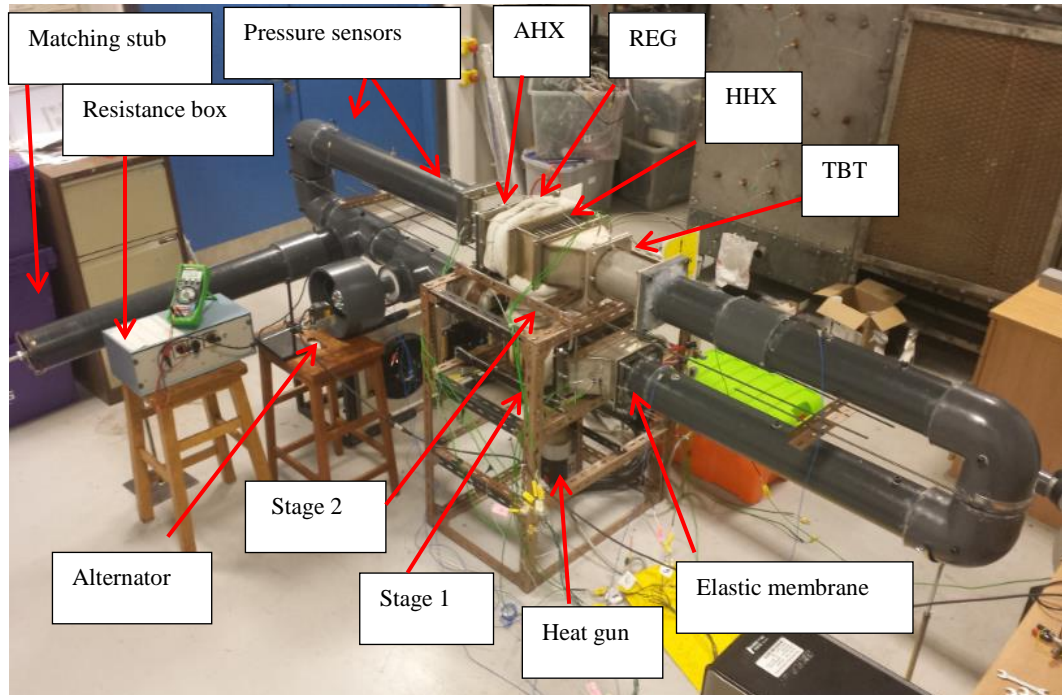


Figure 3. 26 Photograph of the experimental apparatus of the two-stage electricity generator

About 24 centimetres away from the end flange of TBT, a branch pipe is connected to the loop. The branch pipe is about 24 centimetres in length, and the alternator is installed at the end. In this branch, some of the acoustic power produced is extracted by the audio loudspeaker (8 inch B&C 8 BG51 sub-woofer), to convert the acoustic power into electrical output. About 45 centimetres away from the first branch, a second branch pipe is connected to the loop. Here is the stub which is a PVC disc that slides inside the pipe to change the volume of the branch pipe. The “stub” tube is placed here in order to improve the impedance matching between the branched alternator and the loop. The remaining part of the rig is the first feedback pipe (FBP1) that is connected to the second stage, with an inner diameter of 128 mm

and a total length of 2.375 m (length from end of first stage to the beginning of second stage). In the second stage the the acoustic power is amplified in the regenerator and fed into the second feedback pipe (FBP2) that has a length of 2.36 m to start a new loop.

D. Instrumentation and experimental procedure

All instrumentation and types of pressure sensors, thermocouples and the laser displacement sensor used in this generator are as described in section 3.2.3. However, the heating power system and cooling water system are different. As shown in Figures 3.25, 3.26 and 3.27, five pressure sensors (microphones) have been installed and marked P1 to P5. Pressure sensors P1 to P4 are distributed in the loop to measure the acoustic oscillations within the engine and the transducer P5 is placed near the end of stub1 to measure the amplitude and phase of the acoustic pressure in front of the loudspeaker. The pressure sensors P1 and P2 are placed in FBP1 with a distance of 700 mm to measure the acoustic power flow between stage1 and stage2 and also using P2 to estimate the pressure drive ratio of stage 2. Similarly, the pressure sensors P3 and P4 are placed in FBP2 to measure the acoustic power flow between (stage 2) and (stage 1) and also using P4 to estimate the pressure drive ratio of stage 1. Thermocouples of type-K are distributed in the system in order to achieve certain measurements as seen in Figure 3.25. One thermocouple is placed in the middle and two thermocouples at two ends of each regenerator to measure the temperature profile in the regenerators. In each stage, one thermocouple is placed in the centre of the HHX to measure the gas temperature and one thermocouple is placed at the end of the TBT. Six thermocouples to measure the heat flux absorbed by the HHXs were distributed along the heating air flow: two at the bottom of stage 1, two at the top of stage1 and two at the top of stage 2. Finally, two thermocouples to measure the inlet and outlet cooling water temperature in order to measure the amount of rejected heat in the ambient heat exchanger in each stage. As seen in Figure 3.24a and Figure 3.25, the heat power applied to the HHXs is mainly supplied by a three-phase 16 kW electric heat gun (LHS 61L) that provides hot air flow at any verified and controlled temperature but not higher than 650° C. As shown in Figure 3.27, the air flow that is heated in the heater is provided by a powerful centrifugal compressor (ASO-blower) that can

deliver up to 13500 l/min of air flow. The air flow can be controlled using an inverter to verify the frequency of the electric motor of the compressor. In order to accurately measure the air flow for the heating power calculations, the air flow has to be fully developed before entering the heat gun. This was ensured by doing the calculations to obtain the entrance length using the following equation for turbulent flow (Zhi-qing, 1982):

$$El = 1.359DRe_D^{\frac{1}{4}} \quad (3.11)$$

where El is the entrance length, D is the pipe diameter and Re_D is the Reynolds number based on the pipe diameter.

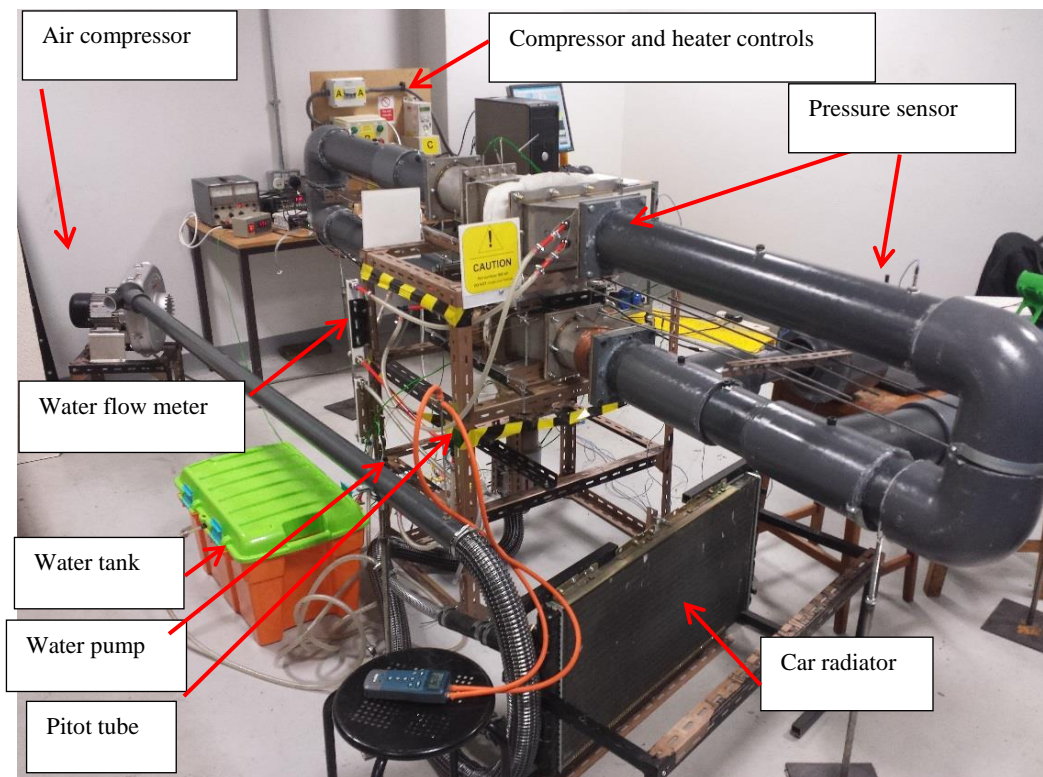


Figure 3. 27 Photograph of the water cooling system of the generator.

From the calculations and for the range of flow rates provided by the compressor, the maximum length obtained is 1.81 m. Therefore, the pipe length of 2 m was chosen, as seen in Figure 3.27. The air velocity was measured using a Pitot-static tube and a differential digital pressure manometer with an accuracy of 0.15%. The fully developed air flow velocity was then calculated using the measured pressure difference and the well-known Bernoulli equation.

$$u = \sqrt{\frac{2(P_t - P_s)}{\rho}} \quad (3.12)$$

where P_t is the stagnation pressure, P_s is the static pressure and ρ is the air density.

As a result, having the average temperature of the hot air flow before and after each stage, the absorbed heat flux can be estimated as:

$$\dot{Q}_h = \rho_a u A c_{p,a} (T_{a,in} - T_{a,out}) \quad (3.13)$$

where ρ_a is the density of the hot air, u is the velocity of air flow in the PVC pipe between the compressor and the heater, A is the cross sectional area of the PVC pipe ($2.3 \times 10^{-3} \text{m}^2$), $c_{p,a}$ is the specific heat of the hot air flow and $T_{a,in}$, $T_{a,out}$ are the temperature of the hot air flow before and after the HHX, respectively.

The heat supplied to the HHXs is removed from the AHXs by the cooling water system. As shown in Figure 3.27, the cooling water system beside the AHXs is composed of a water tank of 80 litres in size, 12 V DC positive displacement water pump that provides 6 litre/min of water, two powerful 12 V DC cooling fans fitted with a car radiator and flow-meter to measure the flow rate of water. Using the temperature readings from the thermocouples at the water inlet and outlet of each AHX, the reading of the flowmeter and Equation (3.13) the heat rejected from the AHXs can be estimated as follows:

$$\dot{Q}_c = \rho_w U_w c_{p,w} (T_{w,in} - T_{w,out}) \quad (3.14)$$

where ρ_w is the density of water, U_w is the volumetric flow of water, $c_{p,w}$ is the specific heat of water, $T_{w,in}$, $T_{w,out}$ are the water temperature at the inlet and outlet of the AHX respectively. It should be noted that the water flow in the measurement was kept at a low rate in order to establish at least 10 °C temperature rise. This is to reduce any uncertainty in water temperature measurements.

The testing and experiments of the two-stage generator concentrated on the impact of the matching stub length, the impact of the load applied to the loudspeaker and the impact of the heating power on the electrical power output and the generator efficiency. Details of these experiments and their results are given in Chapter 4.

3.4 Summary

Based on the electricity needs, natural energy resources in remote areas in developing countries, and practical engineering assumptions, prototypes of thermoacoustic electricity generators have been designed, built and tested. The thermoacoustic core of the 54-mm resonator diameter (2 inch) generator prototype has already been designed and built for a different configuration (Yu et al., 2012). This thermoacoustic core has been simulated in a loop and a side branch alternator using DeltaEC. Furthermore, the model has been experimentally verified using a propane gas burner as heat source. Following the potential advantages of a side branch alternator and multi-stage configurations, the work has been extended by building a DeltaEC model of a two-stage travelling wave looped-tube electricity generator. This was preceded by two preliminary steps of building and modeling the single-stage engine and the single-stage generator using the same components as intended for the two-stage system in order to understand the sub-system behavior. The two-stage generator model was optimized from the high electrical power output point of view. Subsequently, the model was re-optimized taking into account the feasibility of using low cost and commercially available components. Based on the optimization results, the generator has been built and tested in the laboratory using 16 kW electric heat gun as heat source. In all experiments conducted using all prototypes, the two microphone method and piston or loudspeaker method have been used to measure the acoustic power. The experimental results and their comparisons with modeling are presented and discussed in Chapter 4.

CHAPTER 4

RESULTS AND DISCUSSIONS

This chapter presents the predicted results of DeltaEC models and measured results of testing of all prototype configurations described in Chapter 3. This chapter also gives a comparison between calculated and experimental results for the same operating conditions. In section 4.1, the simulated and measured results of the 54-mm diameter one-stage electricity generator are presented and illustrated. The results of the simulations and the experimental work of the 128-mm diameter, one-stage thermoacoustic engine are presented and debated in section 4.2. Here the effects of the acoustic streaming and the working frequency are included. In section 4.3, the results of the computations and experimental work of the 128-mm diameter, single-stage electricity generator are shown and discussed. In this section the effects of the electric load and the heat input on the performance of the generator are included. The results of calculations and measurements of the 128-mm diameter, two-stage electricity generator are presented and discussed in section 4.4. Here the effects of the matching stub length, load resistance and the heating power input are considered. Finally, the concluding remarks on this chapter are reported in section 4.5.

4.1 The 54-mm Diameter Single-stage Looped-tube Travelling Wave Thermoacoustic Electricity Generator

In this section, the results obtained from DeltaEC simulations and experiments relating to the 54-mm diameter electricity generator are shown in sections 4.1.1 and 4.1.2, respectively.

4.1.1 Simulation results

Usually, the work related to the development of thermoacoustic devices involves iterative work including modelling, experimental validation, subsequent rig modifications to go back to modelling the modified design. It is not unusual to carry out this recurrent process for a few “cycles” until the modified device and numerical models are close to at least a satisfactory level. This was clearly the case in the current work. However, it needs to be recognised that the slow convergence of these

two methods (experiments and modelling) led to a widely adopted routine within the thermoacoustic community of presenting only the final results in any scientific publications. This is also a reasonable approach for brevity sake when writing up a PhD thesis. Therefore, the results presented throughout this thesis also adopt this approach of presenting the final models and results, whilst omitting the laborious route of consecutive improvements.

With the above caveat, the simulation results discussed in this section are based on the final design of the prototype as shown in Figures 3.2 and 3.3. The calculations were carried out under the following conditions: air was used as the working gas, the mean pressure was 0.1 MPa, the length of the stub was 450 mm, the load resistance was 12 Ω , and the temperature difference between the two ends of the regenerator was maintained at 430 K. The calculation results of the distributions of the acoustic power flow and the acoustic field in the system are shown in Figure 4.1.

Figure 4.1a shows the measured and simulated pressure amplitude distribution along the system. There are two maxima and two minima of pressure amplitude along the loop and one sharp pressure drop. The pressure drop is caused by the flow resistance of the regenerator. The pressure amplitude changes smoothly along all other parts. The pressure distributions were different in the two stubs. The reason for this is that two stubs with different ends (the first stub is open end, while the second stub is closed end) reduce to different boundary conditions: $|p_1| = 0$ for the open end, and $|U_1| = 0$ for the closed end). Additionally, results confirmed that the open end of the branch resonator with the alternator becomes the node of the sound pressure and the closed end of the tuning stub becomes the anti-node of the sound pressure. Good agreements can be seen in the graph between measured and simulated values.

Figure 4.1b shows the distribution of volumetric velocity along the system. There were also two maxima and two minima along the loop. One maximum was on the first T-type junction where $x = 790$ mm, and the other was near the end of the feedback tube where the minimum of the pressure amplitude was located. One minimum of the volumetric velocity is at the cold end of the regenerator, while the other is close to the middle of the feedback tube.

The small volumetric velocity within the regenerator is preferred to avoid high viscous dissipation, which was one of the design strategies behind the current concept. It can also be seen that the volumetric velocity increases significantly along the regenerator. This is due to the sharp temperature gradient along the regenerator. Furthermore, at the location of the stub, there was a sudden decrease in the volumetric velocity. Along all other parts, the volumetric velocity changes smoothly. Additionally, results confirmed that the open end of the branch resonator with the alternator becomes the anti-node of the particle velocity, and the closed end of the tuning stub becomes the node of the particle velocity. Figure 4.1c shows the acoustic impedance along the system. It can be seen that the acoustic impedance is highest at the cold end of the regenerator. The impedance drops quickly because the pressure amplitude decreases (see Figure 4.1a) while the volumetric velocity increases sharply from the cold to the hot end of the regenerator (see Figure 4.1b).

The stub introduces a sudden increase of the acoustic impedance along the loop. This is because the pressure amplitude at the stub junction is constant, while the volumetric velocity has been shunted partly to the stub. From Figure 4.1c, one can also find that the alternator is very close to the minimum of acoustic impedance. This is also a carefully designed feature of the device, introduced to obtain sufficient volumetric velocity to drive the alternator to the maximum excursion which subsequently maximizes the electrical power output.

Figure 4.1d shows the phase difference between pressure and velocity oscillation along the system. It can be found that the regenerator works in the region of $(-12^\circ < \phi < 18^\circ)$. It is indicated that the regenerator can realize the conversion from heat to acoustic energy by both the standing-wave and travelling-wave (Kang et al., 2010a). The phase difference in the first stub is positive, while the phase difference in the second stub is negative. The reason is that the open end of the first tube is the node of the sound pressure and the closed end of the second tube is the node of the sound velocity (Kang et al., 2010b). From Figure 4.1d, one can also find that the phase difference in first stub is closer to zero than that in the second stub. The reason is that there is more acoustic power transferring into the first stub than that in the second stub (cf. Figure 4.1e), and subsequently the travelling wave ratio

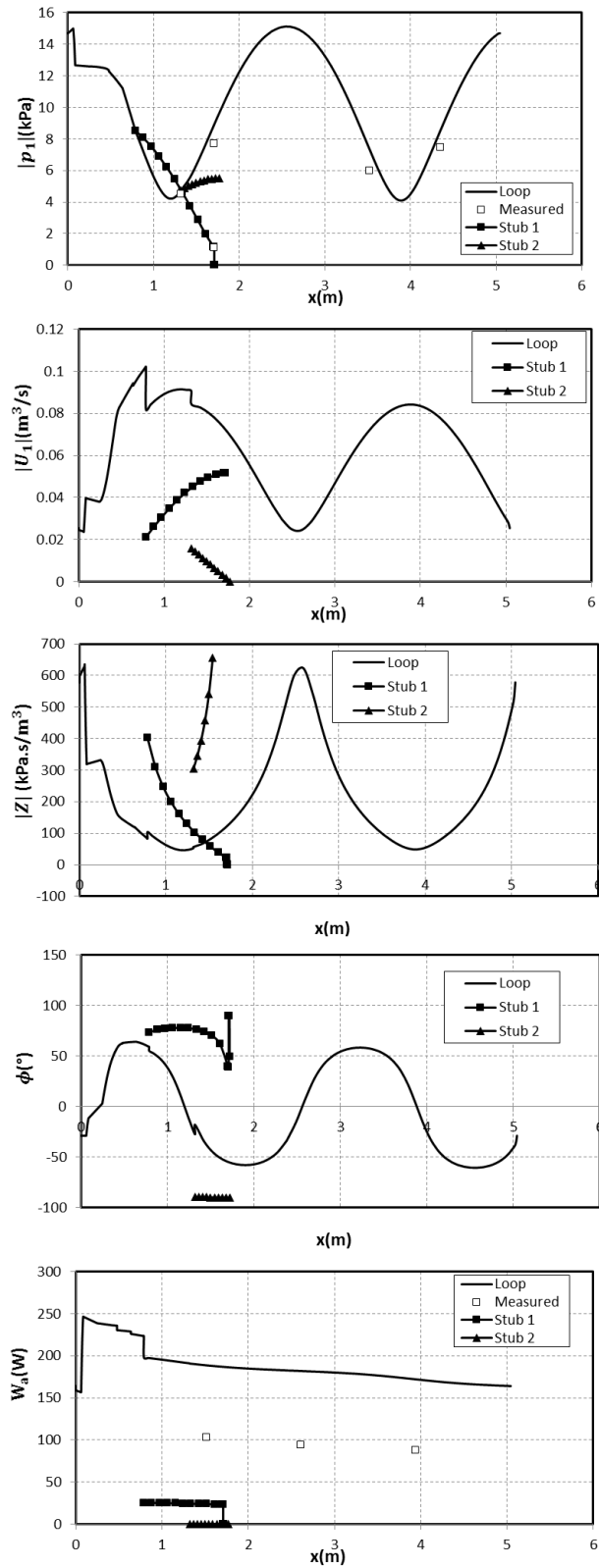


Figure 4. 1 The calculation results of the distributions of the acoustic power flow and the acoustic field in the 54-mm diameter electricity generator. (a) Pressure amplitude, (b) Volumetric velocity, (c) Acoustic impedance (d) Phase angle and (e) Acoustic power

on which the acoustic power transfer relies in the first stub is more than that in the second stub. It leads to the phase difference in the first stub being closer to zero, and then changing to 90° after the acoustic power is extracted in the speaker (Kang et al., 2009).

Figure 4.1e shows the acoustic power flow along the system. It can be found that around 160.8 W of acoustic power is fed into the cold heat exchanger which dissipates around 2.2 W. The remaining 156.6 W is fed into the cold end of the regenerator. Within the regenerator, the acoustic power is amplified to around 246.4 W which is the level of acoustic power flowing out from the hot end of the regenerator. The hot heat exchanger and thermal buffer tube dissipate around 14.2 W. The acoustic power of 25.0 W enters the first stub and the alternator extracts about 22.8 W of acoustic power. In this simulation, the alternator produces 13.6 W of electricity. As mentioned above, the required input heat is 560.8 W for this case. Therefore, the calculated thermal-to-acoustic efficiency is 23.0%, acoustic-to-electric efficiency is 59.7%, and thermal-to-electric efficiency is 3.5%.

4.1.2 Experimental and calculated results

The experiments of this generator were achieved using a 5 kW propane gas burner as heat source to power the shell and tube hot heat exchanger. A fixed load resistance of 12Ω was connected to the alternator to consume the electric power output whereas the stub length was fixed at 450 mm. During the experiments the cooling water came from an underground water tank and was at an unmeasured fixed flow rate. The heat input at the hot heat exchanger was managed by gradually increasing the heating temperature. This heating temperature controlled the opening valve of the gas burner. The adjustment of the gas burner valve was to achieve an average of about 35°C increment of the wall temperature at the centre of the HHX. This wall temperature reading was according to the three thermocouples placed inside the HHX. When the temperature difference between the hot and ambient ends of the regenerator reached 255 K, the acoustic oscillation started and electricity output was extracted.

Figure 4.2 shows the comparison between the measured and calculated results of the influence of the temperature difference of two ends of the regenerator on the electric power produced by the alternator. As represented in the graph, the calculated

results are shown in square white symbols whereas the calculated results are shown in a solid line. It is shown that there is a similar trend between the measurements and calculations and the electrical output is proportional to the temperature difference of the regenerator. It can be seen from the graph, that as the regenerator temperature difference increases from 255 K, the measured electricity increases linearly from 1.54 W to achieve a maximum of 13 W of electric power at a temperature difference around 430 K across the regenerator. It can also be seen from the graph that DeltaEC calculations and measurements have the same tendency of a linear increase as the temperature difference of the regenerator increases. Results show that the measured and predicted values of the electricity agree at higher temperature differences whereas a considerable discrepancy occurs at lower temperature differences.

In both simulation and measurements, the effect of increasing the temperature difference across the regenerator on the coil displacement of the alternator can be clearly seen in Figure 4.3. The predicted results are shown in square white symbols while the calculated results are shown by a solid line. There was a broadly similar trend when the calculations and measurement results were compared.

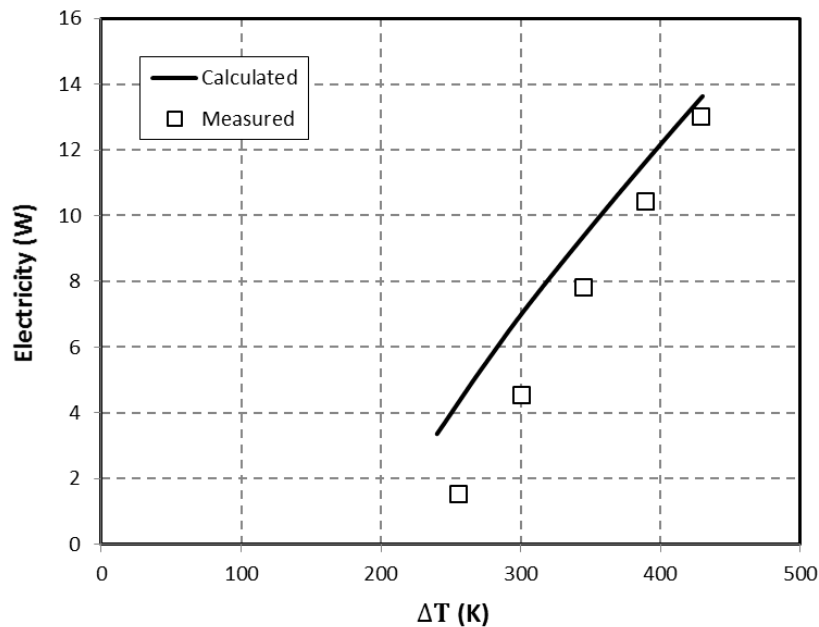


Figure 4. 2 The relationship between the temperature difference of two ends of the regenerator and the electricity output.

It is clear from the graph that the coil displacement increases as the difference between the cold and hot temperature increases. The measured coil displacement

improves gradually from around 2 mm to approximately 5.8 mm when the temperature difference rises from 255 K to 430 K. The calculated and the measured displacements show a good agreement at high temperature differences practically when they reach 388 K and 430 K at 5.2 mm and 5.8 mm of diaphragm displacement, respectively. However, obvious disagreement between results shows up at lower temperature differences.

The acoustic power extracted by the alternator is also simulated and measured in this work. Figure 4.4 shows the comparison between the predicted and measured results of the effects of the temperature difference across the regenerator on the acoustic power consumed by the alternator. It is clear from the graph that the acoustic power extraction is proportional to the temperature difference of the regenerator and a similar trend is obtained between the measured and calculated results. The experimental values increase from 2.5 W gradually to achieve maximum of 24 W while the calculated values rose from 5.8 W to 22.85 W when the temperature difference across the regenerator was increased from 255 K to 430 K respectively. From the chart it can be seen that there is good agreement between the predictions and the measurements specifically at high temperature differences.

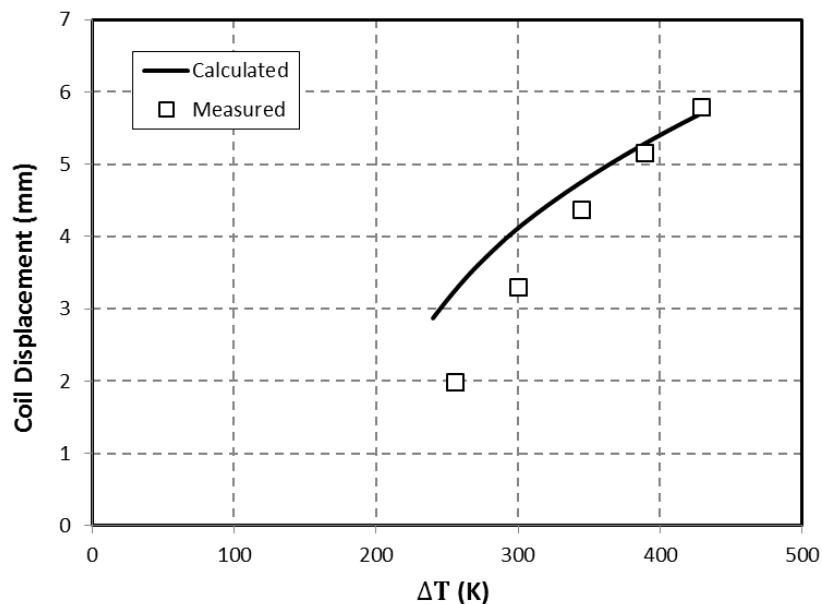


Figure 4. 3 Effects of the temperature difference at two ends of the regenerator on the coil displacement of the alternator

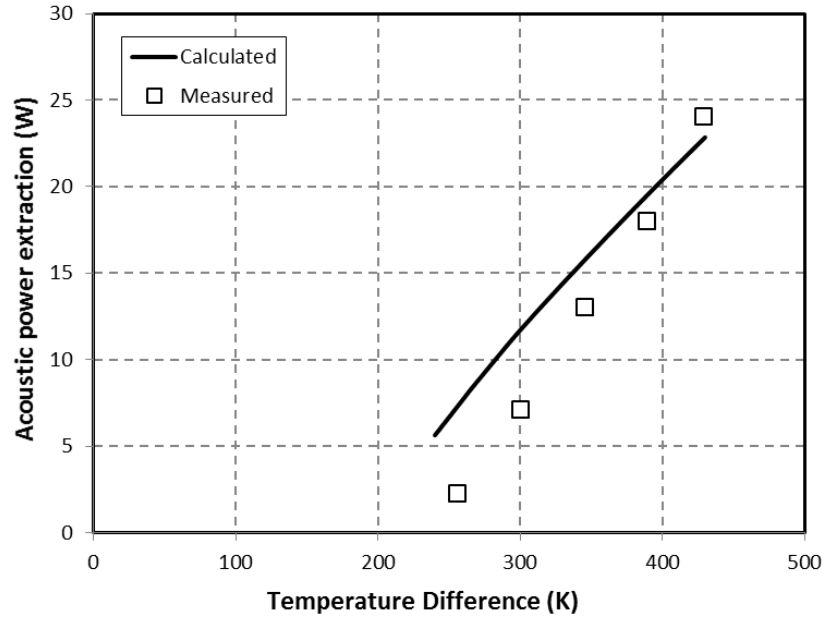


Figure 4. 4 Effects of the temperature difference of two ends of the regenerator on the acoustic power extraction of the alternator

One of the important measurements to evaluate the performance of the generator is the efficiency of the alternator. For both simulation and experiments, Figure 4.5 shows the effects of regenerator temperature difference on the alternator efficiency. There is no similarity in trend between both experimental and calculated results in the graph. It is clear in the graph that the predicted value of the efficiency is fixed at 59% with various temperature differences while the measured value falls from 67% to 54% as the temperature difference increases from 255 K to 430 K. In the model, the phase of the electric current the phasing of the electrical impedance of the alternator is targeted to 180° . This is to ensure the load connected to the alternator is completely resistive and extracts electric power from the alternator. In the experiments and according to Equation (2.68), if the load resistance R_L is fixed, the only parameter that affects the efficiency is the magnetic force of the alternator (Bl). Moreover, as the power input increases, the coil displacement of the alternator increases as shown in Figure 4.3, the coil in the actual alternator jumps out of the magnetic gap at higher power inputs while in the calculation there is no such limitation. This might be the reason for the disagreement between the calculated and measured results.

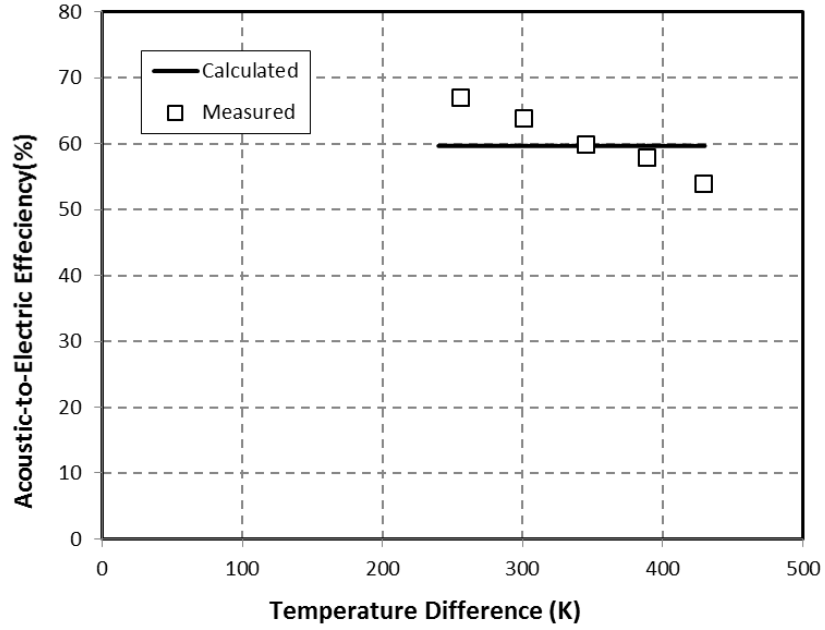


Figure 4. 5 Effect of the temperature difference at two ends of the regenerator on the acoustic-to-electric efficiency of the alternator.

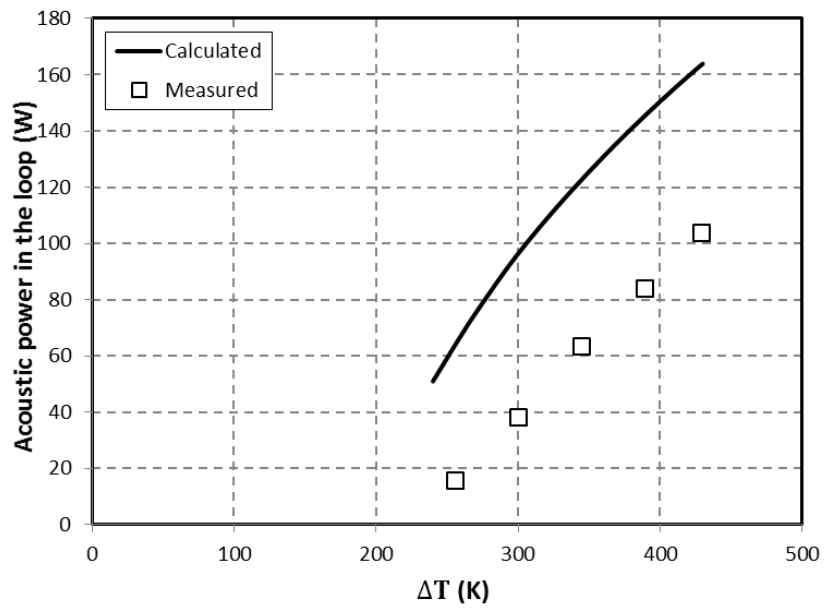


Figure 4. 6 Effects of the temperature difference of the two ends of the regenerator on the acoustic power flow in the feedback pipe.

Figure 4.6 shows the effect of the temperature difference across the regenerator on the predicted and measured results of the acoustic power flow in the feedback pipe. As seen from the graph, both measurement and calculated values have a similar trend as they increase with the increase of the temperature differences

of the regenerator. The measured acoustic power increases from 15.65 W to around 103.9 W while the calculations show a higher level of acoustic power as it increased from 50.9 to 163.5 W. The disagreement between the experiments and calculations is lower at low temperature differences and it increases as the temperature difference increases. The discrepancy is attributed to the error in the measurement of the pressure phasing differences. Moreover, the non-linear effects that occur at high pressure amplitudes – and are neglected by DeltaEC – also contribute to the disagreement.

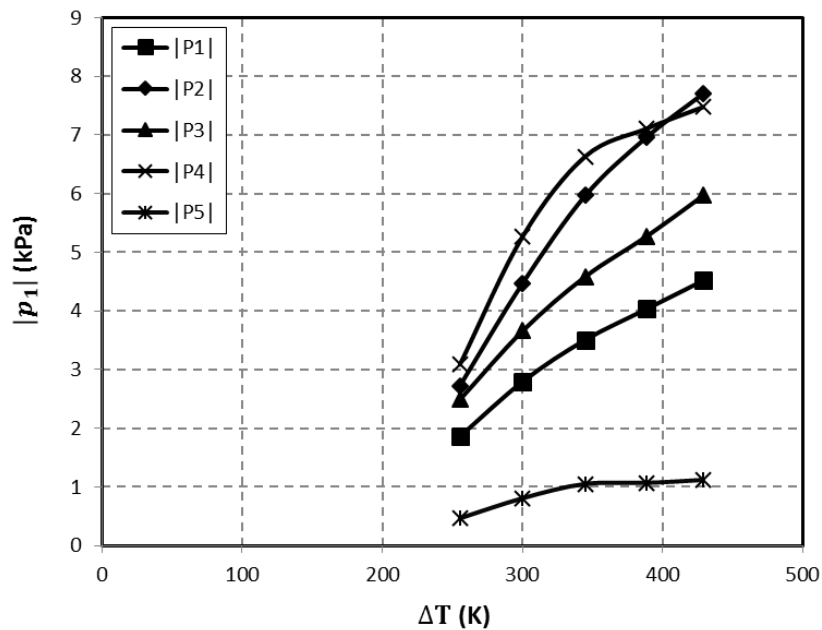


Figure 4. 7 The effect of the temperature difference at two ends of the regenerator on pressure amplitudes.

Pressure transducers (microphones) were placed along the loop of the generator, as seen in Figure 3.2. These measured the pressure amplitudes during experiments. Figure 4.7 displays the effect of the regenerator temperature difference on the pressure amplitudes. As seen in Figure 4.1a and Figure 4.7, sensor P1 is located in the region of the pressure node, P2 and P3 are both located between the node and anti-node region whereas P4 is located at the anti-node region close to the thermoacoustic core. As stub 1 is branched to shunt part of the acoustic power to the alternator, most of the pressure in Equation (2.40) is converted into volumetric velocity due to the soft surface (the alternator) and pressure node located at the end

of stub 1. It can be noted from the graph that pressure amplitude values at, or close to, the pressure anti-node regions are steeper than the others while they grow.

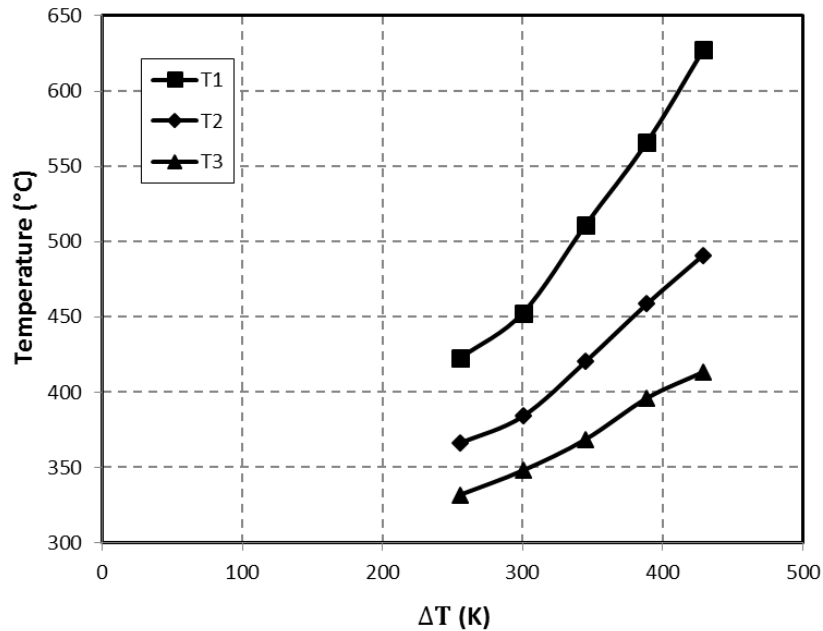


Figure 4.8 The effect of the temperature difference at two ends of the regenerator on the temperature distribution in the HHX.

As mentioned in section 3.2.2, the heat exchanger has three thermocouples to observe the temperature profile in the hot heat exchanger. The distribution of the heating temperature of the tube-wall (oscillation side) in the hot heat exchanger is shown in Figure 4.8 where T1, T2 and T3 are located at the bottom, the centre and the top of the hot heat exchanger respectively. Since the gas burner provides an external combustion heating power to the hot heat exchanger, the temperature distribution in the heat exchanger is not uniform and varies within the vertical axis as seen in Figure 4.8.

4.2 A 128-mm Diameter One-stage Travelling Wave Engine

In this section, DeltaEC simulations and experimental results of the 128-mm diameter one-stage looped-tube thermoacoustic engine are presented and discussed. The results obtained from the simulation of DeltaEC along the loop of the generator are shown as pressure amplitude distributions, volumetric velocity distributions,

acoustic impedance and its phasing and, finally the acoustic power distribution. The simulated results are shown and discussed in section 4.2.1. The effect of the stub length on the engine performance in the presence of the acoustic streaming and after suppressing the streaming using the elastic membrane are presented and discussed in section 4.2.2. Finally, the effects of stub length at different working frequencies on the performance of the engine are shown and discussed in section 4.2.3.

4.2.1 Simulation results

The results shown in this section were obtained from the simulations of the prototype according to the block diagram shown in Figure 3.6 in Chapter 3. The calculations were carried out under the following conditions: air was used as the working gas, the mean pressure was 101 kPa, the calculated working frequency was 70.56 Hz, and optimum length of the matching stub of 450 mm. The results of the simulation are based on guessing the heating power at the HHX to target the pressure amplitude of 5.55 kPa of pressure sensor P4 that was obtained from the experiments. The pressure sensors P1, P2, P3, P4, P5 and P6 were placed at 1.22, 2.02, 2.57, 3.04, 3.555, and 4.355 m away from the ambient heat exchanger, respectively, whereas the total length of the loop was 4.685 m. The results of the simulation of the thermoacoustic engine are presented in Figure 4.9.

Figure 4.9a shows the pressure amplitude distribution along the loop of the thermoacoustic engine. The simulated pressure amplitudes are represented by the solid line whereas the measured amplitudes are represented by the black squares. There are two maxima and two minima of pressure amplitude along the loop. There is a pressure drop located at $x = 0.149$, due to the flow resistance of the regenerator. Along the rest of the loop there is a smooth pressure change. The differences between the measured and simulated pressure amplitudes are presented in Table 4.1. Good agreement between the measured and calculated values is shown in the graph with an average error of 8.286%.

Table 4. 1 The results of measured and simulated pressure amplitudes along the loop of the engine

P	x (m)	$ p_l _{(Measured)}$ (kPa)	$ p_l _{(Calculated)}$ (kPa)	Error (%)
P1	1.22	2.23	1.75	21.5
P2	2.02	4.69	4.63	1.23
P3	2.57	6.29	6.18	1.81
P4	3.07	5.55	5.55	0 (targeted)
P5	3.555	2.95	3.28	10.3
P6	4.355	3.03	2.85	6.6

Figure 4.9b shows the distribution of volumetric velocity amplitudes along the loop of the engine. There are two maxima and two minima along the loop. In order to suppress the acoustic streaming without disturbing the sound wave, the fixable membrane is placed at the minimum amplitude in the loop. In order to minimise the viscous effect of high volumetric velocity, the regenerator is located near a minimum location of the volumetric velocity. However, the regenerator introduces high and steep raise of the volumetric velocity as shown in Figure 4.b. This is caused by the temperature gradient that occur in the regenerator. In 896 mm away from the regenerator, there is a second sharp increase in the volumetric velocity amplitude. This occurred at the T-junction where there is the matching stub that shunts volumetric flow into the loop. Along the rest of the loop, the volumetric velocity is distributed smoothly.

Figure 4.9c presents the distribution of the acoustic impedance in the loop of the thermoacoustic engine. From the graph it can be seen that there is a sudden increase in the acoustic impedance in the ambient heat exchanger followed by a sharp decrease in the regenerator. The first increase is caused by the acoustic dissipation due to acoustic velocity drop in the small passages of the ambient heat exchanger. Due to the sharp increase in the volumetric velocity in the regenerator as shown in Figure 4.9b, the acoustic impedance experiences a sudden decrease. However, the level of dropping the acoustic impedance in the regenerator of the engine and the generator are different. As mentioned earlier this is because of the

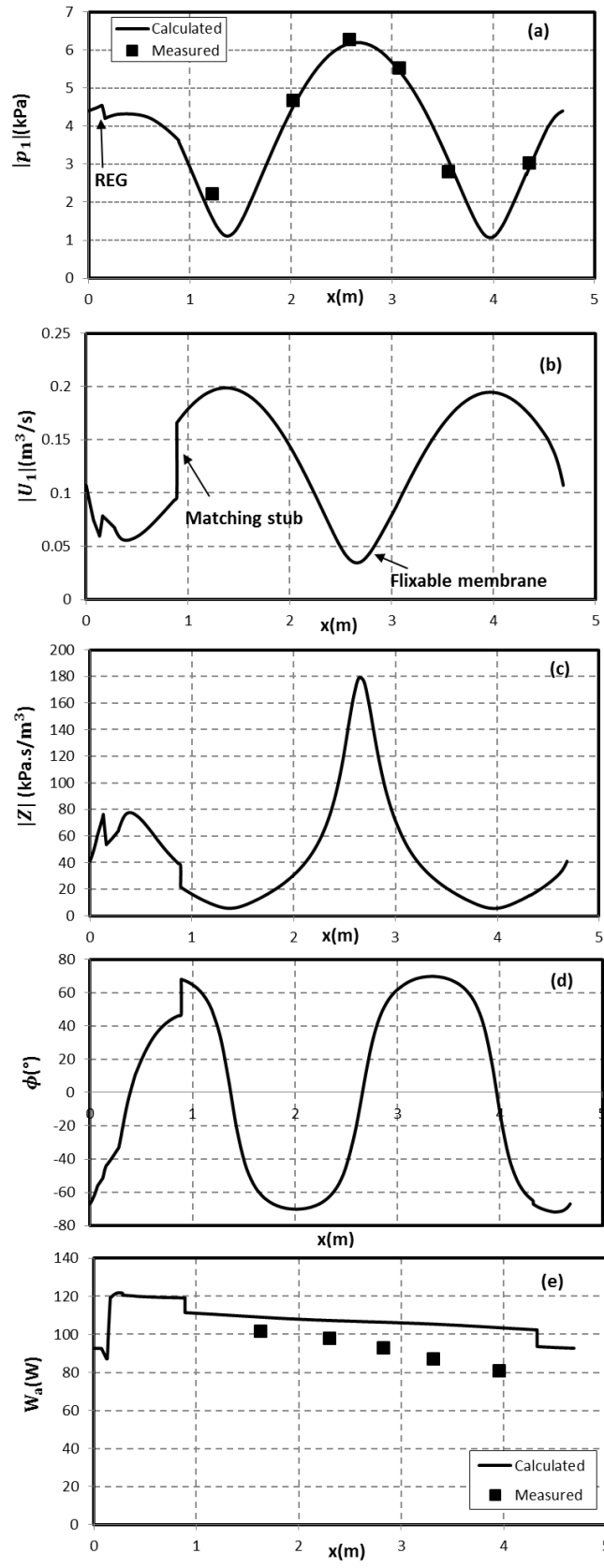


Figure 4. 9 The simulation results of the acoustic field in the 128-mm diameter thermoacoustic engine. (a) Pressure amplitude, (b) Volumetric velocity, (c) Acoustic impedance, (d) Phase difference and (e) Acoustic power flow.

higher acoustic velocities caused by higher temperature gradient in the regenerator. The sharp drop of the acoustic impedance at the T-type connection due to the presence of high volumetric flow introduced to the loop the stub. Apart from these sharp changes, the acoustic impedance is smooth along the loop.

Figure 4.9d presents the distribution of the phase difference between the acoustic pressure and velocity along the loop. It can be seen from the graph that the phasing of the acoustic impedance along the regenerator ranges between $-52.53 < \phi < -43.2$. One can notice that this is not the preferred phase difference at the regenerator of the travelling wave system. However, it should be taken into account that the thermoacoustic core of this generator was initially designed for the two-stage generator. Accordingly, the acoustic field in the loop will be different and hence a further optimisation is required to adjust the phasing of the regenerator.

Figure 4.9e shows the measured and simulated acoustic power distribution along the loop. From the graph, it can be seen that the regenerator produces around 32 W of net acoustic power and around 92.6 W flows in the loop to feedback into the thermoacoustic core. Good agreement between the measured and simulated results was achieved when the acoustic power enters the feedback loop but there is some disagreement when the power enters the thermoacoustic core.

4.2.2 Effect of the acoustic streaming on the performance of the engine at different stub lengths

In this section, a set of experiments has been conducted on the experimental rig of the thermoacoustic engine to investigate the behaviour of the engine by changing the stub length. The investigation also involved the effect of the acoustic streaming on the performance of the engine. In the experiments, the compressed air flow rate was set around 1015 litre/minute, the heating temperature of the heat gun was fixed at 570°C and the flow rate of the cooling water was 0.4 litre/minute. Additionally, the experimental working frequency was 70.31 Hz. The first set of experiments was carried out without inserting the elastic membrane into the loop and acoustic streaming was observed. Later, the membrane was placed in the loop to suppress the streaming. During these experiments, the stub length was increased from 300 mm to

600 mm with a step of 50 mm. At each stub length, all data were collected after allowing the temperatures around 9 minutes for stabilisation.

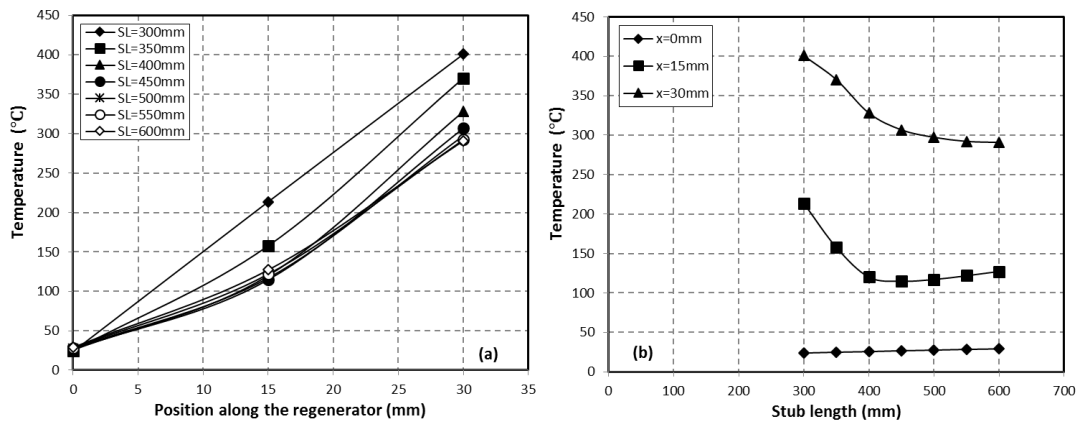


Figure 4.10 Effect of the stub length on temperature along the regenerator without membrane in the loop. (a) Temperature versus position of thermocouple. (b) Temperature versus stub length.

The effect of the acoustic streaming within the loop is clearly seen in the temperature distribution along the regenerator, as seen in Figures 4.10a and 4.10b. Figure 4.10a represents the temperature gradient along the regenerator while Figure 4.10b displays the effect of the stub length on the temperature of each location in the regenerator. It is clear from the graph that the acoustic streaming in the loop is in the direction of the acoustic power flow. The streaming becomes more significant as the stub length increases from 300 mm to 450 mm, and grows steadily for further stub lengths as seen from the graphs.

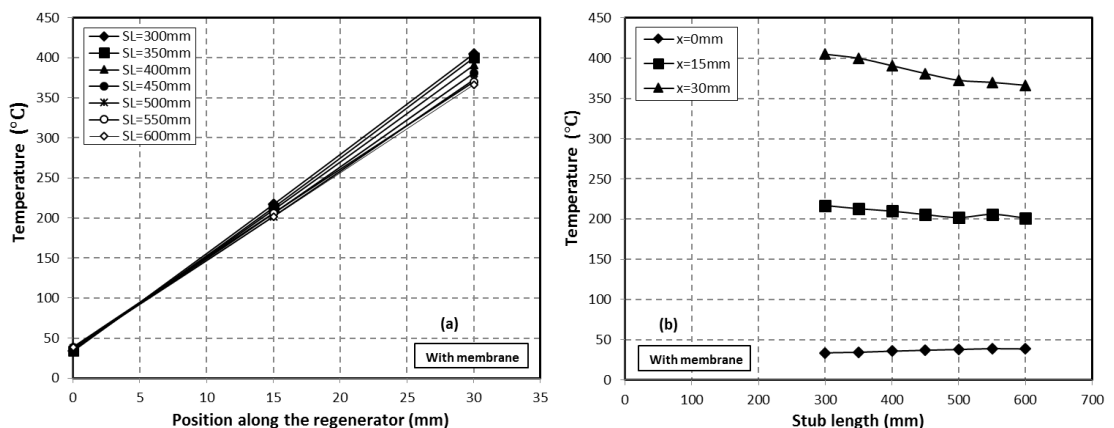


Figure 4.11 Effect of the stub length on temperature along the regenerator with a membrane inserted into the loop. (a) Temperature versus position of thermocouple. (b) Temperature versus stub length.

This is clear when the temperature of the hot end of the regenerator dropped sharply from 401.3 to 306.67°C and then steadily decreased to 290.84°C. Nevertheless, when the fixable membrane was placed into the loop near the velocity node of the volumetric velocity, the acoustic streaming was stopped, as seen in Figures 4.11a and 4.11b. In Figure 4.11a, a linear temperature profile can be seen, while in Figure 4.11b, a steady drop in the hot side and mid-point temperatures due to the increase of the stub length can be identified.

The effects of acoustic streaming can also be observed in Figure 4.12 which gives the temperature difference between the two ends of the regenerator for the two cases studied. The diamonds represent the case of the streaming present in the loop while the squares show the case after suppressing the streaming. In contrast to a relatively mild and almost linear drop of temperature difference when the membrane was inserted, a sharp decrease in the temperature difference can be seen when streaming was present in the loop. Furthermore, the ratio of slopes (the concept will be discussed in more detail in section 4.4.2) also yields a clear observation of the acoustic streaming in the loop, as seen in Figure 4.13. When the acoustic streaming exists in the loop, the ratio of slopes falls dramatically as the stub length is increased. On the other hand, if the membrane is inserted in the loop, the streaming is suppressed and the ratio of slopes becomes around 1.

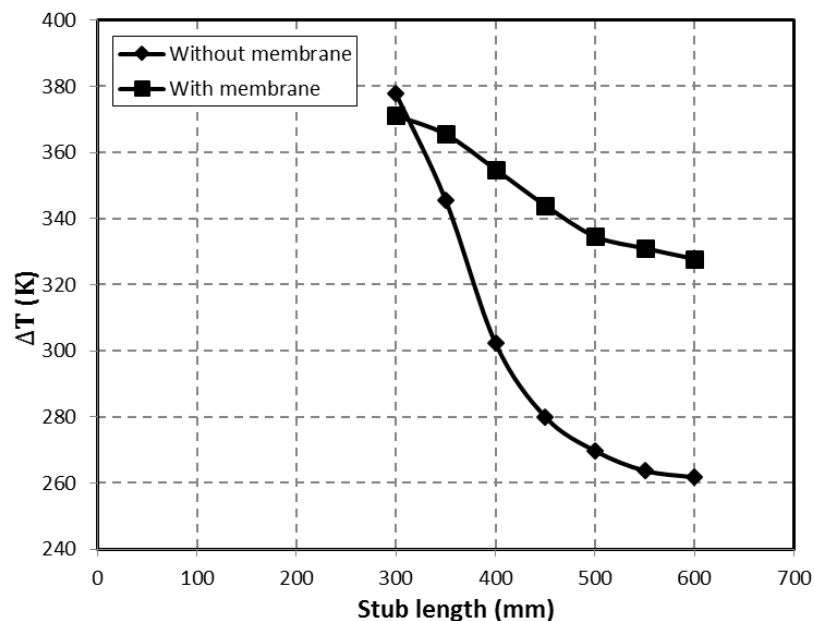


Figure 4.12 Effect of the stub length on the temperature difference in the regenerator.

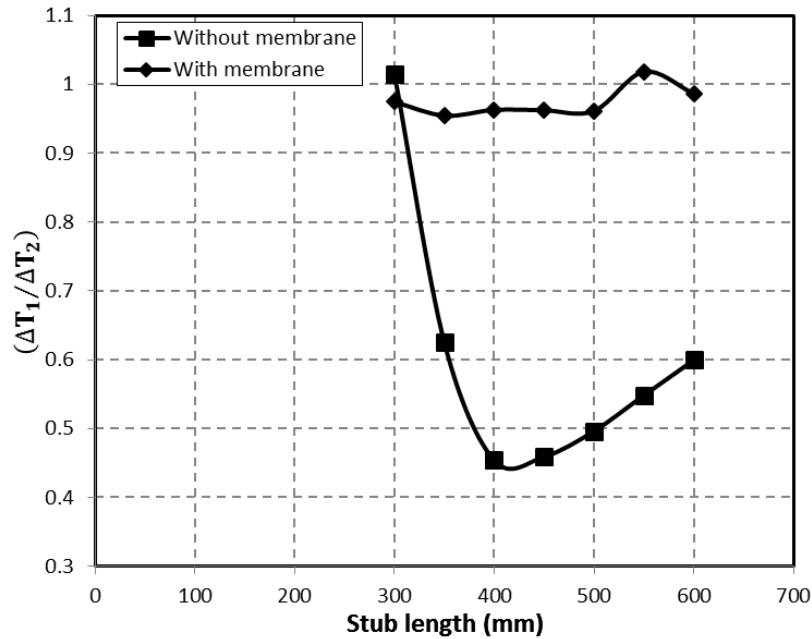


Figure 4. 13 Effect of the stub length on the ratio of temperature slopes.

Figure 4.14 shows the effect of the stub length on the pressure amplitude distribution along the loop in the presence of the acoustic streaming while Figure 4.15 presents the effects after the acoustic streaming is eliminated. The increase of the stub length will increase the pressure amplitudes. However, the pressure amplitudes in the presence of the acoustic streaming are lower than those in the absence of the streaming. For example, the pressure amplitude of P4 in the case of streaming is 4.15 kPa while it is 5.55 kPa for the identical stub length of 450 mm. As discussed earlier, this was caused by the streaming that takes heat away. Further discussion of these effects will be provided in section 4.4.2.

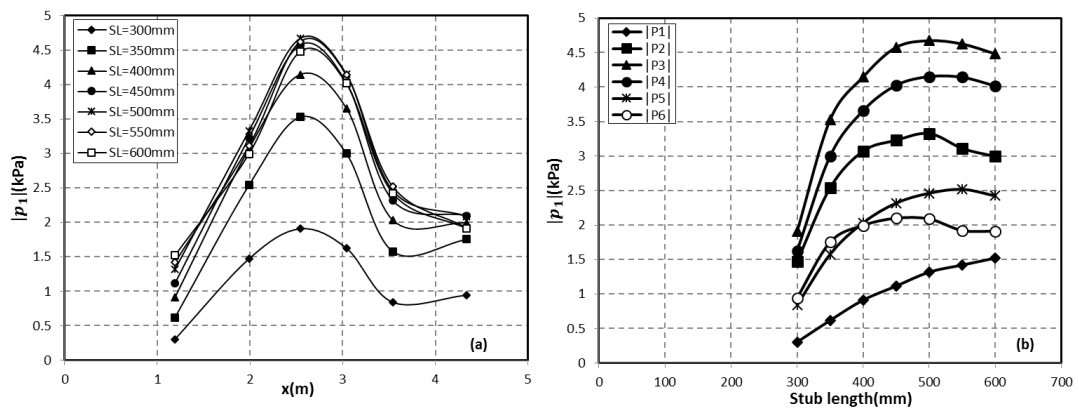


Figure 4. 14 Effect of the stub length on acoustic pressure distribution along the loop without a membrane in the loop. (a) Pressure amplitude versus loop length, and (b) Pressure amplitude versus stub length

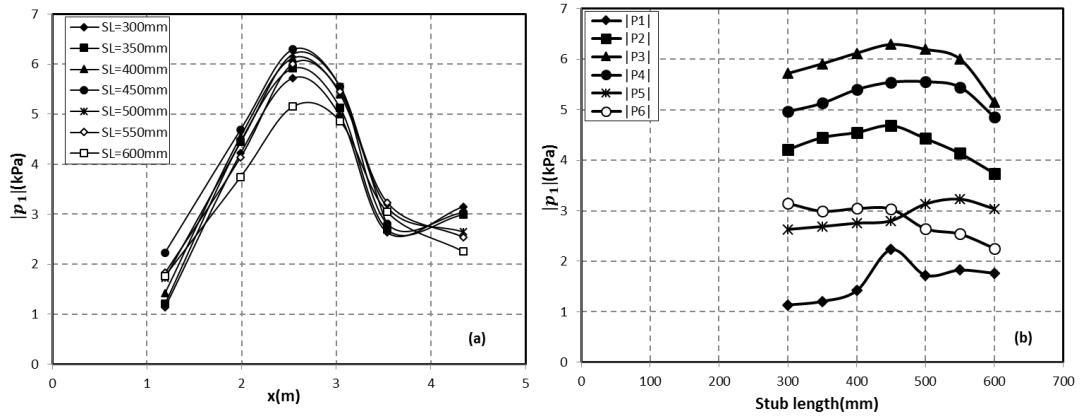


Figure 4.15 Effects of the stub length on pressure amplitudes along the loop with a membrane in the loop. (a) Pressure amplitude versus loop length and (b) Pressure amplitude versus stub length.

Figure 4.16 presents the effect of the stub length on the acoustic power distribution in the loop of the thermoacoustic engine. The effects of the acoustic streaming can be seen in Figure 4.16a, while Figure 4.16b shows the effects of the stub length after the suppression of the acoustic streaming. It is clear that increasing the stub length increases the acoustic power flow in the loop, as seen in Figure 4.16a. However, this increase is almost doubled when the acoustic streaming is eliminated by the elastic membrane, as seen in Figure 4.16b. As seen from both graphs, the optimal stub length that tuned the acoustic field to produce the maximum acoustic power was around 550 mm.

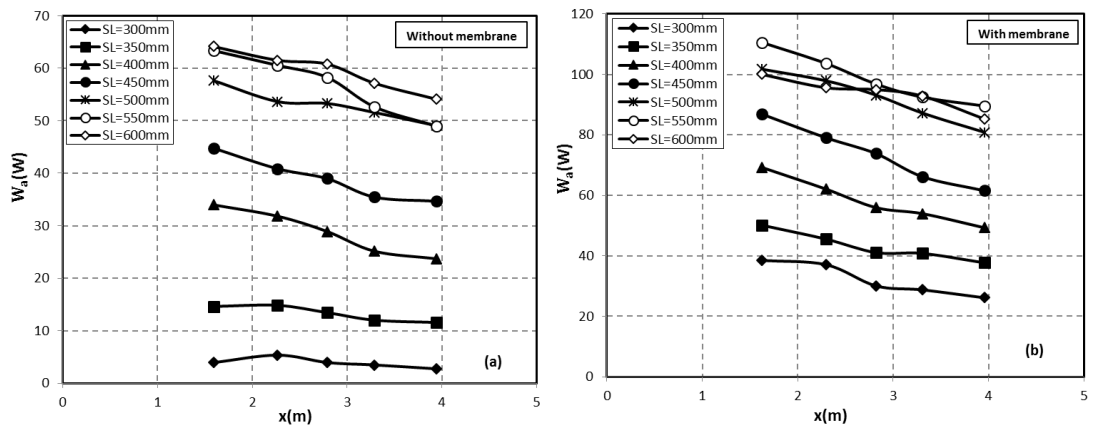


Figure 4.16 Effect of the stub length on the acoustic power flow along the loop. (a) Without membrane and (b) With a membrane installed in the loop.

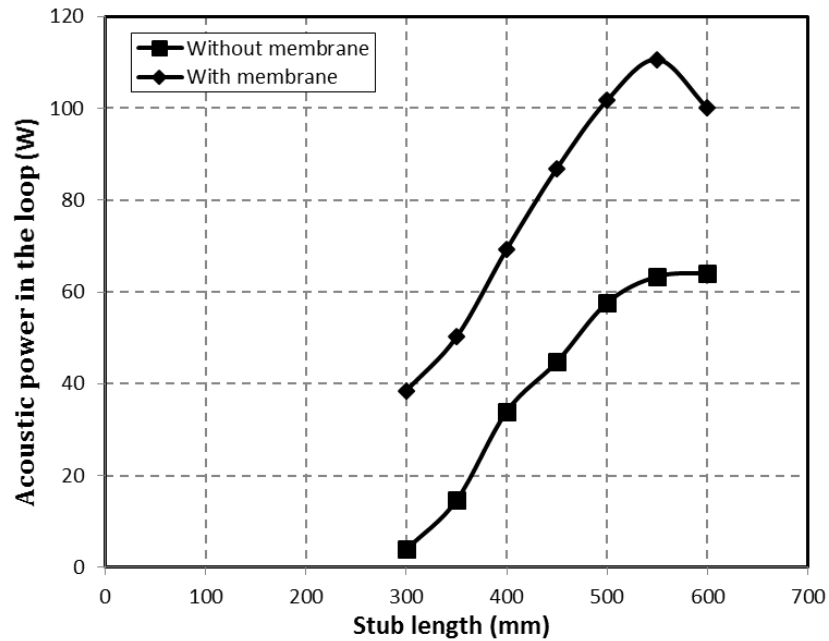


Figure 4. 17 Effect of the stub length on the acoustic power delivered to the loop.

The results of the effect of the stub length on the acoustic power that enters the feedback pipe are also represented in Figure 4.17. Here the acoustic power increases from 38.45 W to reach around 110.6 W at the optimal stub length. However, when acoustic streaming takes place, the acoustic power does not exceed 63.4 W at this length. It is useful to note, that DeltaEC does not predict streaming as this is beyond the scope of linear theory. However, as discussed in section 4.2.1, the acoustic power levels measured within the feedback pipe are broadly in agreement with those predicted when the streaming is stopped by the membrane.

4.2.3 Effects of different working frequencies

Although the system was tested at working frequency of 70.31, it was intended to practically investigate two more frequencies to estimate the optimal one for the system when the alternator is not attached to the loop. This would investigate the optimal frequency of a particular regenerator characteristics. On the other hand, this would also highlight the required resonance frequency of an alternator that should be used when connected to the system in order to achieve high acoustic-to-electric conversion efficiency. Therefore, this section involves the investigation of the effect of the stub length on the performance of the engine at two different working frequencies. These frequencies should be close to the range of the resonance

frequencies of commercial linear alternators. Frequencies of 48.82 and 64.45 Hz were selected. These working frequencies corresponded to loop lengths of 6.44 m and 4.92 m respectively. In the experiments, the compressed air flow rate was set at around 964 litre/minute and the heating temperature of the heat gun was fixed at 550°C, the flow rate of the cooling water was 0.8 litre/minute. Six pressure sensors were placed on the feedback pipe to estimate the acoustic power flow. Additionally, in the experiments the acoustic streaming was blocked by the fixable membrane inserted near the volumetric velocity in the loop. During these experiments, the stub length was increased from 350 mm to 800 mm with a step of 50 mm. Results of the experiments are presented and discussed.

Figure 4.18 shows the effect of the stub length on the temperature gradient along the regenerator at a working frequency of 48.82 Hz, while Figure 4.19 shows the corresponding effect at the working frequency of 64.45 Hz. It can be seen from both graphs that the temperatures of the hot side and the mid-point of the regenerator at the frequency of 64.45 Hz were higher than those at the frequency of 48.82 Hz along the stub lengths. This difference can also be seen in Figure 4.20. It presents the effect of the stub length on the temperature difference between the two ends of the regenerator at the two working frequencies. Here, also the differences in temperature are higher in the case of the frequency of 64.45 Hz.

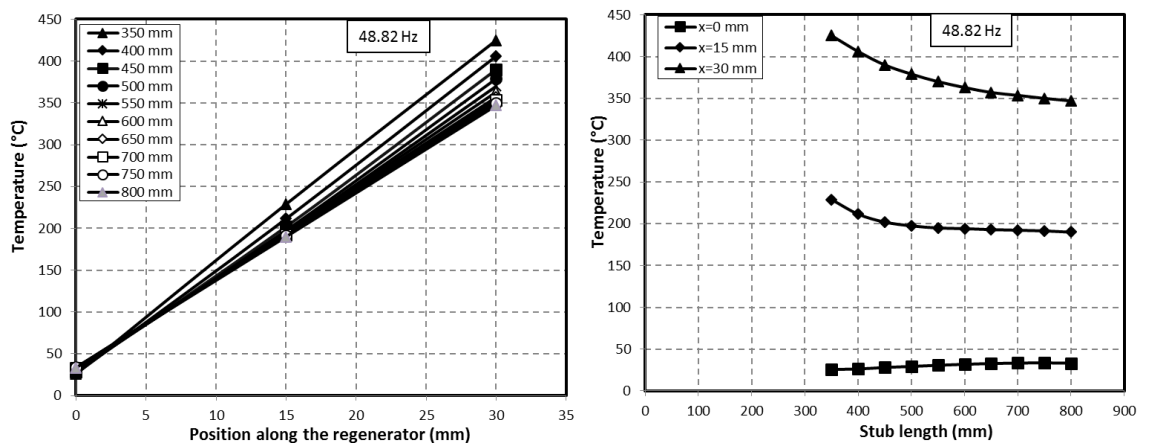


Figure 4.18 Effect of the stub length on the temperature profile in the regenerator and working frequency of 48.82Hz. (a) Temperature versus length of the regenerator and (b) Temperature versus stub length

The thermal penetration depth δ_k is considerably affected by the temperature, the mean pressure and the working frequency, as seen in Equation (2.3). At fixed mean pressure, the ratio δ_k/r_h is influenced by the stub length that reduces the temperature in the regenerator and working frequency as seen in Figure 4.21. The gradual fall in temperature by the stub length increases the working air density and gradually decreases δ_k . On the other hand, the jump in the working frequency from 48.82 to 64.45 Hz dramatically decreased the ratio δ_k/r_h .

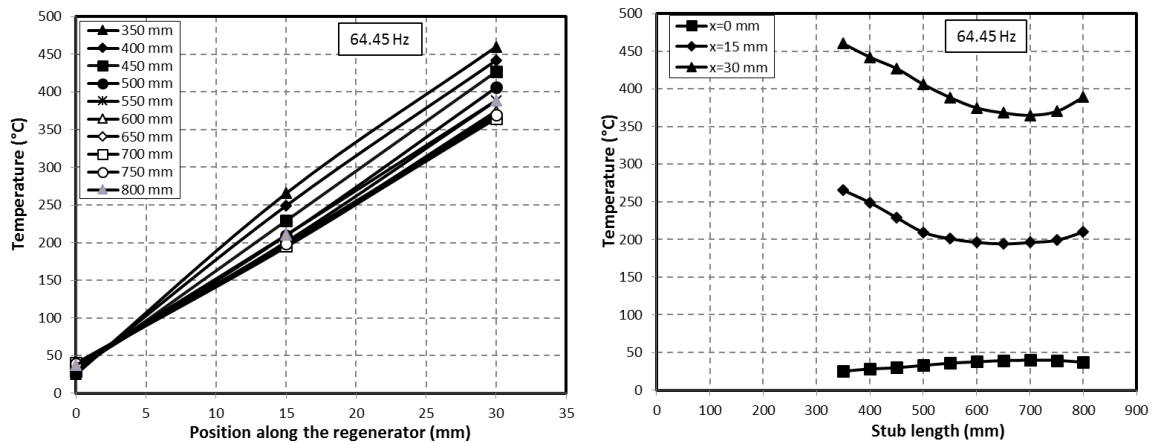


Figure 4.19 Effects of the stub length on the temperature profile in the regenerator and working frequency of 64.45Hz. (a) Temperature versus length of the regenerator and (b) Temperature versus stub length.

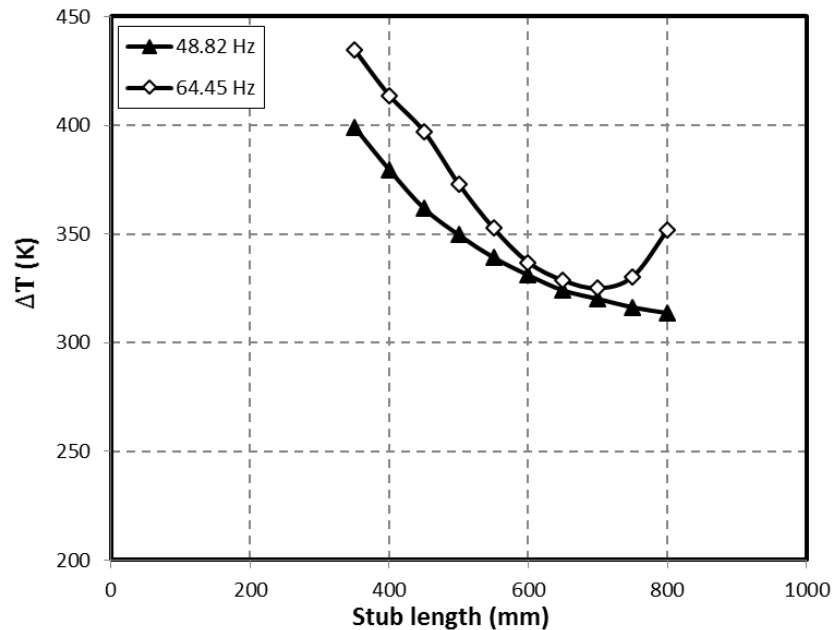


Figure 4.20 Effect of the stub length on the temperature difference in the regenerator for the frequencies 48.82 and 64.45 Hz.

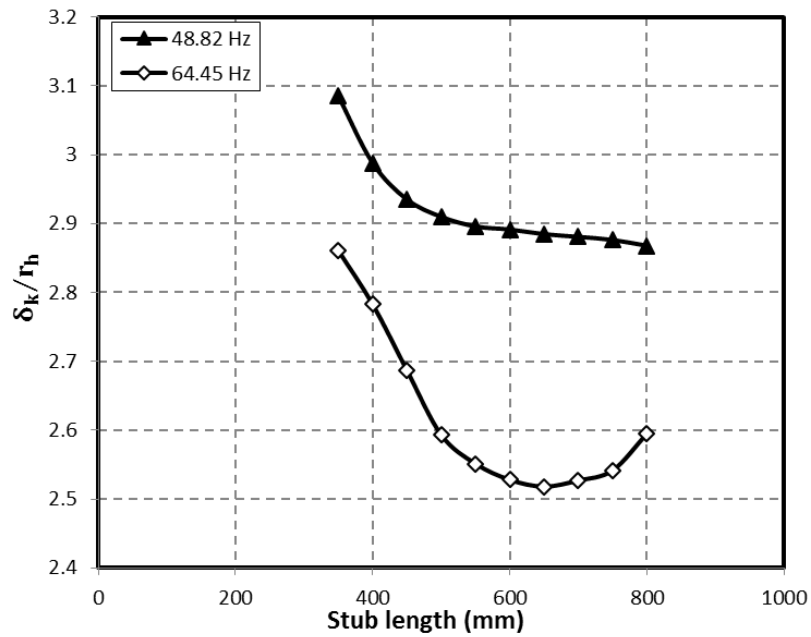


Figure 4. 21 Effect of the stub length on the ratio of the thermal penetration depth to the hydraulic radius in the regenerator for the frequencies 48.82 and 64.45 Hz.

Among the set of pressure sensors used, sensor P6 was placed around 240 mm away from the ambient heat exchanger to estimate the pressure ratio of the engine for both frequencies. Figure 4.22 presents the effect of the stub length on the drive ratio of the engine for the frequencies 48.82 and 64.45 Hz. From the graph, the maximum pressure drive ratio is around 2.6% obtained at the frequency of 64.45 Hz. It is also clear that the pressure drive ratio increased sharply when the stub length was increased at the frequency of 64.45 Hz, while the increase was gradual in the case of 48.82 Hz. The effects of different frequencies can also be observed in the increase in the acoustic power flow in the loop, as seen in Figure 4.23. At 700 mm of the stub length, the acoustic power flow in the feedback pipe significantly increased from 136 W to around 165 W when the working frequency was raised from 48.82 to 64.45 Hz.

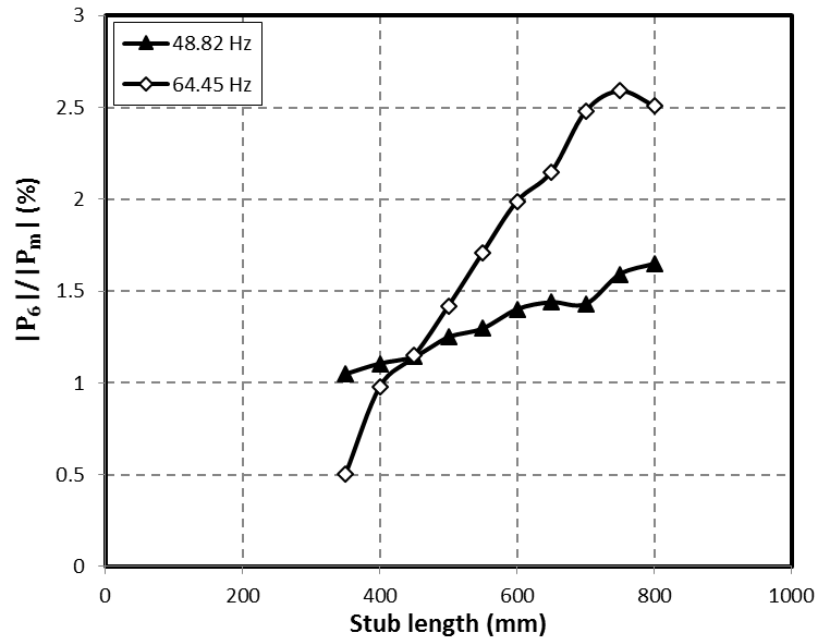


Figure 4. 22 Effects of the stub length on the pressure ratio for the frequencies 48.82 and 64.45 Hz.

The increase in the working frequency from 48.82 to 64.45 Hz decreases the ratio δ_k/r_h which reduces the thermal contact between the oscillating air and the regenerator material. However, the power density in the engine is linearly proportional to the working frequency (Swift, 2002). Therefore, the increase in the frequency will increase the volumetric velocity, as shown in Equation (2.5). As a result, the heat input to the hot heat exchanger increases and causes a rise in the temperature difference of the regenerator, as shown in Figure 4.20, and a rise in the pressure amplitudes, as seen in Figure 4.22. The rise in the pressure amplitude and the volumetric velocity will significantly increase the acoustic power, as seen in Equation (2.40). However, the increase of the frequency should be limited to the optimal value where further increase in frequency leads to viscous dissipation and significantly reduces the thermal penetration depth in the regenerator. This is clearly seen in Figure 4.17 where the frequency of 70.31 Hz reduced the acoustic power to 110.63 W at the optimal stub length of 550 mm. It should be also noted from Figures 4.17 and 4.23 that the optimal stub length degrades when the frequency is increased. Here one can see that the optimal lengths at the frequencies 48.82, 64.45, and 70.31 Hz are around 800, 750 and 550 mm.

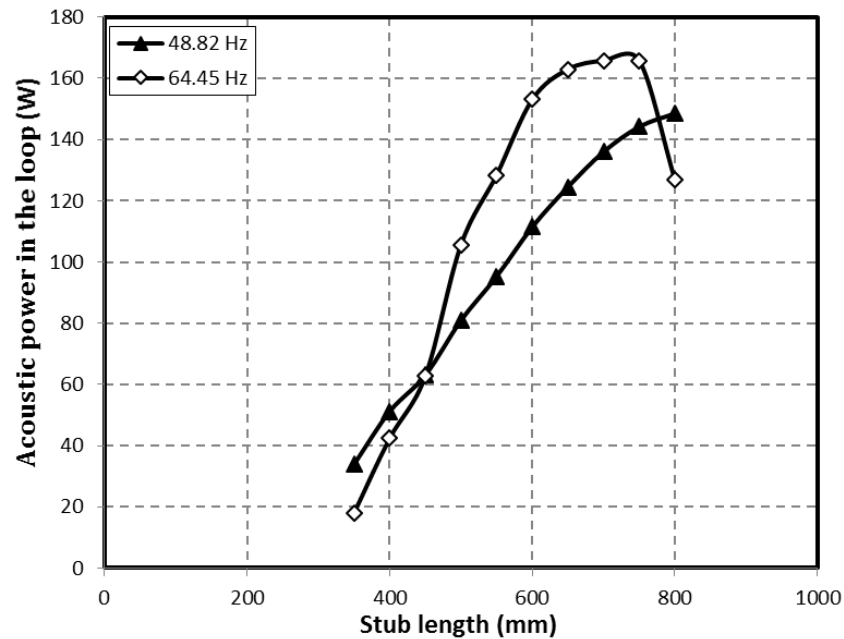


Figure 4. 23 Effects of the stub length on the acoustic power in the loop for the frequencies 48.82 and 64.45 Hz.

4.3 A 128-mm Diameter One-stage Electricity Generator

In this section, DeltaEC simulations and experimental results of the 128-mm diameter one-stage looped-tube electricity generator are presented. The results obtained from the simulation of DeltaEC along the loop of the generator are shown as pressure amplitude distributions, volumetric velocity distributions, acoustic impedance and its phasing and finally the acoustic power distribution. The simulated results are shown and discussed in section 4.3.1. Comparisons between the experimental results and the calculated results of the generator regarding the effect of the load resistance on the generator performance are presented and discussed in section 4.3.2. Finally, the effect of the heating power supplied to the HHX on the general performance is presented by comparison between calculated and measured results in section 4.3.3.

4.3.1 Simulation results

The results shown in this section are obtained from the simulations of the prototype according to the block diagram shown in Figure 3.9 in Chapter 3. The calculations were carried out under the following conditions: air is used as the working gas, the mean pressure is 0.1 MPa, the calculated working frequency is 55.87 Hz and the load resistance is 10 Ω . Although, 55.87 Hz is away from the

resonance frequency of the alternator, however, it is a trade-off between the optimal frequency of the regenerator (64.45 Hz) and the alternator resonance frequency (39.77 Hz) in order to achieve high acoustic power production.

The results of the simulation are based on guessing the heating power at the HHX to target the pressure amplitude of 5.67 kPa of pressure sensor P3 that is obtained from the experiments. Pressure sensors P1, P2, P3, P4 and P5 are placed at 1.63, 2.75, 3.14, 3.74, and 5.52 m away from the ambient heat exchanger, respectively, whereas the total length of the loop is 5.9 m. The results of the simulation of the one-stage generator are presented in Figure 4.24.

Figure 4.24a shows the measured and calculated pressure amplitudes distribution along the loop. The difference between the measured and simulated pressure amplitudes is presented in Table 4.2. For the same thermoacoustic core used in the engine, that was shown in Figure 4.9a that the pressure amplitudes distribution follows the same trend. However, the different locations and number of pressure sensors and longer loop length are shown in Figure 4.24a. When Figures 4.9a and 4.24a are compared, one can see that the pressure drop in the regenerator in the case of the generator is higher than that in the engine. This is due to the higher flow resistance occurred in the regenerator.

Figure 4.24b shows the distribution of volumetric velocity amplitudes along the loop of the single generator that is follow the same trend in the case of the engine as was shown earlier in Figure 4.9b. However, the regenerator of single generator introduces higher and steeper raise of the volumetric velocity as shown in Figure 4.24b. This is caused by the higher temperature gradient that occur in the regenerator of the single generator. Comparing to Figure 4.9b, the second sharp increase in the volumetric velocity amplitude that occurred at the T-junction caused by the presence of the alternator branch in the single generator.

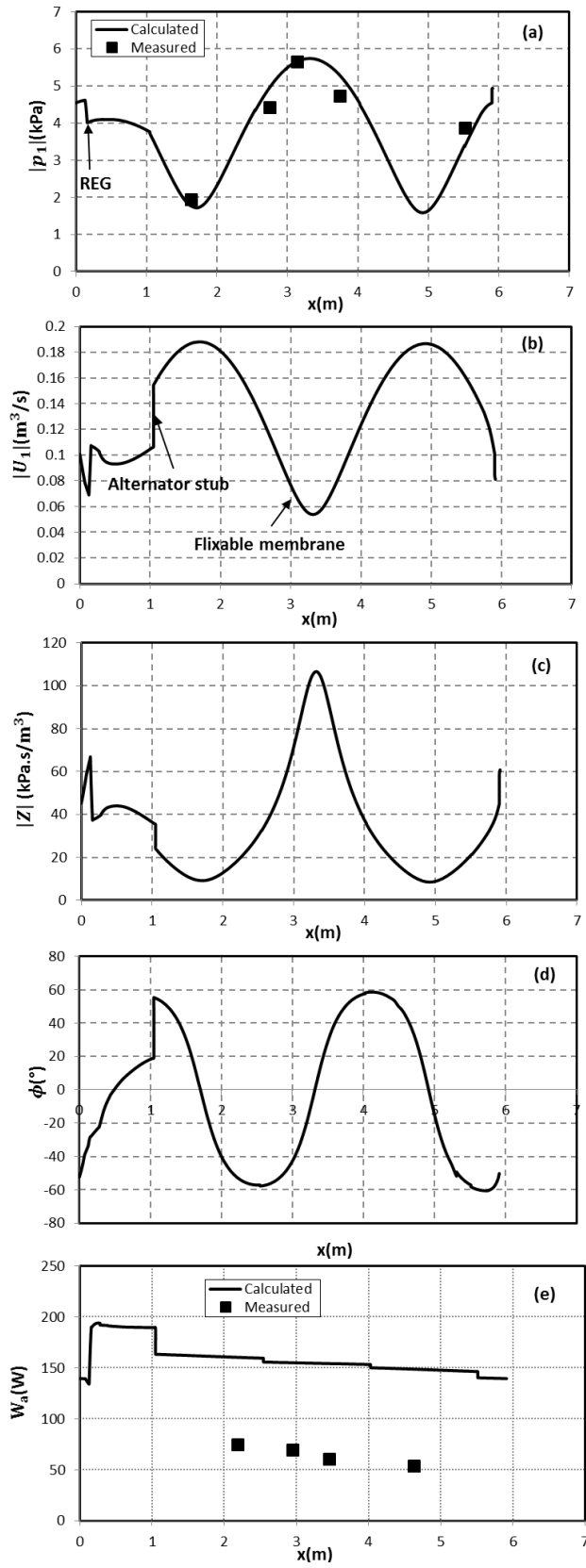


Figure 4. 24 The calculation results of the acoustic field in the large diameter, one stage electricity generator. (a) pressure amplitude (b) volumetric velocity (c) acoustic impedance (d) phase angle and (e) acoustic power flow.

Figure 4.24c presents the distribution of the acoustic impedance in the loop of the single generator. From the graph it is seen the distribution is similar to that in Figure 4.9c. However, here one can see a sharper and steeper dropping the acoustic impedance in the regenerator compared to that in Figure 4.9c. The higher acoustic velocities caused by higher temperature gradient in the regenerator of the single generator are involved. The second sharp drop of the acoustic impedance in the loop is by the branch of the alternator.

Figure 4.24d presents the distribution of the phase difference between the acoustic pressure and velocity along the loop of the single generator. Generally speaking, a similar trend of the distribution can be seen from the graph. However, the phasing of the acoustic impedance along the regenerator ranges between $-32.24 < \phi < -27.57$. This is a closer to the preferred phase difference at the regenerator of the travelling wave system compared to that of the engine in Figure 4.9d. However, if a matching stub is connected to the loop, the phasing and the acoustic impedance in the loop can also be tuned further.

Figure 4.24e shows the measured and simulated acoustic power distribution along the loop. From the graph, it can be seen that around 139.4 W of acoustic power enters the AHX that dissipates 5.2 W. The regenerator amplifies the acoustic power from 134.2 to 190 W producing a net acoustic power of around 55.8 W. At a calculated heating power of around 528 W, the calculated thermoacoustic efficiency is around 10.6%. The acoustic power of around 20.43 enters the stub and dissipates around 2.1 W in the stub before it reaches the alternator at 18.33 W. The remaining power (approximately 168 W) is fed into the thermoacoustic core through the loop. There are four pressure sensors to measure the acoustic power flow in the loop and good agreement is obtained in measuring the pressure amplitudes as seen in Figure 4.24a. However, a considerable discrepancy between the measured and calculated acoustic power can be found. This was due to the standing wave ratio in the measurement being higher than that in the simulations (Yu and Jaworski, 2012).

As mentioned above, Table 4.2 shows a comparison between the measured and calculated pressure amplitudes along the loop. As seen from the table, the pressure amplitude at ($x = 3.14$ m) is essentially measured and targeted in the simulation. Pressure sensor P6 is located at the alternator around 1.49 m away from

the T-junction. The overall error between the measured and simulated pressure amplitudes was around 9.8%. In this simulation, the alternator produces a maximum of 10.13 W of electrical power. The heating power input of the HHX is 528.28 W. As a result, the calculated maximum thermal-to-acoustic efficiency of the generator is around 3.47%, the thermal-to-electric efficiency is 2.53%, and the acoustic-to-electric efficiency is 51.9%.

Table 4. 2 The results of measured and simulated pressure amplitudes along the loop of the single-stage generator

P	x (m)	$p_1 _{(Measured)}$ (kPa)	$p_1 _{(Calculated)}$ (kPa)	Error (%)
P1	1.63	1.95	1.78	9.15
P2	2.75	4.43	4.96	10.76
P3	3.14	5.67	5.67	0 (targeted)
P4	3.74	4.73	5.3	10.68
P5	5.52	3.88	3.41	13.8
P6	At alternator	0.88	0.92	4.55

4.3.2 Effects of load resistance on performance of one-stage generator

The one-stage electricity generator was constructed as shown in Figures 3.10 and 3.11. This configuration does not have a separate matching stub when compared to the single-stage engine. However, an impedance matching device (54-mm diameter PVC tube) was introduced into the stub to match between the alternator and the loop. The elastic membrane was placed near the velocity node in the loop to suppress harmful acoustic streaming.

The first set of experiments was conducted to find the optimum load resistance that extracts maximum electrical power. In the experiments, the heating temperature of the heat gun was fixed to 535°C, the air flow was set to around 605 litre/minute and the cooling water flow rate was set to be 0.7 litre/minute. Throughout the

experiments, the load resistance ranged from 1 to 20 Ω with a step of 1 Ω . With each step, the temperatures were allowed around 8 to 10 minutes to become stabilised before collecting the data. During the experiments, the recorded working frequency was 54.69 Hz with an error of 2.11%.

Figure 4.25 shows the effect of the load resistance on the coil displacement of the alternator. The solid line represents the simulation results, while the black diamonds represent the measurements. Simulations and measurements share a similar trend. When the load resistance increases from 1 to 20 Ω , the measured displacement increases from 3.45 to around 5.71 mm, while the simulated displacement increases from 4.477 to 6.26 mm. The average error between the measured and simulated values was around 18.5%.

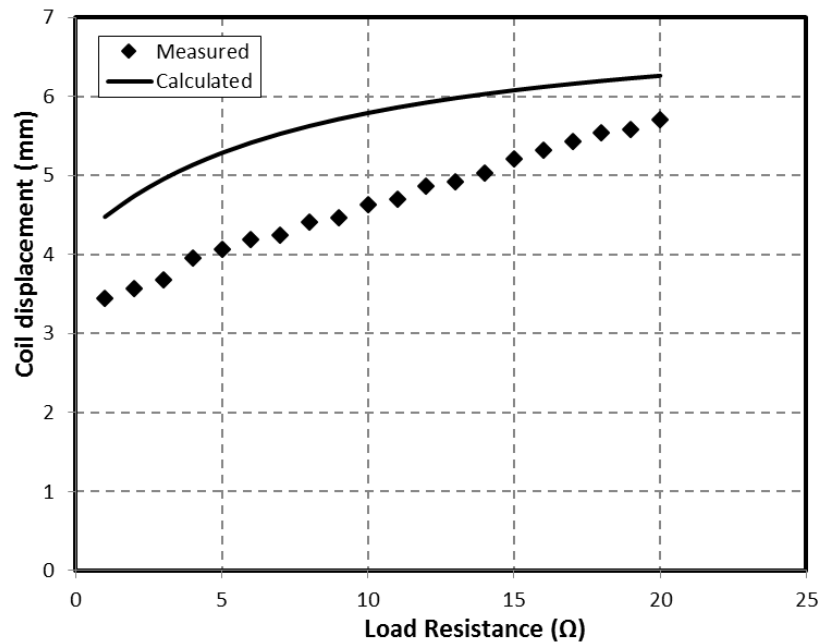


Figure 4. 25 Effect of the load resistance on the coil displacement of the alternator.

Figure 4.26 shows the calculated and measured results with regard to the effect of the load resistance on the acoustic power extracted by the alternator. It is clear from the graph that the increase in the load resistance from 1 to 20 Ω will decrease the measured acoustic power from 21.17 to around 9.8 W and the calculated acoustic power from around 24 to 14.22 W. Figure 4.49 presents the compared simulated and measured results of the load effect of the engine efficiency. Since the heat input was fixed, the increase of the load linearly decreases the efficiency as a

result of the acoustic power reduction. As a result, the measured and calculated engine efficiencies dropped gradually to reach 1.785 and 2.54% respectively.

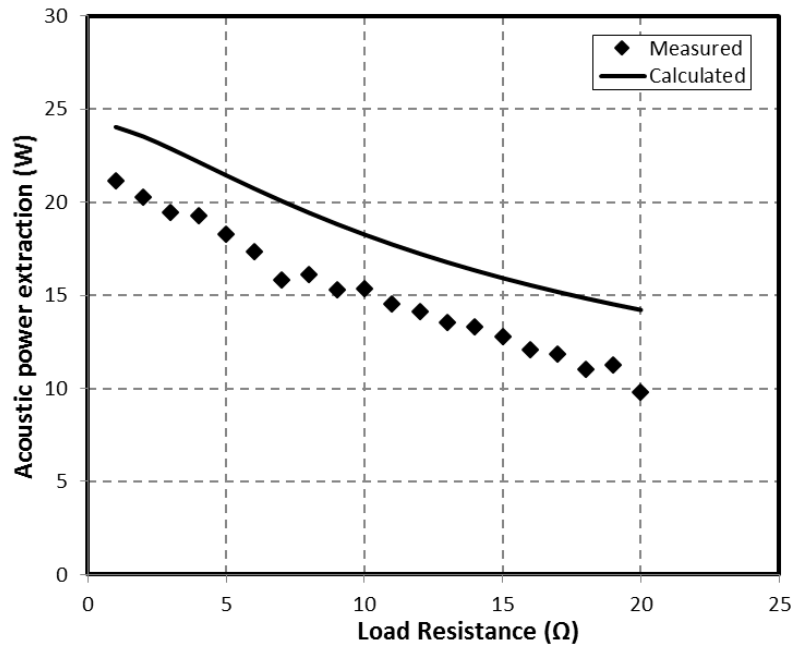


Figure 4. 26 Effect of the load resistance on the acoustic power extracted by the alternator.

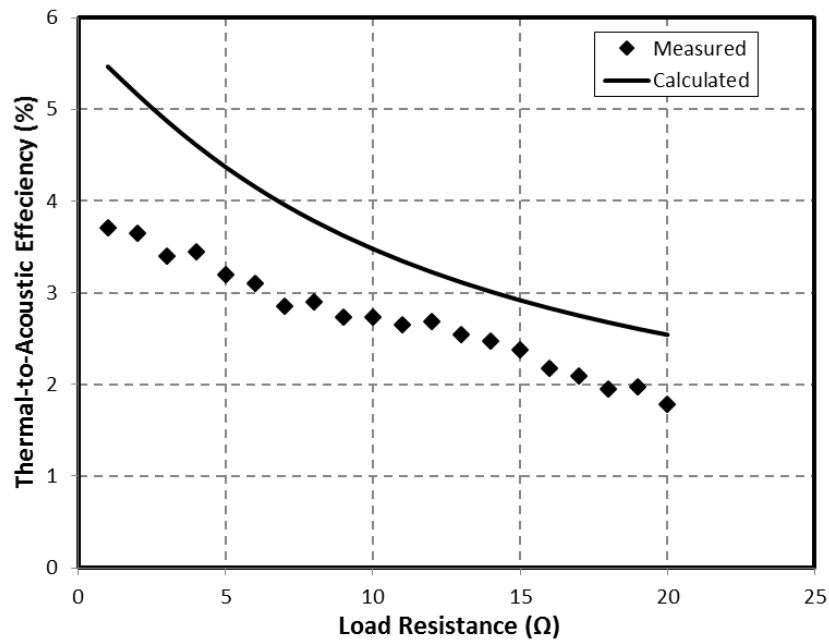


Figure 4. 27 Effect of the load resistance on the thermoacoustic engine efficiency.

Figure 4.28 shows the effect of the load resistance on the measured and simulated electrical power produced by the alternator. It is clear from the graph that the optimal load resistance was around 9 Ω . At this load resistance the measured electrical power extracted was around 8.46 W and the maximum calculated power was 10.13 W. Good agreement between the measured and calculated electrical power can be seen at lower loads.

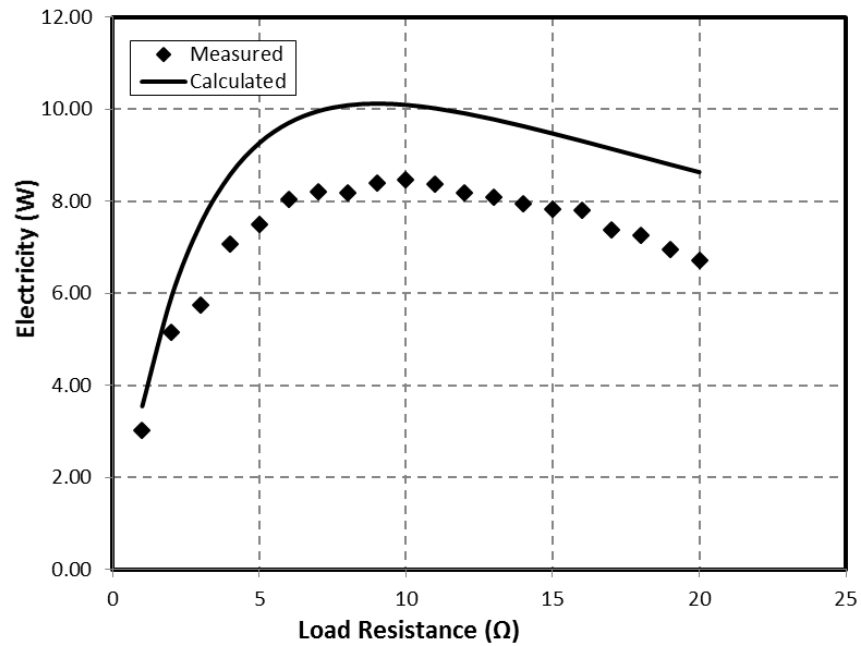


Figure 4. 28 Effect of the load resistance on the electricity produced by the alternator

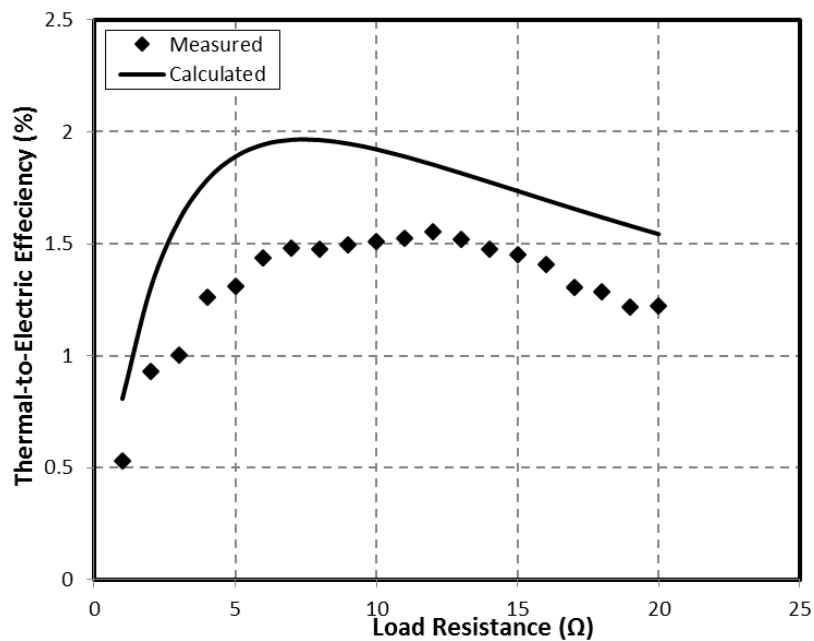


Figure 4. 29 Effect of the load resistance on the total efficiency of the generator

Figure 4.29 shows the effect of the load resistance on the thermal-to-electrical efficiency for both the calculated and measured results. It is shown that at the optimal load the maximum calculated efficiency was around 1.96%, and the measured efficiency was around 1.51%.

Figure 4.30 shows the effects of the load on the alternator efficiency. The measured efficiency increased gradually from 14.29% to around 68.5% when the load increased from 1 to 20 Ω . Good agreement between the experimental and simulated values can be seen in the graph.

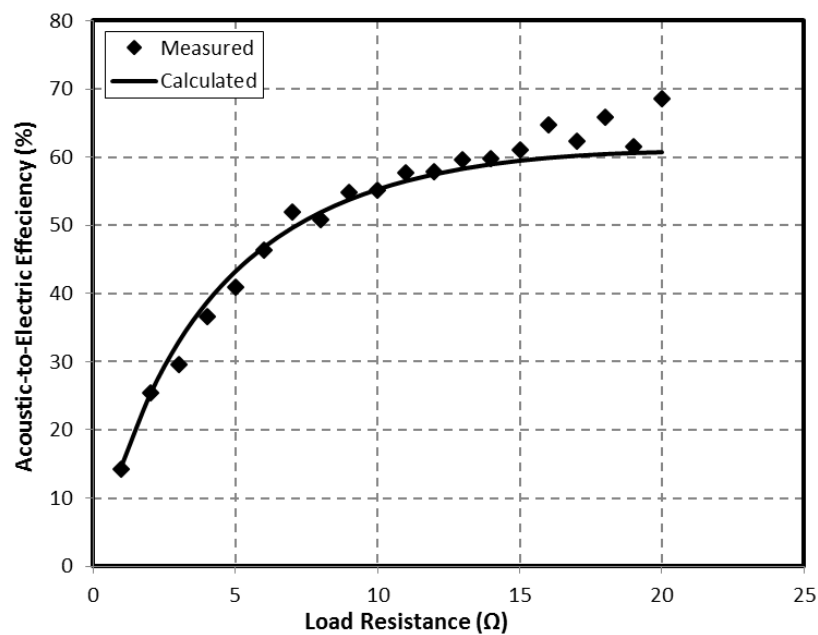


Figure 4. 30 Effect of the load resistance on the alternator efficiency.

4.3.3 Effects of heating power on one-stage electricity generator

In this section, the effects of the heating power input on the performance of the generator are investigated and discussed. During the experiments, load resistance is fixed to the optimal value of 9 Ω . The heating temperature of the heat-gun was gradually changed from zero to 550° C. At the beginning of the experiments, the flow rate of air that was provided by the compressor was set at around 657 litre/minute. The reading of the rotameter reads fixed flow rate of cooling water at 0.7 litre/minute.

The generator started the oscillation when the temperature difference between the two ends of the regenerator reached 215.7 K. At this stage, the temperatures were allowed around 9 minutes to stabilise in order to collect all data. This procedure was repeated for the heating temperature of the heat gun from 335 to 550° C with a step of 15° C.

Figure 4.31 presents the effects of the heat input of the hot heat exchanger on the temperature gradient along the regenerator. The temperature distribution along the regenerator was measured at three locations: 0, 15, and 30 mm away from the cold side of the regenerator. Since there was no streaming in the loop (the flexible membrane was placed in the loop), the temperature gradient at all heat inputs was linear. The graph shows that the slope of the temperature gradient increases as the heat input increases. When the heating temperature of the heat gun was raised from 335 to 550° C, the measured heat input increased from around 215 to nearly 581 W. The increase of the heat input in the hot heat exchanger as well as the heat rejected from the ambient heat exchanger are presented as a comparison between the measured and calculated values in Figure 4.32.

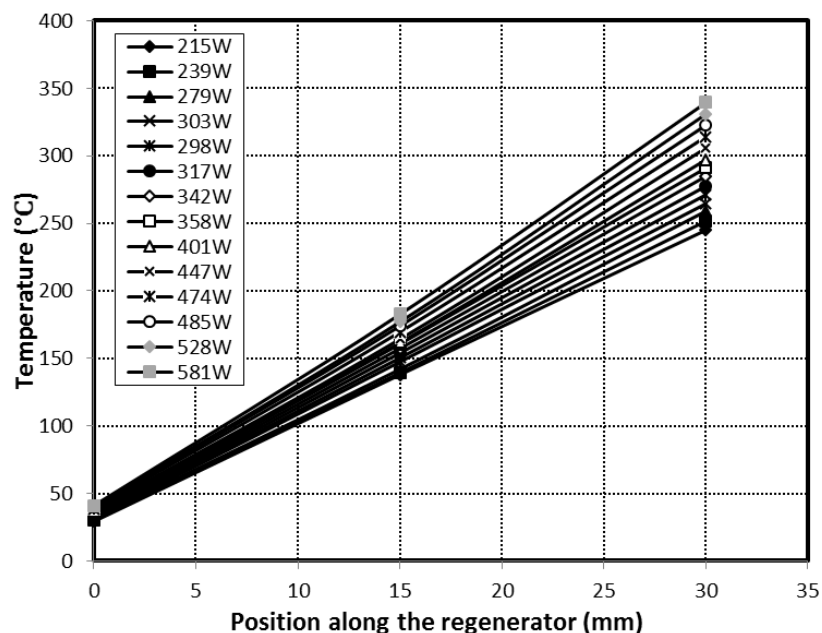


Figure 4. 31 Effect of the heat input on the temperature profile of the regenerator.

In order to draw a comparison between the measured and calculated heat input and heat rejected, the heat was represented as a function of the measured and calculated (targeted in the simulation) pressure ratio $|P_3|/|P_m|$. Along the increase of the heating temperature of the heat gun from 335 to 550° C, the pressure ratio at P3 rises from around 2.35% to around 5.59% and corresponds to raising measured heat input from 215 to 581W and raising measured heat rejected from 131.54 to 487 W. As seen in the graph, good agreement between the measured and calculated heat rejected was obtained whereas discrepancies between the measured and calculated heat input were found. This was due to errors occurring when measuring the heat input, as will be later discussed in section 4.4.

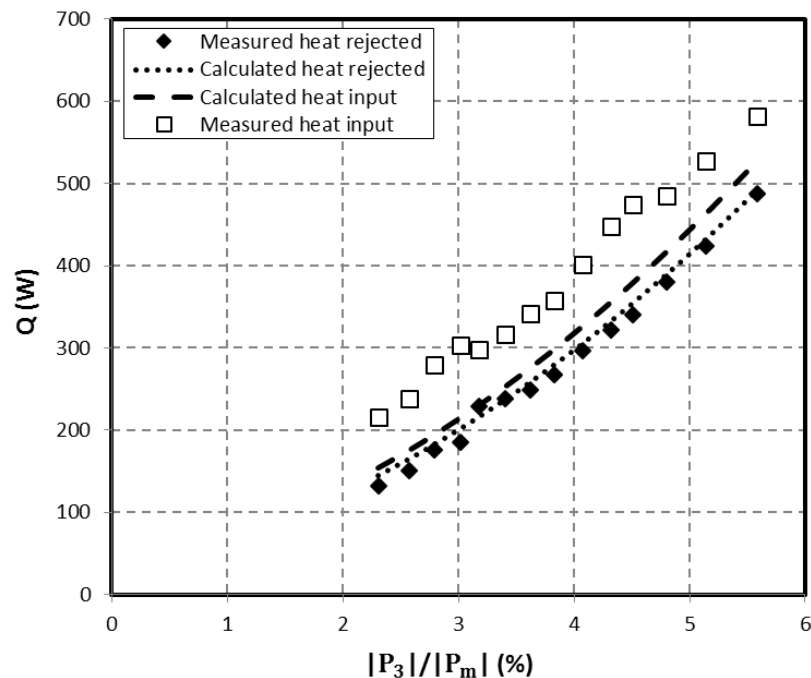


Figure 4. 32 Relationship between the pressure ratio and the heat input and heat rejected.

Figure 4.33 shows the measurements of the effect that the heat input had on the temperature difference between the two ends of the regenerator. The linear relationship between the heat input and the temperature differences is clearly shown in the graph. The temperature difference steadily increases to reach the maximum value of 298.3°C.

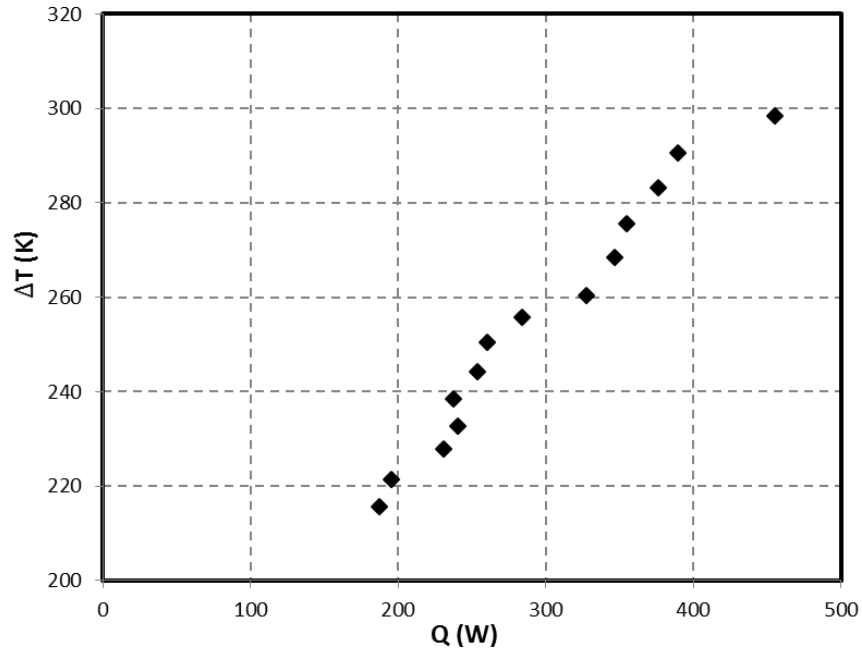


Figure 4.33 Effect of the increasing the heating power on the temperature difference in the regenerator.

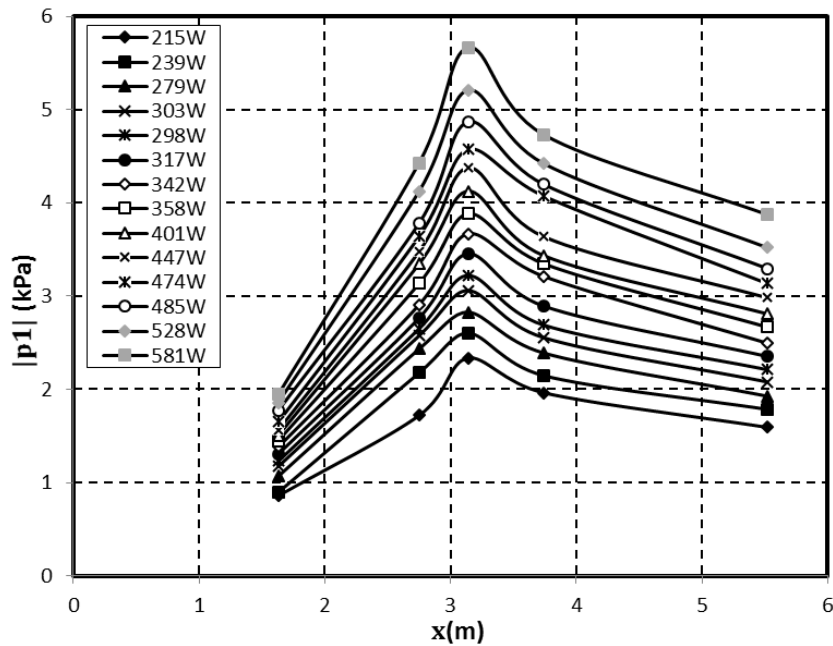


Figure 4.34 Effect of increasing the heat input on the acoustic pressure amplitudes along the loop.

Figure 4.34 displays the measurements of the heat input effects on the pressure amplitude distribution along the loop. The power density of the device is linearly proportional to the heat input. Therefore, the pressure amplitudes of P5 near the ambient heat exchanger increased to 3.87 kPa. The effect of the heat input on the measured acoustic power distribution along the loop is shown in Figure 4.35. As the

heat input is increased from 215 W to 581 W, the acoustic power that was fed into the loop increased from 19.96 to 119.45 W, while the acoustic power fed into the ambient heat exchanger increased from 15.67 to 91.86 W. The average acoustic power dissipated along the loop was around 28% of the power fed into the loop.

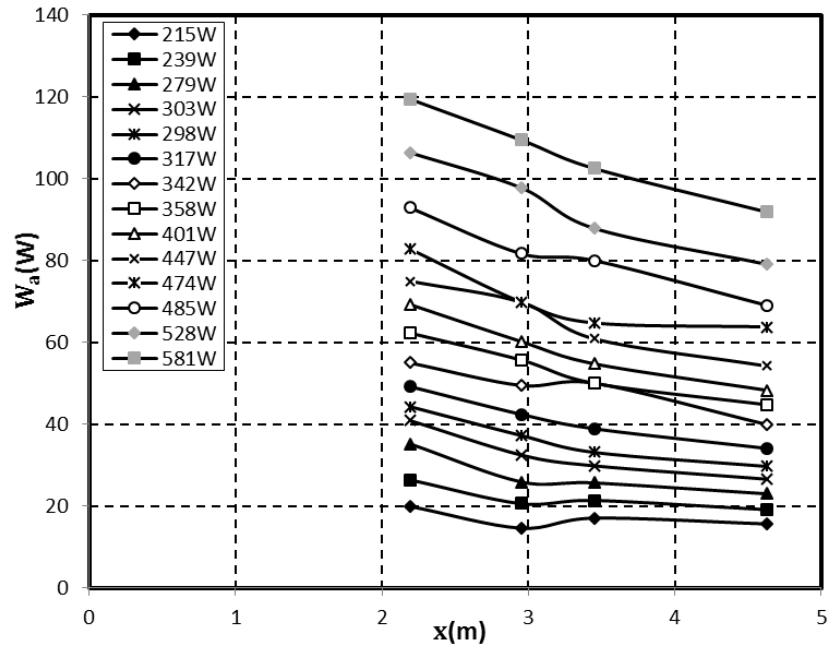


Figure 4.35 Effect of the heating power on the acoustic power flow in the loop.

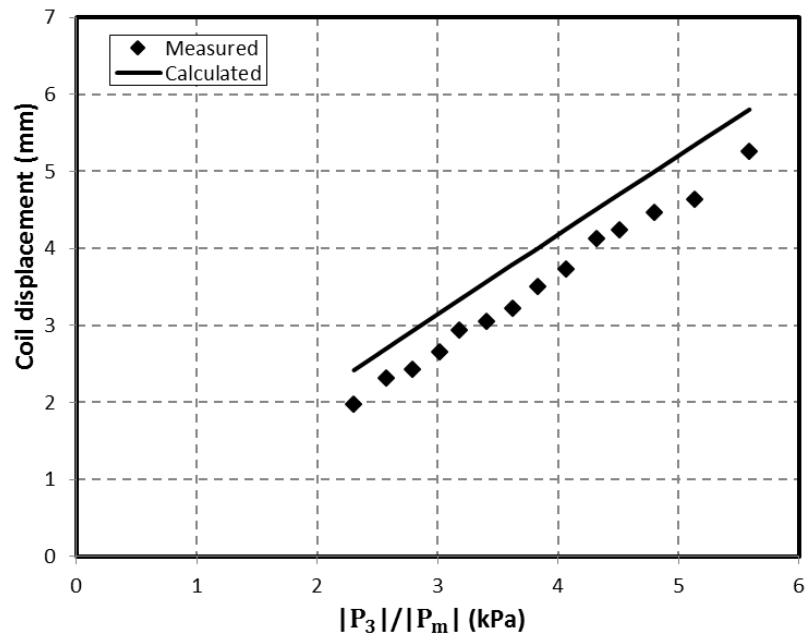


Figure 4.36 Influence of the heat input on the relationship between the pressure ratio and the coil displacement of the alternator.

Figure 4.36 shows the effects of the heat input on the relationship between the pressure ratio and the coil displacement of the alternator. The effects are presented as a comparison between the measured and calculated values. The measured values are shown as black diamonds while the calculated values are presented as a solid line. Here, both the measured and the calculated coil displacements have linear relationships with the pressure ratio and also with the heat input. The maximum measured coil displacement achieved was 5.26 mm at a pressure ratio of 5.59% and corresponding heat input of 581 W.

Figure 4.37 presents a comparison of the calculated and measured results due to the effect of heat input on the relationship between the pressure ratio and the acoustic power extracted by the alternator. A similar trend appears between the measured and calculated results. From the graph, at a maximum pressure drive ratio of 5.59%, the maximum measured and calculated acoustic power extractions are 16 W and 18.33 W, respectively.

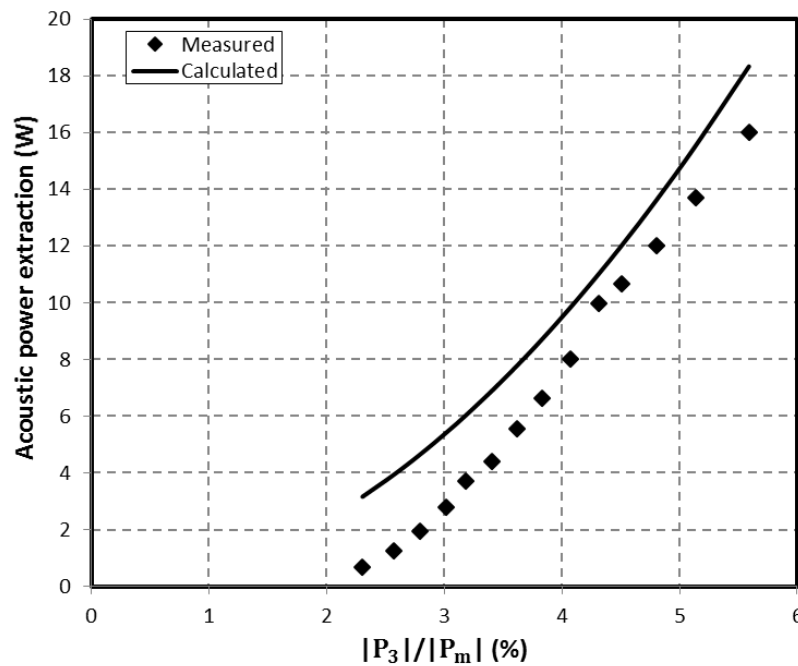


Figure 4. 37 Effect of the heat input on the relationship between the pressure ratio and acoustic power extracted by the alternator

Figure 4.38 shows the relationship between the pressure ratio of the pressure amplitude P3 and the thermal-to-acoustic efficiency. With the increase of the pressure drive ratio, the measured and the calculated efficiency increases gradually to reach around 2.75% and 3.47%, respectively. A similar trend between the

measured and calculated values can be seen in the graph. The disagreement between the measured and calculated efficiencies can be attributed to the fact that some of the heating power is lost by conduction in the stainless steel tubes and frame.

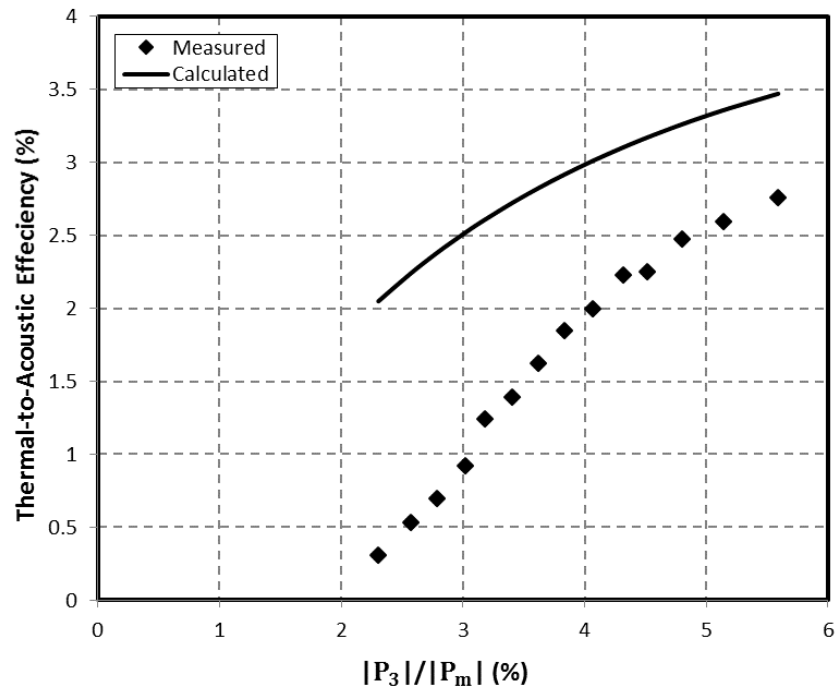


Figure 4.38 Effect of the heat input on the relationship between the pressure ratio and the engine efficiency.

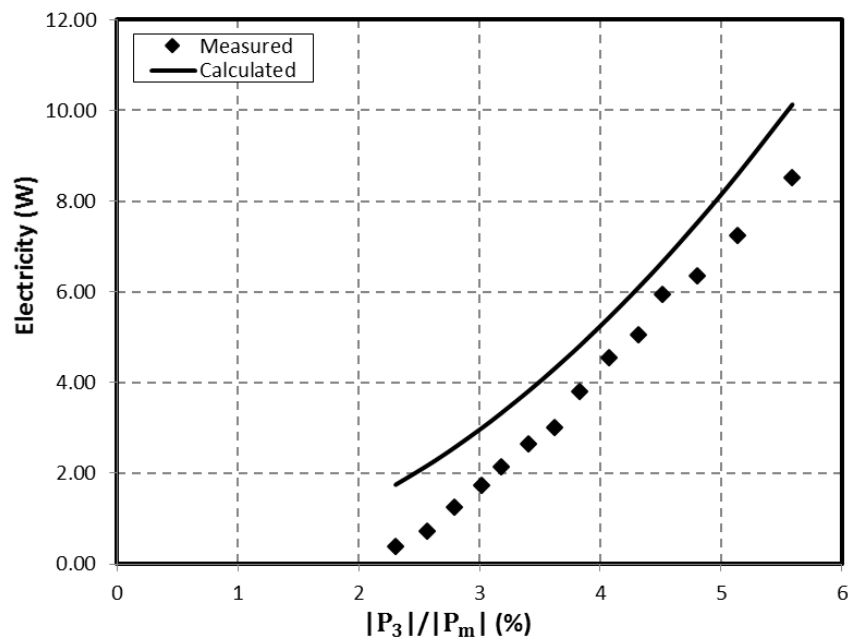


Figure 4.39 Effect of the heat input on the relationship between the pressure ratio and the electricity.

It should be mentioned that if the extraction of the acoustic power increases and the load is fixed, the electrical power produced by the alternator also increases. This can be seen clearly in Figure 4.39. In this graph, the measured and simulated effects of the heat input on the relationship between the pressure ratio and the electric output are presented. The electrical power increases almost linearly as the heat input is increased. A similar trend and reasonable agreement exists between the measurements and the calculations at higher pressure ratios. Finally, the predicted and measured electrical output was 10.13 W and 8.52 W, respectively when the calculated and measured heat inputs were 528 W and 581 W, respectively. Consequently, at these values the predicted and measured thermal-to-electrical efficiencies are around 1.9% and 1.5%, respectively, as shown in Figure 4.40.

Figure 4.41 shows the measurements and calculations of the influence of the heat input on the relationship between the pressure ratio and the alternator efficiency. A reasonable agreement between the measured and the predicted results can be seen from the graph. The calculated efficiency was 53.76% while the measured efficiency fluctuated between 50.7% and 60%.

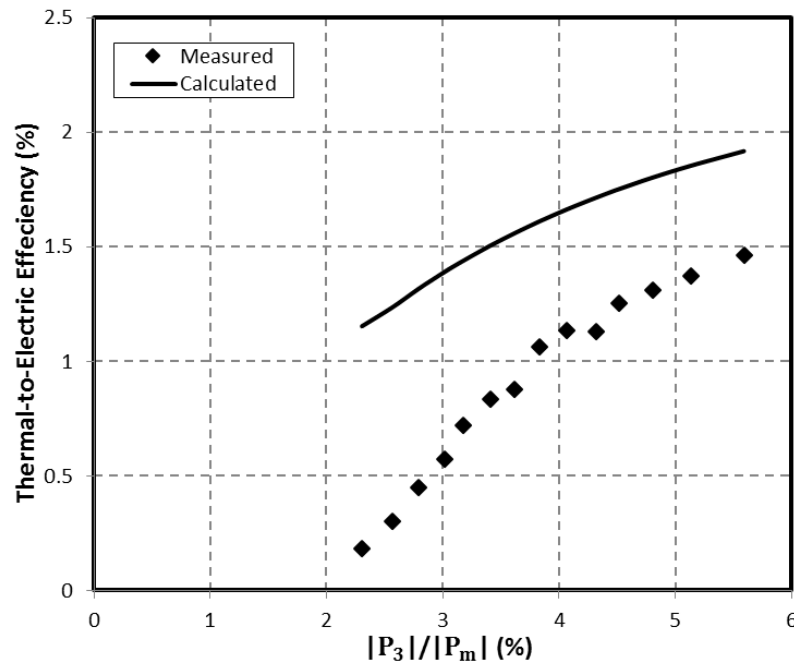


Figure 4. 40 Effect of the heating power on the relationship between the pressure ratio and the thermal-to-electric efficiency.

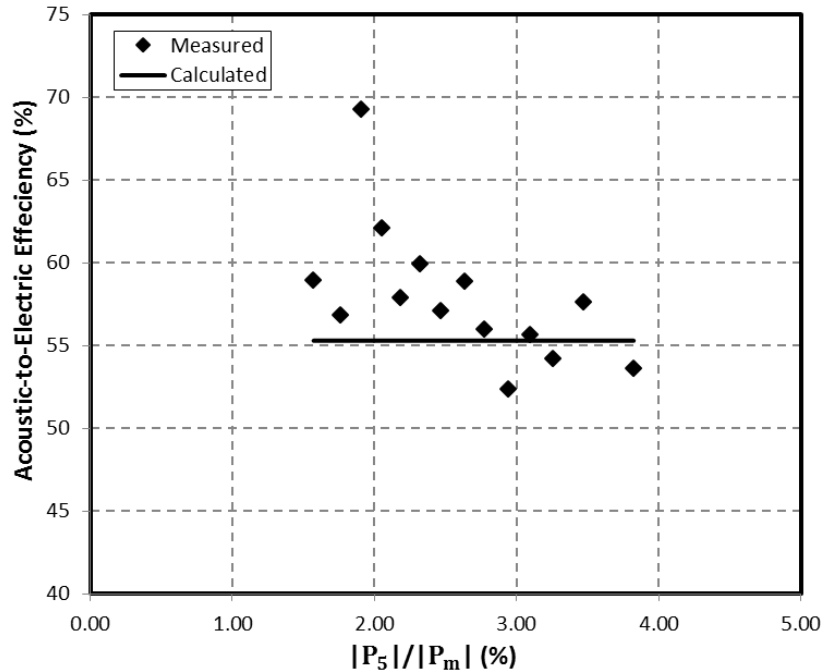


Figure 4. 41 Effect of the heat input on the relationship between the pressure ratio and the acoustic-to-electric efficiency.

4.4 A 128-mm Diameter Two-stage Looped-tube Electricity Generator

In this section, DeltaEC simulations and experimental results for the 128-mm diameter two-stage generator are presented. The results obtained from the DeltaEC simulations along the loop regarding pressure amplitude distributions, volumetric velocity distributions, acoustic impedance and its phasing and, finally, the acoustic power distribution are presented in section 4.4.1. Experimental results of the effect of the stub length on the generator performance as well as calculated vs. measured comparisons are presented in section 4.4.2. In section 4.4.3, the effects of load resistance on the electricity output and the generator efficiency are shown. Finally, the effect of the heating power supplied to the HHX on the general performance, is presented in section 4.4.4.

4.4.1 Simulation results

The results shown in this section are obtained from the simulations of the final design of this prototype according to the block diagram shown in Figure 3.12. The calculation was carried out under the following conditions: air was used as the

working gas, the mean pressure was 0.1 MPa, working frequency of 50.9 Hz, the length

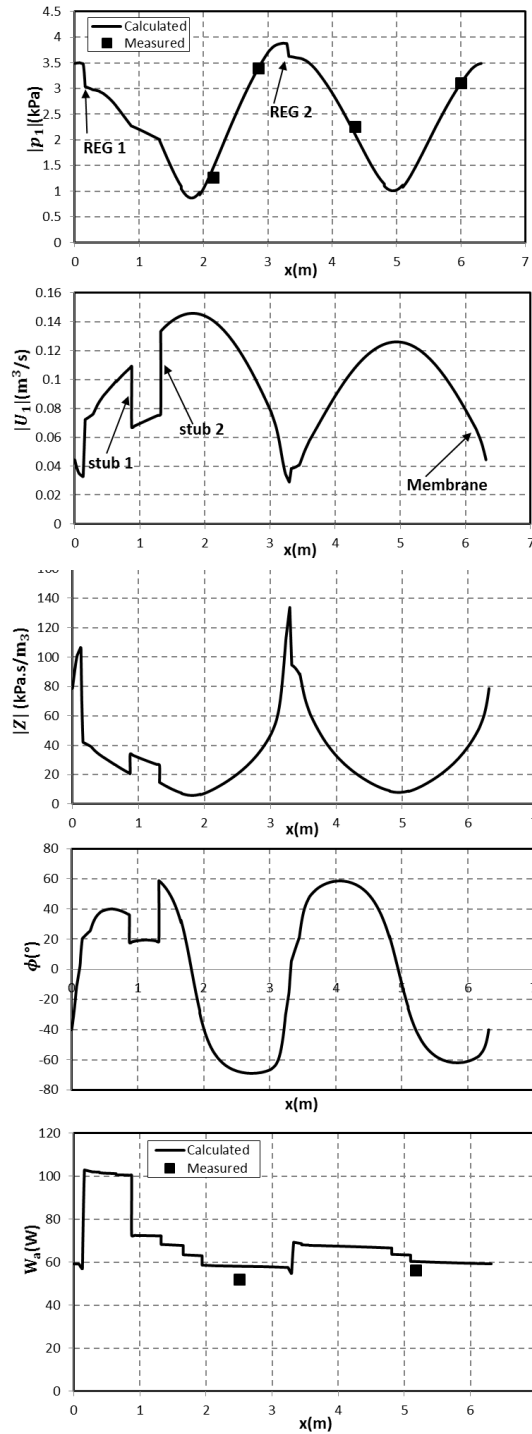


Figure 4. 42 The numerical simulations of the acoustic field in the 128-mm diameter, two-stage electricity generator. (a) Pressure amplitude (b) Volumetric velocity (c) Acoustic impedance (d) Phase angle and (e) Acoustic power flow.

of the stub was 1090 mm and the load resistance was 8 Ω . The results of the simulation are based on guessing the heating power at the HHX 1 and the HHX 2 to target the pressure amplitudes of pressure sensors P2 and P4 obtained from the experiments. Pressure sensors P1, P2, P3, and P4 are placed at 2.15, 2.85, 4.35, and 6 m from the start edge of the ambient heat exchanger as seen in Figure 3.12, respectively. The calculation results of the distributions of variables of interest along the loop are shown in Figure 4.42.

Figure 4.42a shows the pressure amplitude distribution along the system. The calculated pressure amplitude is denoted by the solid line, whereas the measured amplitude is represented by black squares. There are two maxima and two minima of pressure amplitude along the loop and two sharp pressure drops. Both regenerators are located near the maxima of pressure amplitude. The flow resistance of both regenerators causes the pressure drops. The pressure amplitude changes smoothly along all other parts. As P2 and P4 were targeted in the simulation, the measured P1 and P4 achieved very good agreement with the calculated values.

Figure 4.42b shows the distribution of volumetric velocity along the system. There are also two maxima and two minima along the loop. One maximum is located in the FBP 1 about 530 mm away from the T-junction of stub 2, and the other is located in the FBP2 where the minimum of the pressure amplitude is located. One minimum of the volumetric velocity is at the cold end of the regenerator of stage 1, while the other is located at the cold side of the regenerator of stage 2. The small volumetric velocity within the regenerator is preferred to avoid high viscous dissipation, which is one of the design strategies behind the current concept. It can also be seen that the volumetric velocity increases significantly higher along the REG 1 than in the REG 2. This is due to the temperature gradient along the REG 1 being sharper than the temperature gradient in the REG 2. It can be noted that there is a sudden decrease at ($x = 880$ mm) where stub 1 is located and a sudden increase at ($x = 1320$ mm) where stub 2 is located. The first reduction in the volumetric velocity is due to shifting some volume into the alternator branch while the sudden increase is due to compensating the reduction by volume, available in the matching stub. Along all other parts, the volumetric velocity changes smoothly.

Figure 4.42c shows the acoustic impedance along the system. It can be seen that the acoustic impedance is highest at the second regenerator. This is due to the low volumetric velocity caused by the lower temperature gradient compared to the first regenerator. The impedance drops quickly because the pressure amplitude decreases while the volumetric velocity increases sharply from the cold to the hot end for both regenerators. At stub 1, there is a sudden increase in the acoustic impedance whereas at the location of stub 2 there is a dramatic fall in acoustic impedance. This is because the volumetric velocity has been shunted from the loop to stub 1 and from stub 2 to the loop while the pressure amplitude at both stub junctions is constant. The function of the matching stub is to improve the matching of acoustic impedance between the loop and the alternator (Yu and Jaworski, 2012). This is clear from Figure 4.42c where the matching stub (stub 2) decreases the increase of the acoustic impedance caused by stub 1 to match the acoustic impedance of the loop.

Figure 4.42d shows the phase difference between pressure and velocity oscillation along the system. It can be seen that REG 1 works in the region of ($5^\circ < \phi < 21^\circ$) whereas REG 2 works in the region ($-11^\circ < \phi < 6^\circ$). Phase differences of both regenerators are close to the travelling wave mode. However, the phasing in the second regenerator is more preferable due to establishing zero phasing at the centre of the regenerator which is one of the design strategies behind the current concept. There is a dramatic change in acoustic phasing at the T-junctions of stub 1 and stub 2. The first change was in the range of ($18^\circ < \phi < 36^\circ$) and second change in the range of ($18^\circ < \phi < 56^\circ$). Thus the phasing at the first stub was closer to the travelling wave mode than the second stub. The reason is that there is more acoustic power transferring into the first stub where the alternator is located than that in the matching stub. Therefore, the travelling wave ratio on which the acoustic power transfer relies in the first stub is more than that in the second stub. Furthermore, increasing the length of the matching stub (stub 2) tunes the acoustic impedance at the cold side of both regenerators to the travelling wave mode (Yu et al, 2010b).

Figure 4.42e shows the acoustic power flow along the system. It can be found that around 60.2 W of acoustic power is fed into the AHX 1 which dissipates around 2.3 W. The remaining 57.3 W is fed into the cold end of REG 1. Within the

regenerator, the acoustic power is amplified to around 104.9 W which is the level of acoustic power flowing out from the hot end of the regenerator. The hot heat exchanger and thermal buffer tube dissipate around 3.1 W. The acoustic power of 27.5 W enters the first stub and the alternator extracts about 26.9 W of acoustic power. The remaining acoustic power of 74.3 W is dissipated along the loop to around 60.1 W which enters AHX 2. Acoustic power of 2.8 W is dissipated in the AHX 2 and the remaining power is amplified in REG 2 to around 70.2 W. The hot heat exchanger and thermal buffer tube of the second stage dissipate around 1.7 W. The rest is fed into the AHX of stage 1 at 60.2 W after dissipating 8.3 W in the FBP 2.

In this simulation, the alternator produces 13.9 W of electrical power. The heating power input to the HHX of the first stage and the second stage are 405.6 W and 146.1 W respectively. As a result, the calculated thermal-to-acoustic efficiency of the first and second stages calculated separately is 11.6% and 8.85%, respectively. However, the calculated thermal-to-acoustic efficiency of the entire generator is 4.87%. This is represented as the acoustic power extracted by the alternator to the total heating power input. Moreover, the acoustic-to-electric efficiency is 51.9% (the alternator efficiency), and thermal-to-electric efficiency is 2.53% (the total efficiency of the generator).

4.4.2 Effect of the length of the matching stub

After the prototype of the two-stage generator has been constructed, following the lessons from single stage engine and generator, the first measurements have been conducted to evaluate the effects of the matching stub on the performance of the prototype and also to find the optimal length of the matching stub. The measurements in this section are divided into two parts. The first part investigates the effect of the stub length on the generator performance when the elastic membrane is not placed in the loop. In this case, the acoustic streaming in the loop was observed. In the second part the membrane was placed in the loop to suppress the acoustic streaming and the effects of the stub length were observed. In these experiments, the load resistance that is connected to the alternator is 8 Ω and the heating temperature of the heat-gun was fixed to 530° C at a fixed flow rate of air of around 1935 l/min and a fixed flow rate of water at 1.2 l/min.

After setting the heating temperature and observing all rising temperatures to become stabilised in the regenerators and heat exchangers, the generator started the acoustic oscillation when the stub length was 770 mm. At this stage, the temperatures were allowed to stabilise for around 9 minutes. This procedure was repeated for lengths from 770 mm to 1220 mm with an interval of 50 mm. Data from all sensors placed on the rig (cf. Figure 3.25 and 3.26) were collected. These include all temperatures, pressure amplitudes, pressure phases, cone displacements of the alternator, and the voltage at the load resistance and the measured working frequency of around 49 Hz.

The effect of different lengths of the matching stub on the temperature profile along both regenerators is presented in Figures 4.43 and 4.44. Figure 4.43 includes the effects of acoustic streaming and Figure 4.44 includes the suppression of the streaming by using an elastic membrane. It can be seen from the graphs that the temperature distributions of the regenerator of the first and second stage are measured at $x = 0, 15$ and 30 mm away from the AHX.

Comparing Figure 4.43 and 4.44 there is a difference in the temperature distribution in the first regenerator before and after introducing the membrane. As the stub length increases from 770 mm to 1150 mm, the temperature of the hot side of the first regenerator falls from 437.2°C to 318°C when there is streaming as seen in Figure 4.43a. However, in Figure 4.44a the temperature of the hot side of the regenerator drops from 438.3°C to 354°C . In the regenerator of the second stage, the temperature of the hot end drops from 362.8°C to 241.2°C in Figure 4.43b, whereas it drops from 363°C to 291°C in Figure 4.44b. It is clearly seen that the acoustic streaming takes place in the loop with no membrane (Figure 4.43) and – in contrast to Figure 4.44 – it causes the temperatures of the hot ends of regenerators in both stages to drop at longer stub lengths.

In Figure 4.43, the streaming starts to increase temperatures in the centre of both regenerators at short stub lengths. However, at longer stub lengths, the acoustic streaming changes its direction where the temperature in the middle of the regenerators starts to drop. In Figure 4.44 the temperatures in the middle of both regenerators start to rise at short stub length, while the temperature profiles are linear at longer stub lengths. It is seen that the membrane stopped the Gedeon

streaming completely in the loop. However, it can be found that the acoustic streaming at short stub lengths is local streaming and it still exists in the regenerator even after installing the elastic membrane. The temperature profiles of the hot heat exchanger and the hot side of the regenerator of both stages are not identical. The temperature distributions decrease along the vertical axis (from the bottom to the top of REGs and HHXs) and vary along the horizontal axis. This is due to the hot air provided by the heat-gun from the bottom in a vertical direction, and also the air turbulence that caused different air flow distribution between the channels of the HHX. This regenerator streaming might be attributed to this reason where the viscosity of the oscillating gas varies with the variable temperature distribution.

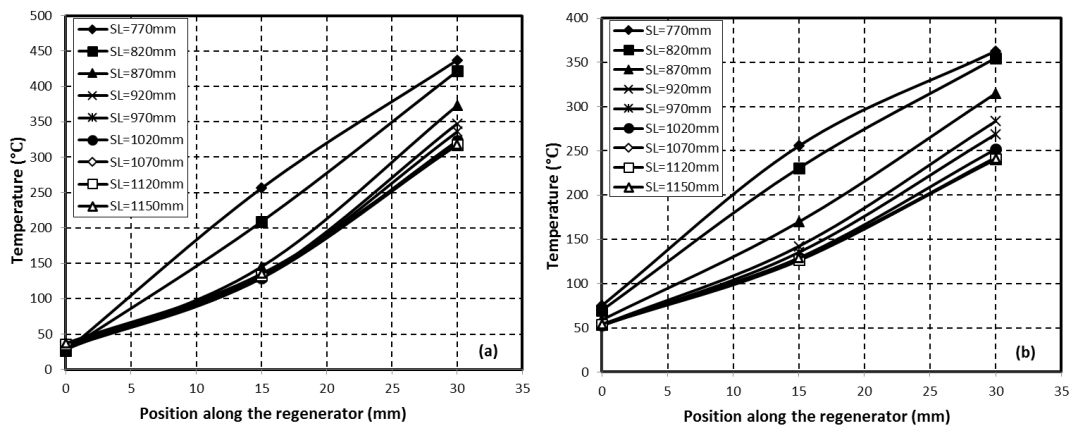


Figure 4.43 Effect of stub length on temperature distribution along the regenerator, including the effects of acoustic streaming. (a) The first stage and (b) the second stage.

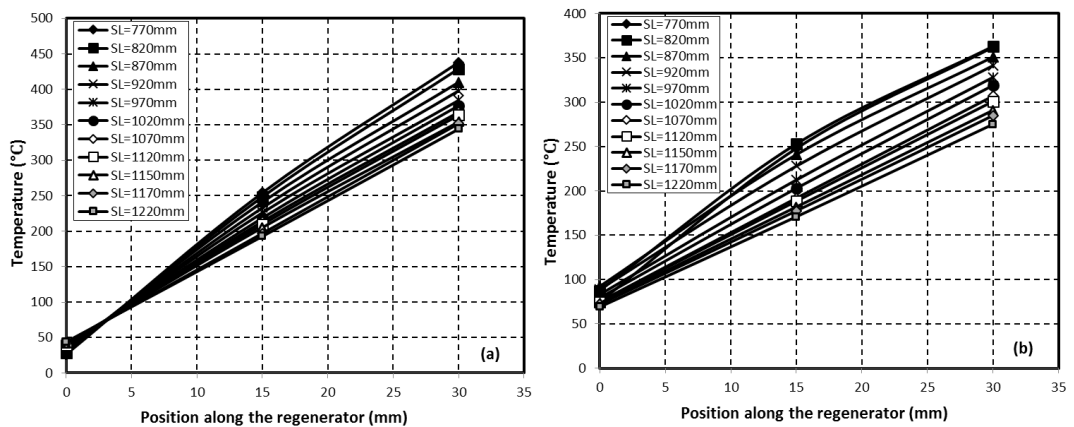


Figure 4.44 Effect of stub length on temperature distribution along the regenerator after installing the membrane and the suppression of the acoustic streaming in the loop. (a) The first stage and (b) the second stage.

It should be noted that when the length of the stub is increased, it adds volume to the loop. In both regenerators, the increase in the volumetric velocity leads to an increase in the gas particle velocity and displacements (since there is no change in the cross sectional area). As a result, this will cause the heat transfer to increase from the hot air flow to the oscillating flow and since the heating temperature of the heat-gun is fixed to 530°C, the temperature of the oscillating flow inside the HHX drops. Thus, the temperature of the hot ends of the regenerators will drop. Although the working frequency of the loop drops slightly by the increase of the stub length, this drop would slightly increase the thermal penetration depth as shown in Equation (2.3) and therefore the heat transfer contact between the regenerator and working gas increases as well. The heat transfer rate is even higher if acoustic streaming exists in the loop. This is due to the heat being taken away from the HHX to the loop by the streaming without being converted to acoustic power in the regenerator.

The effect of the stub length on the hot side temperatures in the regenerators can also be seen in the temperature difference across each regenerator, since the change in the temperature of the cold sides are minor compared to the hot sides. Figure 4.45 shows the relationship between the length of the matching stub and the temperature difference across both regenerators. The black diamond symbols represent the temperature difference in the regenerator of stage 1 while the square white symbols represent the temperature difference in the second stage regenerator. Figure 4.45a represents the case of acoustic streaming present in the loop while Figure 4.45b indicates the case when the streaming was suppressed. In both graphs, increasing the stub length would cause temperature differences in the regenerators. However, the temperature drops even further when the acoustic streaming effects take place in the loop, as seen in Figure 4.45a. Furthermore, streaming in the loop reduces the temperature differences in non-linear fashion and when the stub length reaches 1090 mm the temperature difference becomes almost constant, which indicates that streaming is at its peak value. As shown in Figure 4.45b, this does not occur as the drop in the temperature differences along the increase of the stub length is almost linear.

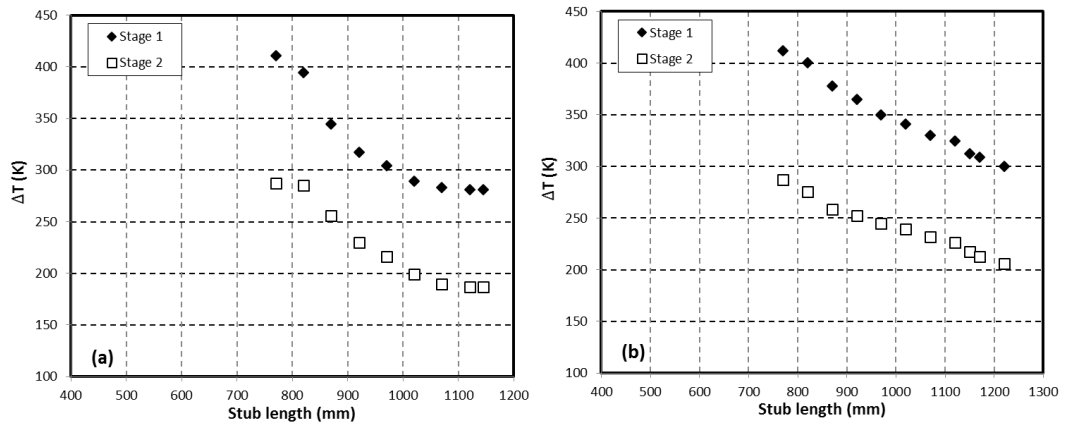


Figure 4.45 Effect of stub length on the temperature difference in the regenerator. (a) Without the membrane and (b) with the membrane.

The effect of the stub length on the heating input power to HHXs and on the rejected heat from AHXs (for both stages) is presented in Figure 4.46 and Figure 4.47, respectively. Figures 4.46a and 4.47a represent the case where the acoustic streaming takes place in the loop while Figures 4.46b and 4.47b show the effect of the stub length where there is a membrane installed and the streaming is stopped. A comparison between the measured and calculated results is also shown in the graphs in Figure 4.46b and 4.47b. It is clear from the graphs that because the first stage is located just at the top of the heat gun, the heat input to HHX1 is higher than that to HHX2 and so was the heat rejected from the AHXs.

It can be seen from Figures 4.46 and 4.47 that the heating power input of the HHXs and the rejected heat from the AHXs are proportional to the stub length. As mentioned above, the increase in the stub length will cause oscillating gas displacement to be increased in the HHXs resulting in the heat transfer being increased. The heating power that is transferred to the HHXs will also be transferred through the oscillating gas to the AHXs. However, when acoustic streaming exists in the loop, the heat input to the HHXs is higher. However, and as mentioned before, the streaming would drag a considerable amount of heat away from the HHX in the direction of the acoustic power flow. This streaming will reduce the heat transferred to the AHX and, in turn, the heat rejected from the AHX will also be reduced.

Since the acoustic streaming in the loop is not considered in the calculations, the acoustic streaming in the experimental rig was also cancelled by introducing a fixable membrane into the loop near the ambient heat exchanger of the first stage,

good agreement between calculations and measurements were seen, especially in Figure 4.47b.

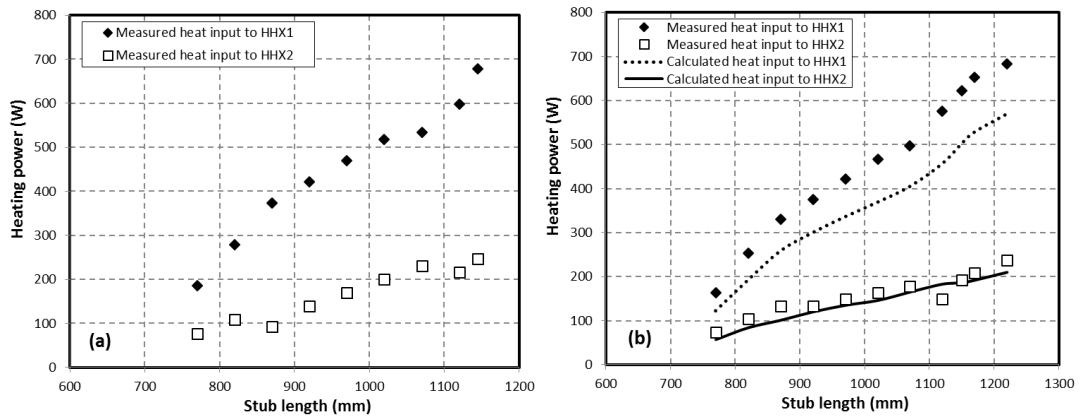


Figure 4.46 Effect of changing stub length on the heating power. (a) Without the membrane and (b) with the membrane.

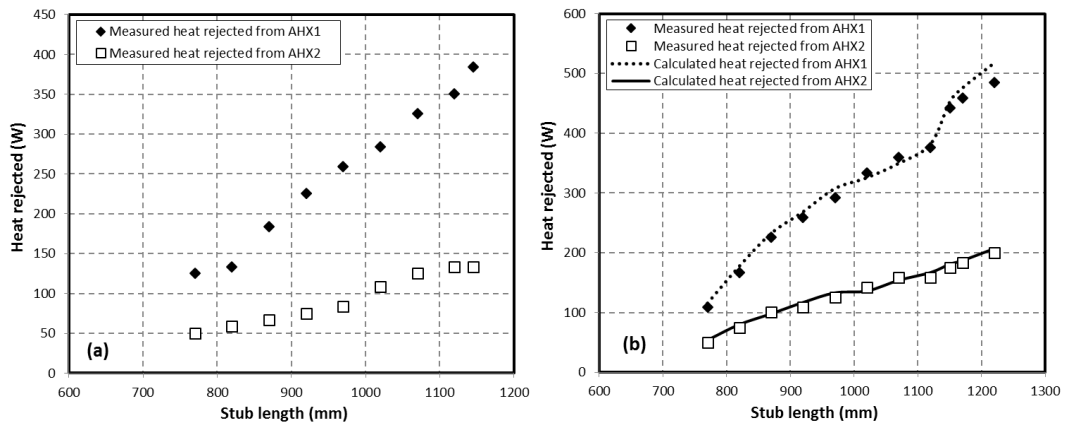


Figure 4.47 Effect of stub length on the heat rejected from ambient heat exchangers. (a) Without the membrane and (b) with the membrane.

The minor discrepancy shown in Figure 4.46b is due to the difficulty of accurately measuring the temperature that may be caused by the high turbulence of the air flow.

As mentioned earlier, there have been two types of streaming occurring in the two-stage generator. The first acoustic streaming is Gedeon streaming that induces the flow along the loop in the direction of the acoustic power flow and which is cancelled when the membrane is placed in the loop. The second type of streaming is the streaming inside the regenerator which seems to occur at short stub lengths even when the membrane is installed. Its direction is from the hot side to the cold side of the regenerator. However, this phenomenon is suppressed at extended stub lengths.

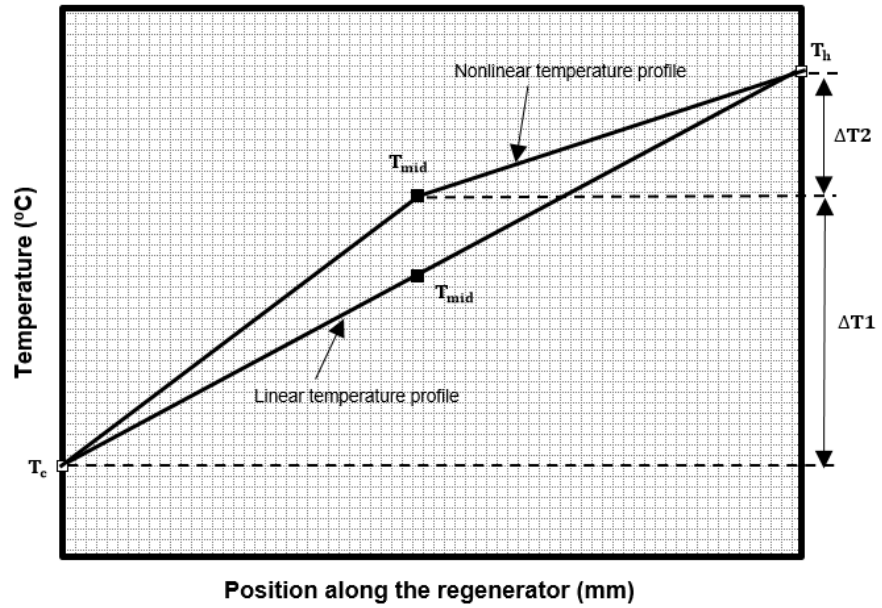


Figure 4. 48 The slope ratio of the temperature distribution in a regenerator.

The non-linearity of the curves in the temperature profiles caused by both types of streaming (cf. Figures 4.43 and 4.44) can be estimated by “the slope ratio” of the curves. The slope ratio (or ratio of slopes) is measured by taking the ratio of difference between the ambient and middle temperatures to the difference between the middle and hot temperatures of the regenerator. This can be represented as follows:

$$\Delta T_1 = T_{mid} - T_a \quad (4.1)$$

$$\Delta T_2 = T_h - T_{mid} \quad (4.2)$$

where T_a , T_{mid} and T_h are the temperatures of ambient, mid-point and hot side of the regenerator, respectively.

The slope ratio can be presented in a schematic graph as shown in Figure 4.48. It is seen from the graph that a straight line has one slope while the “broken” line (non-linear curve) has two slopes.

The temperature profile in Figure 4.48 can be summarised in three different cases:

- When $\Delta T_1 = \Delta T_2$, the temperature distribution is linear and there is no acoustic streaming in the regenerator.

- If $\Delta T_1 > \Delta T_2$, the distribution is non-linear and the temperature in the middle of the regenerator T_{mid} is higher than its value in the linear case. In this instance, the acoustic streaming direction is towards the ambient end of the regenerator.
- If $\Delta T_1 < \Delta T_2$, the distribution is non-linear and the temperature in the middle of the regenerator T_{mid} is lower than its value in the linear case. In this instance, the acoustic streaming direction is towards the hot end of the regenerator (in the direction of the acoustic power flow).

The effect of the matching stub length on the linearity of the temperature profile of both regenerators, when there is streaming in the loop, is presented in Figure 4.49. In the first 100 mm of the stub length, both ratios of slope dropped dramatically from the region where $\Delta T_1 > \Delta T_2$. However, at stub lengths longer than 870 mm, the ratio of slopes in the regenerators remained almost in the region where ΔT_1 is near to the half of ΔT_2 . From the graph, it is obvious that when the acoustic oscillation started at a stub length of 770 mm, the streaming in the regenerator started and caused the central temperature of the regenerator to increase. However, the Gedeon streaming that occurs at higher pressure amplitudes in the direction of the acoustic power will cancel the streaming in the regenerator and cause the temperature to drop rapidly.

After installing the flexible membrane in the loop, the resulting ratio of slope profiles are slightly different from the previous one for both regenerators, as seen in Figure 4.50. It is seen that when the stub length increases, the slope of ratio of REG 1 decreases from around 1.23 to around 0.98 while it drops from 1.51 to 0.97 in REG 2. Although, the presence of the elastic membrane eliminated the Gedeon streaming in the loop, the streaming within the regenerator was still active at short stub lengths and it is brought down by increasing the length of the stub. Finally, the ratio of slope for both regenerators was close to 1 where the temperature gradients along the regenerators were almost linear.

It is worth noting that a similar analysis was made for a single-stage engine and presented in Figure 4.13. However, the streaming pattern seemed much simpler – most likely due to just Gedeon streaming, because the installation of the

membrane brought the ratio of slopes down to values very near to 1. This was not the case for two-stage system, where other types of streaming seem to be at play.

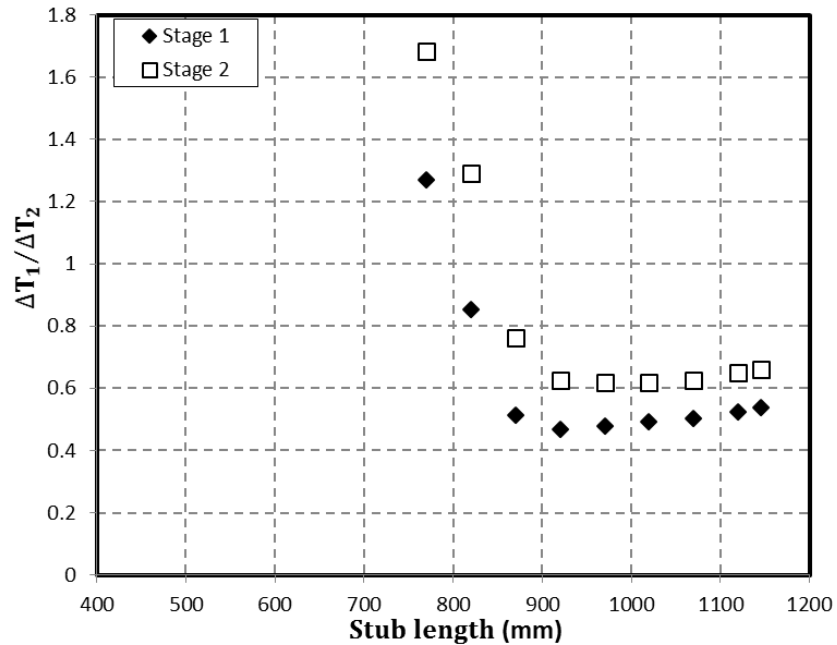


Figure 4. 49 Relationship between stub length and temperature slope ratio in the regenerator (without a membrane in the loop).

It is well known that the pressure amplitudes in thermoacoustic engines are proportional to the heating power input. Accordingly to Figure 4.46, an increase in the stub length in the generator will also raise the pressure amplitudes. Figure 4.51 shows the effect of the stub length on the pressure amplitude at different locations along the loop. These pressure amplitudes are measured using the pressure sensors that are shown in Figure 3.25. The pressure amplitudes shown in Figure 4.51 correspond to the pressure sensors P1 to P4 that are located at 2.15 m, 2.85 m, 4.35 m, and 6 m from the starting point of the AHX 1, respectively. The pressure sensors P1 and P3 are placed near pressure nodes and P2 and P4 are located near pressure anti-nodes. It can be seen that all pressure amplitudes increase rapidly at the stub lengths 820 and 870 mm and more slowly at stub lengths from 920 mm to 1120mm. The changes in stub lengths from 1150 to 1220 mm have small influence on the pressure amplitudes.

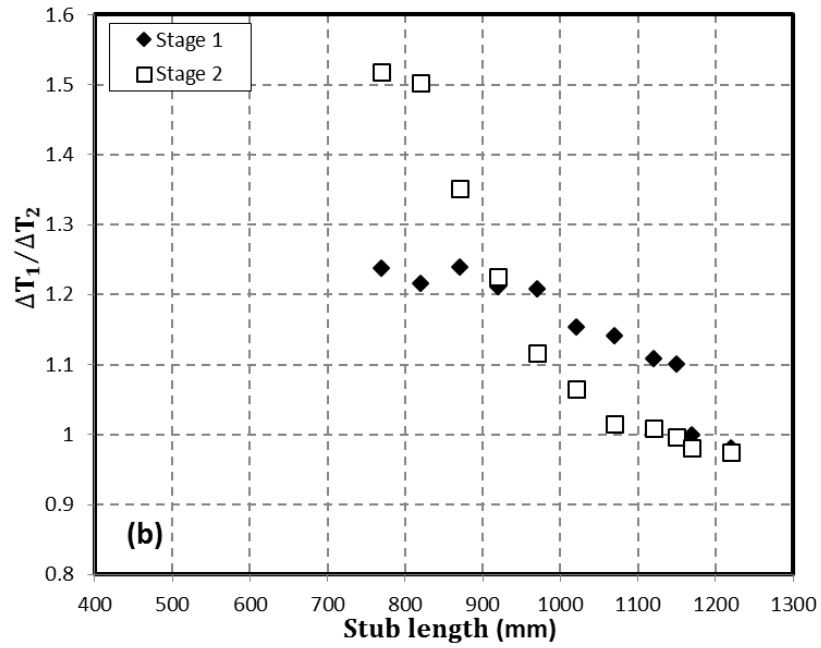


Figure 4. 50 Relationship between stub length and temperature slope ratio in the regenerator (with the membrane in the loop).

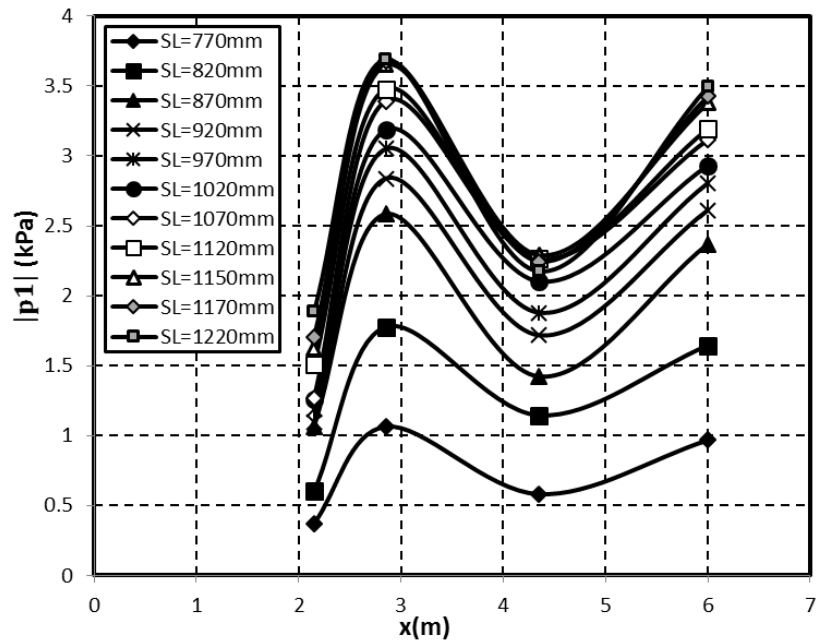


Figure 4. 51 The pressure amplitude distribution along the loop at different stub lengths. (a) Pressure amplitude versus the loop length and (b) Pressure amplitude versus the stub length.

The effects of the stub lengths on the pressure amplitudes (including the pressure amplitude of the sensor P5) can also be seen in Figure 4.52 by plotting the

pressure amplitudes versus the stub lengths for five sensors used. It was noticed that the highest pressure amplitudes are for sensors P2 and P4 which are located in the pressure anti-node regions close to the ambient heat exchangers of stage 2 and stage 1, respectively. The lowest pressure amplitude in the system was shown to be at the end of stub 1 where the alternator is located. This is a region where the acoustic impedance is low (high volumetric velocity and low pressure amplitude) to drive the alternator efficiently (Yu et al., 2010a).

The alternator is a significant part of the generator since it converts the acoustic power into electric power. Therefore, the performance of the alternator is investigated by the effect of the main parameters including the stub length. The effect of the stub length on the alternator performance is shown in Figures 4.53 – 4.58).

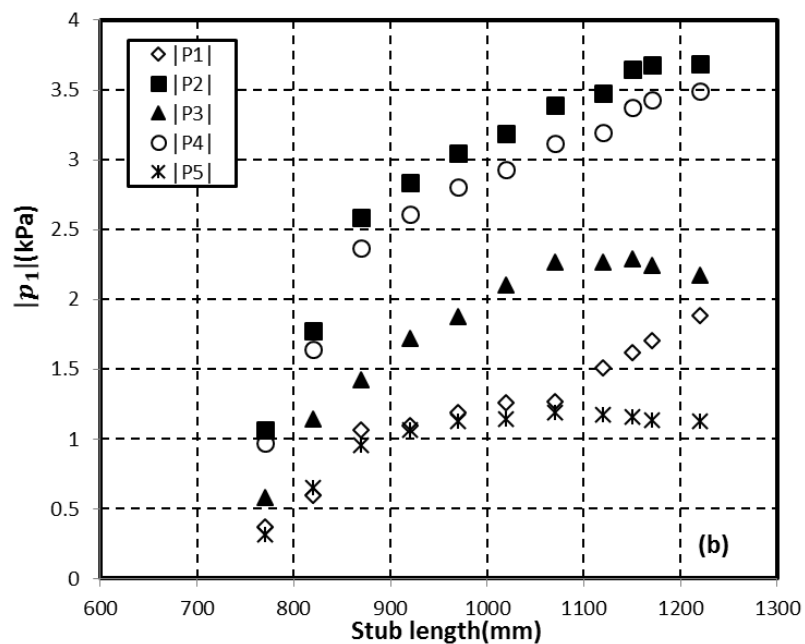


Figure 4. 52 Effect of the stub length on the pressure amplitude at different locations in the loop.

Figure 4.53 shows the comparison between the calculated and measured results of the effect of the stub length on the displacement of the diaphragm of the alternator. The diamond symbols represent the measured results while the solid line indicates the calculations. There is a similar trend between the measurements and calculations. From the graph, both calculated and measured results have optimal

stub length that corresponds to the highest displacement. The increase of the stub length of 300 mm sharply increases the measured displacement from 1.94 mm to around 6.8 mm which is above the maximum displacement of the alternator (6.5 mm). However, the calculated displacement increases even more to around 7.37 mm. Nevertheless, further increasing of the length of 150 mm away from the optimal length will decrease the measured displacement of the diaphragm to around 6.27 mm.

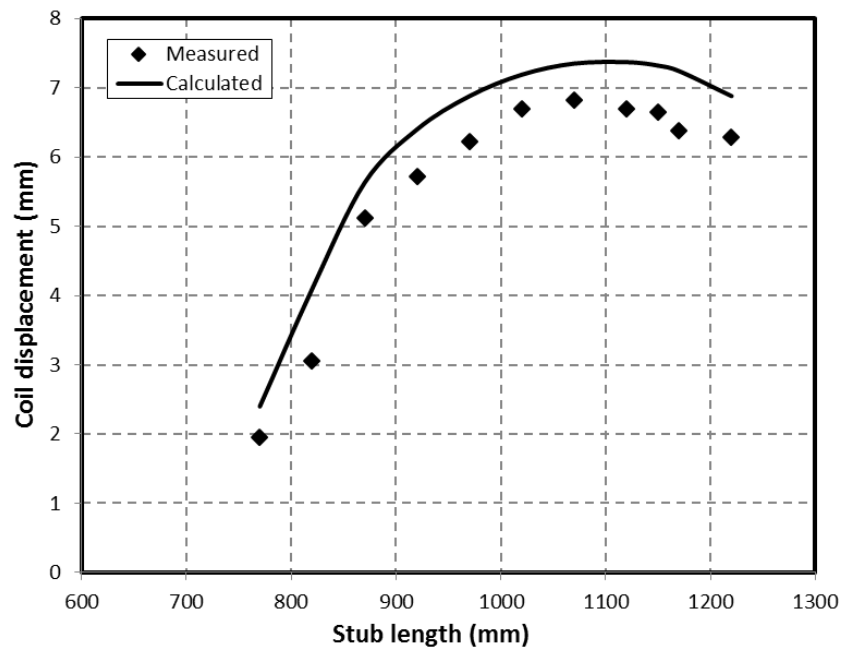


Figure 4. 53 Effect of stub length on the coil displacement of the alternator.

The calculated and measured relationships between the stub length and the acoustic power absorbed by the alternator are compared in Figure 4.54. The comparisons between the calculated results and measured results are presented as a solid line and black diamond symbols respectively. As the length increases from 770 mm to 1090 mm, the measured extraction of the acoustic power rises dramatically from 2.8 to 25.6 W while the calculated extraction improves to 28.13 W. It is seen that the optimal stub length for the generator is close to 1090 mm. However, at further length increases the alternator stops extracting more acoustic power which falls rapidly to 19.85 W at a length of 1220 mm. It can be found that increasing the length of the stub has a great effect on the acoustic power that is extracted by the

alternator. This considerable effect is also seen by the electricity that is produced by the alternator. Figure 4.55 presents the influence of the stub length on the thermal-to-acoustic efficiency of the generator for both simulation and experiments. This efficiency is calculated as the ratio of the acoustic power extracted by the alternator to the heating power of both hot heat exchangers and is also known as the engine efficiency. From the graph, the optimal stub length corresponding to the maximum efficiency for the measurements and calculations is slightly different. This may be due to the error in measuring the heating power input. From the graph, a dramatic growth can be seen in the efficiency from around 1.2% to 4.3%, when the length of the stub rises from 770 to 920 mm. The increase is then followed by a considerable drop to around 2.2% when the length was raised to 1220 mm.

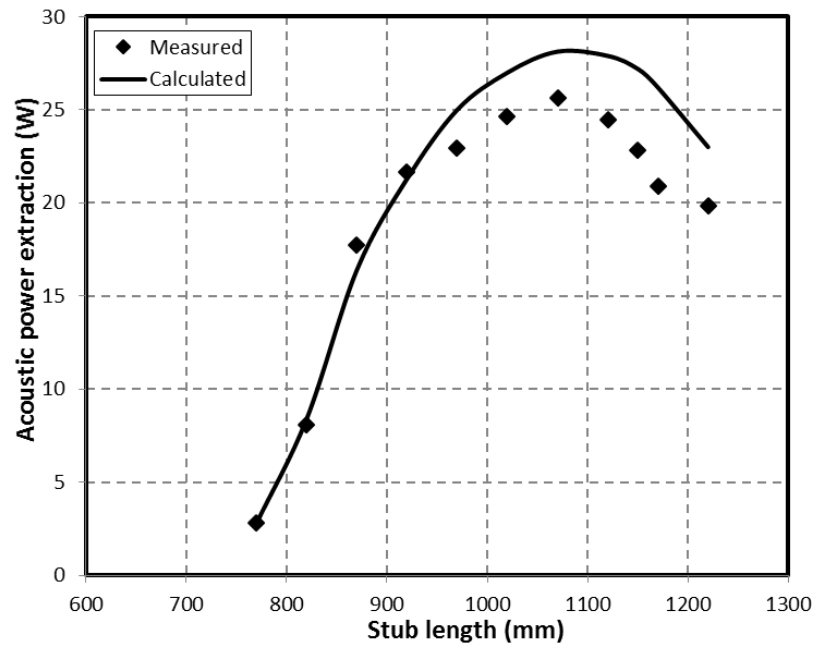


Figure 4. 54 Effect of stub length on the acoustic power extracted by the alternator.

Figure 4.56 presents (for both simulation and experiments) the effects of the stub length on the electrical output that is extracted from the alternator and dissipated by an 8Ω load resistance. From the graph, measurements and calculations share the same optimum stub length that enables the maximum electric power production. There is a sharp increase in the measured electric power from 1.28 W to reach its peak value at 13.78 W, while the calculated electricity jumps to 14.55 W,

when the length is increased to 1090 mm. Then a sudden fall in the measured electricity to around 11.64 W appears when the length is increased 150 mm away from the optimal length.

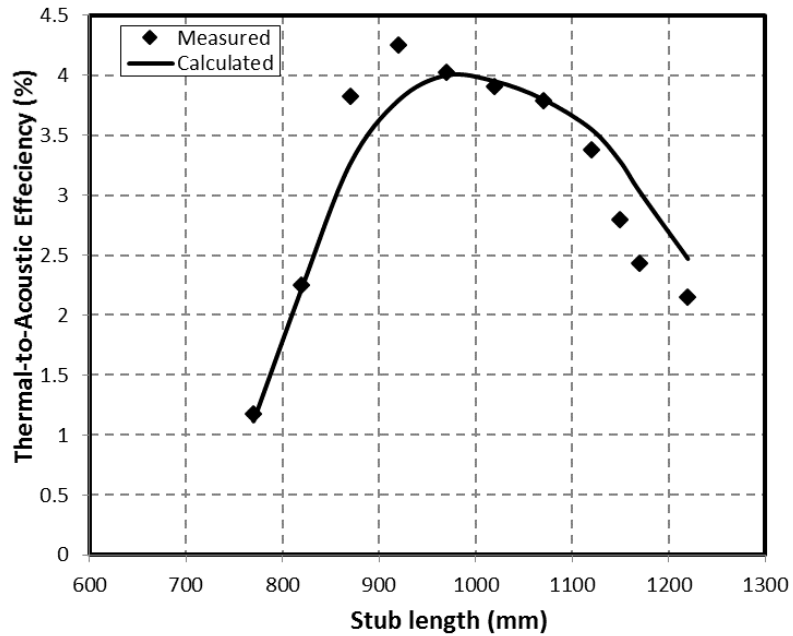


Figure 4. 55 Effect of stub length on the thermal-to-acoustical efficiency.

The electrical generator efficiency is also one of the important considerations that measure the generator performance. Figure 4.57 displays the effect of the stub length on the predicted and experimental generator efficiency. The generator efficiency is represented as the ratio of the electricity extracted from the alternator to the heating power input of the HHXs. From the graph, the measured efficiency goes up sharply to reach its peak value around 2.1%, at a length of 1020 mm. But, the efficiency falls rapidly to around 1.3% at the end of the stub length range. Following the same trend, the calculated efficiency jumps from 0.8% to around 2.7% and then drops suddenly to 1.51% for the same stub lengths.

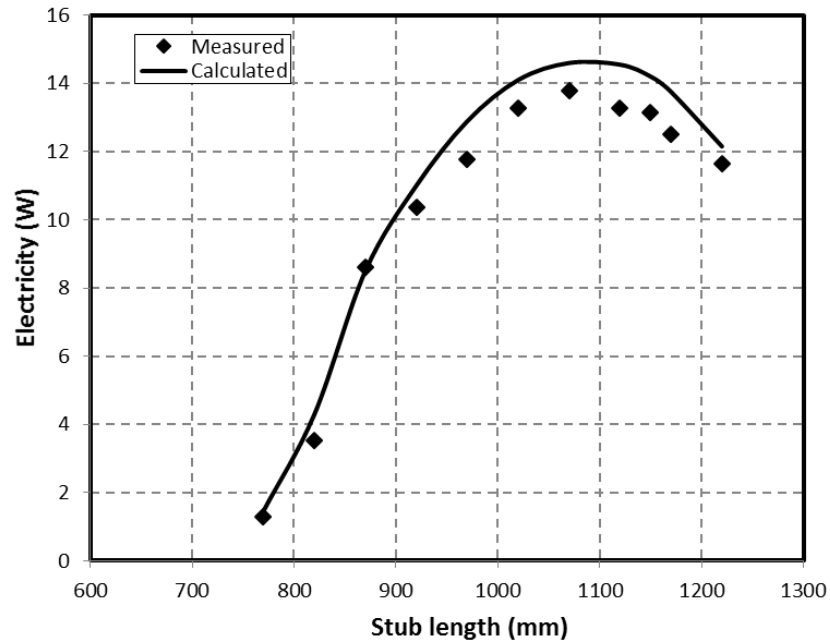


Figure 4. 56 Effect of the stub length on the electricity produced.

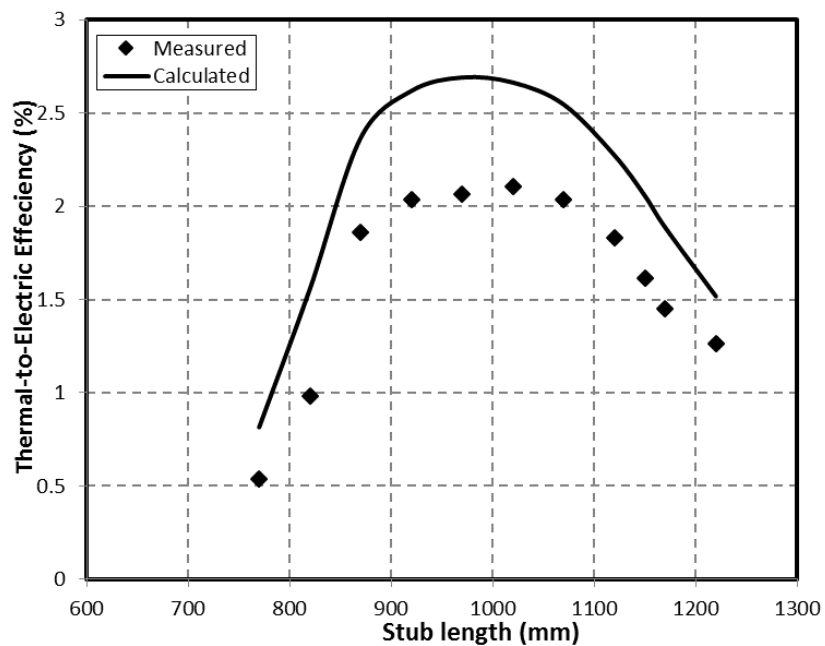


Figure 4. 57 Effect of stub length on the total efficiency of the generator.

From the previous graphs in Figures 4.53 to 4.57, it is observed that the performance of the alternator is critically influenced by the stub length. As mentioned earlier, the stub is a side branch tube to tune the acoustic phasing in the loop and match the acoustic impedance between the loop and the alternator. Therefore, by increasing the length of the stub, the volumetric velocity in the loop increases which causes the acoustic impedance of the loop to decrease. As a result,

the alternator reduces its reflection to the acoustic power that enters the branch of the alternator (Yu et al., 2012). At this stage, the alternator increases its displacement, the extraction of the acoustic power and the electrical power production until they reach their peak values when the stub length is optimal. Nevertheless, the alternator starts to reduce its extraction of the acoustic power and reflects it back to the loop when the acoustic impedance of the loop is further decreased by increasing the stub length. Besides the influence of the stub that decreases the engine and generator efficiencies at longer lengths, the increase of the heating power along the stub length also contribute to the reduction of the efficiencies. One can find from the graphs that the optimal stub length is in the range between 1050 and 1100 mm. Finally, overall there is good agreement between calculated and experimental results particularly at short stub lengths. Nevertheless, discrepancies start to occur at longer lengths which may be due to non-linear effects that are excited by high pressure amplitudes (Kang et al., 2015).

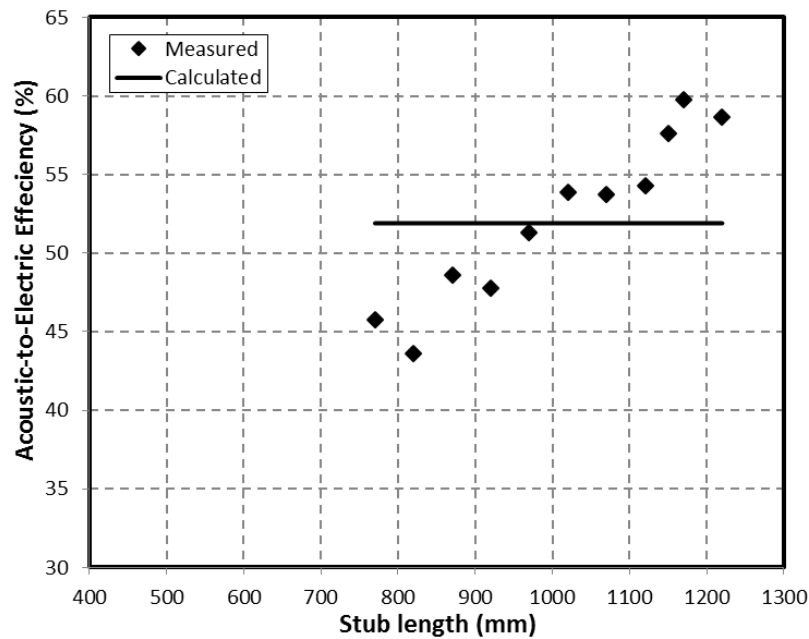


Figure 4. 58 Effect of stub length on the alternator efficiency.

Figure 4.58 shows the comparison between simulation and measurement for the effects of the stub length on the acoustic-to-electric efficiency of the alternator. The solid line represents the calculations, whereas the diamond symbols are the

measurements. The graph shows that the experimental efficiency increases from around 45.7% at a stub length of 770 mm to its maximum value of 58% when the length is 1220 mm. However, the calculated efficiency is presented as a straight horizontal line in the graph that is fixed at 51.9% along the range of the stub length. In the model, the phase of the electric impedance of the alternator is targeted to be 180° to force the load resistance that is connected to the alternator to be completely resistive in order to extract electric current from the alternator. As a result, the calculated efficiency of the alternator stays fixed at 51.9% unless the load resistance has been altered, as discussed in section 2.4. On the other hand, the measured efficiency is proportional to the stub length. As the length increases the frequency decreases towards the resonance frequency of the alternator which leads to reduction of the mechanical losses and increases the efficiency in the alternator.

4.4.3 Effect of load resistance

The load resistance is a resistive electric resistance that is connected to the alternator to dissipate the electric power extracted from the alternator. Here a variable resistance from 1Ω to 100Ω is used as load resistance (cf. blue variable resistance box located next to alternator in Figure 3.26). In this section, the goal of the experiments is to investigate the effect of the load resistance on the performance of the generator. In these experiments, the stub length was fixed to the optimal length of 1090 mm and the heating temperature of the heat-gun was changed gradually from zero to 530°C at a fixed flow rate of air at 1929 l/min and fixed flow rate of water at 1.2 l/min.

At the beginning the load resistance was set at 1Ω and the heating temperature was gradually increased to reach 530°C . At this stage, the temperatures took around 9 minutes to become stabilised. This procedure was repeated for load resistances from 1Ω to 12Ω with an interval of 1Ω . In every increment of the load resistance, all data were collected.

Figure 4.59 shows the effect of the load resistance on the temperature profile at the cold end of the regenerator, the centre of the regenerator, the hot end of the regenerator, the centre of the hot heat exchanger and the temperature at the beginning of the feedback pipe for both stages. These temperatures are represented

by T1 to T5 respectively. It can be seen from the graph that there is a very slight change in temperatures as the load resistance was increased from 1 to 12 Ω .

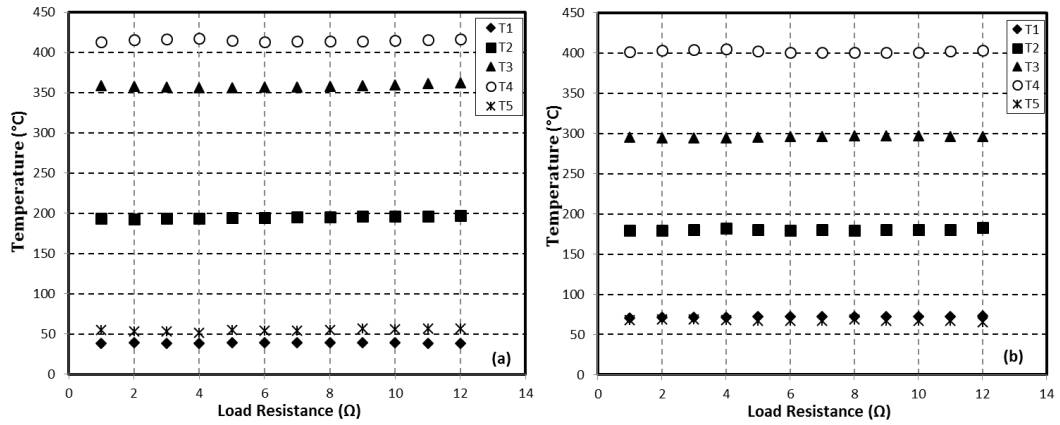


Figure 4. 59 Effect of the load resistance on temperature profiles in the thermoacoustic core. (a) the first stage and (b) the second stage.

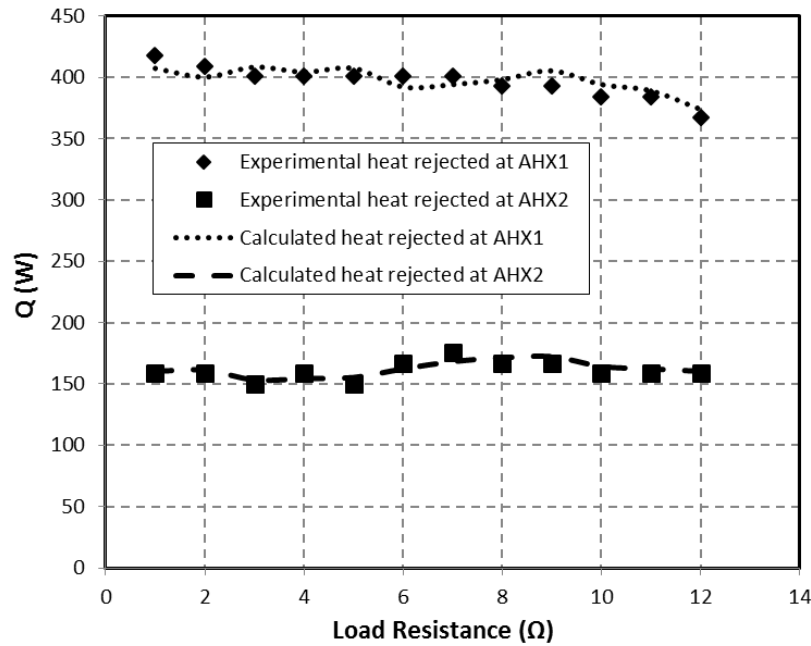


Figure 4. 60 Heat rejected at ambient heat exchanger versus load resistance.

Figure 4.60 shows simulated and measured results of the effect of the load resistance on the heat rejected from the ambient heat exchangers. It can be seen that the measured heat rejected from AHX 1 decreased from 417.6 W to 367.5 W while in AHX 2 it fluctuated between 150.33 W and 175.4 W when the resistance

increased from 1 to 12 Ω . Good agreement was observed between the calculated and measured results.

Tables 4.3 and 4.4 show the effect of the load resistance on the heating power input and rejected, for stages 1 and 2, respectively. In the tables, the symbols Q_h and Q_c represent the heat input and heat rejected respectively. It can be seen from Table 4.3 that the increase in the load from 1 to 12 Ω caused a decrease in the measured heat input from 472.9 to 535.2 W and consequently the heat rejected will also be reduced from 417.6 to 367.5 W. A good agreement was obtained between the measurements and calculations of the rejection of the heat from the ambient heat exchanger with error percentage ranging from 0.78 to 3.18%. However, this does not apply to the heat input of the hot heat exchanger where the error ranges between 10.12 and 15.92%. This error may be due to the difficulty of accurately measuring the temperatures of the turbulent hot air flow.

Table 4. 3 The effect of load resistance on the heat input, heat rejected at the first stage

Load Ω	Q_{h1}(Calculated) (W)	Q_{h1}(Measured) (W)	Error (%)	Q_{c1}(Calculated) (W)	Q_{c1}(Measured) (W)	Error (%)
1	456	535.23	14.80	407	417.59	2.54
2	450	535.23	15.92	400	409.24	2.26
3	460	535.23	14.06	408	400.89	1.77
4	456	519.60	12.24	404	400.89	0.78
5	460	519.60	11.47	407	400.89	1.53
6	441	504.00	12.50	392	400.89	2.22
7	443	504.00	12.10	394	400.89	1.72
8	448	504.00	10.98	398	392.53	1.39
9	457	519.60	12.05	405	392.53	3.18
10	453	504.00	10.12	394	384.18	2.56
11	438	488.41	10.32	389	384.18	1.25
12	419	472.85	11.39	374	367.48	1.77

Table 4. 4 The effect of load resistance on the heat input, heat rejected at the second stage

Load Ω	$Q_{h2}(\text{Calculated})$ (W)	$Q_{h2}(\text{Measured})$ (W)	Error (%)	$Q_{c2}(\text{Calculated})$ (W)	$Q_{c2}(\text{Measured})$ (W)	Error (%)
1	166	194.97	14.86	160	158.68	0.83
2	165	194.97	15.37	161	158.68	1.46
3	159	194.97	18.45	153	150.33	1.77
4	162	209.96	22.84	154	158.68	2.95
5	161	194.97	17.42	155	150.33	3.11
6	167	224.96	25.77	162	167.04	3.01
7	172	209.96	18.08	168	175.39	4.21
8	175	194.97	10.24	171	167.04	2.37
9	176	194.97	9.73	172	167.04	2.97
10	170	209.96	19.03	164	158.68	3.35
11	168	209.96	19.99	162	158.68	2.09
12	165	224.96	26.65	160	158.68	0.83

In Table 4.4 along with the increase of the load there was a fluctuation in the measured heat input between 194.97 and 224.96 W, the measured heat rejected changed between 150.33 and 175.39 W. From the table there is good agreement between the calculated and the measured heat rejected when errors in measurement are low and ranges between 0.83 and 4.21%.

The change in the heat input has an effect on the pressure amplitudes in the loop. Figure 4.61 shows the effect of the load on the pressure amplitude profiles in the generator. It can be seen there are minor fluctuations within the pressure profiles as the load increases. This fluctuation is due to the slight change in the load resistance. However, the pressure amplitude at the front of the alternator (P5) falls from 1.72 kPa to 1.16 kPa as the load resistance increases from 1 to 12 Ω . As the load resistance R_L increases, the electric impedance of the alternator decreases and therefore the alternator drops its acoustic pressure difference Δp to match its acoustic impedance as seen in Equation (2.70). Consequently, the engine reduces the

heating power input in order to match this pressure drop as is seen clearly in Tables 4.3 and 4.4.

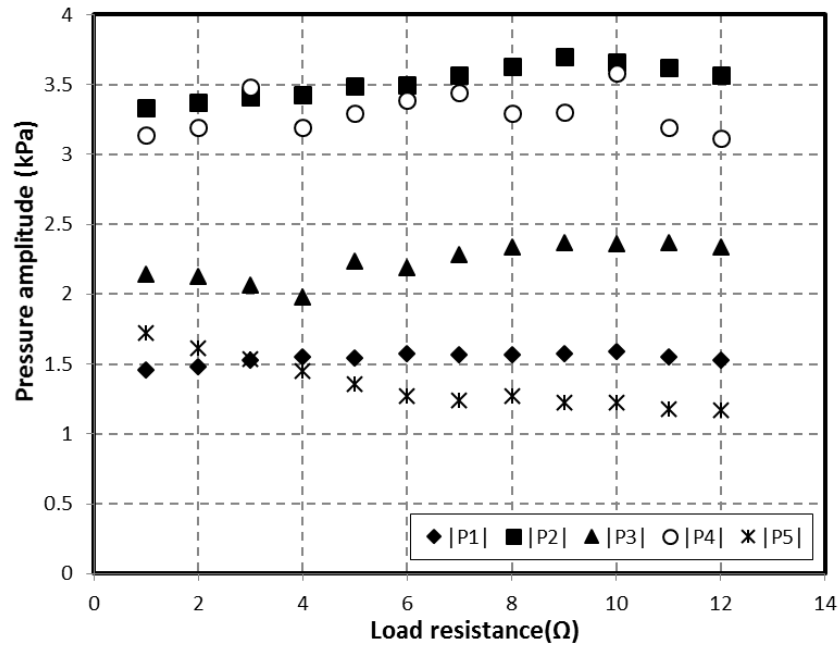


Figure 4. 61 Effect of load resistance on the pressure amplitude distribution.

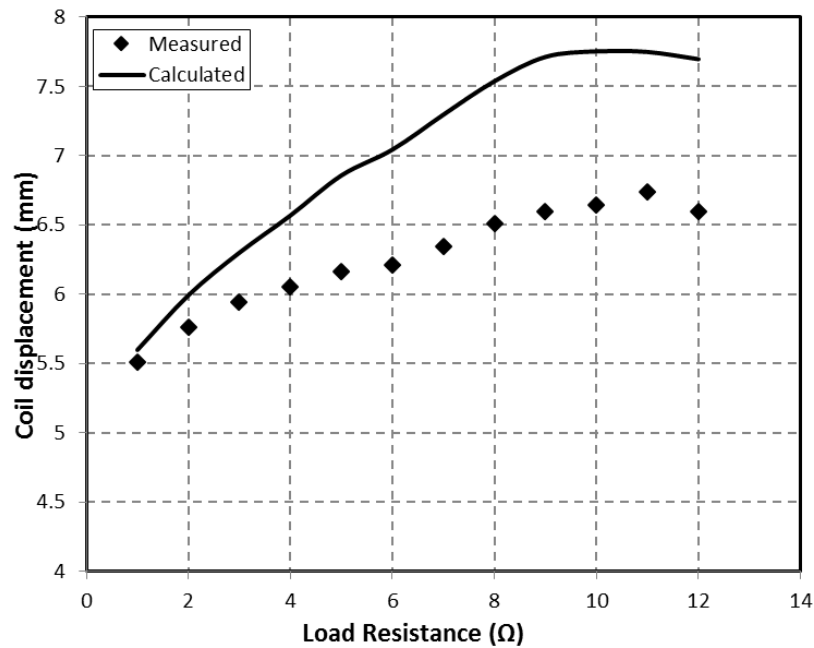


Figure 4. 62 Effect of load resistance on the coil displacement of the alternator.

Due to the influence of the load resistance on the engine and the loop – and since the load is electrically connected to the alternator – the displacement of the alternator, the acoustic power extraction, the electrical output and the alternator

efficiency are significantly affected by the change in the electrical resistance as shown in Figures 4.62 – 4.67, respectively.

Figure 4.62 shows the calculated and measured results of the effect of increasing the electrical resistance on the coil displacement in the alternator. The measured results are shown by black diamond symbols while the calculated results are presented as a solid line. As seen from the graph, the displacement is proportional to load resistance and both the measured and calculated results have a similar trend. When the load is increased from 1 to 12 Ω , the measured coil displacement grows steadily from 5.51 to 6.59 mm whereas the calculated displacement rises from 5.53 to around 7.69 mm. Moreover, it can be noted that the measured displacement fluctuates between 6.59 and 6.64 mm while the calculated displacement is almost stable at 7.74 mm when the load resistance exceeds 9 Ω . As seen from the graph, there is a good agreement between the calculated and the experimental results at loads 1 and 2 Ω . However, the difference between the measured and calculated results increases when the load is further increased. When the load resistance R_L is increased, as seen in Equation (2.70), the electric impedance of the alternator increases. This increase is caused by the effects of slightly increasing volumetric velocity and displacement and a slight drop in the acoustic pressure difference across the alternator diaphragm.

Similar trends for measured and calculated values of the coil displacements were already observed for the single-stage generator in Figure 4.25. However, the displacement in the single-stage generator started from 3.45 mm. Also in the single-stage generator the displacement reached 5.71 mm at a resistance of 20 Ω while in the two-stage configuration it exceeds its maximum value of 6.5 mm when the resistance is 12 Ω . This was attributed to the difference in the heat input to the generator. For example, at 1 Ω , the heat input to the single stage generator was around 571 W whereas it was around 730 W in the case of the two-stage generator.

Figure 4.63 presents a comparison between calculations and measurements of the effect of the electric resistance that is connected to the alternator on the acoustic power absorbed by the alternator. The graph indicates that both the measured and calculated acoustic power extraction is inversely proportional to the load resistance. Along the increase of the load, the extraction of the measured acoustic power

reduces gradually from 29.44 to 19.5 W while the calculated one declines from 30.8 W to 24.38 W. It is clearly seen that the increase of the load resistance R_L reduces the extraction of the acoustic power and this can be understood from Equation (2.63). Although there is a slight increase in the volumetric velocity caused by the increase of the load, as seen in Figure 4.62, the term $(R_e + R_L)^2$ on the right hand side of the Equation significantly decreases the acoustic power P_a as the load resistance increases. Similar effects were already identified for the single-stage generator (cf. Figure 4.26). The difference between the two cases is the level of the heat input to the two generators as mentioned above.

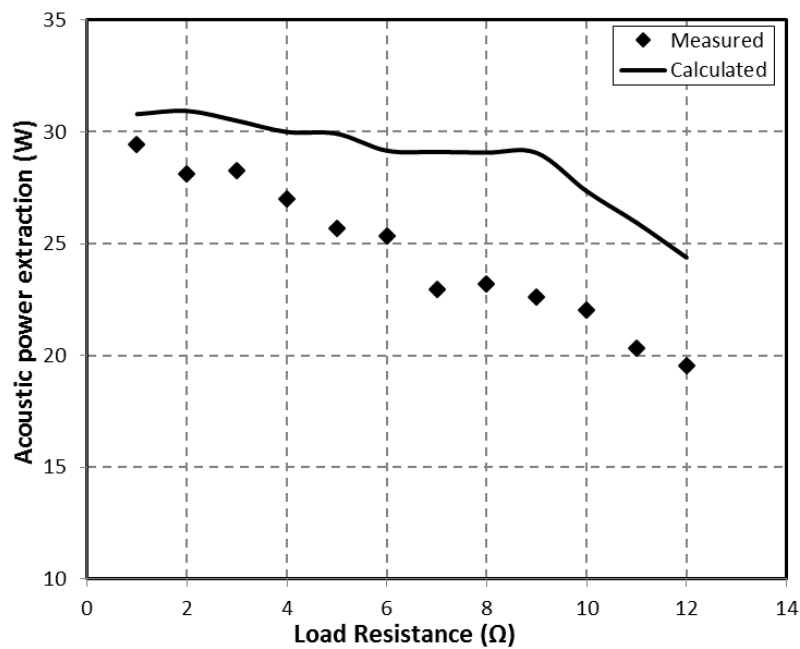


Figure 4. 63 Effect of load resistance on the acoustic power extracted by the alternator.

The engine efficiency contributes to the evaluation of the thermoacoustic engine. Figure 4.64 shows the effect of the load on the thermal-to-acoustic efficiency of the generator. As a result of dropping the acoustic power extraction from Figure 4.63, the measured efficiency drops from around 4% to around 2.8% with increases of the load, whereas the calculated efficiency falls slightly from 5% to 4.24%. There was relatively good agreement between calculations and measurements at small loads and a clear discrepancy at higher loads, as seen Figure 4.63.

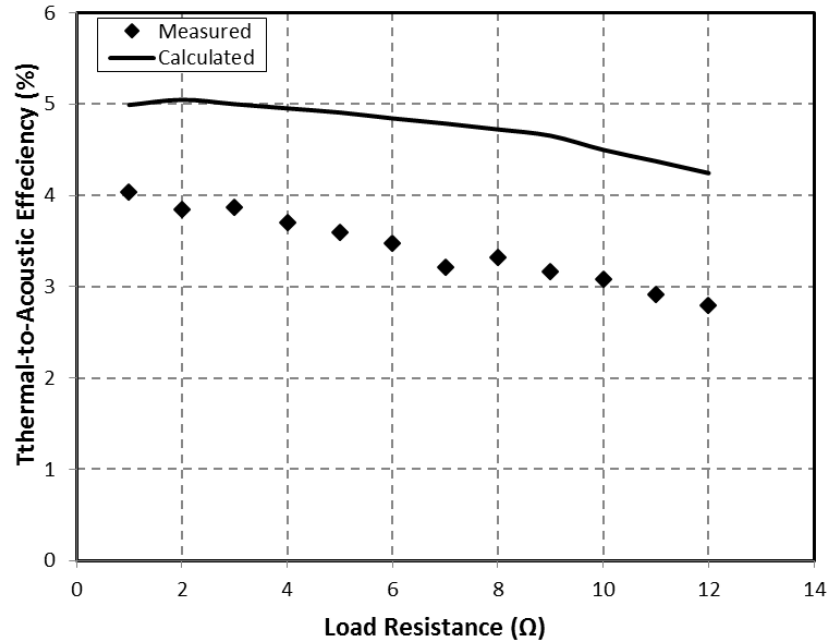


Figure 4. 64 Effect of load resistance on the efficiency of the thermoacoustic engine.

Figure 4.65 shows the effect of the load on the electrical output of the alternator in both simulation and experiments. Here, the electricity is also proportional to the load resistance when the load is raised from 1 to 9 Ω. As a result, the electric power extracted from the alternator is almost doubled when increasing from 7.3 W to around 14 W. However, when the load was further increased to 12 Ω, the electrical power dropped slightly to 13.44 W. So it is clear that a resistance of 9 Ω is the optimum load that extracts the maximum electric power from the alternator. According to Equation (2.65), the electric power extracted from the alternator greatly depends on the load resistance R_L when the volumetric velocity of the diaphragm $|U_1|$ is constant. In this case, the optimum load resistance that can extract the maximum electric power from the alternator is when $R_L = R_e$. However, the displacement of the alternator is not fixed and it slightly increases when the load is increased, therefore, the optimum load R_L will be greater than the electric resistance of the alternator R_e . As presented above, the optimal load is found to be 9 Ω. On the other hand, the impedance of the alternator is greatly affected by the load resistance, as seen in Equation (2.70). Further increase in the load resistance beyond the optimal value will reduce the electric impedance of the alternator. Therefore, the equivalent acoustic impedance reduces the acoustic pressure of the alternator in order to be consistent with acoustic impedance of the loop. From the graph, good

agreement between predicted and measured electrical output can be seen. Similar effects have already been found in the single-stage generator (cf. Figure 4.28).

Since there is a slight change in the heating power input when changing the load, the trend of the thermal-to-electric efficiency should also be proportional to the load resistance. Consequently, the simulated and measured generator efficiency can also be presented. Figure 4.66 presents a comparison between simulation and calculations related to the effect of the electric resistance on the total efficiency of the electric generator. There is a similarity in the trend between the calculated and measured results. From the graph it is clear that increasing the load will increase the generator efficiency. Within the increased load from 1 to 12 Ω , the efficiency steadily improves from around 1% to around 1.92%. However, when the load resistance reaches 9 Ω , both efficiencies reach their maximum values and start to fall. From the graph, the optimal load is 9 Ω at which point the calculated efficiency is 2.5% and measured efficiency is around 1.97%. It is also clear that the two-stage generator is more efficient than the single-stage one where the maximum calculated and measured generator efficiencies were 1.97% and 1.52%, respectively.

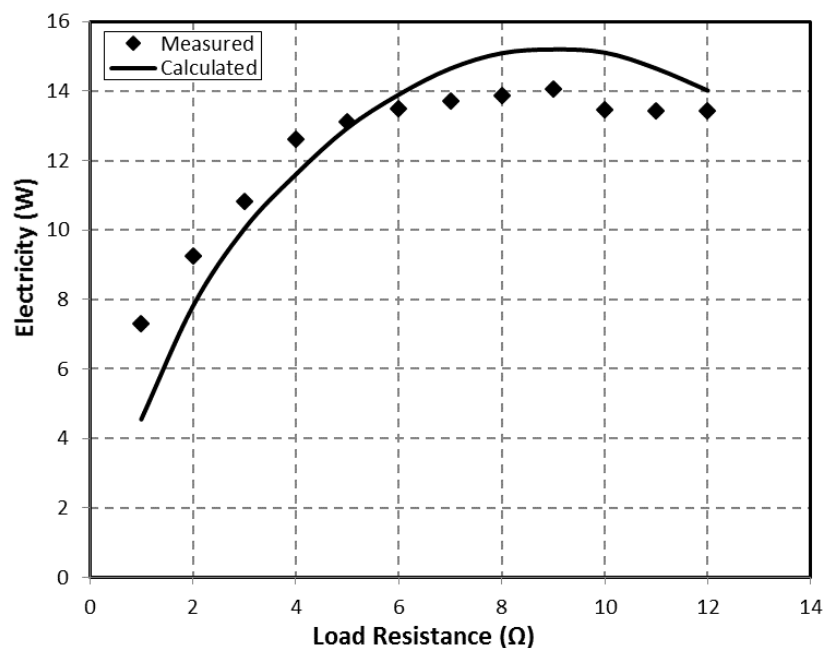


Figure 4. 65 Effect of load resistance on the electrical output

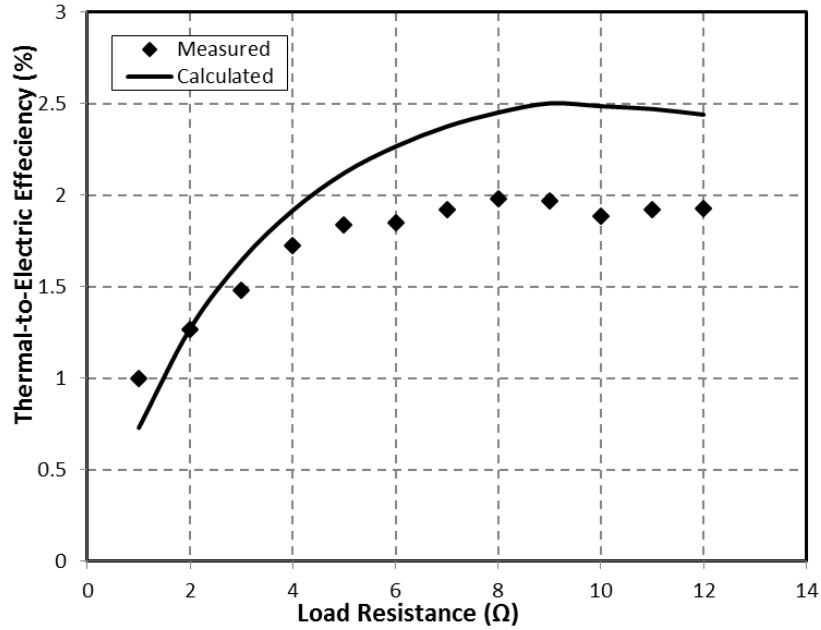


Figure 4. 66 Effect of load resistance on the thermal-to-electrical efficiency of the generator.

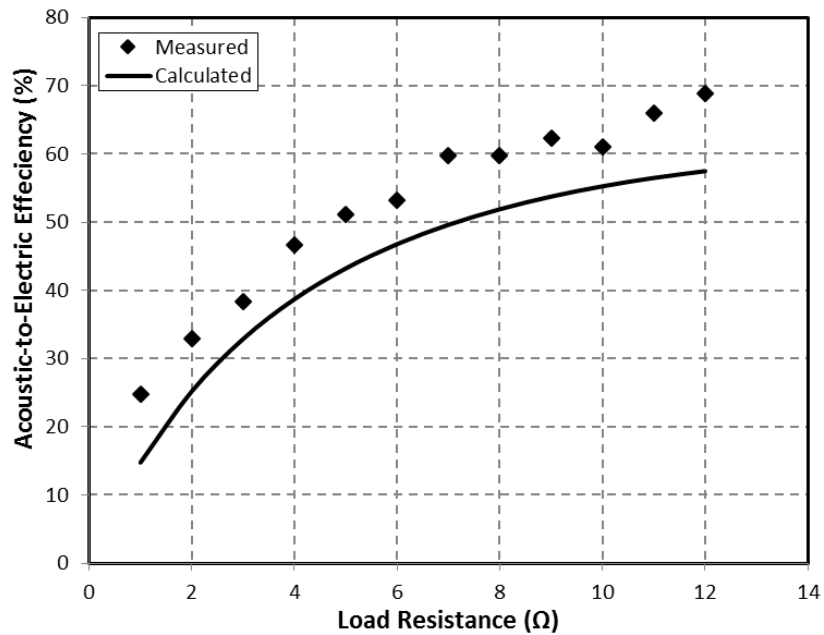


Figure 4. 67 Effect of load resistance on the efficiency of the alternator.

Figure 4.67 presents the comparison between measured and calculated results related to the effect of the variable load on the efficiency of the alternator. The measured alternator efficiency increases gradually from 24.8% to around 68.9% with the increase of the load resistance. In the same manner, the calculated efficiency increases from around 14.8% at 1 Ω to 57.5% at 12 Ω. By referring to

Equation (2.68), the maximum acoustic-to-electric efficiency that can be achieved is when $R_L = 21.73 \Omega$. Unfortunately, the load cannot be adjusted to this resistance due to the limitation of the alternator displacement. Similar behaviour was seen in the alternator efficiency values of the single-stage generator (cf. Figure 4.30). However it was possible there to increase the load to 20Ω due to different operating conditions of the alternator.

4.4.4 Effect of heating power input

In this set of experiments, the goal was to investigate the effect of the heating power input to the HHXs on the performance of the generator. During these experiments, the stub length was fixed to the optimal length of 1090 mm and load resistance was fixed to the optimal value of 9Ω . The heating temperature of the heat gun was changed gradually from zero to 530°C . The flow rate of air provided by the compressor was set at around 1965 l/min. However, due to the increase of the heating temperature of the heat gun to 530°C , the viscosity of the hot air raises at this temperature to more than factor of 2. Accordingly, the fan is presented with a higher pressure drop that leads to drops the volumetric flow. The water flow rate was fixed at 1.2 l/min.

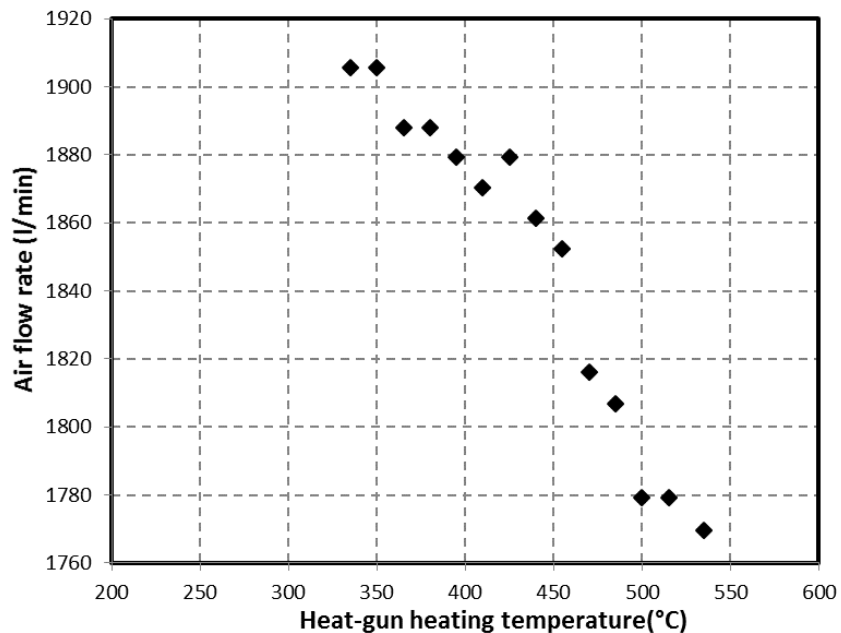


Figure 4. 68 The effect of the heating temperature of the heat gun on the hot air flow.

The generator started the oscillation when the temperature difference between the two ends of the first and second regenerator reached 227.3 K and 168.2 K, respectively. At this stage, the temperatures were allowed to stabilise for between 9 to 12 minutes before the data was collected. This procedure was repeated for the heating temperature of the heat gun from 335 to 535° C with an interval of 15° C. Accordingly, the air flow rate dropped as the heating temperature increased as seen in Figure 4.68.

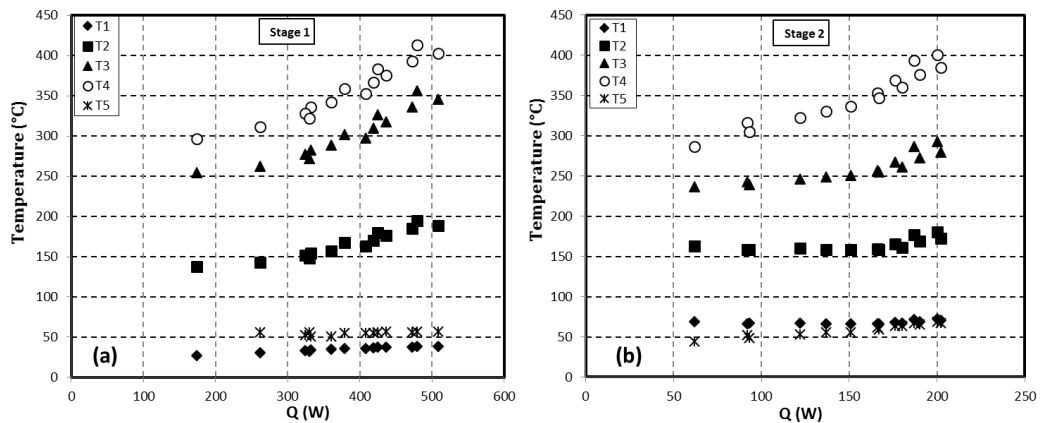


Figure 4.69 Effect of heating power on the change in temperature along the stage. (a) the first stage, and (b) the second stage.

The effect of the heat input can be seen in the increase of temperature at different locations in the thermoacoustic core of both stages as seen in Figures 4.69a and 4.69b. From the graph, T1 (black diamonds) is the temperature at the ambient end of the regenerator, T2 (black squares) is the temperature at the centre of the regenerator, T3 (black triangles) is the temperature at the hot end of the regenerator, T4 (white circles) is the hot heat exchanger gas temperature, and T5 (stars) is the temperature at the end of the thermal buffer tube. It is shown in both graphs that the temperatures at the centre and hot side of regenerators and in the HHXs (T2, T3 and T4) are proportional to the heat input.

The heating power input mainly affects the temperature gradient of the regenerator. Figure 4.70a shows the effect of the heat input on the temperature profile along the first regenerator while Figure 4.70b presents the temperature profile of the second regenerator. It can be seen from Figure 4.70a that the

temperatures at the hot side of the regenerators increase from 254.7° C to 356° C as a result of increasing the heat input from around 147 to around 447 W. Due to the heat extracted by the HHX1, the temperature of the heating air flow drops and, therefore, lower heating temperature was provided to HHX2. This can be clearly seen in the temperature profile of the second regenerator. Here the temperature of the hot side of the regenerator increases from 237 to 292.7° C as the heat input rises from 49 to 182 W. It can also be seen that the temperature distributions of both regenerators are linear.

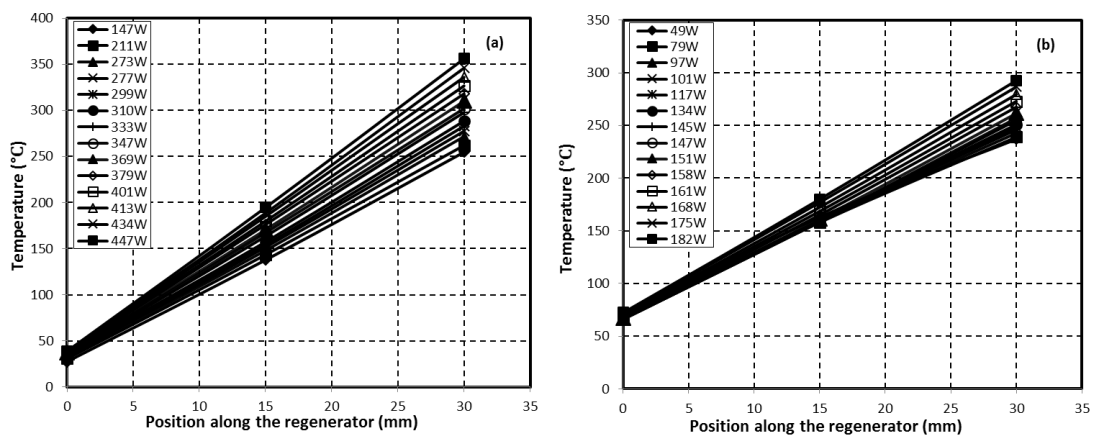


Figure 4.70 Effect of heating power on the profile of temperatures in the regenerator. (a) the first stage and (b) the second stage.

The effects of the heat input can also be seen on the temperature difference between the two ends of the regenerator as presented in Figure 4.71. The graph shows that the temperature difference across the regenerators of both stages has a linear relationship with the heat input. When the heat input to the HHX1 increases from around 173 to 508 W, the temperature difference in REG 1 rises from 227.3 to around 307°C. Meanwhile, the temperature difference of REG 2 jumps from around 168.2 to 220.4°C which is caused by the rise in the heat input to the HHX2 from around 61 around 200 W. It is clear from the graph that the difference in the heat input between the two heat exchangers is caused by the difference in the heating temperature of hot air flow that is pushed over the external surface of the heat exchangers. As mentioned earlier, because both HHXs share the same passage of the hot air flow, lower heating temperature will reach the HHX 2.

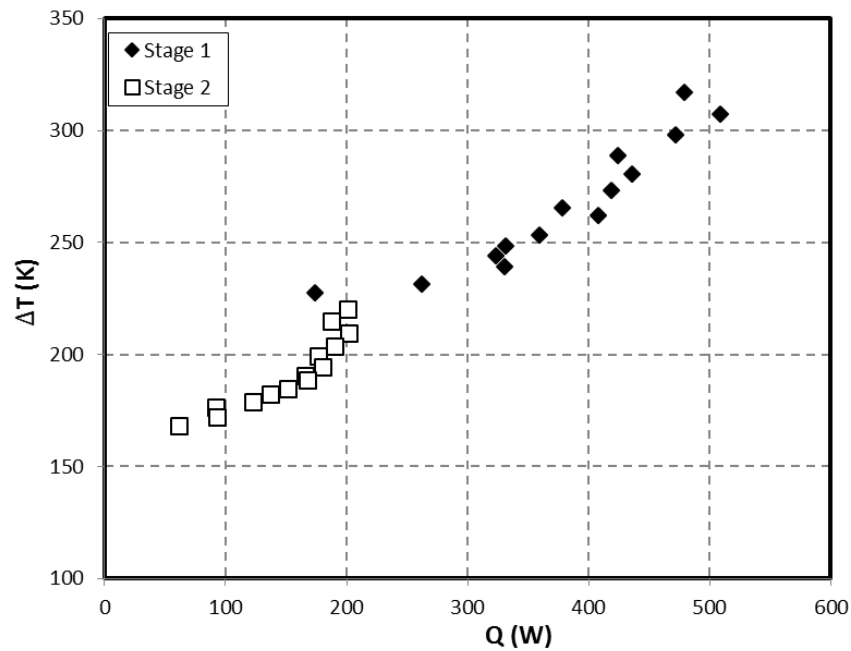


Figure 4. 71 Effect of heating power on temperature difference in the two regenerators.

The increase in the heat input to the HHX and rejected from the AHX for both stages are listed in Tables 4.5 and 4.6. It can be seen from the tables that the increase of the measured heat input of both hot heat exchangers has fluctuations. As mentioned before, the fluctuations are caused by the errors in measuring the temperature differences between the stages. The challenge of measuring accurate temperature difference is likely due to the air flow turbulence that affects the distribution of the heating temperature between stages. On the other hand, good agreement was achieved between calculated and measured heat rejected from the AHX for both stages. The error in measurements ranged between 0.96 to 6.08% in the first stage while in the second stage it ranged from 1.1 to 9.22%.

Table 4. 5 The increase of the heat input and rejected in Stage 1

Q_{h1}(Calculated) (W)	Q_{h1}(Measured) (W)	Error (%)	Q_{c1}(Calculated) (W)	Q_{c1}(Measured) (W)	Error (%)
147	174	18.14	133	125	5.81
227	262	15.47	195	192	1.49
273	330	21.03	249	234	6.08
277	324	16.86	252	242	3.89
299	332	10.89	271	267	1.38
312	360	15.25	281	275	2.14
341	408	19.61	301	284	5.66
347	378	9.22	312	309	0.96
369	419	13.46	331	326	1.60
379	435	14.88	340	334	1.74
401	424	5.84	357	342	4.08
413	472	14.18	367	359	2.15
434	509	17.23	384	376	2.13
447	479	7.17	394	384	2.49

The effect of the heat power input on the acoustic pressure amplitudes along the loop is also included in the study. Figure 4.72a shows the effect of the heating power on the pressure along the loop and 4.72b presents the relationship between the heat input and the pressure amplitude at different locations in the loop. From both graphs it is shown that P2 and P4 are located near pressure anti-node whereas P1 and P3 are placed close to pressure anti-nodes. The pressure amplitudes have a linear relationship with the heat input (Kang et al., 2015). This is clear when the pressure amplitudes in all locations increase linearly with the increase in the total heating power input from 196 W to around 629 W as seen in Figure 4.72b. The pressure amplitudes P4 and P2 are close to the ambient heat exchanger of stage 1 and stage 2, respectively. Therefore, at the maximum total heat input, the maximum pressure amplitudes P4 and P2 are around 3.29 and 3.6 kPa which correspond to drive ratios of 3.25 and 3.55%, respectively.

Table 4. 6 The increase of the heat input and rejected at Stage 2

Q_{h1} (Calculated) (W)	Q_{h1} (Measured) (W)	Error (%)	Q_{c1} (Calculated) (W)	Q_{c1} (Measured) (W)	Error (%)
49	62	25.94	46	42	9.22
79	93	17.18	76	75	1.10
97	92	5.45	95	100	5.50
101	122	21.08	99	103	4.04
117	137	17.03	114	117	2.57
134	151	13.00	131	125	4.37
145	167	15.42	142	133	6.34
147	166	12.77	144	142	1.40
151	180	19.19	146	142	2.75
158	176	11.67	154	150	2.38
161	190	18.12	157	147	6.37
168	202	20.03	164	150	8.33
175	187	7.00	171	159	7.20
182	201	10.21	177	167	5.65

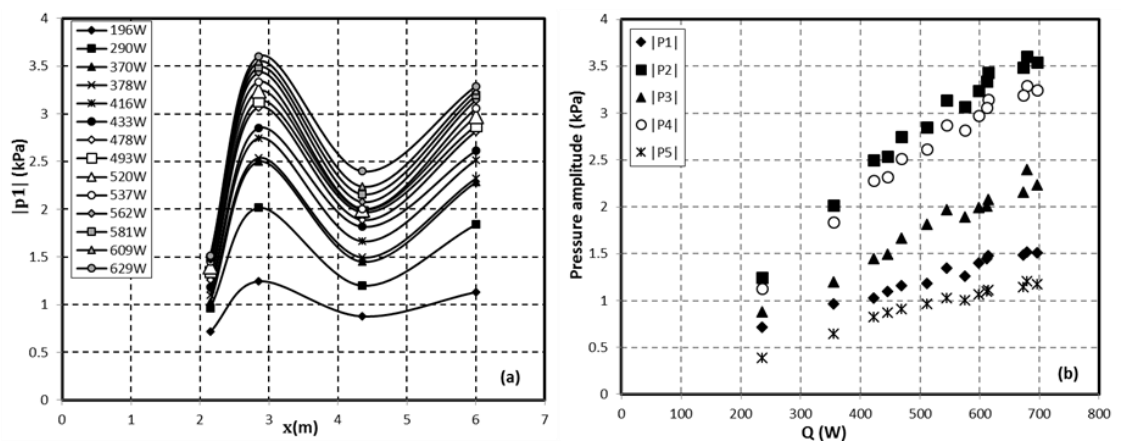


Figure 4. 72 Effect of heating power on the pressure amplitude distribution along the loop. (a) pressure amplitude versus loop length and (b) pressure amplitude versus heat input.

Because there is a difference between the measured and calculated heat input, one of the measured pressure amplitudes that was used as a target in the calculations should be appropriate to represent the increase in the heating power. In the following graphs, the pressure amplitude P4 was selected and it is presented as a

drive ratio of the first stage of the generator. Figure 4.73 shows a comparison between the simulation and the measurements related to the effect of the pressure ratio of stage 1 ($|P_4|/|P_m|$) on the coil displacement of the alternator. The calculations and measurements have a similar trend to the linear increase of the coil displacement. The measured results are shown as black diamonds while DeltaEC calculated results are presented as a solid line. The increase of the measured pressure ratio from 1.11% to 3.25% causes a gradual rise in the coil displacement from 1.91 mm to around 6.73 mm. From Figure 4.72a, the pressure drive ratio 1.11 and 3.25% correspond to the heat input of 196 W and 629 W, respectively.

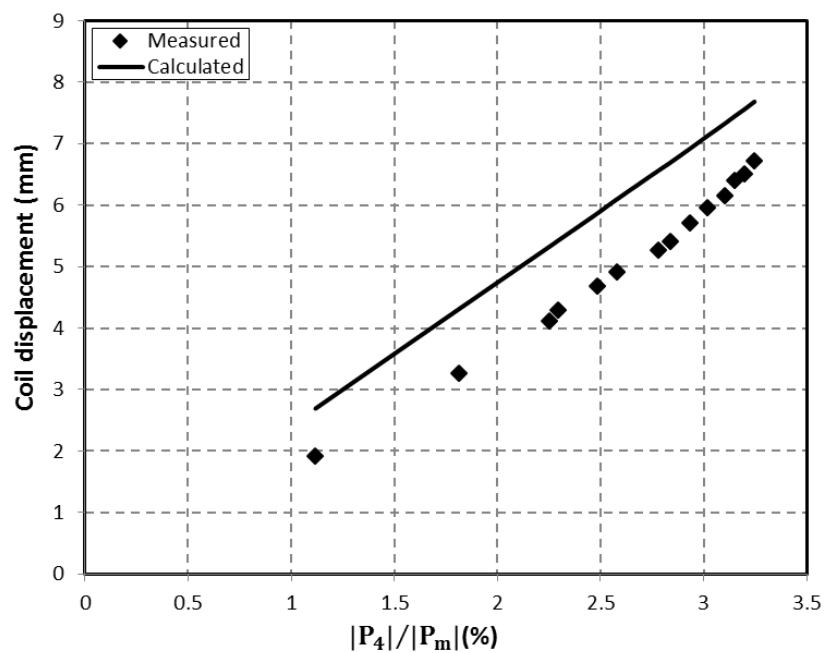


Figure 4. 73 Effect of heating power on the relationship between the pressure drive ratio and the coil displacement of the alternator.

Figure 4.74 shows a comparison between the calculated and measured effects of the drive ratio on the acoustic power that is extracted by the alternator. The graph clearly shows that both the calculated and measured results of the acoustic power extraction have an almost linear relationship with the drive ratio. The increase in the pressure ratio increases the measured extraction of the acoustic power to the maximum value of around 29.27 W. At high pressure ratios, it can be seen that there is a good agreement between calculations and simulations. The thermal-to-acoustic efficiency can be presented in an analogous way.

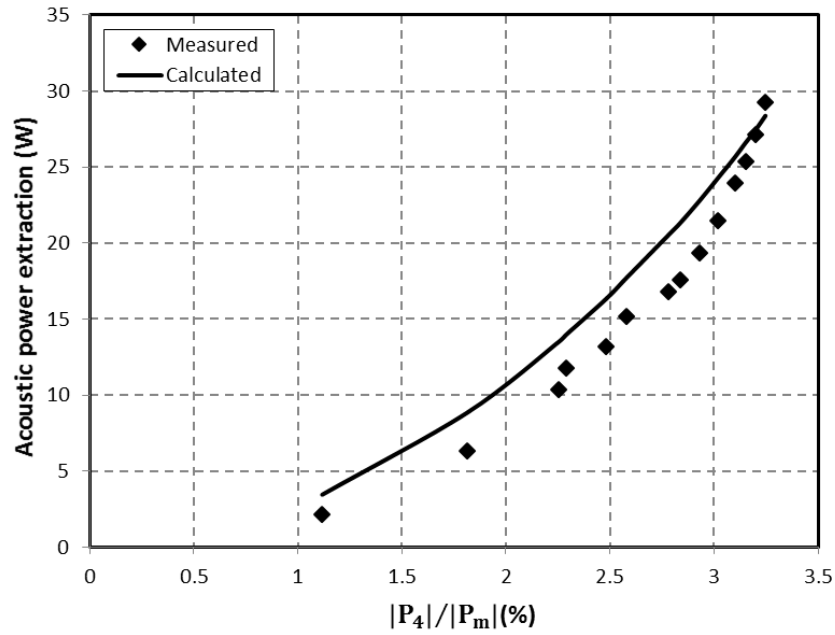


Figure 4.74 Effect of heating power on the relationship between the pressure ratio and the acoustic power extraction of the alternator.

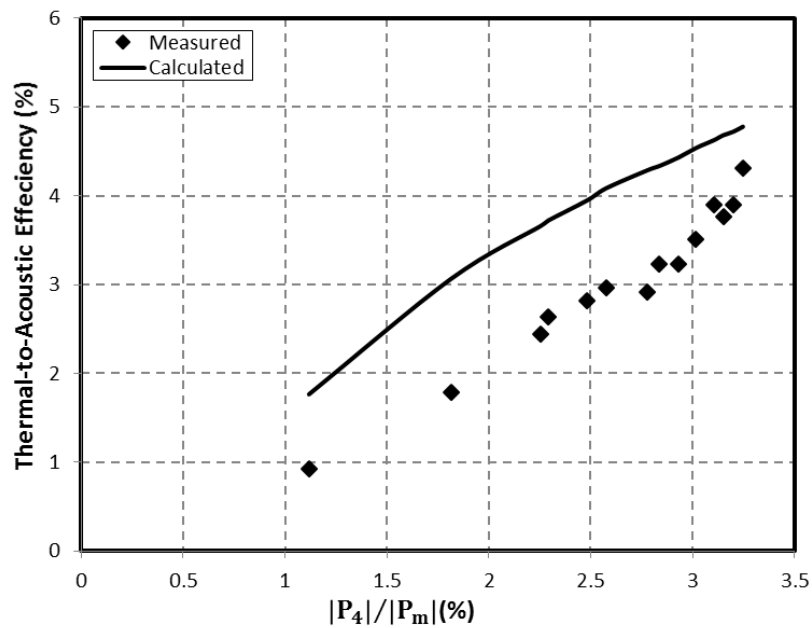


Figure 4.75 Effect of heating power input on the relationship between the pressure drive ratio and the thermoacoustic efficiency.

Figure 4.75 shows the effect of the heat input on the relationship between the pressure ratio of the first stage and the thermal-to-acoustic efficiency. As can be seen in the graph, there is a comparison between the simulations the experimental results. Both simulated and measured results show a similar trend to the linear relationship when the efficiency increases with the increase of the heat input. The

results presented in Figures 4.74 and 4.75 are of course similar to those already presented in Figures 4.37 and 4.38. However it should be noted that the acoustic power extracted increased from 16.18 W to around 29 W, while the thermal-to-acoustic efficiency (measured) increased from 2.75 to 4.4%.

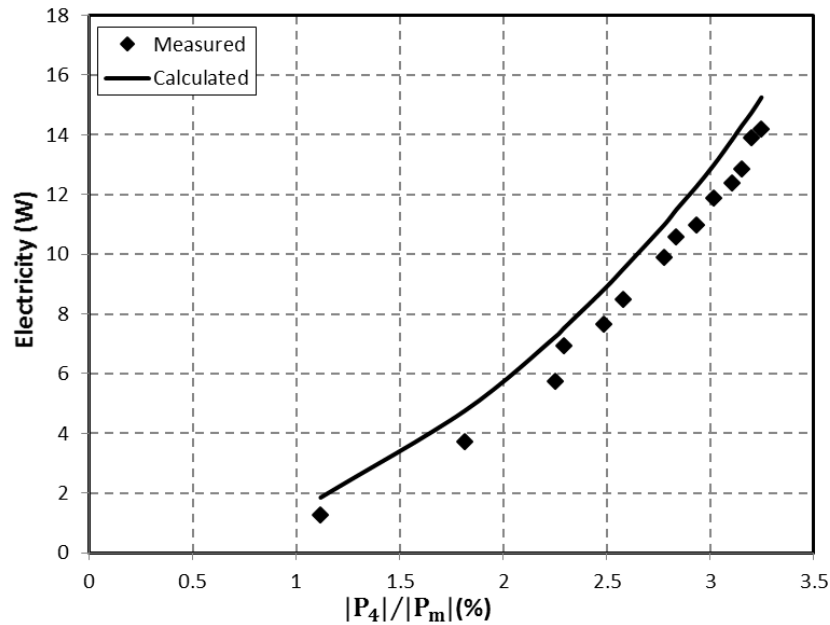


Figure 4.76 Effect of the heat input on the relationship between the pressure ratio and the electrical output

Figure 4.76 shows the effect of the heat input on the relationship between the pressure ratio of the first stage and the electrical output of the generator. The relationship is presented as a comparison between the calculated and measured results. It can be seen from the graph that there is a linear relationship between the electricity and the pressure ratio. Since the pressure ratio is linear with the heat input, the electrical output is also linear with the heat input. The measured electrical power as seen in the graph increases from around 1.28 to 14.18 W when the drive ratio rises from 1.11 to around 3.24%. Generally, the calculated results agree very well with the measured results. Figure 4.77 presents simulated vs. calculated results related to the effect of the heat input on the relationship between the pressure ratio and the thermal-to-electric efficiency. Here also a linear relationship is clear when the measured generator efficiency increases from 0.54 to around 2.1% while the

calculated efficiency rises from 0.95 to 2.57% at the same range of pressure drive ratio of 1.11 to 3.25%.

Figure 4.78 shows the comparison between measured and calculated results in relation to the effect of the heating power input on the relationship between the pressure ratio and alternator efficiency. It is seen from the graph that both measured and calculated results fall onto a relatively flat horizontal line when plotting their dependence on the pressure drive ratio. Because the load resistance R_L is fixed at 9Ω , there is no effect on the alternator efficiency according to Equation (2.68). The calculated results have a fixed value of 53.76% while the measurements fluctuate between 59.16 and 55.38% along the increase of the pressure ratio. There is a relatively good agreement between the simulation and the measurements. At high pressure amplitudes, the actual coil of the alternator has high displacement and comes out of the magnetic gap which is not considered in the simulation. As a result, the acoustic-to-electric efficiency drops to 48.46% at a coil displacement 6.72 mm. In broad terms, this behaviour is congruent with already discussed results presented in Figure 4.41 in relation to the single-stage generator.

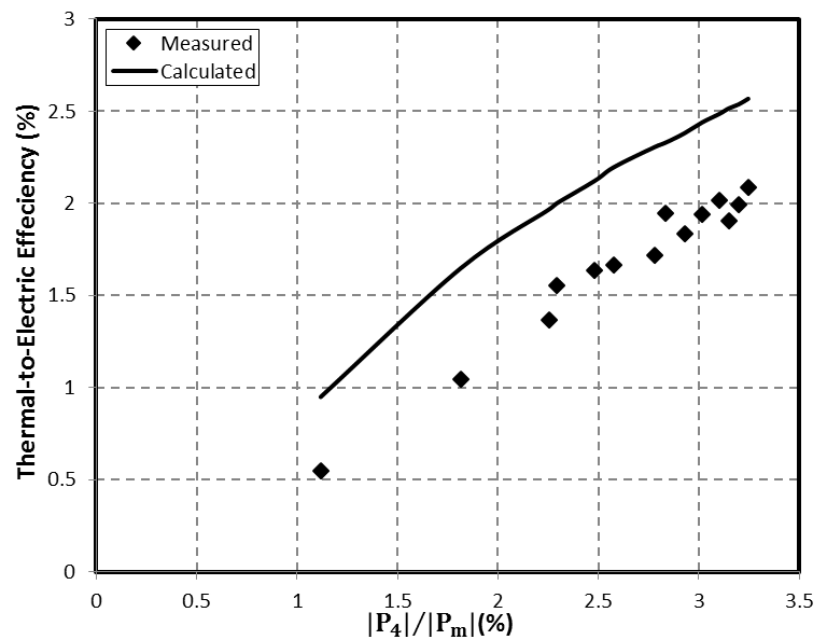


Figure 4.77 Effect of heating power on the relationship between the pressure ratio and the entire efficiency of the generator

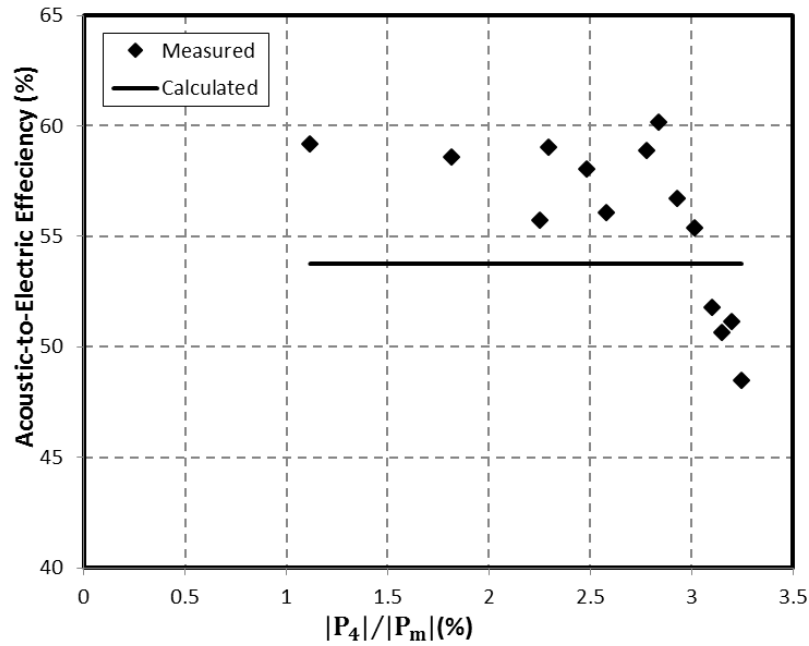


Figure 4. 78 Effect of heating power input on the relationship between the pressure ratio and the alternator efficiency.

4.5 Summary

This chapter outlines the numerical and experimental evaluation of the prototypes described in Chapter 3. This includes two main strands of the work: (i) the 54-mm diameter single-stage generator and (ii) the 128-mm diameter two-stage generator (with additional preliminary work on the engine with no load and the 128-mm diameter single-stage generator). In all experimental works, the two microphone method and the piston method have been used to estimate the acoustic power in all tested devices. The 54-mm diameter single-stage electric generator has been tested at a fixed load of 12 Ω of electrical resistance and an optimum stub length of 450 mm. The generator was able to produce 13 W of electricity at a temperature difference between the two ends of the regenerator of 430 K.

The work on the 128-mm diameter device included preliminary prototyping of a single-stage engine (with no alternator attached) and a single-stage generator in order to better understand the potential problems in the ultimate construction of the two-stage device.

The experiments on the thermoacoustic engine investigated the effect of the harmful acoustic streaming and the working frequency at different stub lengths. At 70.31 Hz of working frequency and 600 mm of the stub length, it was found that the acoustic

streaming significantly reduced the temperature difference between the two ends of the regenerator from 327 to 261.7°C and decreased the acoustic power in the loop from around 100 to 64.15 W. It was also found that reducing the length of the loop of the engine from 6.44 to 4.92 m increased the acoustic power in the loop by around 38% at stub length of 600 mm. Among the three tested frequencies, it was found that the optimal frequency of this regenerator is 64.45 Hz. This is clearly reflected on the level of the acoustic power in the loop as discussed earlier. Therefore, in order to achieve high produced electricity and efficiency, this loop should be connected to an alternator with resonance frequency near 64.45 Hz. It was also noticed that the optimal stub length is proportional to the loop length.

The 128-mm diameter single-stage generator was tested with different load resistances and heat inputs. It could achieve a maximum electrical power and thermal-to-electrical efficiency of 8.52 W and 1.47% respectively at 9 Ω . Indeed, the single-stage generator could provide a minimum of 6.72 W of electrical power along the range from 6 to 20 Ω . The investigation of the single stage engine and generator helped in the way of developing the two-stage generator. From the experiments of the single stage generator, it was found that the acoustic field in the generator should be tuned using a matching stub. Moreover, the data collected from experiments of the single stage generator used in the DeltaEC model to develop and upgrade the design to the two-stage generator.

The 128-mm diameter two-stage electric generator has been tested. The effects of the stub length, load resistance, and heat input were investigated. The highest electrical power extracted from the alternator was achieved at a load resistance of 9 Ω and optimal stub length of 1070 mm was around 14.18 W. Certainly, the electrical power of 13.44 W is reachable for a higher load resistance of 12 Ω . In addition, at this operational point the maximum thermal-to-electrical efficiency was 2.1%.

Although the flattened-tube configuration hot heat exchanger was not efficient enough to deliver high heat input compared to the heat exchanger of the 54-mm diameter generator, it was found that the efficiency of the two-stage generator that contain two simple and cost-effective heat exchangers can be comparable to one but expensive heat exchanger.

CHAPTER 5

CONCLUSION AND FUTURE WORK

5.1 Conclusion

The main aim of the study has been to explore the potential of producing small-scale electrical power for remote and rural areas of developing countries by utilising thermoacoustic technology. A few watts of electrical power would be enough to power a set of LED lamps, operate a radio or even charge a mobile phone or a set of batteries. The abundance of biomass fuel in these areas would be especially beneficial to power thermoacoustic electricity generators where there is no access to the electricity grid. Furthermore, from simplicity and cost-effectiveness point of view, it is feasible to build thermoacoustic electricity generators using easy manufacture methods (including the build of the hot heat exchangers) and commercially available materials. Of course, this involves the standard PVC materials that can handle working air at atmospheric pressure and an inexpensive ordinary loudspeaker as an alternator to convert the acoustic power into electricity.

The current study has focused on the looped-tube travelling wave thermoacoustic configuration engine due to its simplicity and efficiency. The work has been mainly divided into two studies of two different systems. The first study addressed a system of a looped-tube, single-stage generator that has a thermoacoustic core which was previously developed under SCORE project. This relies on resonator diameter of a 54 mm inside diameter. The second study covered a new challenge of the investigation of a large diameter (5 inch) two-stage looped-tube generator. This work was carried out in separate stages to include (i) a study of a single stage engine with no electricity generation; (ii) a study of a single-stage electricity generator; and (iii) a study of a final two-stage electricity generator. Although the two generators (single- and two-stage) used the same alternator, there were considerable differences between them regarding the size, shape, source of the heat input and the types of heat exchanger.

Throughout this PhD research, the objectives (a)-(g) outlined in section 1.3 have been carried out. Specifically, objective (a) concerned the study of the 54-mm generator while objectives (b)-(g) included the work on the 128-mm diameter

configurations (subsystems for final two-stage integrated system). The work towards all of the objectives set out in section 1.3 is presented in Chapters 3 and 4 as follows:

Objective “a”:

The evaluation of the the 54-mm diameter diameter single-stage electricity generator arising from previous work under SCORE project has been carried out. This in particular included DeltaEC modelling with a new configuration of a side-branched linear alternator that was connected to a previously designed and developed thermoacoustic core. The modelling (carried out in tandem with experimental work) provided a clear picture of the acoustic field in the loop including the pressure and velocity amplitudes, the amplitude and phasing of the acoustic impedance, the acoustic power distribution and the electric power extracted from the alternator. However, the modelling also gave a deep insight into the behaviour of the generator when the experimental data has been applied in the model as detailed in section 4.1. A number of DeltaEC models that were achieved in the study are listed in Appendix B.

The prototype has been tested at a working frequency of 64.5 Hz, 12 Ω of load resistance connected to the alternator and an optimal stub length of 450 mm. The temperature difference between the two ends of the regenerator was increased from 255 to 430 K in the experiments to evaluate the impact of the heat input. The maximum electrical power of 13 W was extracted from the alternator at a regenerator temperature difference of 430 K which had a corresponding heating temperature of 627.4°C provided by the flue gas of the propane combustion. The results presented in section 4.1 showed good agreement between experiments and calculations. Furthermore, the verified model of the generator showed the calculated heat input and the thermal-to-electrical efficiency of 560.8 W and 3.5%, respectively.

Objectives “b” and “c”:

The DeltaEC design and modelling for the larger size thermoacoustic engine that consisted of a thermoacoustic core, a 128-mm diameter feedback pipe and a matching stub have been accomplished. Based on a commercially available car heater used as an ambient heat exchanger and a “flattened-tube”, simple to manufacture, hot heat exchanger, the model was initiated. In order to obtain the optimal operational conditions, the model was improved through a series of numerical optimisations of different geometrical parameters before reaching the final version. The optimisation process provided links to understand the impact of these parameters on the performance of the generator. However, from the simplicity and cost-effectiveness point of view, the dimensions of the optimised parameters were slightly adjusted to match the closest standard sizes. Based on the model, the physical prototype of the single stage engine has been built as presented in section 3.3.1. For working frequencies of 48.82, 64.45 and 70.31 Hz, a set of experiments has been conducted as discussed in section 4.2. The engine was first examined at the working frequency of 70.31 to investigate the effects of Gedeon streaming. At 600 mm of stub length, it was found that the acoustic power in the loop falls from 110.63 to 63.4 W by streaming. However, the acoustic power increased from 111.45 to 153 W at the stub length of 600 mm when the working frequency was increased from 48.82 to 64.45 Hz.

Objectives “d” and “e”:

The DeltaEC model of the 128-mm diameter resonator single-stage generator has been achieved. The loop included one side branch for the alternator with two different cross sectional areas to match the acoustic impedance between the loop and the alternator. Based on the loop and the branch length, defined in the model, the experimental apparatus has been constructed and tested. Investigation of the effects of the load resistance and heating power input has been conducted. The degrading effects of the Gedeon streaming were eliminated by inserting a membrane near the velocity node. The preliminary results of the experimental work were

applied to the model to simulate the actual performance of the generator. At air temperature of 550°C and 581 W of heat input, the system could generate 8.52 W of electricity and 1.47% of thermal-to-electric efficiency for a 9 Ω load. Moreover, the prototype provided a minimum of 6.72 W of electric power for load ranges of 6 to 20 Ω .

Objectives “f” and “g”:

The 128-mm diameter two-stage looped-tube thermoacoustic electrical generator has been modelled. The design included two identical stages of the designed engine, a branched linear alternator and a matching stub. Based on the final version of the DeltaEC model, the construction of the experimental rig of the designed prototype has been implemented as discussed in section 3.3.3. The two identical stages of the generator were connected in series by a set of 128-mm diameter PVC pipes and fittings within a total loop length of 6.3 m.

The experimental work of the two-stage generator has been conducted. Firstly, the encountered problem of the harmful acoustic streaming in the loop has been evaluated and solved. This was achieved by the debugging process of placing a flexible membrane in the loop, as discussed in section 4.4 (following the lessons from single stage engine and generator). Later, a number of influences on the performance of the generators have been investigated. These included the effects of the stub length, the load resistance and the heating power input as discussed in section 4.4.2, 4.4.3 and 4.4.4 respectively. The results showed that the prototype could generate electrical power of 14.18 W to be consumed by a load resistance of 9 Ω at a stub length of 1070 mm and a heating temperature of the heat gun of 550°C. Of course this result highlighted the satisfactory thermal-to-electrical efficiency achieved of around 2.1%. In addition, it was shown that the generator can still generate an electric power of 13.44 W at the maximum load applied of 12 Ω . This maximum load was at maximum stroke displacement of the alternator. The DeltaEC model showed a powerful potential to agree with the experimental results.

5.2 Future Work

Although most of the objectives included in section 1.3 were achieved during the current project, there are still some issues which need to be investigated and a number of strategies to improve device performance need to be fulfilled. Some of these are summarised and listed below:

- (a) Investigation of streaming in the loop of the 54-mm diameter generator. This would need to add more thermocouples to check the temperature gradient in the regenerator. Practically finding the velocity node in all loops would support the elastic membrane inserted to pass the sound wave smoothly.
- (b) Further investigations into improving the phase difference between the acoustic pressure and velocity in the loop and particularly in the regenerator. Besides the function of the matching stub, this would be implemented by adjusting the inertance and compliance along the loop.
- (c) Additional inspections of the optimum position of the matching stub to improve the acoustic impedance matching and reduce the phase angle between pressure and velocity. Moreover, the feasibility to add a second matching stub in the loop, especially in the case of the two-stage generator, can improve the acoustic field in the loop as well.
- (d) Further studies of the relationship between the resonance frequency of the alternator on one hand and the loop length and the appropriate size of the regenerator on the other hand. This may significantly increase the performance of the device.
- (e) Intensive theoretical and experimental studies of the simple and easy manufactured flattened-tube hot heat exchangers should be considered. This would need at least to investigate the impact the hydraulic radius and porosity on the performance of the heat exchanger.
- (f) Investigations into improving the performance by enhancing the heat transfer into the hot heat exchangers. This has been done in a very preliminary form by inserting stainless steel springs or twisted tapes in the channels to disturb the boundary layer of the acoustic flow and mix the oscillating air near walls.

The preliminary tests did not improve the performance, but further work is needed in heat transfer enhancement.

- (g) Improving the heat input to the second stage in the two-stage generator. This would be achieved by arranging the two stages horizontally in order to receive equal heating temperature of the heat gun. Of course this would also need to manage and equalise the air flow rate for both stages.
- (h) Improving the performance of all systems could also be achieved by increasing the mean pressure by a few hundreds of kilopascals. This could be implemented since some PVC pipes can withstand up to 1.6 MPa.
- (i) It would be interesting to design a cooler into the loop of the two-stage generator. This would convert the acoustic power that flows in the loop of the thermoacoustic engine into cooling effects thus providing an additional (or alternative) capability.

BIBLIOGRAPHY

Abdoulla, K., Kang, H. and Jaworski, A., 2013. Travelling wave thermoacoustic electricity generator for rural areas using a side-branch alternator arrangement. In: *The World Congress on Engineering 2013 (WCE 2013)*, London, UK.

Abdoulla, K.O.A., Yu, Z. and Jaworski, A.J., 2012. Design of a low-cost two-stage thermoacoustic electricity generator for rural communities in developing countries. In: *19th International Congress on Sound and Vibration, ICSV 2012*, Vilnius, Lithuania.

Abduljalil, A. S., Yu, Z. and Jaworski, A. J., 2011b. Selection and experimental evaluation of low-cost porous materials for regenerator applications in thermoacoustic engines. *Materials & Design* 32(1), 217-228.

Abduljalil, A.R.S., Yu, Z. and Jaworski, A.J., 2009b. Performance studies of travelling-wave thermoacoustic engine for selected low-cost regenerators. In: *Proceedings of SEM Annual Conference*, Albuquerque, New Mexico, USA.

Abduljalil, A.S., Yu, Z. and Jaworski, A.J., 2011a. Design and experimental validation of looped-tube thermoacoustic engine. *Journal of Thermal Science*, 20(5), pp.423-429.

Abduljalil, A.S., Yu, Z., Jaworski, A.J. and Shi, L., 2009a. Construction and Performance Characterization of the Looped-Tube Travelling-Wave Thermoacoustic Engine with Ceramic Regenerator. *World Academy of Science, Engineering and Technology, International Journal of Mechanical, Aerospace, Industrial, Mechatronic and Manufacturing Engineering*, 3(1), pp.19-22.

Arnott, W.P., Bass, H.E. and Raspet, R., 1991. General formulation of thermoacoustics for stacks having arbitrarily shaped pore cross sections. *The Journal of the Acoustical Society of America*, 90(6), pp.3228-3237.

Atchley, A.A., 1992. Standing wave analysis of a thermoacoustic prime mover below onset of self-oscillation. *The Journal of the Acoustical Society of America*, 92(5), pp.2907-2914.

B&C speakers. <http://www.bcspeakers.com/products/lf-driver/8-0/8/8bg51> [Accessed: 13 April 2015].

Backhaus, S. and Swift, G.W., 1999. A thermoacoustic Stirling heat engine. *Nature*, 399(6734), pp.335-338.

Backhaus, S. and Swift, G.W., 2000. A thermoacoustic-Stirling heat engine: Detailed study. *The Journal of the Acoustical Society of America*, 107(6), pp.3148-3166.

Backhaus, S. and Swift, G.W., 2003. An acoustic streaming instability in thermoacoustic devices utilizing jet pumps. *The Journal of the Acoustical Society of America*, 113(3), pp.1317-1324.

Backhaus, S., Tward, E. and Petach, M., 2004. Traveling-wave thermoacoustic electric generator. *Applied Physics Letters*, 85(6), pp.1085-1087.

Bauwens, L., 1995. Near-isothermal regenerator-A perturbation analysis. *Journal of thermophysics and heat transfer*, 9(4), pp.749-756.

Belcher J. R. et. al., 1999. "Working gases in thermoacoustic engines". *J. Acoust. Soc. Am.*, 105(5) May, pp. 2677-2684.

Bi, T., Wu, Z., Zhang, L., Yu, G., Luo, E. and Dai, W., 2015. Development of a 5kW traveling-wave thermoacoustic electric generator. *Applied Energy*.

Bryan Walsh. (2013). Blackout: 1 Billion Live Without Electric Light. Available: <http://business.time.com/2013/09/05/blackout-1-billion-live-without-electric-light/>. Last accessed 14/12/2015.

Carter, R.L., White, M. and Steele, A.M., 1962. Private communication of atomics international division of North American aviation. Inc., September, 24.

Ceperley, P.H., 1979. A pistonless Stirling engine-The traveling wave heat engine. *The Journal of the Acoustical Society of America*, 66(5), pp.1508-1513.

Ceperley, P.H., 1984. Gain and efficiency of a short traveling wave heat engine. *The Journal of the Acoustical Society of America*, 75(S1), pp.S35-S35.

Ceperley, P.H., 1985. Gain and efficiency of a short traveling wave heat engine. *The Journal of the Acoustical Society of America*, 77(3), pp.1239-1244.

Chen, B.M., Riley, P.H., Abakr, Y.A., Pullen, K., Hann, D.B. and Johnson, C.M., 2013. Design and development of a low-cost, electricity-generating cooking Score-Stove™. *Proceedings of the institution of mechanical engineers, Part A: Journal of Power and Energy*, p.0957650913498733.

Dai, W., Luo, E., Zhang, Y. and Ling, H., 2006. Detailed study of a traveling wave thermoacoustic refrigerator driven by a traveling wave thermoacoustic engine. *The Journal of the Acoustical Society of America*, 119(5), pp.2686-2692.

De Blok K. Novel 4-stage traveling wave thermoacoustic power generator. In ASME 2010 3rd Joint US-European Fluids Engineering Summer Meeting collocated with 8th International Conference on Nanochannels, Microchannels, and Minichannels 2010 Jan 1 (pp. 73-79). American Society of Mechanical Engineers.

De Blok, K. and Systemen, A.T., 2012, July. Multi-stage traveling wave thermoacoustics in practice. In *19th International Congress on Sound and Vibration, Vilnius*.

Douglas F. Barnes, Robert Van Der Plas, Willem Floor. (1997). Tackling the Rural Energy Problem in Developing Countries. Available: <https://www.imf.org/external/pubs/ft/fandd/1997/06/pdf/barnes.pdf>. Last accessed 13/12/2015

Feldman, K.T., 1968. Review of the literature on Rijke thermoacoustic phenomena. *Journal of Sound and Vibration*, 7(1), pp.83-89.

Feldman, K.T., 1968. Review of the literature on Sondhauss thermoacoustic phenomena. *Journal of Sound and Vibration*, 7(1), pp.71-82.

- Gardner, D.L. and Swift, G.W., 2003. A cascade thermoacoustic engine. *The Journal of the Acoustical Society of America*, 114(4), pp.1905-1919.
- Gifford, W.E. and Longworth, R.C., 1966. Surface heat pumping. In *Advances in Cryogenic Engineering* (pp. 171-179). Springer US.
- Gomez-Meda, R., 1991, October. Measurement of the thiele-small parameters for a given loudspeaker, without using a box. In *Audio Engineering Society Convention 91*. Audio Engineering Society.
- Hu, Z., Li, Q., Xie, X., Zhou, G. and Li, Q., 2006. Design and experiment on a mini cascade thermoacoustic engine. *Ultrasonics*, 44, pp.e1515-e1517.
- Hu, Z.J., Li, Q., Li, Q. and Li, Z.Y., 2006. A high frequency cascade thermoacoustic engine. *Cryogenics*, 46(11), pp.771-777.
- Hu, Z.J., Li, Z.Y., Li, Q. and Li, Q., 2010. Evaluation of thermal efficiency and energy conversion of thermoacoustic Stirling engines. *Energy Conversion and Management*, 51(4), pp.802-812.
- Huan, T., Jianying, H., Limin, Z. and Ercang, L., 2015. Experimental Study of an Acoustic Resonant Cooling System. *Physics Procedia*, 67, pp.445-450.
- Huang, Y., Luo, E., Dai, W., Wu, Z., 2005. Experimental investigation on a room-temperature traveling wave thermoacoustic refrigerator. In: *Proceedings of the Twentieth International Cryogenic Engineering Conference (ICEC 20)*, Beijing, China.
- Kang, H., Cheng, P., Yu, Z. and Zheng, H., 2015. A two-stage traveling-wave thermoacoustic electric generator with loudspeakers as alternators. *Applied Energy*, 137, pp.9-17.
- Kang, H., Jiang, F., Zheng, H. and Jaworski, A.J., 2013. Thermoacoustic travelling-wave cooler driven by a cascade thermoacoustic engine. *Applied Thermal Engineering*, 59(1), pp.223-231.

- Kang, H., Li, Q. and Zhou, G., 2009. Optimizing hydraulic radius and acoustic field of the thermoacoustic engine. *Cryogenics*, 49(3), pp.112-119.
- Kang, H., Zhou, G. and Li, Q., 2010a. Heat driven thermoacoustic cooler based on traveling–standing wave. *Energy Conversion and Management*, 51(11), pp.2103-2108.
- Kang, H., Zhou, G. and Li, Q., 2010b. Thermoacoustic effect of traveling–standing wave. *Cryogenics*, 50(8), pp.450-458.
- Kays, W.M. and London, A.L., 1984. Compact heat exchangers.
- Ling, H., Luo, E. and Dai, W., 2006. A numerical simulation method and analysis of a complete thermoacoustic-Stirling engine. *Ultrasonics*, 44, pp.e1511-e1514.
- Luo, E.C., Ling, H., Dai, W. and Yu, G.Y., 2006. Experimental study of the influence of different resonators on thermoacoustic conversion performance of a thermoacoustic-Stirling heat engine. *Ultrasonics*, 44, pp.e1507-e1509.
- Merkli, P. and Thomann, H., 1975. Thermoacoustic effects in a resonance tube. *Journal of fluid mechanics*, 70(01), pp.161-177.
- Migliori, A. and Swift, G.W., 1988. Liquid-sodium thermoacoustic engine. *Applied Physics Letters*, 53(5), pp.355-357.
- Mikulin, E.I., Tarasov, A.A. and Shkrebyonock, M.P., 1984. Low-temperature expansion pulse tubes. In *Advances in cryogenic engineering* (pp. 629-637). Springer US.
- Miwa, M., Sumi, T., Biwa, T., Ueda, Y. and Yazaki, T., 2006. Measurement of acoustic output power in a traveling wave engine. *Ultrasonics*, 44, pp.e1527-e1529.
- Nouh, M.A., Arafa, N.M., Larsson, K., Abdel-Rahman, E., 2009. Design study of anharmonic standing wave thermoacoustic heat engine. In: *The 16th International Congress on Sound and Vibration (ICSV 16)*, Krakow, Poland.
- Press, W.H., Teukolsky, S.A., Vetterling, W.T. and Flannery, B.P., 1992. *Numerical recipes in FORTRAN* (Cambridge).

- Putnam, A.A. and Dennis, W.R., 1956. Organ-Pipe Oscillations in a Burner with Deep Ports. *The Journal of the Acoustical Society of America*, 28(2), pp.260-269.
- Qiu, L.M., Sun, D.M., Tan, Y.X., Deng, X. and Chen, G.B., 2006, April. Investigation on Gedeon streaming in a traveling wave thermoacoustic engine. In *Advances in Cryogenic Engineering: Transactions of the Cryogenic Engineering Conference-CEC* (Vol. 823, No. 1, pp. 1115-1122). AIP Publishing.
- Rayleigh, J.W.S.B., 1896. *The theory of sound* (Vol. 2). Macmillan.
- Riley, P., 2007. <http://www.score.uk.com/>. [Accessed: 15 February 2013].
- Rott, N., 1969. Damped and thermally driven acoustic oscillations in wide and narrow tubes. *Zeitschrift für angewandte Mathematik und Physik ZAMP*, 20(2), pp.230-243.
- Rott, N., 1973. Thermally driven acoustic oscillations. Part II: Stability limit for helium. *Zeitschrift für angewandte Mathematik und Physik ZAMP*, 24(1), pp.54-72.
- Rott, N., 1975. Thermally driven acoustic oscillations, Part III: Second-order heat flux. *Zeitschrift für angewandte Mathematik und Physik ZAMP*, 26(1), pp.43-49.
- Saechan, P., Kang, H., Mao, X. and Jaworski, A. J., 2013. Thermoacoustic Refrigerator Driven by a Combustion-Powered Thermoacoustic Engine – Demonstrator of Device for Rural Areas of Developing Countries. In: *Proceedings of the World Congress on Engineering 2013, WCE 2013, London, U.K.*
- So, J.H., Swift, G.W. and Backhaus, S., 2004. An acoustic streaming instability within regenerator-based thermoacoustic devices. *The Journal of the Acoustical Society of America*, 115(5), pp.2381-2381.
- So, J.H., Swift, G.W. and Backhaus, S., 2006. An internal streaming instability in regenerators. *The Journal of the Acoustical Society of America*, 120(4), pp.1898-1909.
- Swift, G. W., “Thermoacoustics: A Unifying Perspective for Some Engines and Refrigerators”. New York, Acoustical Society of America, 2002.

Swift, G. W., 1988. "Thermoacoustic engines". J. Acoust. Soc. Am., 84(4), October, pp. 1145-1180.

Swift, G. W., 2002. Thermoacoustics: A Unifying Perspective for Some Engines and Refrigerators ASA: The Journal of the Acoustical Society of America.

Swift, G., 2007. Thermoacoustics. In Springer Handbook of Acoustics (pp. 239-255). Springer New York.

Swift, G.W. and Keolian, R.M., 1993. Thermoacoustics in pin-array stacks. The Journal of the Acoustical Society of America, 94(2), pp.941-943.

Swift, G.W., 1988. Thermoacoustic engines. The Journal of the Acoustical Society of America, 84(4), pp.1145-1180.

Swift, G.W., 1992. Analysis and performance of a large thermoacoustic engine. The Journal of the Acoustical Society of America, 92(3), pp.1551-1563.

Swift, G.W., 2000, July. Streaming in thermoacoustic engines and refrigerators. In NONLINEAR ACOUSTICS AT THE TURN OF THE MILLENNIUM: ISNA 15, 15th International Symposium (Vol. 524, No. 1, pp. 105-114). AIP Publishing.

Taconis, K.W., Beenakker, J.J.M., Nier, A.O.C. and Aldrich, L.T., 1949. Measurements concerning the vapour-liquid equilibrium of solutions of He 3 in He 4 below 2.19° K. Physica, 15(8), pp.733-739.

Tijani, H., Spoelstra, S. and Poignand, G., 2008. Study of a thermoacoustic-Stirling engine. Journal of the Acoustical Society of America, 123(5), p.3541.

Tijani, M.E.H., Zeegers, J.C.H. and De Waele, A.T.A.M., 2002. Design of thermoacoustic refrigerators. Cryogenics, 42(1), pp.49-57.

Tijani, M.E.H., Zeegers, J.C.H. and De Waele, A.T.A.M., 2002. Prandtl number and thermoacoustic refrigerators. The Journal of the Acoustical Society of America, 112(1), pp.134-143.

Ward, B., Clark, J. and Swift, G. W., 2008. Design Environment for Low-Amplitude ThermoAcoustic Energy Conversion (DELTAEC) programme. Version 6.2 b3, Los Alamos National Laboratory, New Mexico, USA.

Ward, W.C. and Swift, G.W., 1994. Design environment for low-amplitude thermoacoustic engines. *Journal of the Acoustical Society of America*, 95(6), pp.3671-3674.

Wheatley, J., Hofler, T., Swift, G.W. and Migliori, A., 1983. An intrinsically irreversible thermoacoustic heat engine. *The Journal of the Acoustical Society of America*, 74(1), pp.153-170.

Wheatley, J., Hofler, T., Swift, G.W. and Migliori, A., 1983. Experiments with an intrinsically irreversible acoustic heat engine. *Physical review letters*, 50(7), p.499.

Wheatley, J., Hofler, T., Swift, G.W. and Migliori, A., 1985. Understanding some simple phenomena in thermoacoustics with applications to acoustical heat engines. *American Journal of Physics*, 53(2), pp.147-162.

Wu, Z., Dai, W., Man, M. and Luo, E., 2012. A solar-powered traveling-wave thermoacoustic electricity generator. *Solar Energy*, 86(9), pp.2376-2382.

Wu, Z., Man, M., Luo, E., Dai, W. and Zhou, Y., 2011. Experimental investigation of a 500 W traveling-wave thermoacoustic electricity generator. *Chinese Science Bulletin*, 56(19), pp.1975-1977.

Wu, Z., Yu, G., Zhang, L., Dai, W. and Luo, E., 2014b. Development of a 3kW double-acting thermoacoustic Stirling electric generator. *Applied Energy*, 136, pp.866-872.

Wu, Z., Zhang, L., Dai, W. and Luo, E., 2014a. Investigation on a 1kW traveling-wave thermoacoustic electrical generator. *Applied Energy*, 124, pp.140-147.

Yazaki, T. and Tominaga, A., 1998, August. Measurement of sound generation in thermoacoustic oscillations. In *Proceedings of the Royal Society of London A: Mathematical, Physical and Engineering Sciences* (Vol. 454, No. 1976, pp. 2113-2122). The Royal Society.

Yazaki, T., Iwata, A., Maekawa, T. and Tominaga, A., 1998. Traveling wave thermoacoustic engine in a looped tube. *Physical Review Letters*, 81(15), p.3128.

Yazaki, T., Tominaga, A. and Narahara, Y., 1979. Stability limit for thermally driven acoustic oscillation. *Cryogenics*, 19(7), pp.393-396.

Yazaki, T., Tominaga, A. and Narahara, Y., 1980. Experiments on thermally driven acoustic oscillations of gaseous helium. *Journal of low temperature physics*, 41(1-2), pp.45-60.

Yu, G., Dai, W. and Luo, E., 2010d. CFD simulation of a 300Hz thermoacoustic standing wave engine. *Cryogenics*, 50(9), pp.615-622.

Yu, G.Y., Luo, E.C., Dai, W. and Wu, Z.H., 2007. An energy-focused thermoacoustic-Stirling heat engine reaching a high pressure ratio above 1.40. *Cryogenics*, 47(2), pp.132-134.

Yu, Z. and Jaworski, A. J., 2012. Demonstrator of a combustion driven thermoacoustic electricity generator for remote and rural areas of developing countries. In: 19th International Congress on Sound and Vibration, ICSV 2012, Vilnius, Lithuania.

Yu, Z. and Jaworski, A.J., 2010a. Impact of acoustic impedance and flow resistance on the power output capacity of the regenerators in travelling-wave thermoacoustic engines. *Energy conversion and management*, 51(2), pp.350-359.

Yu, Z. and Jaworski, A.J., 2010b. Optimization of thermoacoustic stacks for low onset temperature engines. *Proceedings of the Institution of Mechanical Engineers, Part A: Journal of Power and Energy*, 224(3), pp.329-337.

Yu, Z., Jaworski, A.J. and Abduljalil, A.S., 2010c. Fishbone-like instability in a looped-tube thermoacoustic engine. *The Journal of the Acoustical Society of America*, 128(4), pp.EL188-EL194.

Yu, Z., Jaworski, A.J. and Backhaus, S., 2010a. A low-cost electricity generator for rural areas using a travelling-wave looped-tube thermoacoustic engine. *Proceedings*

of the Institution of Mechanical Engineers, Part A: Journal of Power and Energy, 224(6), pp.787-795.

Yu, Z., Jaworski, A.J. and Backhaus, S., 2010b, January. Design of a Low-Cost Thermoacoustic Electricity Generator and Its Experimental Verification. In ASME 2010 10th Biennial Conference on Engineering Systems Design and Analysis (pp. 191-199). American Society of Mechanical Engineers.

Yu, Z., Jaworski, A.J. and Backhaus, S., 2012. Travelling-wave thermoacoustic electricity generator using an ultra-compliant alternator for utilization of low-grade thermal energy. *Applied Energy*, 99, pp.135-145.

Yu, Z., Li, Q., Chen, X., Guo, F. and Xie, X., 2004. Study on the optimal characteristic dimension of regenerator in a thermoacoustic engine.

Yu, Z., Saechan, P. and Jaworski, A.J., 2011. A method of characterising performance of audio loudspeakers for linear alternator applications in low-cost thermoacoustic electricity generators. *Applied acoustics*, 72(5), pp.260-267.

Yu, Z.B., Li, Q., Chen, X., Guo, F.Z. and Xie, X.J., 2005. Experimental investigation on a thermoacoustic engine having a looped tube and resonator. *Cryogenics*, 45(8), pp.566-571.

Zhi-qing, W., 1982. Study on correction coefficients of liminar and turbulent entrance region effect in round pipe. *Applied Mathematics and Mechanics*, 3(3), pp.433-446.

Zhou, G., Li, Q., Li, Z.Y. and Li, Q., 2008. A miniature thermoacoustic stirling engine. *Energy Conversion and Management*, 49(6), pp.1785-1792.

APPENDICES

Appendix A: List of publications.

- 1- Abdoulla, K.O.A., Yu, Z. and Jaworski, A.J., 2012. Design of a low-cost two-stage thermoacoustic electricity generator for rural communities in developing countries. In: 19th International Congress on Sound and Vibration, ICSV 2012, Vilnius, Lithuania.
- 2- Abdoulla, K., Kang, H. and Jaworski, A., 2013. Travelling wave thermoacoustic electricity generator for rural areas using a side-branch alternator arrangement. In: The World Congress on Engineering 2013 (WCE 2013), London, UK.

Appendix B: List of DeltaEC models.

B1. Simulation of the 54-mm diameter electricity generator

```
!----- 0 -----
BEGIN
1.0100E+05 a Mean P Pa
 64.687 b Freq Hz G
479.94 c TBeg K G
1.4704E+04 d |p| Pa G
 0.0000 e Ph(p) deg
2.5427E-02 f |U| m^3/s G
 28.677 g Ph(U) deg G
164.02 h Htot W G
air Gas type
!----- 1 -----
DUCT Dummy to allow for JOIN
9.5030E-03 a Area m^2 Mstr 1.4704E+04 A |p| Pa
 0.34557 b Perim m 1a -2.7577E-06 B Ph(p) deg
1.0000E-06 c Length m 2.5427E-02 C |U| m^3/s
5.0000E-04 d Srough 28.676 D Ph(U) deg
164.02 E Htot W
ideal Solid type 164.02 F Edot W
!----- 2 -----
RPN ChangeMe
 0.0000 a G or T 4.7395 A ChngeMe
U1 mag w / 1.32e-2 / 1000 *
!----- 3 -----
JOIN Adiabatic/isothermal interface
1.4704E+04 A |p| Pa
-2.7577E-06 B Ph(p) deg
2.4640E-02 C |U| m^3/s
28.676 D Ph(U) deg
164.02 E Htot W
158.93 F Edot W
```

```

479.94 G TBeg K
479.94 H TEnd K
!----- 4 -----
TX      Change Me
sameas 1a a Area m^2      1.5005E+04 A |p| Pa
6.0000E-02 b GasA/A      -3.1601 B Ph(p) deg
6.0000E-02 c Length m    2.3810E-02 C |U| m^3/s
3.0000E-03 d radius m    25.542 D Ph(U) deg
-313.89 e HeatIn W      G -149.88 E Htot W
300.00 f SolidT K      =4H 156.69 F Edot W
479.94 G GasT K
ideal   Solid type      300.00 H SolidT K
!----- 5 -----
RPN     Phase(Z)
-5.2195 a G or T      -28.702      A ChngeMe
4B 4D -
!----- 6 -----
RPN     Zn
0.0000 a G or T      18.601      A ChngeMe
p1 U1 4a // mag rho / a /
!----- 7 -----
DUCT    Cold gap
sameas 1a a Area m^2    Mstr 1.5006E+04 A |p| Pa
0.34557 b Perim m      7a -3.1626 B Ph(p) deg
1.0000E-03 c Length m  2.3614E-02 C |U| m^3/s
1.0000E-04 d Srough    24.668 D Ph(U) deg
-149.88 E Htot W
ideal   Solid type      156.68 F Edot W
!----- 8 -----
RPN     Phase
0.0000 a G or T      -27.831      A ChngeMe
7B 7D -
!----- 9 -----
RPN     Zn
0.0000 a G or T      18.756      A ChngeMe
p1 U1 7a // mag rho / a /
!----- 10 -----
STKSCREEN Screen regenerator - using bare e_s
sameas 1a a Area m^2    1.2677E+04 A |p| Pa
0.8200 b VolPor        -6.3124 B Ph(p) deg
2.3000E-02 c Length m  3.9789E-02 C |U| m^3/s
1.1000E-04 d rh m      5.8291 D Ph(U) deg
0.1500 e ksFrac        -149.88 E Htot W
246.55 F Edot W
479.94 G TBeg K
stainless Solid type    909.94 H TEnd K
!----- 11 -----
RPN     Rh
0.0000 a G or T      0.1229      A ChngeMe
10d dk /
!----- 12 -----
RPN     Zn
0.0000 a G or T      10.618      A ChngeMe
p1 U1 / mag 10a * 10b * rho / a /
!----- 13 -----
RPN     Phase(Z)
0.0000 a G or T      -12.141      A ChngeMe
10B 10D -
!----- 14 -----
RPN     Enet
0.0000 a G or T      89.876      A ChngeMe
10F 7F -
!----- 15 -----
DUCT    Hot gap
sameas 10a a Area m^2    Mstr 1.2677E+04 A |p| Pa
0.34557 b Perim m      15a -6.3169 B Ph(p) deg

```

```

1.5332E-03 c Length m          3.9676E-02 C |U|  m^3/s
1.0000E-04 d Srough          5.0757 D Ph(U) deg
ideal      Solid type          -149.88 E Htot W
                                246.53 F Edot W
!----- 16 -----
TX      Combustion TX
sameas 15a a Area m^2          1.2604E+04 A |p| Pa
0.1957 b GasA/A              -9.1056 B Ph(p) deg
0.1600 c Length m            3.7952E-02 C |U|  m^3/s
4.0000E-03 d radius m        -12.263 D Ph(U) deg
389.91 e HeatIn W            G    240.03 E Htot W
800.00 f SolidT K            238.81 F Edot W
ideal      Solid type          909.94 G GasT K
                                967.72 H SolidT K
!----- 17 -----
RPN      Eff
0.0000 a G or T              0.23051          A ChngeMe
14A 16e /
!----- 18 -----
RPN      Dt
430.00 a G or T              =18A 430.00          A ChngeMe
16G 4G -
!----- 19 -----
STKDUCT TBT 1
sameas 1a a Area m^2 Mstr 1.2501E+04 A |p| Pa
0.34557 b Perim m 19a -9.628 B Ph(p) deg
0.1780 c Length m 7.3643E-02 C |U|  m^3/s
7.3000E-04 d WallA m^2 -68.738 D Ph(U) deg
                                240.03 E Htot W
                                236.32 F Edot W
                                909.94 G TBeg K
stainless Solid type          847.74 H TEnd K
!----- 20 -----
STKCONE TBT 2
sameas 1a a Areal m^2 Mstr 1.2354E+04 A |p| Pa
0.34557 b Periml m 20a -9.9765 B Ph(p) deg
5.4000E-02 c Length m 8.2965E-02 C |U|  m^3/s
2.3520E-03 d AreaF m^2 Mstr -72.575 D Ph(U) deg
0.17192 e PerimF m 20d 240.03 E Htot W
1.0000E-03 f f_wall 235.85 F Edot W
                                847.74 G TBeg K
stainless Solid type          789.90 H TEnd K
!----- 21 -----
MINOR Minor loss due to Area Sudden Change of Cone
2.3520E-03 a Area m^2 1.2295E+04 A |p| Pa
0.1000 b K+ -9.4412 B Ph(p) deg
1.0000 c K- 8.2965E-02 C |U|  m^3/s
                                -72.575 D Ph(U) deg
                                240.03 E Htot W
                                230.49 F Edot W
!----- 22 -----
STKDUCT TBT-3 (2" Pipe)
sameas 20d a Area m^2 Mstr 1.1219E+04 A |p| Pa
0.17192 b Perim m 22a -11.866 B Ph(p) deg
0.1600 c Length m 9.4315E-02 C |U|  m^3/s
1.0000E-04 d WallA m^2 -76.226 D Ph(U) deg
                                240.03 E Htot W
                                228.93 F Edot W
                                789.90 G TBeg K
stainless Solid type          705.10 H TEnd K
!----- 23 -----
JOIN Adiabatic/isothermal interface
                                1.1219E+04 A |p| Pa
                                -11.866 B Ph(p) deg
                                9.3215E-02 C |U|  m^3/s
                                -76.226 D Ph(U) deg

```

```

240.03 E Htot W
226.26 F Edot W
705.10 G TBeg K
705.24 H TEnd K
!----- 24 -----
HX      Secondary ambient HX
sameas 22a a Area m^2      1.1197E+04 A |p| Pa
      0.4000 b GasA/A      -11.898 B Ph(p) deg
      1.0000E-03 c Length m      9.3244E-02 C |U| m^3/s
      2.0000E-03 d y0 m      -76.235 D Ph(U) deg
      -13.958 e HeatIn W      G      226.07 E Htot W
      300.00 f SolidT K      =24H      226.07 F Edot W
      705.24 G GasT K
ideal   Solid type      300.00 H SolidT K
!----- 25 -----
RPN     ChangeMe
      1.0000 a G or T      =25A      1.0000      A ChngeMe
H2k Edot /
!----- 26 -----
RPN     ChangeMe
      297.00 a G or T      297.00      A ChngeMe
26a =Tm
!----- 27 -----
RPN     ChangeMe
      0.0000 a G or T      17.380      A ChngeMe
U1 mag w / 1.32e-2 / 1000 *
!----- 28 -----
ANCHOR  Change Me
!----- 29 -----
DUCT    Short Section after 2nd AHX
sameas 24a a Area m^2      Mstr      8510.7 A |p| Pa
      0.17192 b Perim m      29a      -19.96 B Ph(p) deg
      0.1500 c Length m      0.10212 C |U| m^3/s
      5.0000E-04 d Srough      -79.023 D Ph(U) deg
      223.41 E Htot W
ideal   Solid type      223.41 F Edot W
!----- 30 -----
TBRANCH Change Me
      1.1316E+05 a Re(Zb) Pa-s/m^3 G      8510.7 A |p| Pa
      3.8570E+05 b Im(Zb) Pa-s/m^3 G      -19.96 B Ph(p) deg
      2.1173E-02 C |U| m^3/s
      -93.609 D Ph(U) deg
      25.365 E HtotBr W
      25.365 F EdotBr W
      198.04 G EdotTr W
!----- 31 -----
DUCT    Change Me
      2.2900E-03 a Area m^2      Mstr      1176.9 A |p| Pa
      0.16964 b Perim m      31a      -66.715 B Ph(p) deg
      0.9100 c Length m      5.1496E-02 C |U| m^3/s
      5.0000E-04 d Srough      -106.74 D Ph(U) deg
      23.205 E Htot W
ideal   Solid type      23.205 F Edot W
!----- 32 -----
CONE    Change Me
sameas 31a a Areal m^2      Mstr      1154.3 A |p| Pa
      0.16964 b Periml m      32a      -68.045 B Ph(p) deg
      1.0000E-02 c Length m      5.1715E-02 C |U| m^3/s
      2.2000E-02 d AreaF m^2      Mstr      -107.04 D Ph(U) deg
      0.52579 e PerimF m      32d      23.198 E Htot W
      5.0000E-04 f Srough      23.198 F Edot W
ideal   Solid type
!----- 33 -----
IESPEAKER Change Me
sameas 32d a Area m^2      11.356 A |p| Pa
      5.1600 b R ohms      -17.232 B Ph(p) deg

```

```

4.8000E-04 c L H 5.1711E-02 C |U| m^3/s
11.090 d BLProd T-m -107.04 D Ph(U) deg
2.7400E-02 e M kg 9.7105E-04 E Htot W
1773.0 f K N/m 9.7105E-04 F Edot W
1.2300 g Rm N-s/m -13.844 G Workln W
1.5190 h |I| A G 18.228 H Volts V
-107.69 i Ph(l) deg G 1.5190 I Amps A
180.00 J Ph(Ze) deg
1147.2 K |Px| Pa
ideal Solid type 111.52 L Ph(Px) deg
!----- 34 -----
RPN ChangeMe
180.00 a G or T =34A 180.00 A ChngeMe
33J
!----- 35 -----
RPN ChangeMe
12.000 a G or T =35A 12.000 A ChngeMe
33H 33I /
!----- 36 -----
RPN Ee
0.0000 a G or T 13.844 A ChngeMe
33G -1 *
!----- 37 -----
RPN Eloss
0.0000 a G or T 23.197 A ChngeMe
32F 33F -
!----- 38 -----
RPN Eff
0.0000 a G or T 59.679 A ChngeMe
36A 37A / 100 *
!----- 39 -----
RPN ChangeMe
0.0000 a G or T 5.7832 A ChngeMe
U1 mag w / 33a / 1000 *
!----- 40 -----
DUCT Change Me
sameas 32d a Area m^2 Mstr 3.8196E-12 A |p| Pa
0.52579 b Perim m 40a 122.82 B Ph(p) deg
1.0000E-02 c Length m 5.1715E-02 C |U| m^3/s
5.0000E-04 d Srough -107.04 D Ph(U) deg
-6.3669E-14 E Htot W
ideal Solid type -6.3669E-14 F Edot W
!----- 41 -----
SOFTEND Change Me
0.0000 a Re(z) =41G 3.8196E-12 A |p| Pa
0.0000 b Im(z) =41H 122.82 B Ph(p) deg
5.1715E-02 C |U| m^3/s
-107.04 D Ph(U) deg
-6.3669E-14 E Htot W
-6.3669E-14 F Edot W
-2.5593E-15 G Re(z)
-3.0351E-15 H Im(z)
297.00 I T K
!----- 42 -----
DUCT Feedback Pipe before Stub
2.2900E-03 a Area m^2 Mstr 4749.1 A |p| Pa
0.16964 b Perim m 42a -112.57 B Ph(p) deg
0.5300 c Length m 9.0541E-02 C |U| m^3/s
5.0000E-04 d Srough -85.282 D Ph(U) deg
191.07 E Htot W
ideal Solid type 191.07 F Edot W
!----- 43 -----
RPN ChangeMe
0.0000 a G or T -27.284 A ChngeMe
p1 U1 / arg
!----- 44 -----

```

TBRANCH Change Me
 1969.2 a Re(Zb) Pa-s/m³ G 4749.1 A |p| Pa
 -3.0348E+05 b Im(Zb) Pa-s/m³ G -112.57 B Ph(p) deg
 -1.6315E-15 c HtotBr W 1.5648E-02 C |U| m³/s
 -22.938 D Ph(U) deg
 0.2411 E HtotBr W
 0.2411 F EdotBr W
 190.83 G EdotTr W

!----- 45 -----

DUCT Change Me
 sameas 42a a Area m² Mstr 5515.1 A |p| Pa
 0.16964 b Perim m 45a -112.7 B Ph(p) deg
 0.4500 c Length m 2.9092E-18 C |U| m³/s
 5.0000E-04 d Srough 116.57 D Ph(U) deg
 -5.2347E-15 E Htot W
 ideal Solid type -5.2347E-15 F Edot W

!----- 46 -----

HARDEND Change Me
 0.0000 a R(1/z) =46G 5515.1 A |p| Pa
 0.0000 b I(1/z) =46H -112.7 B Ph(p) deg
 2.9092E-18 C |U| m³/s
 116.57 D Ph(U) deg
 -5.2347E-15 E Htot W
 -5.2347E-15 F Edot W
 -6.1518E-17 G R(1/z)
 -7.1441E-17 H I(1/z)

!----- 47 -----

DUCT Other
 sameas 42a a Area m² Mstr 1.4828E+04 A |p| Pa
 0.16964 b Perim m 47a -179.64 B Ph(p) deg
 1.0600 c Length m 2.9635E-02 C |U| m³/s
 5.0000E-04 d Srough -146.01 D Ph(U) deg
 182.95 E Htot W
 ideal Solid type 182.95 F Edot W

!----- 48 -----

DUCT L1
 sameas 47a a Area m² Mstr 8290.6 A |p| Pa
 0.16964 b Perim m 48a 150.76 B Ph(p) deg
 1.0700 c Length m 7.4228E-02 C |U| m³/s
 5.0000E-04 d Srough 95.908 D Ph(U) deg
 177.14 E Htot W
 ideal Solid type 177.14 F Edot W

!----- 49 -----

DUCT L2
 sameas 48a a Area m² Mstr 7767.0 A |p| Pa
 0.16964 b Perim m 49a 24.169 B Ph(p) deg
 0.8400 c Length m 7.5472E-02 C |U| m³/s
 5.0000E-04 d Srough 79.064 D Ph(U) deg
 168.55 E Htot W
 ideal Solid type 168.55 F Edot W

!----- 50 -----

DUCT L3
 sameas 47a a Area m² Mstr 1.4662E+04 A |p| Pa
 0.16964 b Perim m 50a 0.22804 B Ph(p) deg
 0.7300 c Length m 2.8682E-02 C |U| m³/s
 5.0000E-04 d Srough 38.904 D Ph(U) deg
 164.15 E Htot W
 ideal Solid type 164.15 F Edot W

!----- 51 -----

CONE Cone next to AHX
 sameas 50a a Areal m² Mstr 1.4704E+04 A |p| Pa
 0.16964 b Periml m 51a 9.2463E-14 B Ph(p) deg
 2.5000E-02 c Length m 2.5427E-02 C |U| m³/s
 9.5040E-03 d AreaF m² Mstr 28.677 D Ph(U) deg
 0.34559 e PerimF m 51d 164.02 E Htot W
 5.0000E-04 f Srough 164.02 F Edot W

```

ideal      Solid type
!----- 52 -----
RPN      Set p1 mag
  1.0000 a G or T      =52A   1.0000      A ChngeMe
p1 mag 0d /
!----- 53 -----
RPN      Set p1 phase
  1.0000 a G or T      =53A   1.0000      A ChngeMe
p1 arg 0e - 1 +
!----- 54 -----
RPN      Set mag U1
  1.0000 a G or T      =54A   1.0000      A ChngeMe
U1 mag 0f /
!----- 55 -----
RPN      Set U1 phase
  1.0000 a G or T      =55A   1.0000      A ChngeMe
U1 arg 0g - 1 +
!----- 56 -----
RPN      Set Hdot
  1.0000 a G or T      =56A   1.0000      A ChngeMe
1E H2k /

```

B2. Simulation of the 128-mm diameter one-stage thermoacoustic engine

```

!----- 0 -----
BEGIN    Change Me
  1.0133E+05 a Mean P Pa
  70.563 b Freq Hz G
  305.00 c TBeg K G
  4223.3 d |p| Pa G
  -70.193 e Ph(p) deg G
  9.6133E-02 f |U| m^3/s G
  0.0000 g Ph(U) deg
  91.347 h Htot W G
air      Gas type
!----- 1 -----
RPN      ChangeMe
  0.0000 a G or T      22.562      A ChngeMe
Htot Edot -
!----- 2 -----
DUCT     Change Me
  3.7700E-02 a Area m^2      4293.0 A |p| Pa
  0.8400 b Perim m          -70.611 B Ph(p) deg
  7.0000E-02 c Length m     6.4050E-02 C |U| m^3/s
  5.0000E-04 d Srough       -10.576 D Ph(U) deg
  91.347 E Htot W
ideal    Solid type        68.669 F Edot W
!----- 3 -----
DUCT     Change Me
  2.8200E-02 a Area m^2      4298.0 A |p| Pa
  0.6900 b Perim m          -70.65 B Ph(p) deg
  5.0000E-03 c Length m     6.2412E-02 C |U| m^3/s
  5.0000E-04 d Srough       -11.443 D Ph(U) deg
  91.347 E Htot W
ideal    Solid type        68.662 F Edot W
!----- 4 -----
HX       CHX
  2.8200E-02 a Area m^2      4358.0 A |p| Pa
  0.6208 b GasA/A          -71.768 B Ph(p) deg
  4.9000E-02 c Length m     5.0425E-02 C |U| m^3/s
  5.0000E-04 d y0 m        -17.429 D Ph(U) deg
  -252.58 e HeatIn W G     -161.23 E Htot W
  296.00 f SolidT K        64.056 F Edot W
  305.00 G GasT K
ideal    Solid type        299.01 H SolidT K

```

```

!----- 5 -----
RPN   ChangeMe
305.00 a G or T   =5A   305.00           A ChngeMe
Tm
!----- 6 -----
DUCT   Change Me
2.8200E-02 a Area m^2           4363.0 A |p| Pa
0.6900 b Perim m               -71.818 B Ph(p) deg
7.0000E-03 c Length m          4.8258E-02 C |U| m^3/s
5.0000E-04 d Srough            -19.289 D Ph(U) deg
-161.23 E Htot W
ideal   Solid type           64.046 F Edot W
!----- 7 -----
RPN   ChangeMe
0.0000 a G or T           1.6232           A ChngeMe
dk 11d /
!----- 8 -----
RPN   ChangeMe
0.0000 a G or T           -52.529          A ChngeMe
p1 U1 / arg
!----- 9 -----
RPN   ChangeMe
0.0000 a G or T           6.2921           A ChngeMe
p1 U1 / mag rho / a / 6a *
!----- 10 -----
RPN   ChangeMe
0.0000 a G or T           5.5558           A ChngeMe
p1 U1 / mag rho / a / 11a * 11b *
!----- 11 -----
STKSCREEN Regenerator
3.0000E-02 a Area m^2           4258.4 A |p| Pa
0.8300 b VolPor               -73.74 B Ph(p) deg
1.5000E-02 c Length m          5.4476E-02 C |U| m^3/s
1.9800E-04 d rh m              -26.663 D Ph(U) deg
0.1000 e ksFrac               -161.23 E Htot W
78.992 F Edot W
305.00 G TBeg K
stainless Solid type           392.55 H TEnd K
!----- 12 -----
STKSCREEN Change Me
3.0000E-02 a Area m^2           4102.9 A |p| Pa
0.8300 b VolPor               -76.105 B Ph(p) deg
1.5000E-02 c Length m          6.1474E-02 C |U| m^3/s
1.9800E-04 d rh m              -33.063 D Ph(U) deg
0.1000 e ksFrac               -161.23 E Htot W
92.169 F Edot W
392.55 G TBeg K
stainless Solid type           489.15 H TEnd K
!----- 13 -----
RPN   ChangeMe
0.0000 a G or T           2.5097           A ChngeMe
dk 11d /
!----- 14 -----
RPN   ChangeMe
0.0000 a G or T           489.15           A ChngeMe
Tm
!----- 15 -----
RPN   ChangeMe
0.0000 a G or T           -43.042          A ChngeMe
p1 U1 / arg
!----- 16 -----
RPN   Net Power
0.0000 a G or T           14.946           A ChngeMe
11F 6F -
!----- 17 -----
VXQ1   HHX

```

```

3.0000E-02 a Area m^2      4184.3 A |p| Pa
0.4000 b GasA/A          -77.81 B Ph(p) deg
8.5611E-02 c SolA/A      5.0598E-02 C |U| m^3/s
4.3000E-03 d rh m        -49.616 D Ph(U) deg
8.0000E-03 e LenTS1 m    99.506 E Htot W
0.1040 f Len P1 m        93.300 F Edot W
8.0000E-03 g LenTS2 m    583.01 G TSolBeg P1 K
260.74 h HeatP1 W G      781.30 H TSolEnd P1 K
stainless Solid type
!----- 18 -----
RPN ChangeMe
791.00 a G or T          781.30 A ChngeMe
17H
!----- 19 -----
RPN ChangeMe
753.98 a G or T          715.21 A ChngeMe
Tm
!----- 20 -----
JOIN Change Me
4184.3 A |p| Pa
-77.81 B Ph(p) deg
5.0152E-02 C |U| m^3/s
-49.616 D Ph(U) deg
99.506 E Htot W
92.476 F Edot W
715.21 G TBeg K
715.47 H TEnd K
!----- 21 -----
STKDUCT TBT1
3.0680E-02 a Area m^2    4187.9 A |p| Pa
0.7320 b Perim m        -77.932 B Ph(p) deg
2.8000E-02 c Length m    4.5863E-02 C |U| m^3/s
1.4800E-03 d WallA m^2   -62.098 D Ph(U) deg
99.506 E Htot W
92.392 F Edot W
715.47 G TBeg K
stainless Solid type    709.50 H TEnd K
!----- 22 -----
STKCONE TBT2
3.0680E-02 a Areal m^2   4186.0 A |p| Pa
0.7320 b Periml m       -78.41 B Ph(p) deg
8.0000E-02 c Length m    4.5587E-02 C |U| m^3/s
1.6900E-02 d AreaF m^2   -93.359 D Ph(U) deg
0.5200 e PerimF m       99.506 E Htot W
2.7322E-03 f f_wall      92.184 F Edot W
709.50 G TBeg K
stainless Solid type    687.33 H TEnd K
!----- 23 -----
MINOR Change Me
1.6900E-02 a Area m^2    4184.1 A |p| Pa
1.2200 b K+              -78.403 B Ph(p) deg
1.2200 c K-              4.5587E-02 C |U| m^3/s
-93.359 D Ph(U) deg
99.506 E Htot W
92.140 F Edot W
!----- 24 -----
STKDUCT TBT3
1.6900E-02 a Area m^2    4171.1 A |p| Pa
0.5200 b Perim m        -78.85 B Ph(p) deg
5.0000E-02 c Length m    4.9489E-02 C |U| m^3/s
1.0400E-04 d WallA m^2   -105.81 D Ph(U) deg
99.506 E Htot W
91.993 F Edot W
687.33 G TBeg K
stainless Solid type    574.33 H TEnd K
!----- 25 -----

```

```

MINOR  Change Me
1.3000E-02 a Area  m^2      4170.7  A |p|  Pa
0.1000 b K+      -78.847  B Ph(p) deg
0.1000 c K-      4.9489E-02 C |U|  m^3/s
                    -105.81  D Ph(U) deg
                    99.506  E Htot  W
                    91.983  F Edot  W
!----- 26 -----
STKDUCT  TBT4
1.3000E-02 a Area  m^2      Mstr  3945.2  A |p|  Pa
0.40418 b Perim  m      26a   -82.433  B Ph(p) deg
0.2000 c Length  m      7.0273E-02 C |U|  m^3/s
2.5447E-04 d WallA  m^2      -131.01  D Ph(U) deg
                    99.506  E Htot  W
                    91.704  F Edot  W
                    574.33  G TBeg  K
stainless  Solid type      304.28  H TEnd  K
!----- 27 -----
HX  Change Me
1.3000E-02 a Area  m^2      3942.5  A |p|  Pa
1.0000 b GasA/A      -82.458  B Ph(p) deg
1.0000E-03 c Length  m      7.0394E-02 C |U|  m^3/s
1.0000E-03 d y0  m      -131.11  D Ph(U) deg
-7.8394 e HeatIn  W      G      91.667  E Htot  W
297.00 f SolidT  K      =27H   91.667  F Edot  W
                    304.28  G GasT  K
ideal  Solid type      297.00  H SolidT  K
!----- 28 -----
RPN  ChangeMe
1.0000 a G or T      =28A   1.0000      A ChngeMe
Edot H2k /
!----- 29 -----
RPN ChangeMe
324.44 a G or T      324.44      A ChngeMe
29a =Tm
!----- 30 -----
DUCT  FBP before Stub
1.2868E-02 a Area  m^2      Mstr  3293.3  A |p|  Pa
0.40212 b Perim  m      30a   -89.916  B Ph(p) deg
0.2500 c Length  m      9.9793E-02 C |U|  m^3/s
5.0000E-04 d Srough      -146.13  D Ph(U) deg
                    91.667  E Htot  W
ideal  Solid type      91.370  F Edot  W
!----- 31 -----
TBRANCH  Change Me
143.74 a Re(Zb) Pa-s/m^3 G      3293.3  A |p|  Pa
-4.9372E+04 b Im(Zb) Pa-s/m^3 G      -89.916  B Ph(p) deg
                    6.6704E-02 C |U|  m^3/s
                    -8.2898E-02 D Ph(U) deg
                    0.31979  E HtotBr  W
                    0.31979  F EdotBr  W
                    91.050  G EdotTr  W
!----- 32 -----
DUCT  Stub
1.2868E-02 a Area  m^2      Mstr  3873.4  A |p|  Pa
0.40212 b Perim  m      32a   -89.981  B Ph(p) deg
0.4500 c Length  m      2.0817E-17 C |U|  m^3/s
5.0000E-04 d Srough      4.6627E-02 D Ph(U) deg
                    0.31979  E Htot  W
ideal  Solid type      -1.9406E-17 F Edot  W
!----- 33 -----
HARDEND  Change Me
0.0000 a R(1/z)      =33G   3873.4  A |p|  Pa
0.0000 b I(1/z)      =33H   -89.981  B Ph(p) deg
0.0000 c Htot  W      2.0817E-17 C |U|  m^3/s
                    4.6627E-02 D Ph(U) deg

```

0.31979 E Htot W
 -1.9406E-17 F Edot W
 -7.8980E-20 G R(1/z)
 1.6408E-16 H I(1/z)

!----- 34 -----!

MINOR Change Me
 1.2868E-02 a Area m^2 3267.1 A |p| Pa
 1.1000 b K+ -88.632 B Ph(p) deg
 1.1000 c K- 0.15954 C |U| m^3/s
 -159.64 D Ph(U) deg
 91.347 E Htot W
 84.822 F Edot W

!----- 35 -----!

DUCT Change Me
 1.2868E-02 a Area m^2 Mstr 1489.7 A |p| Pa
 0.40212 b Perim m 35a -110.91 B Ph(p) deg
 0.3000 c Length m 0.18567 C |U| m^3/s
 5.0000E-04 d Srough -163.52 D Ph(U) deg
 91.347 E Htot W
 ideal Solid type 83.975 F Edot W

!----- 36 -----!

RPN P1
 1572.0 a G or T 1489.7 A P1
 p1 mag

!----- 37 -----!

DUCT Change Me
 1.2868E-02 a Area m^2 4102.6 A |p| Pa
 0.40212 b Perim m 113.21 B Ph(p) deg
 0.8000 c Length m 0.13698 C |U| m^3/s
 5.0000E-04 d Srough -173.69 D Ph(U) deg
 91.347 E Htot W
 ideal Solid type 81.701 F Edot W

!----- 38 -----!

RPN P2
 3997.0 a G or T 4102.6 A P2
 p1 mag

!----- 39 -----!

DUCT Change Me
 1.2868E-02 a Area m^2 Mstr 5756.1 A |p| Pa
 0.40212 b Perim m 39a 105.55 B Ph(p) deg
 0.5500 c Length m 3.5615E-02 C |U| m^3/s
 5.0000E-04 d Srough 143.63 D Ph(U) deg
 91.347 E Htot W
 ideal Solid type 80.687 F Edot W

!----- 40 -----!

RPN P3
 4240.0 a G or T 5756.1 A P3
 p1 mag

!----- 41 -----!

DUCT Change Me
 1.1513E-02 a Area m^2 5158.0 A |p| Pa
 0.40212 b Perim m 99.451 B Ph(p) deg
 0.5000 c Length m 8.2568E-02 C |U| m^3/s
 5.0000E-04 d Srough 31.483 D Ph(U) deg
 91.347 E Htot W
 ideal Solid type 79.879 F Edot W

!----- 42 -----!

RPN P4
 5158.0 a G or T =42A 5158.0 A P4
 p1 mag

!----- 43 -----!

DUCT Change Me
 1.2868E-02 a Area m^2 Mstr 3977.5 A |p| Pa
 0.40212 b Perim m 43a 94.605 B Ph(p) deg
 0.3000 c Length m 0.13541 C |U| m^3/s
 5.0000E-04 d Srough 21.729 D Ph(U) deg

```

91.347 E Htot W
ideal Solid type 79.292 F Edot W
!----- 44 -----
DUCT Change Me
1.2868E-02 a Area m^2 Mstr 2877.3 A |p| Pa
0.40212 b Perim m 44a 88.634 B Ph(p) deg
0.2050 c Length m 0.16245 C |U| m^3/s
5.0000E-04 d Srough 18.338 D Ph(U) deg
91.347 E Htot W
ideal Solid type 78.799 F Edot W
!----- 45 -----
RPN P5
2033.0 a G or T 2877.3 A P5
p1 mag
!----- 46 -----
DUCT Change Me
1.2868E-02 a Area m^2 2689.6 A |p| Pa
0.40212 b Perim m -60.626 B Ph(p) deg
0.8000 c Length m 0.16566 C |U| m^3/s
5.0000E-04 d Srough 9.2775 D Ph(U) deg
91.347 E Htot W
ideal Solid type 76.545 F Edot W
!----- 47 -----
RPN P6
3465.0 a G or T 2689.6 A P6
p1 mag
!----- 48 -----
MINOR Change Me
1.2868E-02 a Area m^2 2661.9 A |p| Pa
1.1000 b K+ -62.328 B Ph(p) deg
1.1000 c K- 0.16566 C |U| m^3/s
9.2775 D Ph(U) deg
91.347 E Htot W
69.573 F Edot W
!----- 49 -----
DUCT Change Me
1.2868E-02 a Area m^2 Mstr 3823.1 A |p| Pa
0.40212 b Perim m 49a -68.538 B Ph(p) deg
0.2100 c Length m 0.13916 C |U| m^3/s
5.0000E-04 d Srough 6.4147 D Ph(U) deg
91.347 E Htot W
ideal Solid type 69.060 F Edot W
!----- 50 -----
DUCT Change Me
1.6900E-02 a Area m^2 4008.5 A |p| Pa
0.5200 b Perim m -69.29 B Ph(p) deg
5.0000E-02 c Length m 0.12916 C |U| m^3/s
5.0000E-04 d Srough 5.2599 D Ph(U) deg
91.347 E Htot W
ideal Solid type 68.961 F Edot W
!----- 51 -----
CONE Change Me
1.6900E-02 a Areal m^2 4223.3 A |p| Pa
0.5200 b Periml m -70.193 B Ph(p) deg
0.1000 c Length m 9.6133E-02 C |U| m^3/s
3.7700E-02 d AreaF m^2 9.7704E-14 D Ph(U) deg
0.8400 e PerimF m 91.347 E Htot W
5.0000E-04 f Srough 68.785 F Edot W
ideal Solid type
!----- 52 -----
RPN ChangeMe
1.0000 a G or T =52A 1.0000 A ChngeMe
p1 mag 0d /
!----- 53 -----
RPN ChangeMe
1.0000 a G or T =53A 1.0000 A ChngeMe

```

```

p1 arg 0e - 1 +
!----- 54 -----
RPN    ChangeMe
  1.0000 a G or T    =54A    1.0000          A ChngeMe
U1 mag 0f /
!----- 55 -----
RPN    ChangeMe
  1.0000 a G or T    =55A    1.0000          A ChngeMe
U1 arg 0g - 1 +
!----- 56 -----
RPN    ChangeMe
  1.0000 a G or T    =56A    1.0000          A ChngeMe
Oh H2k /

```

B3. Simulation of the 128-mm diameter single-stage electricity generator

```

!----- 0 -----
BEGIN  Change Me
  1.0135E+05 a Mean P Pa
  55.860 b Freq Hz G
  308.00 c TBeg K G
  4554.2 d |p| Pa G
  -52.128 e Ph(p) deg G
  0.10009 f |U| m^3/s G
  0.0000 g Ph(U) deg
  169.95 h Htot W G
air    Gas type
!----- 1 -----
DUCT  Change Me
  3.7700E-02 a Area m^2          4602.3 A |p| Pa
  0.8400 b Perim m             -52.703 B Ph(p) deg
  7.0000E-02 c Length m        7.8470E-02 C |U| m^3/s
  5.0000E-04 d Srough          -13.431 D Ph(U) deg
  169.95 E Htot W
ideal  Solid type              139.79 F Edot W
!----- 2 -----
DUCT  Change Me
  2.8200E-02 a Area m^2          4605.8 A |p| Pa
  0.6900 b Perim m             -52.757 B Ph(p) deg
  5.0000E-03 c Length m        7.7459E-02 C |U| m^3/s
  5.0000E-04 d Srough          -14.35 D Ph(U) deg
  169.95 E Htot W
ideal  Solid type              139.78 F Edot W
!----- 3 -----
HX AHX
  2.8200E-02 a Area m^2          4624.0 A |p| Pa
  0.6200 b GasA/A              -54.079 B Ph(p) deg
  4.8000E-02 c Length m        6.9655E-02 C |U| m^3/s
  5.0000E-04 d y0 m           -20.762 D Ph(U) deg
  -494.1 e HeatIn W G          -324.15 E Htot W
  300.00 f SolidT K            134.57 F Edot W
  308.00 G GasT K
ideal  Solid type              300.00 H SolidT K
!----- 4 -----
RPN    ChangeMe
  308.00 a G or T    =4A    308.00          A Tc
Tm
!----- 5 -----
RPN ChangeMe
  0.0000 a G or T          494.10          A ChngeMe
3e -1 *
!----- 6 -----
DUCT Cold gap
  2.8200E-02 a Area m^2          4626.7 A |p| Pa
  0.6900 b Perim m             -54.131 B Ph(p) deg

```

```

5.0000E-03 c Length m          6.8778E-02 C |U| m^3/s
5.0000E-04 d Srough           -21.885 D Ph(U) deg
                                -324.15 E Htot W
ideal      Solid type          134.57 F Edot W
!----- 7 -----
RPN ph(Z)
  0.0000 a G or T              -32.246          A ChngeMe
p1 U1 / arg
!----- 8 -----
RPN |Z|
  0.0000 a G or T              4.7037          A ChngeMe
p1 U1 / mag rho / a / 6a *
!----- 9 -----
STKSCREEN Screen regenerator
3.0000E-02 a Area m^2          4014.2 A |p| Pa
  0.8315 b VolPor              -59.078 B Ph(p) deg
3.0000E-02 c Length m          0.10758 C |U| m^3/s
1.9800E-04 d rh m              -31.502 D Ph(U) deg
  0.1000 e ksFrac              -324.15 E Htot W
                                191.41 F Edot W
                                308.00 G TBeg K
stainless  Solid type          523.95 H TEnd K
!----- 10 -----
RPN dk/rh
  0.0000 a G or T              3.0001          A ChngeMe
dk 9d /
!----- 11 -----
RPN |Z|
  0.0000 a G or T              3.6200          A ChngeMe
p1 U1 / mag rho / a / 9a *
!----- 12 -----
RPN ph(Z)
  0.0000 a G or T              -27.575         A ChngeMe
p1 U1 / arg
!----- 13 -----
RPN Net Power
  0.0000 a G or T              56.840          A ChngeMe
9F 6F -
!----- 14 -----
DUCT Hot gap
3.7700E-02 a Area m^2 Mstr    4014.5 A |p| Pa
  0.6883 b Perim m 14a       -59.086 B Ph(p) deg
1.0000E-03 c Length m          0.10741 C |U| m^3/s
5.0000E-04 d Srough           -31.68 D Ph(U) deg
                                -324.15 E Htot W
ideal      Solid type          191.40 F Edot W
!----- 15 -----
VXQ1 HHX
3.0000E-02 a Area m^2          4086.1 A |p| Pa
  0.4000 b GasA/A              -61.783 B Ph(p) deg
8.5611E-02 c SolA/A            0.10276 C |U| m^3/s
4.3000E-03 d rh m              -40.118 D Ph(U) deg
8.0000E-03 e LenTS1 m          207.18 E Htot W
  0.1040 f Len P1 m            195.12 F Edot W
8.0000E-03 g LenTS2 m          614.09 G TSolBeg P1 K
  531.33 h HeatP1 W G          866.32 H TSolEnd P1 K
stainless  Solid type
!----- 16 -----
RPN ChangeMe
  823.00 a G or T              866.32          A ChngeMe
15H
!----- 17 -----
RPN ChangeMe
  753.98 a G or T              531.33          A ChngeMe
15h
!----- 18 -----

```

JOIN Change Me

4086.1 A |p| Pa
-61.783 B Ph(p) deg
0.10183 C |U| m³/s
-40.118 D Ph(U) deg
207.18 E Htot W
193.34 F Edot W
788.33 G TBeg K
788.72 H TEnd K

!----- 19 -----

STKDUCT TBT 1

3.0680E-02 a Area m² 4090.9 A |p| Pa
0.7320 b Perim m -61.976 B Ph(p) deg
2.8000E-02 c Length m 9.8884E-02 C |U| m³/s
1.4800E-03 d WallA m² -44.805 D Ph(U) deg
207.18 E Htot W
193.25 F Edot W
788.72 G TBeg K

stainless Solid type 777.95 H TEnd K

!----- 20 -----

STKCONE TBT 2

3.0680E-02 a Areal m² 4101.0 A |p| Pa
0.7320 b Periml m -62.741 B Ph(p) deg
8.0000E-02 c Length m 9.4799E-02 C |U| m³/s
1.6900E-02 d AreaF m² -55.843 D Ph(U) deg
0.5200 e PerimF m 207.18 E Htot W
2.7322E-03 f f_wall 192.98 F Edot W
777.95 G TBeg K

stainless Solid type 740.71 H TEnd K

!----- 21 -----

MINOR Change Me

1.6900E-02 a Area m² 4093.3 A |p| Pa
1.2200 b K+ -62.754 B Ph(p) deg
1.2200 c K- 9.4799E-02 C |U| m³/s
-55.843 D Ph(U) deg
207.18 E Htot W
192.61 F Edot W

!----- 22 -----

STKDUCT TBT 3

1.6900E-02 a Area m² 4097.0 A |p| Pa
0.5200 b Perim m -63.465 B Ph(p) deg
5.0000E-02 c Length m 9.3959E-02 C |U| m³/s
1.0400E-04 d WallA m² -60.986 D Ph(U) deg
207.18 E Htot W
192.29 F Edot W
740.71 G TBeg K

stainless Solid type 630.76 H TEnd K

!----- 23 -----

MINOR Change Me

1.3000E-02 a Area m² 4095.7 A |p| Pa
0.1000 b K+ -63.466 B Ph(p) deg
0.1000 c K- 9.3959E-02 C |U| m³/s
-60.986 D Ph(U) deg
207.18 E Htot W
192.23 F Edot W

!----- 24 -----

STKDUCT TBT 4

1.3000E-02 a Area m² Mstr 4068.1 A |p| Pa
0.40418 b Perim m 24a -68.947 B Ph(p) deg
0.2000 c Length m 9.4984E-02 C |U| m³/s
2.5447E-04 d WallA m² -76.837 D Ph(U) deg
207.18 E Htot W
191.37 F Edot W
630.76 G TBeg K

stainless Solid type 316.58 H TEnd K

!----- 25 -----

```

HX Dummy 2nd AHX
1.3000E-02 a Area m^2          4067.0 A |p| Pa
  1.0000 b GasA/A              -68.991 B Ph(p) deg
1.0000E-03 c Length m         9.4994E-02 C |U| m^3/s
1.0000E-03 d y0 m             -76.922 D Ph(U) deg
-15.853 e HeatIn W            G 191.32 E Htot W
300.00 f SolidT K              =25H 191.32 F Edot W
                                   316.58 G GasT K
ideal      Solid type           300.00 H SolidT K
!----- 26 -----
RPN      ChangeMe
  1.0000 a G or T              =26A 1.0000          A ChngeMe
Edot H2k /
!----- 27 -----
RPN      ChangeMe
  323.00 a G or T              323.00          A ChngeMe
27a =Tm
!----- 28 -----
DUCT     Change Me
1.2868E-02 a Area m^2      Mstr 3940.7 A |p| Pa
  0.40212 b Perim m        28a -77.555 B Ph(p) deg
  0.2100 c Length m         0.10031 C |U| m^3/s
5.0000E-04 d Srough        -92.414 D Ph(U) deg
                                   191.32 E Htot W
ideal     Solid type           191.05 F Edot W
!----- 29 -----
DUCT     Change Me
sameas 28a a Area m^2      Mstr 3754.0 A |p| Pa
  0.40212 b Perim m        29a -86.381 B Ph(p) deg
  0.2000 c Length m         0.1075 C |U| m^3/s
5.0000E-04 d Srough        -105.4 D Ph(U) deg
                                   191.32 E Htot W
ideal     Solid type           190.77 F Edot W
!----- 30 -----
TBRANCH Alternator branch
5115.5 a Re(Zb) Pa-s/m^3 G    3754.0 A |p| Pa
-4.0749E+04 b Im(Zb) Pa-s/m^3 G -86.381 B Ph(p) deg
                                   9.1408E-02 C |U| m^3/s
                                   -3.5368 D Ph(U) deg
                                   21.371 E HtotBr W
                                   21.371 F EdotBr W
                                   169.40 G EdotTr W
!----- 31 -----
DUCT     Change Me
1.2868E-02 a Area m^2      Mstr 4551.6 A |p| Pa
  0.4021 b Perim m         31a -89.733 B Ph(p) deg
  0.8900 c Length m         3.5838E-02 C |U| m^3/s
5.0000E-04 d Srough        -165.14 D Ph(U) deg
                                   21.371 E Htot W
ideal     Solid type           20.549 F Edot W
!----- 32 -----
MINOR    Change Me
2.3760E-03 a Area m^2          4548.9 A |p| Pa
  0.1000 b K+                -89.604 B Ph(p) deg
  0.1000 c K-                3.5838E-02 C |U| m^3/s
                                   -165.14 D Ph(U) deg
                                   21.371 E Htot W
                                   20.360 F Edot W
!----- 33 -----
DUCT     Change Me
2.3760E-03 a Area m^2      Mstr 963.21 A |p| Pa
  0.1728 b Perim m         33a -143.7 B Ph(p) deg
  0.6000 c Length m         4.4661E-02 C |U| m^3/s
5.0000E-04 d Srough        -169.97 D Ph(U) deg
                                   21.371 E Htot W
ideal     Solid type           19.286 F Edot W

```

```

!----- 34 -----
RPN P6
  0.0000 a G or T          963.21          A P6
p1 mag
!----- 35 -----
IESPEAKER Change Me
2.2000E-02 a Area m^2      3.0716E-12 A |p| Pa
  5.3000 b R ohms          92.121 B Ph(p) deg
4.7000E-04 c L H           4.4657E-02 C |U| m^3/s
  10.694 d BLProd T-m      -169.98 D Ph(U) deg
2.7440E-02 e M kg          11.003 E Htot W
1725.5 f K N/m             -9.4292E-15 F Edot W
  1.3640 g Rm N-s/m        -10.368 G Workln W
  -1.5179 h |I| A G        13.661 H Volts V
-350.64 i Ph(l) deg G     1.5179 I Amps A
                               180.00 J Ph(Ze) deg
                               963.21 K |Px| Pa
ideal Solid type           36.305 L Ph(Px) deg
!----- 36 -----
RPN ChangeMe
  180.00 a G or T          =36A 180.00          A ChngeMe
35J
!----- 37 -----
RPN Load resistance (Ohm)
  9.0000 a G or T          =37A 9.0000          A Ohm
35H 35I /
!----- 38 -----
RPN Electricity (W)
  0.0000 a G or T          10.368          A We
35G -1 *
!----- 39 -----
RPN Heat-Electric Efficiency %
  0.0000 a G or T          1.9514          A H-We-e
35G -1 * 15h / 100 *
!----- 40 -----
RPN Heat-Acoustic Efficiency %
  0.0000 a G or T          3.6298          A H-A-e
33F 15h / 100 *
!----- 41 -----
RPN Acoustic-Electric Efficiency %
  0.0000 a G or T          53.760          A A-We-e
38A 33F / 100 *
!----- 42 -----
RPN Coil displacement (mm)
  6.5000 a G or T          5.7834          A mm
U1 mag w / 35a / 1000 *
!----- 43 -----
SOFTEND Change Me
  0.0000 a Re(z)           =43G 3.0716E-12 A |p| Pa
  0.0000 b Im(z)           =43H 92.121 B Ph(p) deg
  0.0000 c Htot W          4.4657E-02 C |U| m^3/s
                               -169.98 D Ph(U) deg
                               11.003 E Htot W
                               -9.4292E-15 F Edot W
                               -5.2825E-16 G Re(z)
                               -3.8059E-15 H Im(z)
                               323.00 I T K
!----- 44 -----
MINOR 90 degree bend (minor loss)
sameas 28a a Area m^2      3711.5 A |p| Pa
  1.1000 b K+              -85.456 B Ph(p) deg
  1.1000 c K-              0.15476 C |U| m^3/s
                               -140.71 D Ph(U) deg
                               169.95 E Htot W
                               163.69 F Edot W
!----- 45 -----

```

```

DUCT Change Me
1.2868E-02 a Area m^2 Mstr 1782.2 A |p| Pa
0.40212 b Perim m 45a -138.07 B Ph(p) deg
0.5700 c Length m 0.18748 C |U| m^3/s
5.0000E-04 d Srough -151.92 D Ph(U) deg
169.95 E Htot W
ideal Solid type 162.21 F Edot W
!----- 46 -----
RPN P1
2250.0 a G or T 1782.2 A P1
p1 mag
!----- 47 -----
DUCT Change Me
sameas 28a a Area m^2 4376.1 A |p| Pa
0.40212 b Perim m 131.97 B Ph(p) deg
0.9250 c Length m 0.13416 C |U| m^3/s
5.0000E-04 d Srough -171.02 D Ph(U) deg
169.95 E Htot W
ideal Solid type 159.87 F Edot W
!----- 48 -----
RPN ChangeMe
0.0000 a G or T 159.87 A AP(1-2)
Edot
!----- 49 -----
MINOR Change Me
sameas 28a a Area m^2 4346.1 A |p| Pa
1.1000 b K+ 131.36 B Ph(p) deg
1.1000 c K- 0.13416 C |U| m^3/s
-171.02 D Ph(U) deg
169.95 E Htot W
156.15 F Edot W
!----- 50 -----
DUCT Change Me
1.2868E-02 a Area m^2 Mstr 4967.8 A |p| Pa
0.40212 b Perim m 50a 126.27 B Ph(p) deg
0.2050 c Length m 0.10864 C |U| m^3/s
5.0000E-04 d Srough -178.98 D Ph(U) deg
169.95 E Htot W
ideal Solid type 155.75 F Edot W
!----- 51 -----
RPN P2
4403.0 a G or T 4967.8 A P2
p1 mag
!----- 52 -----
DUCT Change Me
sameas 28a a Area m^2 5317.9 A |p| Pa
0.40212 b Perim m 123.22 B Ph(p) deg
0.1500 c Length m 8.9145E-02 C |U| m^3/s
5.0000E-04 d Srough 172.23 D Ph(U) deg
169.95 E Htot W
ideal Solid type 155.49 F Edot W
!----- 53 -----
DUCT Change Me
sameas 28a a Area m^2 5626.4 A |p| Pa
0.40212 b Perim m 119.66 B Ph(p) deg
sameas 29c c Length m 6.5750E-02 C |U| m^3/s
5.0000E-04 d Srough 152.64 D Ph(U) deg
169.95 E Htot W
ideal Solid type 155.17 F Edot W
!----- 54 -----
DUCT Change Me
1.2868E-02 a Area m^2 Mstr 5665.0 A |p| Pa
0.40212 b Perim m 54a 118.99 B Ph(p) deg
4.0000E-02 c Length m 6.2070E-02 C |U| m^3/s
5.0000E-04 d Srough 147.08 D Ph(U) deg
169.95 E Htot W

```

```

ideal      Solid type      155.11  F Edot  W
!----- 55 -----
RPN      P3
5665.0   a G or T      =55A   5665.0      A P3
p1 mag
!----- 56 -----
DUCT     Change Me
sameas 28a a Area  m^2      5290.7  A |p|  Pa
        0.40212 b Perim m      108.93  B Ph(p) deg
        0.6000 c Length m      9.0176E-02 C |U|  m^3/s
        5.0000E-04 d Srough      59.198  D Ph(U) deg
        169.95 E Htot  W
ideal      Solid type      154.20  F Edot  W
!----- 57 -----
RPN      P4
4564.0   a G or T      5290.7      A P4
p1 mag
!----- 58 -----
DUCT     Change Me
sameas 28a a Area  m^2      4514.4  A |p|  Pa
        0.40212 b Perim m      102.63  B Ph(p) deg
        0.2900 c Length m      0.12726 C |U|  m^3/s
        5.0000E-04 d Srough      44.970  D Ph(U) deg
        169.95 E Htot  W
ideal      Solid type      153.67  F Edot  W
!----- 59 -----
MINOR 90 degree bend (minor loss)
sameas 28a a Area  m^2      4487.9  A |p|  Pa
        1.1000 b K+      103.17  B Ph(p) deg
        1.1000 c K-      0.12726 C |U|  m^3/s
        44.970 D Ph(U) deg
        169.95 E Htot  W
        150.49 F Edot  W
!----- 60 -----
DUCT     Change Me
1.2868E-02 a Area  m^2      Mstr    2278.0  A |p|  Pa
        0.40212 b Perim m      60a     74.558  B Ph(p) deg
        0.5800 c Length m      0.17898 C |U|  m^3/s
        5.0000E-04 d Srough      31.580  D Ph(U) deg
        169.95 E Htot  W
ideal      Solid type      149.15  F Edot  W
!----- 61 -----
DUCT     Change Me
sameas 28a a Area  m^2      2595.7  A |p|  Pa
        0.40212 b Perim m      -29.039 B Ph(p) deg
        0.7000 c Length m      0.17403 C |U|  m^3/s
        5.0000E-04 d Srough      20.262  D Ph(U) deg
        169.95 E Htot  W
ideal      Solid type      147.29  F Edot  W
!----- 62 -----
DUCT     Change Me
1.2868E-02 a Area  m^2      Mstr    3417.0  A |p|  Pa
        0.40212 b Perim m      62a     -40.792 B Ph(p) deg
        0.2050 c Length m      0.15812 C |U|  m^3/s
        5.0000E-04 d Srough      16.295  D Ph(U) deg
        169.95 E Htot  W
ideal      Solid type      146.79  F Edot  W
!----- 63 -----
RPN      P5
0.0000 a G or T      3417.0      A P5
p1 mag
!----- 64 -----
MINOR 90 degree bend (minor loss)
sameas 28a a Area  m^2      3375.8  A |p|  Pa
        1.1000 b K+      -41.89  B Ph(p) deg
        1.1000 c K-      0.15812 C |U|  m^3/s

```

```

16.295 D Ph(U) deg
169.95 E Htot W
140.70 F Edot W
!----- 65 -----
DUCT Change Me
sameas 28a a Area m^2 Mstr 4279.7 A |p| Pa
0.40212 b Perim m 65a -49.922 B Ph(p) deg
0.2400 c Length m 0.13267 C |U| m^3/s
5.0000E-04 d Srough 10.489 D Ph(U) deg
169.95 E Htot W
ideal Solid type 140.18 F Edot W
!----- 66 -----
DUCT Change Me
1.6900E-02 a Area m^2 4406.4 A |p| Pa
0.5200 b Perim m -50.902 B Ph(p) deg
5.0000E-02 c Length m 0.12478 C |U| m^3/s
5.0000E-04 d Srough 8.4650 D Ph(U) deg
169.95 E Htot W
ideal Solid type 140.08 F Edot W
!----- 67 -----
CONE Change Me
1.6900E-02 a Areal m^2 4554.2 A |p| Pa
0.5200 b Periml m -52.128 B Ph(p) deg
0.1000 c Length m 0.10009 C |U| m^3/s
3.7700E-02 d AreaF m^2 -2.8799E-14 D Ph(U) deg
0.8400 e PerimF m 169.95 E Htot W
5.0000E-04 f Srough 139.91 F Edot W
ideal Solid type
!----- 68 -----
RPN ChangeMe
1.0000 a G or T =68A 1.0000 A ChngeMe
p1 mag 0d /
!----- 69 -----
RPN ChangeMe
1.0000 a G or T =69A 1.0000 A ChngeMe
p1 arg 0e - 1 +
!----- 70 -----
RPN ChangeMe
1.0000 a G or T =70A 1.0000 A ChngeMe
U1 mag 0f /
!----- 71 -----
RPN ChangeMe
1.0000 a G or T =71A 1.0000 A ChngeMe
U1 arg 0g - 1 +
!----- 72 -----
RPN ChangeMe
1.0000 a G or T =72A 1.0000 A ChngeMe
0h H2k /

```

B4. Simulation of the 128-mm diameter two-stage electricity generator

```

!----- 0 -----
BEGIN
1.0135E+05 a Mean P Pa
50.980 b Freq Hz G
312.00 c TBeg K G
3679.0 d |p| Pa G
0.0000 e Ph(p) deg
4.5925E-02 f |U| m^3/s G
39.387 g Ph(U) deg G
74.803 h Htot W G
air Gas type
!----- 1 -----
DUCT Dummy to allow for JOIN
3.7700E-02 a Area m^2 3691.2 A |p| Pa

```

```

0.8400 b Perim m          -0.37238 B Ph(p) deg
7.0000E-02 c Length m    3.6098E-02 C |U| m^3/s
5.0000E-04 d Srough      11.413 D Ph(U) deg
74.803 E Htot W
ideal      Solid type     65.219 F Edot W
!----- 2 -----
RPN      ph(Z)
0.0000 a G or T          -11.785          A ChngeMe
p1 U1 / arg
!----- 3 -----
DUCT      Change Me
2.8200E-02 a Area m^2    3691.7 A |p| Pa
0.6900 b Perim m        -0.40779 B Ph(p) deg
5.0000E-03 c Length m    3.5874E-02 C |U| m^3/s
5.0000E-04 d Srough      9.5730 D Ph(U) deg
74.803 E Htot W
ideal      Solid type     65.215 F Edot W
!----- 4 -----
HX AHX
2.8200E-02 a Area m^2    3671.7 A |p| Pa
0.6200 b GasA/A          -1.0735 B Ph(p) deg
4.8000E-02 c Length m    3.4220E-02 C |U| m^3/s
5.0000E-04 d y0 m        -3.8755 D Ph(U) deg
-403.27 e HeatIn W      G   -328.47 E Htot W
300.00 f SolidT K        62.747 F Edot W
312.00 G GasT K
ideal      Solid type     298.90 H SolidT K
!----- 5 -----
RPN      ChangeMe
312.00 a G or T          =5A  312.00          A ChngeMe
Tm
!----- 6 -----
DUCT      Cold gap
sameas 4a a Area m^2     3671.4 A |p| Pa
0.6900 b Perim m        -1.1217 B Ph(p) deg
7.0000E-03 c Length m    3.4335E-02 C |U| m^3/s
5.0000E-04 d Srough      -6.609 D Ph(U) deg
-328.47 E Htot W
ideal      Solid type     62.741 F Edot W
!----- 7 -----
RPN      IZI
0.0000 a G or T          7.5252          A ChngeMe
p1 U1 / mag rho / a / 6a *
!----- 8 -----
RPN      ph(Z)
0.0000 a G or T          5.4873          A ChngeMe
p1 U1 / arg
!----- 9 -----
STKSCREEN Screen regenerator
3.0000E-02 a Area m^2    3168.3 A |p| Pa
0.8315 b VolPor          1.1380 B Ph(p) deg
3.0000E-02 c Length m    8.0813E-02 C |U| m^3/s
1.9800E-04 d rh m        -20.645 D Ph(U) deg
0.1000 e ksFrac          -328.47 E Htot W
118.88 F Edot W
312.00 G TBeg K
stainless Solid type     732.56 H TEnd K
!----- 10 -----
RPN dk/rh
0.0000 a G or T          4.2196          A ChngeMe
dk 9d /
!----- 11 -----
RPN      IZI
0.0000 a G or T          4.4977          A ChngeMe
p1 U1 / mag rho / a / 9a *
!----- 12 -----

```

```

RPN    ph(Z)
      0.0000 a G or T          21.783          A ChngeMe
p1 U1 / arg
!----- 13 -----
RPN    Net Power
      0.0000 a G or T          56.137          A POWER N
9F 6F -
!----- 14 -----
DUCT   Hot gap
3.0000E-02 a Area m^2      Mstr    3168.1  A |p| Pa
      0.61401 b Perim m      14a    1.1310  B Ph(p) deg
1.0000E-03 c Length m          8.0892E-02 C |U| m^3/s
5.0000E-04 d Srough          -20.787  D Ph(U) deg
      -328.47  E Htot W
ideal   Solid type          118.88  F Edot W
!----- 15 -----
VXQ1 HHX
3.0000E-02 a Area m^2          3101.4  A |p| Pa
      0.4000 b GasA/A          -1.0788  B Ph(p) deg
8.5611E-02 c SolA/A          8.4899E-02 C |U| m^3/s
4.3000E-03 d rh m            -27.573  D Ph(U) deg
8.0000E-03 e LenTS1 m          130.38  E Htot W
      0.1040 f Len P1 m          117.83  F Edot W
8.0000E-03 g LenTS2 m          810.40  G TSolBeg P1 K
458.84 h HeatP1 W      G      808.15  H TSolEnd P1 K
ideal   Solid type
!----- 16 -----
RPN    ChangeMe
      746.96 a G or T          808.15          A ChngeMe
15H
!----- 17 -----
STKDUCT TBT 1
3.0680E-02 a Area m^2          3095.5  A |p| Pa
      0.7320 b Perim m          -1.2792  B Ph(p) deg
2.8000E-02 c Length m          8.7719E-02 C |U| m^3/s
1.4800E-03 d WallA m^2          -31.107  D Ph(U) deg
      130.38  E Htot W
      117.78  F Edot W
      732.56  G TBeg K
stainless Solid type          721.35  H TEnd K
!----- 18 -----
STKCONE TBT 2
3.0680E-02 a Areal m^2          3065.9  A |p| Pa
      0.7320 b Periml m          -2.0864  B Ph(p) deg
8.0000E-02 c Length m          9.4793E-02 C |U| m^3/s
1.6900E-02 d AreaF m^2          -38.021  D Ph(U) deg
      0.5200 e PerimF m          130.38  E Htot W
2.7322E-03 f f_wall          117.66  F Edot W
      721.35  G TBeg K
stainless Solid type          683.55  H TEnd K
!----- 19 -----
MINOR   Minor loss due to Area Suden change of Cone
1.6900E-02 a Area m^2          3059.1  A |p| Pa
      1.2200 b K+          -1.9939  B Ph(p) deg
      1.2200 c K-          9.4793E-02 C |U| m^3/s
      -38.021  D Ph(U) deg
      130.38  E Htot W
      117.26  F Edot W
!----- 20 -----
STKDUCT TBT 3
1.6900E-02 a Area m^2          3027.7  A |p| Pa
      0.5200 b Perim m          -2.7614  B Ph(p) deg
5.0000E-02 c Length m          9.8192E-02 C |U| m^3/s
1.0400E-04 d WallA m^2          -40.74  D Ph(U) deg
      130.38  E Htot W
      117.17  F Edot W

```

```

683.55 G TBeg K
stainless Solid type 586.22 H TEnd K
!----- 21 -----
MINOR Sudden change
1.3000E-02 a Area m^2 3026.6 A |p| Pa
0.1000 b K+ -2.7444 B Ph(p) deg
0.1000 c K- 9.8192E-02 C |U| m^3/s
-40.74 D Ph(U) deg
130.38 E Htot W
117.10 F Edot W
!----- 22 -----
STKDUCT TBT 4
1.3000E-02 a Area m^2 Mstr 2771.0 A |p| Pa
0.40418 b Perim m 22a -8.8749 B Ph(p) deg
0.2000 c Length m 0.10869 C |U| m^3/s
2.5447E-04 d WallA m^2 -48.005 D Ph(U) deg
130.38 E Htot W
116.82 F Edot W
586.22 G TBeg K
stainless Solid type 344.03 H TEnd K
!----- 23 -----
JOIN Adiabatic/isothermal interface
2771.0 A |p| Pa
-8.8749 B Ph(p) deg
0.10813 C |U| m^3/s
-48.005 D Ph(U) deg
130.38 E Htot W
116.22 F Edot W
344.03 G TBeg K
345.00 H TEnd K
!----- 24 -----
HX Dummy 2nd AHX
1.3000E-02 a Area m^2 2768.4 A |p| Pa
1.0000 b GasA/A -8.9168 B Ph(p) deg
1.0000E-03 c Length m 0.10818 C |U| m^3/s
1.0000E-03 d y0 m -48.043 D Ph(U) deg
-14.208 e HeatIn W G 116.17 E Htot W
300.00 f SolidT K 116.17 F Edot W
345.00 G GasT K
ideal Solid type 329.36 H SolidT K
!----- 25 -----
RPN ChangeMe
1.0000 a G or T =25A 1.0000 A ChngeMe
H2k Edot /
!----- 26 -----
DUCT Change Me
1.2868E-02 a Area m^2 2354.2 A |p| Pa
0.40208 b Perim m -21.155 B Ph(p) deg
0.2350 c Length m 0.1187 C |U| m^3/s
5.0000E-04 d Srough -55.114 D Ph(U) deg
116.17 E Htot W
ideal Solid type 115.89 F Edot W
!----- 27 -----
TBRANCH Alternator branch
2.0974E+04 a Re(Zb) Pa-s/m^3 G 2354.2 A |p| Pa
3.9594E+04 b Im(Zb) Pa-s/m^3 G -21.155 B Ph(p) deg
5.2542E-02 C |U| m^3/s
-83.244 D Ph(U) deg
28.951 E HtotBr W
28.951 F EdotBr W
86.944 G EdotTr W
!----- 28 -----
DUCT Change Me
2.3760E-03 a Area m^2 Mstr 1147.2 A |p| Pa
0.1728 b Perim m 28a -60.829 B Ph(p) deg
0.2200 c Length m 5.4049E-02 C |U| m^3/s

```

```

5.0000E-04 d Srough          -84.619 D Ph(U) deg
28.951 E Htot W
ideal      Solid type      28.367 F Edot W
!----- 29 -----
CONE      Change Me
2.3760E-03 a Areal m^2      Mstr      1110.8 A |p| Pa
0.1728 b Periml m          29a      -65.341 B Ph(p) deg
2.2000E-02 c Length m      Mstr      5.4138E-02 C |U| m^3/s
7.0880E-03 d AreaF m^2      Mstr      -84.87 D Ph(U) deg
0.29845 e PerimF m          29d      28.951 E Htot W
5.0000E-04 f Srough          28.340 F Edot W
ideal      Solid type
!----- 30 -----
RPN      IZI
0.0000 a G or T            1.1846          A ChngeMe
p1 U1 / mag rho / a / 33a *
!----- 31 -----
RPN      ChangeMe
0.0000 a G or T            19.529          A ChngeMe
p1 U1 / arg
!----- 32 -----
RPN      P5
1042.1 a G or T            1110.8          A P5
p1 mag
!----- 33 -----
IESPEAKER BC-6PS38 Loudspeaker (Measured alternator parameters)
2.2000E-02 a Area m^2      2.0725E-09 A |p| Pa
5.3000 b R ohms            154.31 B Ph(p) deg
4.7000E-04 c L H            5.4134E-02 C |U| m^3/s
10.694 d BLProd T-m        -84.871 D Ph(U) deg
2.7446E-02 e M kg          13.715 E Htot W
1725.5 f K N/m              -2.8740E-11 F Edot W
1.3640 g Rm N-s/m          -15.236 G Workln W
-1.840 h ||| A G           16.560 H Volts V
-5305.5 i Ph(l) deg G       1.8400 I Amps A
180.00 J Ph(Ze) deg
1110.8 K |Px| Pa
ideal      Solid type      114.66 L Ph(Px) deg
!----- 34 -----
RPN      IZI
0.0000 a G or T            2.2103E-12      A ChngeMe
p1 U1 / mag rho / a / 33a *
!----- 35 -----
RPN      ph(Z)
0.0000 a G or T            -120.82         A ChngeMe
p1 U1 / arg
!----- 36 -----
RPN Load Resistance
9.0000 a G or T            =36A 9.0000     A Ohm
33H 33I /
!----- 37 -----
RPN      Electrical output
119.30 a G or T            15.236          A We
33G -1 *
!----- 38 -----
RPN      Stage-1- efficiency
0.0000 a G or T            12.234          A S1-e
13A 15h / 100 *
!----- 39 -----
RPN      Stage-2-effeciency
0.0000 a G or T            7.3177          A S2-e
75A 79h / 100 *
!----- 40 -----
RPN      generator efficiency
8.0000 a G or T            2.5567          A H-We-e
37A 15h 79h + / 100 *

```

```

!----- 41 -----
RPN    Heat-Acoustic effeciency
      0.0000 a G or T      4.7557      A H-A-e
29F 15h 79h + / 100 *
!----- 42 -----
RPN    Alternator efficiency %
      0.0000 a G or T      53.761      A A-We-e
37A 29F / 100 *
!----- 43 -----
RPN    Alternator 0-peak stroke
      7.9936 a G or T      7.6819      A mm
U1 mag w / 33a / 1000 *
!----- 44 -----
RPN    Force electrical load to be resistive
      180.00 a G or T      =44A  180.00      A ChngeMe
33J
!----- 45 -----
SOFTEND Change Me
      0.0000 a Re(z)      =45G  2.0725E-09 A |p| Pa
      0.0000 b Im(z)      =45H  154.31 B Ph(p) deg
      0.0000 c Htot W      5.4134E-02 C |U| m^3/s
                          -84.871 D Ph(U) deg
                          13.715 E Htot W
                          -2.8740E-11 F Edot W
                          -1.1324E-12 G Re(z)
                          -1.8981E-12 H Im(z)
                          345.00 I T K
!----- 46 -----
DUCT   Change Me
      1.2868E-02 a Area m^2      2121.4 A |p| Pa
      0.4021 b Perim m      -43.859 B Ph(p) deg
      0.4450 c Length m      8.3659E-02 C |U| m^3/s
      5.0000E-04 d Srough      -56.294 D Ph(U) deg
                          87.219 E Htot W
ideal   Solid type      86.654 F Edot W
!----- 47 -----
TBRANCH Stub branch
      143.82 a Re(Zb) Pa-s/m^3 G      2121.4 A |p| Pa
      -2.1985E+04 b Im(Zb) Pa-s/m^3 G      -43.859 B Ph(p) deg
                          9.6490E-02 C |U| m^3/s
                          45.767 D Ph(U) deg
                          0.6695 E HtotBr W
                          0.6695 F EdotBr W
                          85.984 G EdotTr W
!----- 48 -----
DUCT   Change Me
      1.2868E-02 a Area m^2      2744.9 A |p| Pa
      0.40212 b Perim m      -44.02 B Ph(p) deg
      0.2800 c Length m      7.6549E-02 C |U| m^3/s
      5.0000E-04 d Srough      45.733 D Ph(U) deg
                          0.6695 E Htot W
ideal   Solid type      0.45331 F Edot W
!----- 49 -----
DUCT   Change Me
      1.2868E-02 a Area m^2 Mstr 3562.0 A |p| Pa
      0.4021 b Perim m 49a -44.154 B Ph(p) deg
      0.8000 c Length m      4.4322E-14 C |U| m^3/s
      5.0000E-04 d Srough      -134.12 D Ph(U) deg
                          0.6695 E Htot W
ideal   Solid type      4.5290E-14 F Edot W
!----- 50 -----
HARDEND Change Me
      0.0000 a R(1/z)      =50G  3562.0 A |p| Pa
      0.0000 b I(1/z)      =50H  -44.154 B Ph(p) deg
      0.0000 c Htot W      4.4322E-14 C |U| m^3/s
                          -134.12 D Ph(U) deg

```

0.6695 E Htot W
 4.5290E-14 F Edot W
 2.1141E-16 G R(1/z)
 -3.6848E-13 H I(1/z)

!----- 51 -----

MINOR Change Me
 1.2868E-02 a Area m^2 2089.1 A |p| Pa
 1.1000 b K+ -42.587 B Ph(p) deg
 1.1000 c K- 0.14029 C |U| m^3/s
 -98.561 D Ph(U) deg
 86.550 E Htot W
 82.000 F Edot W

!----- 52 -----

DUCT Change Me
 1.2868E-02 a Area m^2 Mstr 1515.9 A |p| Pa
 0.40212 b Perim m 52a -57.757 B Ph(p) deg
 0.2000 c Length m 0.14838 C |U| m^3/s
 5.0000E-04 d Srough -101.18 D Ph(U) deg
 86.550 E Htot W
 ideal Solid type 81.677 F Edot W

!----- 53 -----

DUCT Change Me
 1.2868E-02 a Area m^2 Mstr 1209.5 A |p| Pa
 0.40212 b Perim m 53a -75.558 B Ph(p) deg
 0.1350 c Length m 0.15151 C |U| m^3/s
 5.0000E-04 d Srough -102.82 D Ph(U) deg
 86.550 E Htot W
 ideal Solid type 81.451 F Edot W

!----- 54 -----

MINOR 90 degree bend (minor losses)
 1.2868E-02 a Area m^2 1151.0 A |p| Pa
 1.1000 b K+ -74.048 B Ph(p) deg
 1.1000 c K- 0.15151 C |U| m^3/s
 -102.82 D Ph(U) deg
 86.550 E Htot W
 76.434 F Edot W

!----- 55 -----

DUCT Change Me
 1.2868E-02 a Area m^2 Mstr 999.56 A |p| Pa
 0.40212 b Perim m 55a -101.24 B Ph(p) deg
 0.1350 c Length m 0.1527 C |U| m^3/s
 5.0000E-04 d Srough -104.3 D Ph(U) deg
 86.550 E Htot W
 ideal Solid type 76.205 F Edot W

!----- 56 -----

DUCT Change Me
 1.2868E-02 a Area m^2 Mstr 1120.8 A |p| Pa
 0.40212 b Perim m 56a -132.64 B Ph(p) deg
 0.1500 c Length m 0.1517 C |U| m^3/s
 5.0000E-04 d Srough -105.94 D Ph(U) deg
 86.550 E Htot W
 ideal Solid type 75.951 F Edot W

!----- 57 -----

MINOR 90 degree bend (minor losses)
 1.2868E-02 a Area m^2 1062.0 A |p| Pa
 1.1000 b K+ -134.25 B Ph(p) deg
 1.1000 c K- 0.1517 C |U| m^3/s
 -105.94 D Ph(U) deg
 86.550 E Htot W
 70.914 F Edot W

!----- 58 -----

DUCT Change Me
 1.2868E-02 a Area m^2 Mstr 1380.1 A |p| Pa
 0.40212 b Perim m 58a -153.81 B Ph(p) deg
 0.1350 c Length m 0.14873 C |U| m^3/s
 5.0000E-04 d Srough -107.35 D Ph(U) deg

```

86.550 E Htot W
ideal Solid type 70.689 F Edot W
!----- 59 -----
DUCT Change Me
1.2868E-02 a Area m^2 Mstr 1610.3 A |p| Pa
0.40212 b Perim m 59a -161.34 B Ph(p) deg
8.0000E-02 c Length m 0.14605 C |U| m^3/s
5.0000E-04 d Srough -108.21 D Ph(U) deg
86.550 E Htot W
ideal Solid type 70.559 F Edot W
!----- 60 -----
RPN P1
0.0000 a G or T 1610.3 A P1
p1 mag
!----- 61 -----
DUCT FBP 2 Feedback Pipe before Stub
1.2868E-02 a Area m^2 Mstr 3603.2 A |p| Pa
0.16443 b Perim m 61a 174.48 B Ph(p) deg
0.7000 c Length m 9.7357E-02 C |U| m^3/s
5.0000E-04 d Srough -119.1 D Ph(U) deg
86.550 E Htot W
ideal Solid type 70.156 F Edot W
!----- 62 -----
RPN P2
3603.2 a G or T =62A 3603.2 A P2
p1 mag
!----- 63 -----
DUCT Change Me
1.2868E-02 a Area m^2 Mstr 3935.8 A |p| Pa
0.40212 b Perim m 63a 172.13 B Ph(p) deg
0.1600 c Length m 8.1343E-02 C |U| m^3/s
5.0000E-04 d Srough -123.79 D Ph(U) deg
86.550 E Htot W
ideal Solid type 69.977 F Edot W
!----- 64 -----
DUCT Change Me
1.6900E-02 a Area m^2 4003.4 A |p| Pa
0.5200 b Perim m 171.63 B Ph(p) deg
5.0000E-02 c Length m 7.4562E-02 C |U| m^3/s
5.0000E-04 d Srough -126.3 D Ph(U) deg
86.550 E Htot W
ideal Solid type 69.921 F Edot W
!----- 65 -----
CONE Change Me
1.6900E-02 a Areal m^2 4077.7 A |p| Pa
0.5200 b Periml m 170.99 B Ph(p) deg
0.1000 c Length m 5.4078E-02 C |U| m^3/s
3.7700E-02 d AreaF m^2 -138.29 D Ph(U) deg
0.8400 e PerimF m 86.550 E Htot W
5.0000E-04 f Srough 69.800 F Edot W
ideal Solid type
!----- 66 -----
DUCT Change Me
3.7700E-02 a Area m^2 4095.8 A |p| Pa
0.8400 b Perim m 170.69 B Ph(p) deg
7.0000E-02 c Length m 3.8334E-02 C |U| m^3/s
5.0000E-04 d Srough -161.92 D Ph(U) deg
86.550 E Htot W
ideal Solid type 69.704 F Edot W
!----- 67 -----
DUCT Change Me
2.8200E-02 a Area m^2 4096.8 A |p| Pa
0.6900 b Perim m 170.67 B Ph(p) deg
5.0000E-03 c Length m 3.7748E-02 C |U| m^3/s
5.0000E-04 d Srough -163.67 D Ph(U) deg
86.550 E Htot W

```

```

ideal      Solid type      69.698 F Edot W
!----- 68 -----
HX AHX
2.8200E-02 a Area m^2      4086.3 A |p| Pa
0.6200 b GasA/A          170.05 B Ph(p) deg
4.8000E-02 c Length m     3.3406E-02 C |U| m^3/s
5.0000E-04 d y0 m        -177.4 D Ph(U) deg
-146.25 e HeatIn W      G   -59.702 E Htot W
340.00 f SolidT K        66.623 F Edot W
                          345.00 G GasT K
ideal      Solid type      340.29 H SolidT K
!----- 69 -----
RPN      ChangeMe
345.00 a G or T      =69A 345.00      A ChngeMe
Tm
!----- 70 -----
DUCT Cold gap
2.8200E-02 a Area m^2      4086.8 A |p| Pa
0.6900 b Perim m          170.01 B Ph(p) deg
7.0000E-03 c Length m     3.3054E-02 C |U| m^3/s
5.0000E-04 d Srough      179.51 D Ph(U) deg
                          -59.702 E Htot W
ideal      Solid type      66.615 F Edot W
!----- 71 -----
RPN |Z|
0.0000 a G or T          9.1500      A ChngeMe
p1 U1 / mag rho / a / 70a *
!----- 72 -----
RPN ph(Z)
0.0000 a G or T          -9.5003      A ChngeMe
p1 U1 / arg
!----- 73 -----
STKSCREEN Screen regenerator
3.0000E-02 a Area m^2      3821.8 A |p| Pa
0.8311 b VolPor          169.80 B Ph(p) deg
3.0000E-02 c Length m     4.0400E-02 C |U| m^3/s
1.9800E-04 d rh m        162.93 D Ph(U) deg
0.1000 e ksFrac          -59.702 E Htot W
                          76.646 F Edot W
                          345.00 G TBeg K
stainless  Solid type      438.05 H TEnd K
!----- 74 -----
RPN dk/rh
0.0000 a G or T          2.6713      A ChngeMe
dk 73d /
!----- 75 -----
RPN Net power
0.0000 a G or T          10.030      A POWER
Edot 70F -
!----- 76 -----
RPN |Z|
0.0000 a G or T          8.3920      A ChngeMe
p1 U1 / mag rho / a / 73a *
!----- 77 -----
RPN ph(Z)
0.0000 a G or T          6.8686      A ChngeMe
p1 U1 / arg
!----- 78 -----
DUCT      Change Me
3.0000E-02 a Area m^2      Mstr 3821.7 A |p| Pa
0.61399 b Perim m        78a 169.79 B Ph(p) deg
1.0000E-03 c Length m     4.0431E-02 C |U| m^3/s
5.0000E-04 d Srough      162.56 D Ph(U) deg
                          -59.702 E Htot W
ideal      Solid type      76.645 F Edot W
!----- 79 -----

```

```

VXQ1 HHX
3.0000E-02 a Area m^2      3786.6 A |p| Pa
0.4000 b GasA/A          168.18 B Ph(p) deg
8.6511E-02 c SolA/A      4.3434E-02 C |U| m^3/s
4.3000E-03 d rh m        145.65 D Ph(U) deg
8.0000E-03 e LenTS1 m    77.369 E Htot W
0.1040 f Len P1 m        75.961 F Edot W
8.0000E-03 g LenTS2 m    488.94 G TSolBeg P1 K
137.07 h HeatP1 W       G 488.94 H TSolEnd P1 K
ideal      Solid type
!----- 80 -----
RPN      ChangeMe
492.57  a G or T          488.94      A ChngeMe
79H
!----- 81 -----
JOIN     Change Me
3786.6  A |p| Pa
168.18  B Ph(p) deg
4.3070E-02 C |U| m^3/s
145.65  D Ph(U) deg
77.369  E Htot W
75.325  F Edot W
438.05  G TBeg K
437.95  H TEnd K
!----- 82 -----
STKDUCT TBT 1
3.0680E-02 a Area m^2      3781.8 A |p| Pa
0.7320 b Perim m          168.04 B Ph(p) deg
2.8000E-02 c Length m     4.6365E-02 C |U| m^3/s
1.4800E-03 d WallA m^2    137.21 D Ph(U) deg
77.369  E Htot W
75.288  F Edot W
437.95  G TBeg K
stainless Solid type      435.42 H TEnd K
!----- 83 -----
STKCONE TBT 2
3.0810E-02 a Areal m^2     3750.8 A |p| Pa
0.7320 b Periml m         167.48 B Ph(p) deg
8.0000E-02 c Length m     5.6223E-02 C |U| m^3/s
1.6900E-02 d AreaF m^2    122.97 D Ph(U) deg
0.5200 e PerimF m        77.369 E Htot W
2.7322E-03 f f_wall       75.196 F Edot W
435.42  G TBeg K
stainless Solid type      425.89 H TEnd K
!----- 84 -----
MINOR    Change Me
1.6900E-02 a Area m^2      3747.4 A |p| Pa
1.2200 b K+                167.53 B Ph(p) deg
1.2200 c K-                5.6223E-02 C |U| m^3/s
122.97  D Ph(U) deg
77.369  E Htot W
75.063  F Edot W
!----- 85 -----
STKDUCT TBT 3
1.6900E-02 a Area m^2      3711.7 A |p| Pa
0.5200 b Perim m          167.02 B Ph(p) deg
5.0000E-02 c Length m     6.1384E-02 C |U| m^3/s
1.0400E-04 d WallA m^2    118.20 D Ph(U) deg
77.369  E Htot W
75.015  F Edot W
425.89  G TBeg K
stainless Solid type      387.85 H TEnd K
!----- 86 -----
MINOR    Change Me
1.3000E-02 a Area m^2      3711.1 A |p| Pa
0.1000 b K+                167.03 B Ph(p) deg

```

```

0.1000 c K-                6.1384E-02 C |U| m^3/s
                            118.20 D Ph(U) deg
                            77.369 E Htot W
                            74.989 F Edot W
!----- 87 -----
STKDUCT TBT 4
1.3000E-02 a Area m^2 Mstr 3423.6 A |p| Pa
0.40418 b Perim m 87a 163.62 B Ph(p) deg
0.2000 c Length m 7.8082E-02 C |U| m^3/s
2.5447E-04 d WallA m^2 107.67 D Ph(U) deg
                            77.369 E Htot W
                            74.844 F Edot W
                            387.85 G TBeg K
stainless Solid type 302.29 H TEnd K
!----- 88 -----
HX Dummy 2nd AHX
1.3000E-02 a Area m^2 3421.0 A |p| Pa
1.0000 b GasA/A 163.60 B Ph(p) deg
1.0000E-03 c Length m 7.8167E-02 C |U| m^3/s
8.1716E-04 d y0 m 107.62 D Ph(U) deg
-2.5658 e HeatIn W G 74.803 E Htot W
300.00 f SolidT K =88H 74.803 F Edot W
                            302.29 G GasT K
ideal Solid type 300.00 H SolidT K
!----- 89 -----
RPN ChangeMe
1.0000 a G or T =89A 1.0000 A ChngeMe
Htot Edot /
!----- 90 -----
RPN ChangeMe
330.00 a G or T 330.00 A ChngeMe
90a =Tm
!----- 91 -----
DUCT Change Me
1.2868E-02 a Area m^2 2205.0 A |p| Pa
0.40212 b Perim m 147.65 B Ph(p) deg
0.5450 c Length m 0.11625 C |U| m^3/s
5.0000E-04 d Srough 93.049 D Ph(U) deg
                            74.803 E Htot W
ideal Solid type 74.253 F Edot W
!----- 92 -----
RPN P3
0.0000 a G or T 2205.0 A P3
p1 mag
!----- 93 -----
DUCT Change Me
1.2868E-02 a Area m^2 Mstr 1419.4 A |p| Pa
0.40212 b Perim m 93a 123.83 B Ph(p) deg
0.3250 c Length m 0.1288 C |U| m^3/s
5.0000E-04 d Srough 87.734 D Ph(U) deg
                            74.803 E Htot W
ideal Solid type 73.859 F Edot W
!----- 94 -----
DUCT Change Me
1.2868E-02 a Area m^2 Mstr 1193.7 A |p| Pa
0.40212 b Perim m 94a 105.59 B Ph(p) deg
0.1350 c Length m 0.13123 C |U| m^3/s
5.0000E-04 d Srough 85.770 D Ph(U) deg
                            74.803 E Htot W
ideal Solid type 73.687 F Edot W
!----- 95 -----
MINOR 90 degree bend (minor losses)
1.2868E-02 a Area m^2 1145.0 A |p| Pa
1.1000 b K+ 106.47 B Ph(p) deg
1.1000 c K- 0.13123 C |U| m^3/s
85.770 D Ph(U) deg

```

```

74.803 E Htot W
70.278 F Edot W
!-----96-----
DUCT Change Me
1.2868E-02 a Area m^2 Mstr 1063.3 A |p| Pa
0.40212 b Perim m 96a 81.923 B Ph(p) deg
0.1350 c Length m 0.13195 C |U| m^3/s
5.0000E-04 d Srough 83.947 D Ph(U) deg
74.803 E Htot W
ideal Solid type 70.105 F Edot W
!-----97-----
DUCT Change Me
1.2868E-02 a Area m^2 Mstr 1066.1 A |p| Pa
0.40212 b Perim m 97a 79.076 B Ph(p) deg
1.5000E-02 c Length m 0.13192 C |U| m^3/s
5.0000E-04 d Srough 83.745 D Ph(U) deg
74.803 E Htot W
ideal Solid type 70.086 F Edot W
!-----98-----
DUCT Change Me
1.2869E-02 a Area m^2 Mstr 1193.0 A |p| Pa
0.40213 b Perim m 98a 55.655 B Ph(p) deg
0.1350 c Length m 0.1307 C |U| m^3/s
5.0000E-04 d Srough 81.921 D Ph(U) deg
74.803 E Htot W
ideal Solid type 69.912 F Edot W
!-----99-----
MINOR 90 degree bend (minor losses)
1.2868E-02 a Area m^2 1147.1 A |p| Pa
1.1000 b K+ 54.515 B Ph(p) deg
1.1000 c K- 0.1307 C |U| m^3/s
81.921 D Ph(U) deg
74.803 E Htot W
66.545 F Edot W
!-----100-----
DUCT Change Me
1.2868E-02 a Area m^2 Mstr 1417.1 A |p| Pa
0.40212 b Perim m 100a 37.297 B Ph(p) deg
0.1350 c Length m 0.12775 C |U| m^3/s
5.0000E-04 d Srough 80.135 D Ph(U) deg
74.803 E Htot W
ideal Solid type 66.375 F Edot W
!-----101-----
DUCT FBP 3 Feedback Pipe after stub
1.2868E-02 a Area m^2 Mstr 3291.0 A |p| Pa
0.40212 b Perim m 101a 4.1190 B Ph(p) deg
0.7750 c Length m 8.1709E-02 C |U| m^3/s
5.0000E-04 d Srough 64.945 D Ph(U) deg
74.803 E Htot W
ideal Solid type 65.541 F Edot W
!-----102-----
RPN P4
3291.0 a G or T =102A 3291.0 A P4
p1 mag
!-----103-----
DUCT Change Me
1.2868E-02 a Area m^2 Mstr 3566.0 A |p| Pa
0.40212 b Perim m 103a 1.3637 B Ph(p) deg
0.1600 c Length m 6.7937E-02 C |U| m^3/s
5.0000E-04 d Srough 58.683 D Ph(U) deg
74.803 E Htot W
ideal Solid type 65.407 F Edot W
!-----104-----
DUCT Change Me
1.6900E-02 a Area m^2 Mstr 3620.8 A |p| Pa
0.46084 b Perim m 104a 0.76871 B Ph(p) deg

```

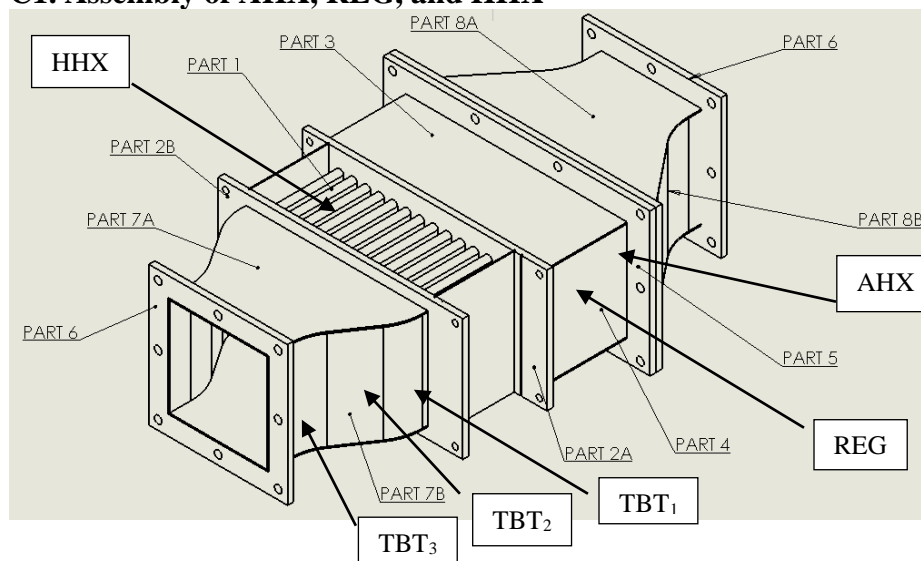
```

5.0000E-02 c Length m          6.2234E-02 C |U| m^3/s
5.0000E-04 d Srough            55.305 D Ph(U) deg
                                74.803 E Htot W
ideal      Solid type          65.370 F Edot W
!-----105 -----
CONE Cone next to AHX
1.6900E-02 a Areal m^2 Mstr 3679.0 A |p| Pa
0.46084 b Periml m 105a -1.7489E-10 B Ph(p) deg
0.1000 c Length m 4.5925E-02 C |U| m^3/s
3.7700E-02 d AreaF m^2 Mstr 39.387 D Ph(U) deg
0.68831 e PerimF m 105d 74.803 E Htot W
5.0000E-04 f Srough 65.290 F Edot W
ideal      Solid type
!-----106 -----
RPN Set p1 mag
1.0000 a G or T =106A 1.0000 A ChngeMe
p1 mag 0d /
!-----107 -----
RPN Set p1 phase
1.0000 a G or T =107A 1.0000 A ChngeMe
p1 arg 0e - 1 +
!-----108 -----
RPN Set mag U1
1.0000 a G or T =108A 1.0000 A ChngeMe
U1 mag 0f /
!-----109 -----
RPN Set U1 phase
1.0000 a G or T =109A 1.0000 A ChngeMe
U1 arg 0g - 1 +
!-----110 -----
RPN Set Hdot
1.0000 a G or T =110A 1.0000 A ChngeMe
1E H2k /

```

Appendix C: Detail of thermoacoustic core design for 128-mm systems

C1. Assembly of AHX, REG, and HHX



C2. Detail of HHX construction

